

**Magnetism and Laser Induced Crystallization of BaTiO<sub>3</sub>,  
and Ultrafast demagnetization of Ni films**

A thesis submitted in partial fulfilment of the requirements for the award of the  
degree of

**DOCTOR OF PHILOSOPHY**

In

**PHYSICS**

By

**S RAMAKANTH**



**Advanced Centre of Research in High Energy Materials  
School of Physics, University of Hyderabad  
Hyderabad - 500 046,  
Telangana, India**

**APRIL 2017**



## DECLARATION

I hereby declare that the matter embodied in this thesis entitled “**Magnetism and laser induced crystallization BaTiO<sub>3</sub> and ultrafast demagnetization of Ni films**” is submitted to the University of Hyderabad in partial fulfillment for the award of **Doctor of Philosophy in Physics** is an original research work carried out by me under the supervision of Prof. K C James Raju, in Advanced Centre of Research in High Energy Materials, School of Physics, University of Hyderabad. I also declare that this work has not been submitted previously in part or in full to this University or any other University or Institute for the award of any degree or diploma.

**A report on plagiarism statistics from University of Hyderabad library is also enclosed.**

Place: Hyderabad

Date:

S Ramakanth  
Reg. No. 09ACPA06



## CERTIFICATE

This is to certify that the thesis entitled, “**Magnetism and Laser Induced Crystallization of BaTiO<sub>3</sub>, and Ultrafast demagnetization Ni films**” Submitted by **S Ramakanth** bearing registration number **09ACPA06**. In the partial fulfilment of the requirements for award of doctor of philosophy in Physics at ACRHEM, School of Physics is a bonafide work carried out by him under my supervision and guidance.

This Thesis is free from plagiarism and has not been submitted previously in part or in full to this or any other University or Institution for award of any degree or diploma. Parts of this thesis have been:

A. Published in the following publications:

1. **S. Ramakanth** and K. C. James Raju, **Solid State Commun.** 187, 59 (2014). (ISSN Number: 00381098), Chapter 3, 4, 5.
2. **S. Ramakanth** and K. C. James Raju, **J. Appl. Phys.** 115, 173507 (2014). (ISSN Number: 00218979), Chapter 3, 4, 5.
3. **S. Ramakanth**, S Hamad, S Venugopal Rao, and K. C. James Raju, **AIP Advances** 5, 057139 (2015). (ISSN Number: 21583226), Chapter 3, 4, 5.
4. M. Venkatesh, **S. Ramakanth**, A.K. Chaudhary and K.C. James Raju, **Optical Materials Express** 6, 2342 (2016). (ISSN Number: 21593930) Chapter 3,7.

B. Presented in the following conferences:

5. INDO-US IWNST at NIST Berhampur, 2013 (International).
6. International Conference IUMRS-ICA-2013 at IISc. Bangalore, 2013 (International).

Further, the student has passed the following courses towards fulfilment of coursework requirement for Ph.D

Course Code	Name	Credits	Pass/fail
AC902	Primer on Lasers	2	pass
AC905	Laser Experiments	3	pass
AC906	High Energy Materials	2	pass
AC907	Shock waves and Detonation	2	pass
AC921	Matlab	2	pass
AC952	Ultrafast optics	2	pass
AC807	Research Methodology	4	pass

Supervisor  
Prof. KC James Raju  
School of  
Physics/ACRHEM

Director  
Dr.K Venkateswara Rao,  
ACRHEM

Dean of School  
Prof. Bindu A Bambah  
School of Physics



Dedicated to  
My Parents



## Acknowledgements

I feel very happy and enthusiastic to write this part of my thesis and express my gratitude to all those who have helped me. I recalled all my memories while writing this section and its great feeling.

It's my great pleasure to express my gratitude to Prof. K. C. James Raju, for his guidance and support during the entire span of my doctoral research. He never discouraged my thinking on various problems and always supportive, and gave me full freedom to think to bring out best in me.

I sincerely thank to Prof. M. Ghanashyam Krishna for his suggestions and encouragement. I sincerely thank to my doctoral committee member Prof. S. Venugopal Rao and Dr. P. Premkiran for their constant encouragement and guidance throughout my Ph.D particularly in the field of optics. I am very gratefully to thank Dr. Anik kumar Chowdary for his help in the field of THz generation.

I thank director ACRHEM Dr.K. Venkateshwara Rao for his encouragement and providing facilities and funding.

I gratefully acknowledge DRDO and DST-SERB for providing fellowship. I am very thankful to our former Dean of SOP and former Director of ACRHEM Prof. S. P. Tewari for his constant encouragement and for providing funding whenever is required.

I thank Prof. Bindu A Bambah, Dean School of Physics, and former Deans Prof. C. Bansal, Prof. S. Chaturvedi and Prof. R. Singh and faculty members of SOP for their co-operation in providing facilities in school.

I also thank Dr. G Manoj kumar for his teaching on laser course, which really helped me in getting along the laser measurements data analysis or instrument understanding.

I thank Prof. S. N. Kaul, former coordinator, Centre for nanotechnology, University of Hyderabad for allowed me to use PPMS and TEM instruments.

I thank Dr. Koteswarao and Dr. Srikanth, SEST, University of Hyderabad, for allowed me to use instruments in their department.

I sincerely, with great respect, express my gratitude to all my M.Sc teachers, who inspired me to pursue research.

I would also like to thank other faculty members of ACRHEM and school of physics.

I thank Mr. Abraham, Mr. Nagaraju, Mr. Md. Rafi, Mr. Subhash and other office staff of ACRHEM and the school for their timely help on every occasion. I am thankful to all the CIL staff members for technical support they provided.

I thank Mr. Turumalaiah, Mr. Lakshmi Narayana, Mr. Ravi Shankar, Mr. Durga Prasad, Ms. Sunitha, Smt. Deepthi for their timely help in providing technical data.

I thank Mr Bansilal and Mr Subbirami Reddy for their help during my research period.

It is with enormous pleasure that I acknowledge the support and encouragements that I received from my seniors Dr. D. Pamu, Dr. Venkata Sarvanan, Dr. Sudheendran, Dr.Uma Mahendra Kumar, Dr. Kiran, Dr. Prashanth, Mr. G. Lakhminarayana Rao, Dr. Rajeeb Brhma, Dr. Rambabu, Dr. K Vasu. In particular the initial guidance by Dr. Venkata Saravana is unforgettable.

I thank postdoctoral fellows in lab Dr Ramesh, Dr.Ahamed for their suggestions in academic issues. My special thanks to Dr. Sachin.

I would like to thank all of my Ph.D batch mates Venkatesh, G Gopala krishna, Ashwin kumar, Md. Ahmad, A Kondaiah, Leela, Nagendra, Kuladeep, Azeem, Vijay kumar, M. Geo Philip, Uma Shankar, D Rajesh for encouraging and making the whole research period worthwhile.

I thank all research scholars from ACRHEM and School of physics, I sincerely thank to all my lab mates T. Anil, S Bashaiah, K. Lakshun Naidu, K. Rama Obulesu, Umar Pasha, Ramesh, M. Sandeep, P. Santanu, Ravi, Pavan, Thirupathi, Ajith for their valuable help.

My special thanks to Anusha and Venkatesh who helped me in optics measurements.

I Thank my dearly juniors S. N. Reddy, G. Pundareekam, S Surya, Andrews, Alkathy, Sandeep Sharma, Shanker Nath , Binoy, Sudhin kumar for their timely help whenever is required.

I thank M.Sc friends from University of Hyderabad Mr. Allah Bakshu, Mr. P Ramu, Mr. Nanda Gopal Krishna, Mr. G. Vijayender, Dr. B. Venkataramana, Mr. Mohan Rao barri, Mr. K. Sreenu, Dr. Narsi reddy, Mr. BAN Murthy, Dr. M Suryanarayana, Dr. Jimin, Dr. Abhishek, Mr. Bharath, Mr. K Rama obulesu, Mr. Balunaik, Dr. R Suvarna, Ms. Daughty John, Pradeep, Pradeep Reddy, Ch. Narasimha Raju, Dr. Kaustubh Waghmare, Mrs. Shanthi, Dr. Deepthi, Mr. Sita Rama Raju, Dr. Malleshwar, Mr. Jais Tom, Mr. Chandra shekar, Dr. Fahem Bajas, Mr. Srikanth.

I thank my dear friends S Rajinikanth, T. Raghu, G.Purushotham and J Ramaveer.

I also thank my colleagues from UPGC, GDK, SU.

I acknowledge with gratitude the unconditional love and support received from my parents, brother, sisters and other members of my family.

At the end I would like to express appreciation to my beloved better half Sandhya and my daughter for always backing me in all times.

S Ramakanth



## Abstract

The present work can be classified into three categories namely the study of emergence of magnetism in Barium Titanate (BTO), crystallization of BaTiO<sub>3</sub> thin films by nano second Excimer laser of wavelength 248 nm and then finally the study of ultrafast demagnetization of Ni films. In the context of memory devices it seems necessary to probe the problem in multiple ways.

The ferromagnetic and ferroelectric bilayer based materials are under intense study. The first principle calculations for structures such as Fe/BaTiO<sub>3</sub> have shown that the interface induced charge can make the ferromagnetic to be sensitive to ferroelectric polarization and the ferroelectrics may become ferromagnetic also. Thus, the interfacial multiferroics are promising in the development of spintronic devices at room temperature. The different parameters like strain, ionic diffusion, orbital reconstruction or charge transfer can effectively alter the interfacial magnetic order. Thus, the detailed understanding of interfacial properties is also crucial in ferromagnetic/ferroelectric hetero structured spintronic devices. The interdiffusion between FE and FM layer cannot be avoided if the temperature is high.

In particular, the Barium titanate (BTO), and Lanthanum strontium manganese oxide (LSMO), ferroelectric and ferromagnetic bilayer based multiferroics are also continually being explored. But these films are not compatible with Silicon because of the diffusivity of film materials into silicon or vice versa. This heavily restricts these materials from being used in memory devices to a maximum extent. Presently the research is focused on to bypass this problem by various routes. One of them is making **BTO itself ferromagnetic by creating defects** in it, or by **reducing the crystallization temperature** of it.

Thus, the study of the origin of magnetism in BTO is highly motivated. The earlier works have explicitly explained how different phenomena in various

compounds lack the full explanation for the magnetism in  $d^0$  materials. It is also pointed out that the theoretically obtained value for a magnetic moment is not matching with experimental results. To consider these facts more accurately, we have taken the charge transfer concept in these perovskite materials (which arises from the oxygen defects) and explained the magnetism in nanocrystalline BTO. Here, we studied in detail how the exchange-correlation interactions are developing in BTO.

The nanoparticles are more suitable systems with higher concentration of defects. The nanoparticles are the best systems in which various interactions can become observable. This enables the nanostructures to exhibit multifunctionality. Thus, Spintronic device implementations require the study of functional properties of these oxides, as the coupled electronic, magnetic and optical properties of these materials are to be utilized.

Thus, as discussed above another objective of this study is reduction of crystallization temperature of ferroelectric compounds. The conventional methods like metal induced crystallization, rapid thermal annealing, the addition of fluxes, sonochemical synthesis, etc. are not successful in decreasing the crystallization temperatures to a great extent. A higher degree of crystallization at reduced temperatures is known to be achievable by the use of lasers of appropriate wavelength and pulse width.

The present vast majority of research is also focused on the speed of these devices in parallel with entanglement based concepts. The memory response time to ultrafast electric and magnetic fields is vital in determining the speed of devices. The speed of these memory structures is the next aspect in making frontier devices with these materials.

Ultrafast demagnetization in the ferromagnetic material is a core phenomenon in the development of ultrafast memory devices. Here in this case, instead of using electric and magnetic fields, the optical pulse of a laser with a

pulse width of few fs is used in flipping the spin. This flipping or demagnetization in ferromagnetic and antiferromagnetic materials is within 1-2 ps.

Initially we have prepared the BTO nanoparticles by two methods. 1. Sol-gel, 2. Sonochemical method. Four different size BTO particles of sizes ranging between 23-54 nm were prepared by sol-gel method. The BTO mesocrystals of 200 nm size were obtained which are constituted of 5-8 nm size particles were prepared by sonochemical synthesis.

The structural (phase) characterization is carried out by X-ray diffraction (XRD) and Transmission Electron Microscopy (TEM) technique. The dislocation and strain existence in the material is also quantified using these two techniques. The 23 nm and 54 nm size range particles showed the presence of compressive strain in it, whereas the 31 nm and 34 nm range particles shown the presence of tensile strain in the material. It is found that the dislocations are responsible for the observed strain in the material.

The sol-gel prepared nanoparticles show band gap variations between 2.53eV-3.20 eV. This high band gap narrowing is explained by considering the strain, electron-phonon interactions and exchange - correlation interactions in the material. The giant band gap narrowing of 2.00 eV is observed for mesocrystals. It is found that the dielectric confinement effect plays an important role in reducing the band gap to such a lower value of 2.00 eV.

The low temperature calcined four different size ranges of nanoparticles in the range of 23 nm- 54 nm exhibited super paramagnetic behavior. It is also observed that the magnetic moment increased with bandgap narrowing and hence confirms the exchange correlation interactions between the carriers. Whereas the high temperature calcined nc-BTO and mesocrystal samples show the presence of charge transfer effects in it. The field and temperature dependent magnetization measurements indicate that samples where charge transfer is absent show super paramagnetic behaviour. The samples where charge transfer is involved show

ferromagnetism with some paramagnetic contribution to it. It is found that the mesocrystals of nc-BTO are showing ferromagnetic ground states with higher  $T_c$  (=131K) compared to sol-gel prepared samples. This gives very strong hint to the increase of electron-electron interactions in these materials through dielectric confinement effect but still the paramagnetic contribution is not nullified completely but the exchange correlation interactions are very much evident from the band gap narrowing and dielectric confinement caused magnetic states. The role of charge transfer effect is discussed in view of the Stoner magnetism.

For laser induced crystallization studies the BTO films were deposited at Room Temperature (RT) by pulsed laser deposition, and then these films are annealed at various energies of Excimer laser. We successfully obtained experimentally the large area room temperature crystallization of complex oxide films using Excimer laser of wavelength 248 nm and pulse duration of 20 ns. The conservation relations based shock wave velocity calculations yield low shock velocity. This low shock speed may support the formation of laser supported combustion waves. This combustion based atomic diffusion and pressure induced lattice mending may be the basic mechanism in the crystallization of these films. The small range order can be expected even in amorphous materials and hence the pores based mending of full lattice could be expected.

As discussed above in the context of memory devices read write speed we have carried out ultrafast demagnetization studies on Ni films. Three different thicknesses of Ni films namely 65 nm, 135 nm and 1018 nm were deposited by RF magnetron sputtering. It is found that the demagnetization and recovery times are in sub ps and few ps respectively. The transfer of angular momentum from spin system to electron system is of importance in the understanding of ultrafast demagnetization phenomena. We also measured the Gilbert damping parameter from FMR measurements and used these values in calculation of demagnetization times. It is observed that the measured and calculated values are in agreement

with measured demagnetization values from pump-probe experiments. This supports the ultrafast unification theory of demagnetization at all - time scales. It is also observed that the Gilbert damping factor is increased with decrease in film thickness. The Gilbert damping factor is inversely proportional to demagnetization time also. In addition to this the films also show THz radiation emission from them and the THz radiation peak-peak amplitude is increased with increase in Gilbert damping factor.

Apart from fundamental understanding, the results hints at the immediate application in fields like

### **I. Photo voltaics/ flexible solar cells**

The band gap narrowing is very important for efficient solar cell development by absorbing solar radiation efficiently to exploit the built in electric field of the ferroelectric, for charge separation.

### **II. Flexible electronics**

As the processing temperature in laser induced crystallization decreased to RT, the materials can be developed on various substrates like paper, plastic, etc. Hence laser induced crystallization is important in the development of flexible electronics also. Thus one can integrate various types of materials extending from inorganic and organic to biological in order to achieve the multi-functionality.

### **III. THz generation and high energy materials detection/defence**

In addition to the above demagnetization of Ni, is the associated generation of THz radiation and which is very important for the detection of explosive materials.



# CONTENTS

<b>1. Introduction</b> .....	3
1.1 Introduction.....	3
1.2 Ferroelectricity.....	3
1.3 Ferromagnetism .....	4
1.4 Multiferroics .....	5
1.4.1 Dzyaloshinskii-Moriya interaction .....	6
1.4.2. Classification of multiferroics.....	7
1.4.3 Bilayer multiferroic materials .....	8
1.5 Crystal structure of BaTiO <sub>3</sub> .....	9
1.5.1 Electronic structure of BaTiO <sub>3</sub> .....	10
1.6 Optical properties of d-band perovskites .....	11
1.7 Laser matter interaction .....	11
1.8 Literature survey .....	13
1.8.1 Magnetism in d <sup>0</sup> materials.....	13
1.8.2 Laser induced crystallization .....	16
1.8.3 Ultrafast demagnetization .....	24
1.9 Aim and Objective .....	27
1.9.1 Organization of the thesis .....	31
References.....	36
<b>2. Characterization techniques</b> .....	49
2.1 X-ray diffraction (XRD) .....	49
2.1.1 Principle .....	50
2.2 Raman spectroscopy .....	51
2.3 Microscopy .....	54
2.3.1 Light Microscopy.....	55
2.3.2. Electron Microscopes.....	55
2.3.2.1 Field Emission-Scanning Electron Microscopy (FE-SEM).....	56
2.3.2.1.1 Principle.....	57

2.3.2.1.2	Technical details of Carl-Zeiss FESEM.....	59
2.3.2.2	Transmission Electron Microscopy (TEM) .....	59
2.3.2.2.1	Modes of operation of TEM.....	60
2.3.2.2.1.1	Bright - Field and Dark - Field Imaging .....	60
2.3.2.2.1.2	Selected Area Electron Diffraction (SAED) .....	61
2.3.2.2.1.3	Convergent beam Electron Diffraction (CBED).....	61
2.3.2.2.1.4	High Resolution Transmission Electron Microscopy (HRTEM).....	61
2.3.3	Atomic force microscopy.....	62
2.3.3.1	AFM Tip or Probe.....	63
2.3.3.2	Position sensitive Photo detector .....	63
2.3.3.3	Piezo electric scanner and feedback mechanism .....	63
2.3.3.4	Operating modes of AFM .....	64
2.3.3.4.1	Contact mode .....	66
2.3.3.4.2	Non contact mode .....	66
2.3.3.4.3	Tapping mode .....	66
2.4	UV/VIS/NIR Spectroscopy.....	67
2.4.1	Instrumentation of UV/VIS/NIR Spectrophotometer .....	67
2.4.2	The light source.....	67
2.4.3	The diffraction grating and the slit.....	67
2.4.4	Sample cell, reference cell .....	68
2.4.5	Detectors .....	68
2.5	Magnetic property characterizations.....	69
2.5.1	Physical Property Measurement System (PPMS).....	69
2.5.2	DC Magnetometry.....	69
2.5.3	Vibrating Sample Magnetometer (VSM).....	70
2.6	Magnetic Resonance .....	70
2.6.1	Electron Spin resonance.....	71
2.6.2	Ferromagnetic resonance .....	72
2.6.2.1	Experimental set up.....	72

2.7 Z - Scan Technique/ Nonlinear optical studies .....	73
2.8 Pump – probe Experimental details .....	74
References.....	76
<b>3. Synthesis and structural, microstructural characterization .....</b>	<b>81</b>
3.1 Introduction.....	81
3.2 Nanocrystalline-BaTiO <sub>3</sub> (nc-BTO) powder preparation.....	83
3.2.1 Sol-gel synthesis .....	83
3.2.1.1 Stoichiometric calculations .....	83
3.2.1.2 Schematic representation of sol-gel method .....	84
3.2.1.3 Drying of sol and calcinations at various temperatures .....	85
3.2.1.4 Nano crystalline BaTiO <sub>3</sub> pellet preparation .....	85
3.2.2 Structural studies by X-ray diffraction (XRD).....	85
3.2.2.1 X-ray diffraction of four different size particles .....	85
3.2.2.2 X-ray diffraction nanocrystalline pellet .....	86
3.2.3 Microstructure studies.....	87
3.2.3.1 Morphological studies by FESEM.....	87
3.2.3.2 Strain studies by TEM .....	88
3.2.3.3 TEM studies of nanocrystalline pellet .....	90
3.3 Mesocrystals .....	91
3.3.1 Mesocrystal growth mechanism.....	91
3.3.1.1 Classical and non-classical crystallization.....	91
3.3.2 Sonochemical synthesis .....	92
3.3.2.1 Irradiation with ultrasonic horn.....	93
3.3.2.2 Schematic diagram of sonochemical method.....	93
3.3.3 Structural studies by X-ray diffraction (XRD).....	94
3.3.4 Morphological studies by FESEM.....	97
3.3.5 Structural studies by Transmission Electron Microscope.....	99
3.4 RF magnetron sputtering.....	100
3.4.1 Working principle .....	101

3.5 Deposition of Ni films on Si substrates by RF magnetron sputtering.....	102
3.5.1 Deposition conditions .....	102
3.5.2 Structural studies.....	103
3.5.3 Micro structural studies by Atomic Force Microscope (AFM).....	104
3.6 Pulsed laser deposition.....	104
3.6.1 Deposition of BaTiO <sub>3</sub> films .....	105
3.7 Summary .....	105
References.....	106
<b>4. Optical Studies on BaTiO<sub>3</sub> Nanoparticles and Mesocrystals....</b>	<b>111</b>
4.1 Introduction.....	111
4.1.1 Significance of band gap narrowing in photovoltaic's .....	112
4.2 Theoretical approach to the observed band gap narrowing .....	114
4.2.1 When the carrier density is nearer to Mott critical density .....	114
4.2.2 Low carrier density with electron-phonon interactions.....	115
4.2.3 The dielectric confinement effects .....	116
4.3 UV/VIS/NIR absorption studies of BTO nanoparticles.....	117
4.3.1 Band structure analysis of BTO Nanoparticles.....	117
4.4 Photoluminescence studies in BTO Nanoparticles .....	119
4.4.1 Charge transfer studies.....	119
4.5 Raman spectroscopy of BTO nanoparticles.....	121
4.5.1 Phonon confinement in BTO Nanoparticles .....	121
4.5.2 Electron-phonon interactions in BTO Nanoparticles.....	125
4.6 Non-linear optical properties of BTO nanoparticles.....	126
4.6.1 Open Aperture Z-scan.....	126
4.6.2 Closed Aperture Z-scan .....	127
4.6.3 Charge carrier density calculation in BTO Nano particles .....	130
4.7 Band gap narrowing in BTO nanoparticles.....	132
4.8. Introduction to mesocrystals and their optical studies .....	134
4.8.1 Raman studies/phonon confinement .....	135

4.8.2 UV/VIS/NIR optical absorption studies .....	136
4.8.3 Photoluminescence .....	137
4.8.4 Giant band gap renormalization (BGR) .....	138
4.9 Summary .....	139
References.....	141
<b>5. Study of origin of magnetism in nc-BTO nanoparticles.....</b>	<b>149</b>
5.1 Introduction.....	149
5.2 Introduction to Stoner magnetism.....	151
5.3 Magnetic properties of BTO nanoparticles.....	152
5.3.1. M-H measurements for BTO nanoparticles .....	152
5.3.2. ZFC-FC measurements for BTO nanoparticles .....	153
5.3.3 Variation of magnetic moment with charge carrier density, band gap .....	156
5.4 Magnetic properties of high temperature annealed BTO .....	159
5.4.1 M-H measurements .....	159
5.4.2 Magnetic properties of BTO mesocrystals.....	161
5.4.3 Charge transfer in BTO.....	164
5.5 Modified Stoner criterion.....	169
5.6 Summary .....	170
References.....	172
<b>6. Laser induced crystallization of BaTiO<sub>3</sub> thin films .....</b>	<b>179</b>
6.1 Introduction.....	179
6.1.1 Nano second laser matter interaction .....	180
6.2 Experimental results.....	181
6.2.1 BaTiO <sub>3</sub> film deposition by pulsed laser deposition.....	181
6.2.2 Laser annealing of PLD deposited films .....	182
6.3 Laser induced crystallization mechanism .....	182
6.4 Results and discussions.....	185
6.4.1 Microstructural studies by FESEM.....	185
6.4.2 X-ray diffraction studies .....	187

6.4.3 Raman studies .....	189
6.5 Summary .....	191
References.....	192
<b>7. Ultrafast demagnetization of Ni films .....</b>	<b>195</b>
7.1 Introduction.....	195
7.2 Magnetic studies of Ni films.....	196
7.2.1 M-H measurements .....	196
7.2.2 FMR measurements .....	197
7.2.3 Gilbert damping parameter calculation from FMR.....	198
7.3 Ultrafast demagnetization studies .....	199
7.3.1 Landau-Lifshitz-Gilbert damping .....	199
7.3.2 Pump-probe experimental setup.....	201
7.3.3 Pump-probe measurements .....	202
7.3.4 Demagnetization time/Gilbert damping from pump-probe measurements....	203
7.4 THz generation from Ni films.....	204
7.4.1 THz generation setup description.....	204
7.4.2 THz radiation temporal profiles for Ni films .....	205
7.4.3 Ultrafast demagnetization and Gilbert damping effects on THz radiation ....	206
7.5 Summary .....	208
References.....	209
<b>8. Conclusions and scope for future work .....</b>	<b>211</b>
8.1 Conclusions.....	211
8.2 Scope for future work .....	214
<b>List of Publications/Proceedings .....</b>	<b>215</b>

# Chapter 1

## Introduction

---

### Abstract

In this chapter we have discussed the basics of ferroelectricity and ferromagnetism. Since the thesis work is intimate related to the materials usage in the spintronic devices, we have briefly discussed the mechanisms responsible for the cause of multiferroicity in prototype multiferroics. The basic properties of BaTiO<sub>3</sub>, like structure and band structure are also discussed. The laser matter interactions fundamentals are also briefed. Then the literature survey on magnetism in  $d^0$  materials, laser induced crystallization and ultrafast demagnetization is introduced. The motivation and objective section in the chapter clearly point out the problems, in the multilayer based multiferroic devices and discusses how BaTiO<sub>3</sub> can emerge as an alternative to this. In this context, the magnetism and laser induced crystallization in BaTiO<sub>3</sub> as well as ultrafast demagnetization of Ni film are studied in support of frontier spintronic device development.



## **1. Introduction**

### **1.1 Introduction**

The Spintronic device implementations require the study of multi functionality in oxides, as the coupled electronic, magnetic and optical properties of these materials are to be utilized. Size reduction of these materials exaggerates the relevant interactions and becomes more pronounced and observable.

In particular, the Barium titanate (BTO) and Lanthanum strontium manganese oxide (LSMO) based ferroelectric and ferromagnetic bilayer multiferroics are presently constantly explored. But these films are not compatible with Silicon because of the diffusivity of film material into the silicon. Presently the research is focused on to bypass this problem by various routes. One of them is making BTO itself a ferromagnetic by creating defects in it, reducing the crystallization temperatures of these oxides. The speed of memory devices is the next concept in making frontier devices using these materials.

In this context we have briefly studied the origin of magnetism, giant band gap narrowing ( $\sim 2$  eV) and crystallization of BTO. The ultrafast demagnetization study of Nickel films was carried out by time resolved pump-probe experiments.

### **1.2 Ferroelectricity**

The ferroelectricity was first discovered in Rochelle salt (sodium potassium tartrate tetrahydrate,  $\text{NaKC}_4\text{H}_4\text{O}_6 \cdot 4\text{H}_2\text{O}$ ) a hydrogen bonded compound. Study of similarity between dielectric properties of Rochelle salt and magnetism in ferromagnetic materials by Valasek lead to the discovery of ferroelectricity. In 1949 the discovery of ferroelectricity in perovskite oxide  $\text{BaTiO}_3$  which is non - hydrogen bonded compound has completely changed the understanding of this phenomena. The soft mode theory independently developed

## *1. Introduction*

by Cochran (1959) and Anderson (1960) is the most accepted modern theory of ferroelectric phase transitions. The crystal structure of high temperature ferroelectric phase of BaTiO<sub>3</sub> was first given by Helen D. Megaw in 1945 and soon confirmed by Miyake and Ueda in (1946) [1, 2]. In the structure of BaTiO<sub>3</sub>, the Ba atoms occupy the corners of the cube in the high temperature phase, oxygen occupies the faces of cube and Ti ion occupying the center of octahedra. The room temperature ferroelectric phase in BaTiO<sub>3</sub> is due to the shifting of oxygen and titanium ions with resultant spontaneous polarization. The high dielectric constant, piezoelectricity and Hysteresis properties of ferroelectrics gave rise to many applications such as capacitors, transducers, and actuators [3] as well as memory applications respectively. In perovskite ferroelectrics (BaTiO<sub>3</sub> and PbTiO<sub>3</sub>) whether the polarization is in (1 0 0) or (1 1 1) direction, the Ti 3d-O 2P hybridization is essential in stabilizing the ferroelectric transition. In BaTiO<sub>3</sub>, Ba-O bonding is ionic in nature. In PbTiO<sub>3</sub> the hybridization between Pb 6s and O 2P electron result in polarization in Pb and strain that stabilizes the tetragonal phase [4].

### **1.3 Ferromagnetism**

In ferromagnetic materials, the strongly coupled magnetic dipole moments try to align parallel. Hence it results in spontaneous magnetization in these materials. Thus these materials show magnetic moment even in the absence of external applied magnetic field. Above Curie temperature the material is paramagnetic, and the transition temperature can be obtained Curie-Weiss law. There are only a few metals (Fe, Ni, Co, Gd, and Dy) and their alloys which exhibit ferromagnetism. In addition, there exists a few ferromagnetic ionic compounds also.

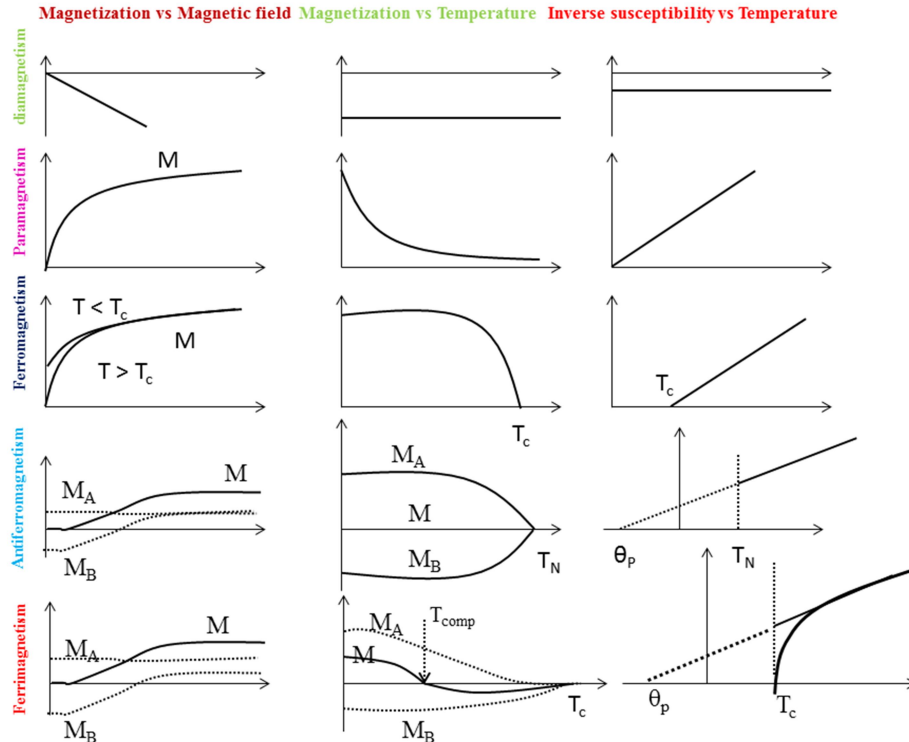


Fig.1.1 Schematic of different magnetic ordering, rows represents the different magnetic ordering and columns represent the thermodynamic quantity.

Fig.1.1 shows the different magnetic ordering and its dependence on temperature and magnetic field. The inverse susceptibility vs. temperature plots for the calculation of transition temperatures in respective magnetic types [5] are also shown.

### 1.4 Multiferroics

The study of materials which show both ferroelectricity and ferromagnetism in one compound or in one phase is an evolved field because of its fundamental and technological importance. Thus, these material based devices can perform multiple functions. These phenomena derive from the fact that electrons have spin as well as charge, giving an extra level of complexity to the physics and an additional degree of freedom in device design.

### **1.4.1 Dzyaloshinskii-Moriya interaction**

There are only a few spin arrangements such as frustrated and helical which can be coupled to ferroelectricity. Models based on Ginzburg-Landau theory are developed to explain the order in these materials [6]. Two microscopic theories are developed to describe the multiferroicity of these compounds. According to these theories, the polarization and the dielectric anomaly is because of atomic displacement and hence the coupling between the phonons and spins is expected in these compounds [7, 8], or the polarization can be from the electric wave function.

Katsura, Nagaosa, and alatsky predicted spin current induced magneto electric effect. The Dzyaloshinskii-Moriya [DM] type interaction is present between the spin and the internal electric field [9, 10]. When the space-time symmetry is broken between two magnetic sites some kind of spiral magnetic order will develop in the material, and the responsible interaction is called the Dzyaloshinskii-Moriya (DM) interaction. According to this interaction an orthogonal spin arrangement will take place in a plane and a vector called DM vector will exist perpendicular to this plane. This interaction is responsible for helimagnetism in many non-Centro symmetric magnets. Thus, antisymmetric exchange interaction is similar to that of Dzyaloshinskii-Moriya (DM) interaction. Dzyaloshinskii first explained the observed weak spontaneous order in antiferromagnetic materials by considering the symmetry arguments. He expanded the thermodynamic potential and obtained the terms representing Heisenberg exchange, magnetic anisotropy and an additional EDM term which is proportional to the cross product of neighboring spins.

$$E_{DM} = -D \cdot (S_i \times S_j) \quad 1$$

where, D is the Dzyaloshinskii-Moriya vector.

Later on, Moriya developed a general theory which can apply to any crystal structure. In many anti ferromagnets, they show small ferromagnetic component of the moments produced perpendicular to the spin-axis of the antiferromagnet. This, kind of weak ferromagnetism is observed in materials like  $\text{MnCO}_3$ ,  $\text{Fe}_2\text{O}_3$  and  $\text{CoCO}_3$ , etc.

#### **1.4.2. Classification of multiferroics**

The origin of multiferroicity is different for different materials. Depending upon the type of material or system the multiferroics are divided into two major groups namely single phase and multiphase. The mechanism of multiferroicity in these materials divide them into two classes called Type 1 and Type 2 multiferroics and composite or multiphase multiferroics.

##### Type 1 multiferroics

In this class, the magnetism and ferroelectricity will exist independently. The nature of coupling is weak. Eg.  $\text{BiFeO}_3$ ,  $\text{BiMnO}_3$ , and  $\text{PbVO}_3$ , etc. The multiferroicity in these materials is because of lone pair electrons. However charge ordering and geometric frustration are the origin of multiferroicity in some of the type 1 multiferroics.

##### Type 2 multiferroics

Because of strong coupling between magnetism and ferroelectricity magnetism can cause ferroelectricity and vice-versa. The ordering temperatures are very low for these compounds. The spiral or collinear magnetic order is the origin of magnetism in these types of materials. Thus ferroelectricity in these materials is because of magnetic ordering in them.  $\text{TbMnO}_3$ ,  $\text{TmMnO}_3$ , and  $\text{YbMn}_2\text{O}_5$ , etc. will come under type 2 multiferroics [11].

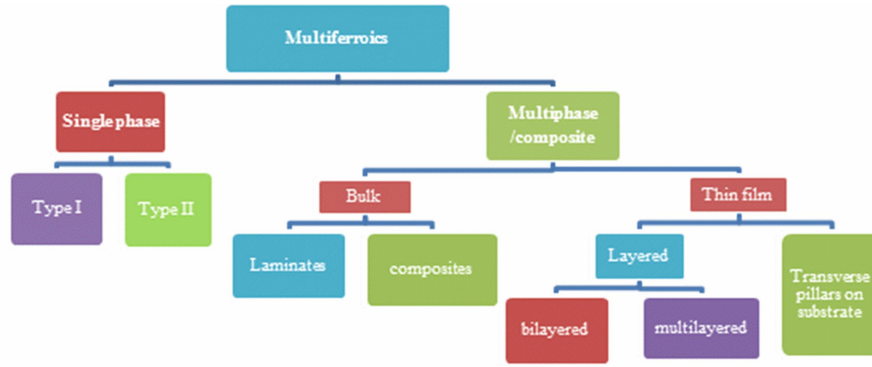


Fig.1.2 Schematic of classification of Multiferroics

### 1.4.3 Bilayer multiferroic materials

Achieving multiferroicity at room temperature or materials development with room temperature transition temperature is a major scientific challenge. The coupling strength between electric and magnetic dipoles is vital in the development of spintronic devices. Devices developed with multiferroics having strong magnetoelectric coupling will work with lower power [12, 13] and that gives direction for the material development efforts.

The ferromagnetic and ferroelectric bilayer based materials are under intense study. The first principle calculations for basic bilayer structures such as Fe/BTO have shown that the interface induced charge can make the ferromagnet to be sensitive to ferroelectric polarization and the ferroelectrics may become ferromagnets. Thus, the interfacial multiferroics are the promising multiferroics in the development of spintronic devices at room temperature [14, 15]. As we know, the ferroelectrics accumulate charge at the interfaces and in materials like  $\text{La}_{1-x}\text{Sr}_x\text{MnO}_3$  the magnetic state is sensitive to its valence state. Thus the electrical switching based on any change in interfacial charge will induce a change in magnetization. The ferroelectric and ferromagnetic materials which show Hysteresis because of their polarization and spin ordering are the only materials which could extensively be used in data-storage devices [16, 17]. At the present

frontier vast majority of research is focused on the speed of these devices in parallel with entangled state based devices. The memory response time to ultrafast electric and magnetic fields is vital in determining the speed of devices.

The study of ultrafast demagnetization in a ferromagnetic material is the core phenomena in the development of ultrafast memory devices. Here in this case instead of using electric and magnetic fields, the optical pulse of the laser with a pulse width of few fs is used in flipping the spin. The flipping or demagnetization in ferromagnetic and antiferromagnetic materials is of 1-2 ps duration [18].

### 1.5 Crystal structure of BaTiO<sub>3</sub>

The ferroelectrics are divided into two groups namely order-disorder and displacive type ferroelectrics. The hydrogen bonded crystals come into the category of order-disorder ferroelectrics, and the ionic crystal structures are of the displacive type.

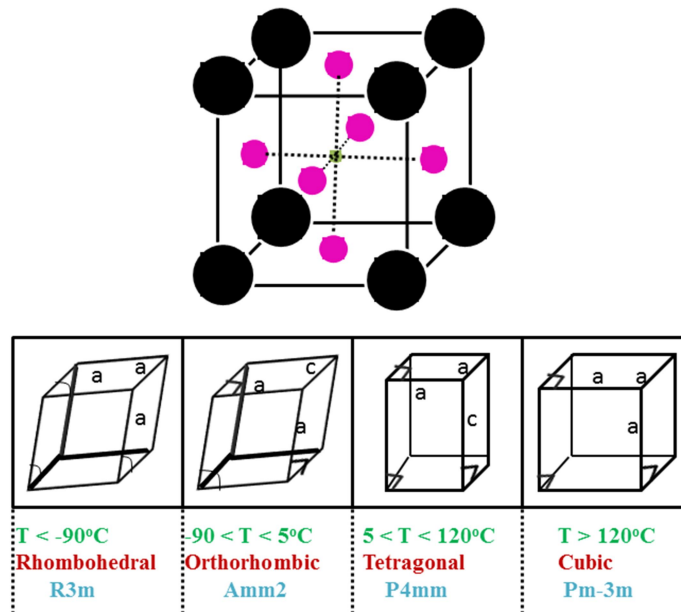


Fig.1.3. The unit cell of perovskite cubic BaTiO<sub>3</sub> and structure as a function of temperature.

The crystal structure of displacive type ferroelectrics is large of perovskite type and ilmenite type. The BaTiO<sub>3</sub> is the prototype ferroelectric material with the tetragonal structure at room temperature, and above the transition temperature, it is cubic in nature, where the Ba<sup>2+</sup> ions are at the corner, O<sup>2-</sup> ions at faces of cube and Ti<sup>4+</sup> at center of the cube. The off-centering of Ti<sup>4+</sup> ions induces the spontaneous polarization in it. Depending on the temperature, it exhibits many crystal structures like Cubic, Tetragonal, Orthorhombic and Rhombohedral [19]. (See fig.1.3)

### 1.5.1 Electronic structure of BaTiO<sub>3</sub>

The band structure of oxygen defective BaTiO<sub>3</sub> is showed in fig.1.4. From the partial density of states, we can see that the valence band is formed of oxygen 2P states and the conduction band is formed of Ti 3d states. When the oxygen defects are present, hybridization of O 2p and 3d states form the defective band below conduction band [20].

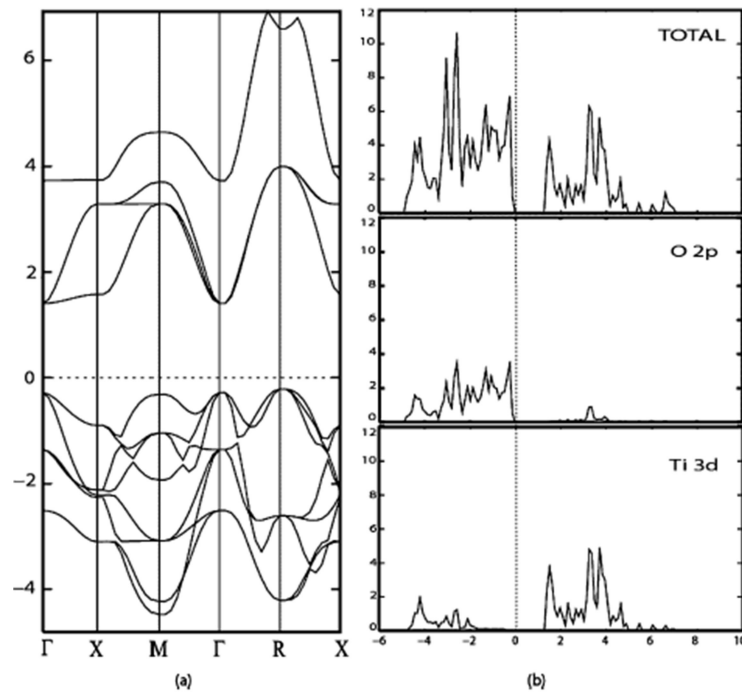


Fig.1.4. Band structure and partial density of states for defective BaTiO<sub>3</sub>

## **1.6 Optical properties of d-band perovskites**

The light or electromagnetic wave has electric and magnetic field components in it. Thus these fields make the radiation to interact with electrons. The oscillating electric field interactions with electrons and ions will lead to various electronic transitions and excitations in the solid.

In ionic solids such as perovskites, the optical absorption mechanism will excite different quasiparticles such as phonons, magnons, etc. in respective solids. The optical phonons are created due to the coupling of infrared region electromagnetic field with the polarization of vibrating ion. The doping of perovskite will create higher no. of charge carriers in the material and like in the case of, metal, the plasmon absorption will occur in the infrared region whereas it can vary from visible to infrared in metals.

When the incident photon energy is higher than the electronic band gap of material, then excitation of an electron from the valence band to conduction band will take place. These kind of transitions are called interband transitions. The interband transitions in insulating perovskites will give the optical properties of these materials in ultraviolet and visible range. The transitions can be direct or indirect band transition depending on whether the phonons are involved in absorption or not [21].

At photon energies lower than the band gap of material there are many other processes which contribute to the absorption process. These may be excitonic absorption or absorption by defect states etc. Inclusion of these states in the electronic structures, during the the study of optical properties is vital in nanomaterials and mesocrystals.

## **1.7 Laser matter interaction**

When an incoherent unpolarized light incident on the materials three processes takes place

1. Absorption, 2. Reflection and 3. Transmittance

The common light electric field ( $E_L \sim 600$  V/m) strength of light is very low compared to the atomic electric field ( $E_a \sim 10^{11}$  V/m). Hence the natural light will not displace the atomic electrons efficiently. It is called weak interaction.

When the laser light is considered the  $E_L$  is very high compared to normal light and hence as the laser light is incident on the material, it displaces the electrons strongly and produces nonlinear effects. The coupling of the laser to a material is very sensitive to laser wavelength and nature of the material.

At weak coupling various non-linear effects like higher harmonic generation, four-wave mixing, multiphoton absorption, etc. can take place. As the laser coupling is strong non-linear effects cannot be explained by perturbation theory. Here the annealing effects will come into the picture [22]. If the laser energy density is further increased, it forms temporally and spatially localized electron plasma in the material. This plasma relaxes via electron-phonon and phonon-phonon coupling and results in the melting of the material.

Much of the laser annealing work is carried out on Si. Here we will be focussing only on the annealing of ferroelectric materials. Most of the ferroelectrics are having band gap above 3.00 eV. Since the Excimer laser wavelength is 248 nm, the energy associated with the photon is much higher than the band gap. Hence most of the laser is absorbed on the surface of the film.

The heat diffusion from the surface of the film into the film is described by heat diffusion equation given below [23, 24]

$$\frac{\partial T}{\partial t} = \frac{\alpha}{\rho C_p} I(z, t) + \frac{1}{\rho C_p} \frac{\partial}{\partial z} \left( \kappa \frac{\partial T}{\partial z} \right) \quad 2$$

Where,  $I$  is the laser power density,  $\alpha$  is the optical absorption coefficient,  $\rho$  is the density,  $c_p$  is the specific heat capacity, and  $\kappa$  is the thermal conductivity.

## **1.8 Literature survey**

### **1.8.1 Magnetism in $d^0$ materials**

Spintronics is a new field of physics and an emerging field of electronics. Here the properties of spin are used instead of charge in the working of devices. It lead to the development of magnetic semiconductors with the magnetic order at room temperature. In the early reports, these dilute magnetic semiconductors (DMS) are termed as semimagnetic semiconductors due to their intermediate properties to that of nonmagnetic and magnetic materials. The DMS compounds are developed by substituting a fraction of the semiconductor constituent with a magnetic element.

There are two widely accepted DMS families II-VI, and III-V group elements formed semiconductors doped with magnetic metals. Among these, the Mn-doped DMS system is one of the heavily studied system.

The DMS also behave as half metals. In particular,  $\text{In}_{1-x}\text{Mn}_x\text{As}$  and  $\text{Ga}_{1-x}\text{Mn}_x\text{As}$  are the frontier compositions [25, 26]. The DMS materials can be doped and made as a semiconductor with a large scope for applications. Whereas the hindrance of these materials is that their Curie temperature lies below room temperature at around  $\sim 170\text{K}$ . However, the enhanced doping will not help in inducing useful ferromagnetic order in these materials. To avoid this, the doping of insulators like  $\text{HfO}_2$ ,  $\text{GaN}$ ,  $\text{CaO}$  and  $\text{ZnO}$  attracted an enormous amount of interest.

The doping of  $\text{ZnO}$  by magnetic element to make dilute magnetic semiconductor is widely studied [27-33]. The magnetism is even observed in non-magnetic doped semiconductors [34, 35].

The subsequent studies reported the existence of magnetic order in the undoped DMS, oxide compounds and metal nanoparticles itself due to the presence of defects or capping on them [36-41].

## *1. Introduction*

The study of multi-functionality or multifunctional materials has received much attention to achieve new functionality in the devices. Single phase multiferroics were under focus for the past few years, but the transition temperatures and magnetoelectric coupling coefficients are not good enough to be used in devices [42-45]. Among the single phase multiferroics, BiFeO<sub>3</sub> is the immensely studied compound [46-49].

There have been constant efforts to develop multiferroic materials with large magneto electric coefficient values. For example in the composites of Ni and BaTiO<sub>3</sub>, for some values of Ni the coefficient values are increased [50]. The combination of ferroelectric and ferromagnetic materials can produce new structures with multi-functionalities [51-53].

As discussed above, in the DMS magnetic properties are also found in undoped perovskite oxides. Notably, the unleashing of the multiferroicity in prototype ferroelectrics seemed to be an immediate opportunity in the memory as well as fundamental d0 magnetism perspective [54-57]. For decades, BaTiO<sub>3</sub> has emerged as the choicest material in exploring the new states as it proved in establishing an absolutely new interpretation of ferroelectricity in contrast to Rochelle salt. Along these lines the magnetic order is also observed in BaTiO<sub>3</sub> and the origin for this is still cryptic and need to be explored fundamentally. The early experimental results on observation of magnetic order in BaTiO<sub>3</sub> along with ferroelectricity are reported by R.V.K. Mangalam et. al in 2009 [58]. Here they explained the observed multiferroic order by considering the first-principle simulations. The ferromagnetism in their nanoparticles has emerged from the defective surfaces whereas the ferroelectricity contribution is assigned to the core of nanoparticles [58].

In a six month span of time D. Cao et. al, [59] discussed the emergence of magnetism in defective BaTiO<sub>3</sub> by considering various vacancies like oxygen and titanium through first-principle calculations. The calculations were carried out for

three different vacancies namely O, Ti and Ba respectively. The outcome of these results is that only Oxygen and Titanium vacancy can induce magnetism. But the Ba-vacancy didn't hint any possibility of magnetism to be induced in BaTiO<sub>3</sub>. The origin of the magnetic state is the partially filled Ti t<sub>2g</sub> and partially polarized oxygen 2p electrons for Oxygen and Titanium vacancy respectively [57]. The Ti<sup>3+</sup> formation is also substantiated from electron spectroscopy for reduced BaTiO<sub>3</sub> (Oxygen deficient BaTiO<sub>3</sub>) [60]. They have also investigated thin films of BaTiO<sub>3</sub> (001) for different terminations. It is observed that the O-vacancy on BaO terminated surface and Ti-vacancy on TiO<sub>2</sub> terminated surface have induced a magnetic moment of 1.12 μ<sub>B</sub> and 3.98 μ<sub>B</sub> respectively. Whereas, the O-vacancy on TiO<sub>2</sub> - terminated surface will not induce any magnetism in it [61].

The nanoporous BaTiO<sub>3</sub> nanoparticles of surface area 107 m<sup>2</sup>/gm, with significant surface defects, will contribute to the ferromagnetic behavior in it. These particles showed multiferroic behavior with large magnetodielectric parameter (11%) at 10 kOe applied magnetic field [62]. There are also few reports on the other perovskites like PbTiO<sub>3</sub> and SrTiO<sub>3</sub> [63, 64].

Multiferroicity in BaTiO<sub>3</sub> is steadily getting explored to unleash their basic mechanism. The peculiarity of multiferroics will be decided by the value of the magnetoelectric coefficient of it, which is the foremost parameter for a material to be used in such devices. The coexistence of ferroelectric and ferromagnetic order in BaTiO<sub>3</sub> procreates the magnetoelectric effect. The recent reports on the magnetoelectric coefficient of BaTiO<sub>3</sub> nanoparticles of size range 16-26 nm are very remarkable. It is found that the magnetoelectric coefficient values are decreased with increase in grain size. This is phenomenal in understanding the origin of magnetism in them and hence the ferroelectricity in defective BaTiO<sub>3</sub> [65].

### **1.8.2 Laser induced crystallization**

The necessity of lowering the crystallization temperature of ferroelectric materials in its thin film form is necessary because of their multi-functionality and to make them compatible with the integrated circuit processing techniques. The present technology combines the semiconductor based and ferroelectric based functional devices separately. Hence the size of devices increases as the processes for both are often incompatible with temperature. Thus obtaining multi-functionalities in same materials or substrates and developing the different functions in the same system is essential for miniaturization of devices. This provides the possibility to make the system on Chip (SoC) with multiple functionalities added to different areas of the substrate by using a different type of functional materials on the same substrate. Semiconductors and ferroelectrics are two essential elements for achieving such multifunctional systems. Because the oxide ferroelectric thin films can give high dielectric constant, tunable dielectric constant, piezoelectricity, pyroelectricity, PTCR effect, etc. which are essential for a plethora of devices which are fabricated separately now. The ferroelectric thin film is processed at high temperature. Whereas, the semiconductor processing temperature is lower. This leads to difficulty in combining these two materials in the same devices. Thus decreasing the processing temperatures of ferroelectric thin films is the key concept for the hetero material based high-quality device development. Hence an understanding of ways to lowering the processing temperatures of ferroelectric thin films is crucial. Lasers made it easy to dream of lowering the crystallization temperature of thin films. It deposits energy to a needed region in the device processing step without damaging the other components of the device. Thus in the present work, we take an initiative to reduce the crystallization temperature of ferroelectric thin films with the objective of making them compatible with multifunctional device processing. Ferroelectrics

are wide band gap materials. Hence the ultraviolet wavelength lasers are capable of the crystallization process by non- thermal process routes.

Research on electromagnetic radiation induced crystallization of semiconducting materials has started way back in the early 1970's.

Lasers basically provide the ability to accurately dump significant amounts of energy into confined regions of a material. During the earlier works with pulsed Ruby lasers, it has been understood that laser interaction with the material can give permanent changes in the material. In semiconductor technology, laser crystallization has been widely used for the advantages of selective absorption and low substrate temperature. Moreover, the irradiation area can be freely selected without heating other regions. Some of the earlier pioneering work in this field is reviewed here.

Constant effort has been made to decrease the crystallization temperature of semiconductors. But the laser induced crystallization (LIC) of materials is confined mostly to semiconductors only.

J. Feinleib, (1971) et.al, observed the crystallization of amorphous chalcogenide films under the exposure of short laser pulses. At higher power levels the crystallized films melt and go back to the amorphous state. According to their model the speed of crystallization is attributed to the large enhancement of crystallization rate under the influence of the photon flux [66]. The study of M. Lovato, et. al. (1979), gives the qualitative understanding of different thermal processes which seem to be problematic in them. The fundamental questions such as why and where the nucleation starts and the energy requirement for an atom to involve in a nucleation process where attempted to be answered by laser induced crystallization (LIC). They imparted photon energy in three modes for the crystallization procedure viz., as continuous and weak power, short pulse with the

## *1. Introduction*

power level of KW/pulse, and nanosecond pulses with MW/pulse. They suggested that the middle-power lasers are the suitable candidates for the study of nucleation and crystallization [67]. According to V. V. Makarov, et. al. (1979), the mechanism for laser induced crystallization (LIC) is the residual ray absorption. According to their studies at lower intensities, the topographic images revealed the presence of linear and planar defects. Minimum of lattice disorder is observed at 50 MW/cm<sup>2</sup> for the laser irradiated regions compared to thermal annealing [68]. Yoshihiko Kanemitsu, (1985), inferred that the picosecond lasers will crystallize the amorphous Silicon. It is having two different thresholds for the crystallization. They found that one of the crystallization is clearly below the amorphization threshold and the other crystallization threshold is well above the amorphization threshold. The presence of small changes in surface height observed even at the unannealed region far outside the central annealed region imply that shock stress generated by picosecond heating is important in the crystallization process. The picosecond single pulses were generated at 1.06 μm in a passively mode-locked Nd-doped YAG laser system. The laser output is successively amplified by a two-stage amplifier. The pulse duration used is 30 ps [69].

According to K. A. Rubin et. al. (1987), study the effect of laser pulse width, and amplitude plays a significant role in understanding the laser induced crystallization (LIC) kinetics. K A Rubin et. al studied the effect of a Gaussian Krypton ion (647 nm) laser pulse width and amplitude on the Kinetics of laser-induced phase transformations of thin film alloys of Te. The phase transformation kinetics (PTK) diagram shows distinct regions of crystallization and amorphization for corresponding power and pulse width. The observed reflection intensity is used in identifying the amorphous and crystalline states of the material. The results were correlated with the temperature modeling to extract various parameters. They reported 50ns, 550ns, and 80 μs as the crystallization

time for Te, Te<sub>80</sub>Sn<sub>20</sub> and Te<sub>90</sub>Ge<sub>10</sub> materials respectively [70]. Here what is reported is the continuous laser based amorphous silicon crystallization on various substrates like quartz, sapphire, etc. The threshold power density for crystallization of Si: H films is higher for films on sapphire substrates than the films on quartz. As the laser beam is incident on the film, heat distribution in the film decides the crystallization power requirement. Thus the thermal conductivity of substrate plays a significant role in heating of films. In the present case, the thermal conductivity of sapphire is greater than that of quartz and hence the threshold power required for crystallizing the films on sapphire is higher [71]. G. B. Reddy, et. al, deposited adherent and pinhole free Sb<sub>2</sub>Te<sub>3</sub> films by vacuum evaporation. The films were crystallized by thermal annealing and laser annealing. The crystallization process is studied as a function of annealing temperature and laser scan speed. The films were formed into Sb<sub>2</sub>Te<sub>3</sub> phase in both processes [72].

James S. Im, et.al. (1993), have used Excimer laser to study the laser induced crystallization (LIC) of Si. The phase transformation mechanisms and the resulting microstructures of crystallized Si films by LIC on SiO<sub>2</sub> were reported. It is shown that at low energy density regime, there is an increase in grain size as the energy density increases. The melt duration also depends on the incident energy density. At high energy density, the grain size is independent of incident laser energy density, and it results in the complete melting of the film. Here they found that the transition region is the suitable regime for large grain sized polycrystalline Si formation [73]. Here also continuous –wave laser power is used for laser induced crystallization (LIC) of Sb<sub>2</sub>S<sub>3</sub>, Sb<sub>2</sub>Se<sub>3</sub>, and Sb<sub>2</sub>Te<sub>3</sub> semiconductor films. They found that the photo-thermal process is responsible for the phase change in all three compounds. The power required for optical contrast at an irradiated site will depend on the film thickness. The optimized power density for above-mentioned samples is of the order of 100 W/cm<sup>2</sup>. [74]

## *1. Introduction*

X. M. Lu et. al and M. Knite et. al (2002): Use of CO<sub>2</sub> laser for thick film crystallization. Pb(ZrTi)O<sub>3</sub> films have excellent ferroelectric, optical, piezoelectric and pyroelectric properties. Formation of ferroelectric perovskite phase of PZT requires temperatures around 600°C which make it difficult to integrate these films with Si monolithic circuits. So decreasing the fabrication temperature for ferroelectric films has been the goal of research recently [75].

The low-temperature continuous wave CO<sub>2</sub> laser annealing technique is adopted to fabricate crystalline ferroelectric PZT thick films of different thickness on a Pt/Ti/SiO<sub>2</sub>/Si substrate using the amorphous films deposited by different techniques. Films with thickness 5 μm showed cracks and rough surface morphology, indicating the importance of controlling the interfacial stress and choosing the appropriate size of mixing powders. Films of 5 μm thickness are annealed at 121 W/cm<sup>2</sup> have exhibited better ferroelectric properties. The CO<sub>2</sub> laser wavelength used is 10.6μm, and beam area is 2.89 cm<sup>2</sup>. PZT films which were deposited by sol-gel method with a thickness of 520±40 nm are pre-annealed at 450°C in a furnace for 1h. The local thermal treatment of the PZT films was provided by a CO<sub>2</sub> laser set-up EPILOG 48 series (SYNARD). Lasers of this series require a 1 μs “tickle” pulse delivered at a 5 kHz clock frequency and operate in a quasi CW mode. The laser output power was controlled by a DC current applied to the analog current input of Synard UC-1000 Laser controller. The output wavelength is maintained near 10.6 μm.

This field is very much involved with the tuneable wavelength lasers and different pulse width. Because of wider applications of ferroelectric materials and the industrial application of Si-compatible ferroelectric films, the crystallization of ferroelectric films at lower temperatures is an emerging field. Some of the work in the last decade is summarized below:

## *1. Introduction*

In 2006 in short communication S Halder et.al, reported the annealing of chemical solution deposited barium strontium titanate films at various fluence and pulses in the temperature range of 25-250°C. The films were crystallized above 100 mJ/cm<sup>2</sup> fluence. It is found that the 250°C substrate temperature maintained films showed the crack free microstructure. The films also showed increased dielectric constant with increase in laser fluence. The 120 mJ/cm<sup>2</sup> annealed film showed a higher dielectric constant of 200 indicating better crystallization[76].

H. Sugita, et. al. in (2007). has proposed the line patterning of c-axis orientated LiNbO<sub>3</sub> crystals by a laser scanning with a power of 0.59 W and a speed of 6µm/s. The Cu<sup>2+</sup> ion has d-d transitions at around 1064 nm. The Cu<sup>2+</sup> present in LN, the 1064 nm wavelength corresponding to the energy absorbed by Cu<sup>2+</sup> ions (d-d transitions) can be converted to the lattice vibrations of surrounding Cu<sup>2+</sup> ions (nonradiative relaxations), giving an effective heating at the laser irradiated local region. The process becomes quite attractive as Nd: YAG laser got an emission at  $\lambda = 1064$  nm resulting in efficient crystallization of LiNbO<sub>3</sub>. In this way, the ferroelectric Lithium niobate LiNbO<sub>3</sub> crystals were formed on the surface of CuO (1 mol%)-doped 25Li<sub>2</sub>O–25Nb<sub>2</sub>O<sub>5</sub>–50TeO<sub>2</sub> glass (mol %) by continuous-wave Nd: YAG laser irradiations with a wavelength of 1064 nm, with a simultaneous heating at 150°C. Micro-Raman scattering spectra confirmed the crystallization of LiNbO<sub>3</sub> ferroelectrics [77].

I. A. Palani, et. al.: Here the PZT films were deposited on glass substrates and frequency tripled pulsed Nd<sup>3+</sup>: YAG laser (355 nm) is used to anneal the films. The surface of laser treated samples was studied by scanning electron microscope and Raman spectroscopy to understand the extent of crystallization and ablation. The one dimensional heat flow equation provides the temperature value for different laser fluencies. They found that the temperature value has increased from 760°C to 1170°C as the fluence increases from 170 mJ/cm<sup>2</sup> to 390 mJ/cm<sup>2</sup>. [78]

## *1. Introduction*

S. S. N. Bharadwaja, et. al. in (2010). They deposited the  $\text{Pb}(\text{Zr,Ti})\text{O}_3$  films on  $\text{LiNbO}_3$  coated silicon substrates by RF-Magnetron sputtering. The kinetics of laser annealed films is investigated for the substrate temperatures below  $400^\circ\text{C}$ . A KrF Excimer laser with 20ns pulse width and energy density of  $\sim 40\text{mJ}/\text{cm}^2$  was used for the crystallization process. They found that 380-400 nm thick films can be fully crystallized for a time exposure of 0.1 to 1 ms. For a minimum number of shots also the crystallization of films is observed without any secondary phases. However, the films which annealed at  $400^\circ\text{C}$  for 10 min without laser exposure showed no evidence of any crystallization. The laser annealed samples shows dielectric and ferroelectric properties consistent with the conventional annealed samples. S. S. N. Bharadwaja et. al. also tried lasers for growing highly textured  $\text{Pb}(\text{Zr}_{0.52}\text{Ti}_{0.48})\text{O}_3$  (PZT) films ( $\sim 300\text{--}350$  nm in thickness) on  $\{111\}$ Pt/ Ti/ $\text{SiO}_2$ /Si or  $\{001\}$ PbTiO<sub>3</sub>/Pt/Ti/ $\text{SiO}_2$ /Si substrates. The obtained remanent polarizations and coercive fields were  $31 \mu\text{C}/\text{cm}^2$  and 86 kV/cm for  $\{001\}$  film while they were  $24 \mu\text{C}/\text{cm}^2$  and 64 kV/cm for  $\{111\}$  oriented PZT film [79].

N.M. Ferreira, et. al. in (2012). The preparation methods of single crystalline LN are cost effective. However different methods to synthesize high purity LN samples are essential. They found that the laser induced crystallization (LIC) is a very promising technique to promote glass -ceramic transformation at low temperatures. In this work, a  $\text{SiO}_2\text{--Li}_2\text{O--Nb}_2\text{O}_5$  glass, prepared by the sol-gel route, was irradiated with the  $\text{CO}_2$  laser and conventional heat-treatments to induce the  $\text{LiNbO}_3$  crystallization at lower temperatures. The structural and morphological studies of these samples crystallized by two different routes reveal the reduction in time in Laser induced crystallization (LIC) compare to conventional heating. A heat-treatment at  $650^\circ\text{C}/4\text{h}$  was necessary to cause crystallization in conventional heating while 4 W/500s was enough for laser

induced crystallization (LIC). The reduction of time in processing by the laser is ~14 000 seconds [80].

According to L Hong, et. al. (2013), the femtosecond lasers have not been used for laser induced crystallization (LIC) earlier because of its difficulty in industrial availability. L Hong et. al discussed the simultaneous crystallization and formation of the nanocone structure on the 1.6 $\mu\text{m}$  thick amorphous silicon (a-Si) film using a one-step femtosecond laser annealing approach. The conical structures of diameters ranging from 160 nm to 1.4 $\mu\text{m}$  are formed upon laser beam irradiation at different fluences. The highest absorption is achieved for 588mJ/cm<sup>2</sup> laser fluence. They believed that for the FemtoSec laser annealing process, ultrafast or non-thermal melting of Si is the dominant mechanism, while in continuous-wave laser annealing and nanosecond Excimer laser annealing, the melting of Si is not very high [81].

In addition to PZT, there is a considerable amount of laser crystallization work is carried out on BST compounds also. The Ba<sub>0.8</sub>Sr<sub>0.2</sub>TiO<sub>3</sub> films were deposited on glass and platinized silicon substrates at 600°C. The as-deposited films are amorphous in nature, and after laser annealing at room temperature, the films are crystallized. The number of pulses incident on the film is also a crucial parameter in obtaining the full crystallization without damaging the film [82].

Studies have also been in progress to understand the mechanism of crystallization of films. By the use of fs laser, it is possible to separate the electronic temperature and lattice temperature as two reservoirs and study how electronic temperature is heating the lattice. In PZT film it is observed that the crystallization can be divided into two parts ultrafast high temperature crystallization and low temperature crystallization which peaks up at the end of pulse [83].

Recently excimer laser annealing is used for re-oxidation of BTO films on Ni foils. It also helped in reducing the oxidation of Ni, and hence the higher

dielectric constant values of around 1000 were observed for BTO. The oxidation of electrodes is the obstacle for the development of good quality dielectric capacitors, and this can be reduced using the laser annealing concept [84].

In conclusion, we can say that the crystallization of amorphous Si using LIC is a standardized process well accepted in the industry. For ferroelectric thin films, an elevated temperature of about 300-400°C is found to be useful for PZT. Cu<sup>2+</sup> doping is necessary to enhance LIC in LN. Lasers used are Nd-YAG, Excimer, and femtosecond, of which the Nd-YAG costs the least and gives the largest number of wavelengths. For other ferroelectric thin films, there are not many investigations reported so far. The studies so far established the veracity of this procedure. The importance of optimizing LIC process heavily depends on the pulse width, wavelength of laser, energy density, thermal conductivity of the substrate and the temperature at which the substrate has to be kept during the annealing process [85-88]

### **1.8.3 Ultrafast demagnetization**

The spin scattering process is fundamental in understanding or manipulating the speed of data storage elements in fs-laser writing through demagnetization of material. However, this ultrafast demagnetization at the microscopic level still needs to be understood to a significant level. The ultrafast handling of magnetization in Ni films is triggered by the discovery of Beaurepaire et. al in 1996 [89] by time resolved pump-probe experiment using 60 fs laser pulse. The successive experiments intensified the research as it has immense potential in the manipulation of speed of devices in sub-ps time scale [90-97].

These results on ultrafast demagnetization time are remarkable since the spin-lattice relaxation time lies in the 100 ps range [98, 99]. From this, it is clear that the spin angular momentum is changing much rapidly than it can transfer to the lattice system [100, 101]. Thus explanation for such ultrafast quenching of

magnetic order has attracted the attention of scientific society. Shortly various explanations were received based on some experimental and theoretical findings. Beaurepaire et. al explained their observation by considering phenomenological three temperature model through interactions between electron, spin, and lattice [89]. The optically excited electrons can transfer their energy lattice within 0.5-1 ps, but the demagnetization is related to angular momentum quenching, and the model will not consider this mechanism. Scholl et.al, based on the results of photoelectron spectroscopy has suggested two distinct mechanisms contributing at different time scales. The rapid sub-ps process is attributed to Stoner excitations whereas the slow process of  $\sim 100$  ps time scale might be due to spin-lattice interaction [102]. It is puzzling that whether the spin quenching is through spin-orbit coupling [103] or because of spin-lattice relaxation [104]. The question of spin angular momentum transfer to orbital angular momentum was answered by Stamm et. al. by XMCD measurements and they have not observed an increase in orbital angular momentum within the sub-ps time scale and hence the spin-lattice relaxation came out as the key mechanism in the explanation for ultrafast demagnetization [105-107].

In parallel, the theoretical studies have also increased the complexity by predicting lower ultrafast demagnetization times. In 1998 W. Hubner et. al proposed that even shorter demagnetization time (10 fs) dynamics are possible in Ni by considering exact diagonalization on ultrafast time scale. The exchange interaction and spin-orbit coupling are responsible for the ultrafast relaxation process [108]. The Second Harmonic Generation (SHG) from Ni films is also observed with pump pulse, but the SHG signal and Kerr rotation intensity dropped marginally within 300 fs, and it is concluded that the ultrafast decrease in magnetic order is not within this timescale [109]. According to Cheskis et al. the ultrafast demagnetization of Ni is due to the Stoner gap collapse in contrast to spin relaxation process. Thus, in addition to the thermal process in the non-

equilibrium state, there are the spin majority, minority populations also [110]. In 2012 a theoretical structure proposed by Mentik et.al, for multi sub lattice, has considered two distinct mechanisms considered namely the relativistic and exchange. In the relativistic case the distinct sub lattice has distinct dynamics. In the exchange dominated case an absurd transitions can happen between parallel and antiparallel order [111].

The physics behind the ultrafast demagnetization of 3d ferromagnetic metals is a highly expanded field. Ultrafast spin dynamics study also carried out in other ferromagnetic metals like Co also. By linking the spin and time-resolved photoemission techniques the spin dependent lifetimes for majority and minority spins are measured [112].

One of the mechanisms is explained by considering the spin-flip process in the Elliot-Yafet electron-phonon scattering due to spin-orbit coupling or from Stoner excitations [95, 113]. The Eigenstates of Heisenberg Hamiltonian are correlated with spin excitations not considered in Stoner model, and these transverse excitations also involve in the demagnetization process [114, 115]. The scattering of quasi-particles seems to be the best method to disclose the ultrafast demagnetization phenomena. Whereas anyone (Stoner like or Heisenberg-like) description of localized magnetic moment is not found satisfactory always. Hence a connection between these two is the local band theory of itinerant ferromagnetism or disordered local moment theory is proposed [116-118].

Recently, Emrah Turgut et. al, explained the ultrafast demagnetization by considering the ultrafast reduction in exchange splitting and excitation of magnons and are strong in the sub-ps time scale whereas exchange can remain up to several ps [119]. There are reports that consider the angular momentum transfer to lattice through electron-phonon scattering by considering anisotropic Hamiltonian [120].

## **1.9 Aim and Objective**

The understanding of magnetism in dilute magnetic semiconductor (DMS) is based on free carriers and is a very broadly accepted concept. According to this, the ferromagnetism in TM–ZnO (TM = Sc, Ti, V, Cr, Mn, Co, Ni, and Cu) is due to the exchange interactions between the sp band charge carriers and localized d-electrons [121, 122]. When the electron concentration crosses the critical value for the above system, the ferromagnetic interactions reduces [123]. Hence the p-d hybridization is crucial in describing the observed magnetism in the above systems [21, 124-128].

Magnetism in nanocrystalline ATiO<sub>3</sub> (A–Ba, Sr, Pb, etc.) perovskite oxides is highly influenced by Ti density of states at the Fermi level and by the presence of oxygen vacancy. These compounds have high magnetic transition temperature, often above room temperature. Without the existence of a magnetic element, they exhibit magnetic properties and there by becoming multiferroics, increasing their scope. Initially, the study on the control of magnetic moment with a ferroelectric layer was reported in bilayered films of Ni nano bar and lead zirconate titanate [129, 130]. Khomskii discussed briefly the ways in which magnetism and ferroelectricity can be combined in the same material [131]. The common feature for dilute magnetic semiconductors and defect based magnetism in oxide materials is the density of charge carriers.

The ferromagnetic and ferroelectric bilayer based materials are under intense study. The ferroelectric and ferromagnetic materials which show Hysteresis because of their polarization or spin ordering are the only materials which are extensively used in data-storage devices. The first principle calculations for basic bilayer structures such as Fe/BaTiO<sub>3</sub> have shown that the interface induced charge can make the ferromagnet to be sensitive to ferroelectric polarization and the ferroelectrics may become ferromagnet also. Thus, the interfacial multiferroics are promising in the development of spintronic devices at

## *1. Introduction*

room temperature. The different parameters like strain, ionic diffusion, orbital reconstruction or charge transfer can effectively alter the interfacial magnetic order [132-135]. Thus the detailed understanding of interfacial properties is also crucial in ferromagnetic/ferroelectric hetero structured spintronic devices.

The interdiffusion between BFO and FM layer cannot be avoided if the temperature is above 100°C. This can reduce the exchange bias to a great level [136-138]. The attention is turned to ferromagnetic manganites and piezoelectric PZT bilayers and multilayers. It is found that the higher temperature processed samples show diffusivity in the material [139]. Recently the multilayers of LSMO/PZT or LCMO/PZT or BTO grew with minimized interfacial diffusion are analyzed for resistivity and magnetoresistance dependence on strain [140-142]. To improve the efficiency of tunneling magnetoresistance and colossal magnetoresistance devices the reduced interdiffusion between LSMO and STO is required. It is found that the interfacial strain and interatomic diffusion are very crucial in ultrathin multilayers of LSMO and STO [143-146].

Perovskite manganites are the most useful class of magnetic materials due to their remarkable colossal magnetoresistance, in addition to its magnetic and electrical properties [147]. Thus in this perovskite manganites, the  $\text{La}_{1-x}\text{Sr}_x\text{MnO}_3$  (LSMO) is the highly researched material as it has the ferromagnetic transition temperature at ~340K for a particular hole doping. The band theory picture of LSMO is peculiar in comparison with the normal band structure of materials [148-150]. As we know the ferroelectrics accumulate charges at the interfaces and in materials like  $\text{La}_{1-x}\text{Sr}_x\text{MnO}_3$ , the magnetic state is sensitive to its valence state. Thus, the electric switching based change in interfacial charge will induce the change in magnetization.

In particular, the Barium titanate (BTO), and Lanthanum strontium manganese oxide (LSMO), ferroelectric and ferromagnetic bilayer based multiferroics are continually being explored. But these films are not compatible

with Silicon because of the diffusivity of film materials into silicon or vice versa. This heavily restricts these materials from being used in memory devices to a maximum extent. Presently the research is focused on to bypass this problem by various routes. One of them is making BTO itself ferromagnetic by creating defects in it, or by reducing the crystallization temperature of it [151]. The exchange bias is improved in laser annealed samples compared to the conventional annealed samples due to its minimized interfacial damage and strengthened coupling between BFO and Co [152]. Recently in BTO, Ni-based multi layered ceramic capacitor (MLCC) using laser re-oxidation of BTO layer is carried out without any NiO layer formation [81]. Thus the laser annealing is being considered as the effective method of improving the interfaces.

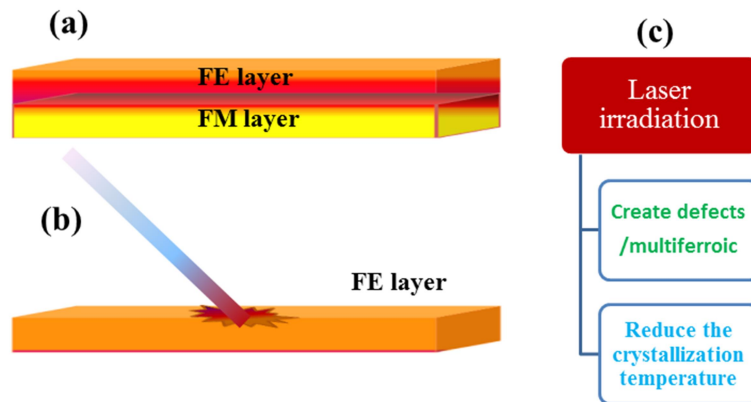


Fig.1.5. (a) Bilayer of FE/FM films, (b) Laser irradiation with FE film, (c) Laser irradiation gives defects creation or crystallization of FE layer.

Thus, the study of the origin of magnetism in BTO is highly motivated. The earlier works have explicitly explained how different phenomena in various compounds lack the full explanation for the magnetism in  $d^0$  materials. It is also pointed out that the theoretically obtained value for a magnetic moment is not matching with experimental results. To consider these facts more accurately, we have taken the charge transfer concept in these perovskite materials (which arises from the oxygen defects) and explained the magnetism in nanocrystalline BTO.

Here, we studied in detail how the exchange-correlation interactions are developing in the BTO.

Thus, creating defects in BTO is also possible in the nanoparticle form of it. The nanoparticles are the best systems in which various interactions can become observable. This enables the nanostructures to exhibit multifunctionality. Thus, Spintronic device implementations require the study of functional properties of these oxides, as the coupled electronic, magnetic and optical properties of these materials are to be utilized. In dilute magnetic semiconductor oxides, the cations are partially replaced by transition metal ions. These materials show strong exchange interactions between charge carriers of semiconductor and doped transition metal d electrons. These types of interactions are vital in determining the spin dependent electrical and optical properties [153]. Size reduction of these materials is essential to understanding the origin and type of interactions in these materials.

Thus, as discussed above another objective of this study is reduction of crystallization temperature of ferroelectric compounds. The conventional methods to decrease the crystallization temperature are metal induced crystallization, rapid thermal annealing, the addition of fluxes, sonochemical synthesis, etc. Metal induced crystallization is widespread in reducing the crystallization of semiconductors. Fluxes are used in bulk materials. In thin films, the residual flux can create problems, especially in a device fabrication process. These methods are not successful in decreasing the crystallization temperatures to a great extent. A higher degree of crystallization at low temperature is known to be achievable by the use of lasers of appropriate wavelength and pulse width. These laser-based crystallization methods are considered to be most suitable and flexible to do the crystallization for a required region of a device without damaging the other parts.

The other use of laser induced crystallization is that the materials can be developed on various substrates like paper, plastic, etc. Hence laser induced

crystallization is important in the development of flexible electronics also. One more objective of this research is to integrate various types of materials extending from inorganic and organic to biological in order to achieve the multifunctionality. This integration can enhance the performance of devices. Organic thin film transistor backplanes have shown adequate performance in various applications.

The present vast majority of research is also focused on the speed of these devices in parallel with entanglement based concepts. The memory response time to ultrafast electric and magnetic fields is vital in determining the speed of devices. The speed of these memory structures is the next concept in making frontier devices with these materials.

Ultrafast demagnetization in the ferromagnetic material is a core phenomenon in the development of ultrafast memory devices. Here in this case instead of using electric and magnetic fields, the optical pulse of a laser with a pulse width of few fs is used in flipping the spin. Thus the flipping or demagnetization in ferromagnetic and antiferromagnetic materials is within 1-2 ps.

In addition to the above demagnetization of Ni is the associated generation of THz radiation and which is very important for the detection of high energy materials. Along with this if the room temperature laser induced crystallization is possible, it is crucial in the development of devices on flexible substrates and have immense scope in the defence technologies as well.

### **1.9.1 Organization of the thesis**

The organization of the thesis is as follows.

#### **Chapter 1: Introduction**

In this chapter, we discussed the basics about ferroelectricity, ferromagnetism, multiferroicity, optical properties of d-band materials and laser-

matter interaction. Achieving multiferroicity at room temperature with higher magnetoelectric coefficient is a complex field. The coupling strength between electric and magnetic field is vital in the development of spintronic devices. This chapter also covers the literature survey and brief about the objective of the work and thesis organization.

### **Chapter 2: Characterization techniques**

This chapter briefly discusses the various techniques which are used in sample characterization in the present work. Here we discussed shortly on the working principle, instrumentation involved and the model of the technique used in the study. The techniques described are structural characterization techniques like XRD, Raman, and TEM, microstructural characterization techniques like FE-SEM, TEM and AFM, magnetic characterization techniques such as FMR, PPMS, VSM and optical characterization techniques such as UV/VIS/NIR spectrometer, Z-scan of nonlinear optical properties characterization, and Pump-probe techniques.

### **Chapter 3: Synthesis, structural and micro structural characterization**

This chapter briefly discusses the synthesis conditions of nanocrystalline - BaTiO<sub>3</sub> (nc-BTO) and deposition of Nickel film. The ferromagnetic Nickel films of three different thicknesses were deposited by RF-magnetron sputtering. Here we have used two chemical methods for BTO nanoparticle synthesis 1. Sol-gel method, 2. Sonochemical method. BTO particles of four different size ranges between 23-54 nm were prepared by sol-gel method. Using the sonochemical method, BTO mesocrystals of 200 nm size were obtained which are constituted of 5-8 nm size particles.

The structural (phase confirmation) characterization is carried out by X-ray diffraction (XRD) and Transmission Electron Microscopy (TEM) technique. The presence of dislocation and strain in the material is also quantified using these two techniques. The 23 nm and 54 nm size range particles showed the

presence of compressive strain in it, whereas the 31 nm and 34 nm range particles has shown tensile strain within them. It is found that the dislocations are responsible for the observed strain in the materials. The Nickel films showed single phase formation and the morphological studies were carried out by Atomic Force Microscopy (AFM).

For the above developed materials, various properties are probed by respective characterization technique and completely discussed in the subsequent chapters.

#### **Chapter 4: Optical studies on BaTiO<sub>3</sub> Nanoparticles and Mesocrystals**

In the present chapter, we discuss the linear and nonlinear optical properties of BaTiO<sub>3</sub> (BTO) nanoparticles and BTO mesocrystals. It is found that the band gap is varied between 2.00 eV to 3.2 eV depending upon the size of the particles and preparation method. The sol-gel prepared nanoparticles show band gap variations between 2.53-3.20 eV. This high band gap narrowing is explained by considering the strain, electron-phonon interactions and exchange - correlation interactions in the material. The giant band gap narrowing of 2.00 eV is observed for BTO mesocrystals. It is found that the dielectric confinement effect plays an important role in reducing the band gap to such a low value of 2.00 eV. It is also discussed in this chapter as to how the band gap narrowing is very important for efficient solar cell development by absorbing solar radiation efficiently to exploit the built-in electric field of the ferroelectric, for charge separation.

#### **Chapter 5: Study of origin of magnetism in nc-BTO nano particles**

In this chapter, the origin of magnetism in nanocrystalline BaTiO<sub>3</sub> (nc-BTO) is discussed. The role of charge transfer effect is discussed in the frame work of Stoner magnetism. The low temperature calcined four different size range of nanoparticles in the range of 23 nm- 54 nm do not show charge transfer mechanism. Whereas the high temperature calcined nc-BTO and mesocrystal samples show the presence of charge transfer effects in it. The field and

temperature dependent magnetization measurements indicate that samples where charge transfer is absent show super paramagnetic behavior. The samples where charge transfer is involved show ferromagnetism with some paramagnetic contribution to it. It is found that the mesocrystals of nc-BTO are showing ferromagnetic ground states with higher  $T_c$  (=131K) compared to sol-gel prepared samples. This gives very strong hint to the increase of electron-electron interactions in these materials through dielectric confinement effect but still the paramagnetic contribution is not nullified completely.

### **Chapter 6: Laser induced crystallization of BaTiO<sub>3</sub>**

The crystallization in complex oxides at low temperatures is a highly challenging work because of their high crystallization temperature and hence the difficulty in making them compatible with silicon-based integrated devices. Therefore making crystalline materials at room/ lower temperatures is highly important. Here we have found an effective way, which is different from the usual methods like metal induced crystallization or sonochemical synthesis etc. In the present work, we have crystallized the ferroelectric complex oxide thin films at room temperature through annealing by Excimer laser of 248 nm wavelength. We successfully obtained experimentally the large area room temperature crystallization of complex oxide films using Excimer laser of wavelength 248 nm and pulse duration of 20 ns. The conservation relations based shock wave velocity calculations yield low shock velocity. This low shock speed may support the formation of laser supported combustion waves. This combustion based atomic diffusion and pressure induced lattice mending may be the basic mechanism in the crystallization of these films. The small range order can be expected even in amorphous materials and hence the pores based mending of full lattice could be expected.

## **Chapter 7: Ultrafast demagnetization of Ni films**

In the present chapter, we studied the ultrafast dynamics of Nickel films by femto-sec pump-probe spectroscopy for three different thicknesses of films, namely 65 nm, 135 nm and 1018 nm. It is found that the demagnetization and recovery times are in sub-ps and few ps respectively. The transfer of angular momentum from spin system to electron system is of importance in the understanding of ultrafast demagnetization phenomena. We also measured the Gilbert damping parameter from FMR measurements and used these values in the calculation of demagnetization times. The measured and calculated values are in agreement with measured demagnetization values from pump-probe experiments. Thus, supports the ultrafast unification theory of demagnetization at all-time scales. The Gilbert damping factor is increased with the decrease in film thickness. The Gilbert damping factor is inversely proportional to demagnetization time also. In addition to this, the films also show THz radiation emission from them, and the THz radiation peak-peak amplitude is increased with increase in Gilbert damping factor.

## **Chapter 8: Conclusions and scope for future work**

The primary outcomes of the present thesis work are given in this chapter. We found that there is great scope for the work in the direction of laser induced crystallization of complex oxides and in understanding the underlying mechanism.

**References**

1. H.D. Megaw, *Nature* 155 484 (1945).
2. S. Miyake and R. Ueda, *J. Phys. Soc. Jap.* 1 32 (1946).
3. L. E. Cross, *Mater. Chem. Phys.* 43, 108 (1996).
4. R. E. Cohen, H. Krakauer, *Ferroelectrics* 136, 95 (1992).
5. M. Reis, “Fundamentals of Magnetism” Pg. no. 8-12, Elsevier, (2013).
6. M. Mostovoy, *Phys. Rev. Lett.* **96**, 067601 (2006).
7. I. A. Sergienko and E. Dagotto, *Phys. Rev. B* **73**, 094434 (2006).
8. I. A. Sergienko, C. Sen and E. Dagotto, *Phys. Rev. Lett.* **97**, 227204 (2006).
9. I. Dzyaloshinskii, *J. Phys. Chem. Solids* **4**, 241 (1958).
10. T. Moriya, *Phys. Rev.* **120**, 91 (1960).
11. H. Zabel and M. Farle, “Magnetic nanostructures spin dynamics and spin transport” pg.no.175-185, Springer-Verlag Berlin Heidelberg (2013).
12. C. Binek, and B. Doudin, *J. Phys.: Condens. Matter.* 17, L39 (2005).
13. Y-H Chu, et al., Electric-field control of local ferromagnetism using a magnetoelectric multiferroic. *Nature Mater.* 7, 478 (2008).
14. C-G Duan, S. S. Jaswal, and E. Y. Tsymbal, *Phys. Rev. Lett.* 97, 047201 (2006).
15. Y Kitagawa, et al. *Nature Mater.* 9, 797 (2010).
16. J. F. Scott, C. A. P. de Araujo, *Science*, 246, 1400 (1989).
17. D. Singh Rana, I. Kawayama, K. Mavani, K. Takahashi, H. Murakami, and M. Tonouchi, *Adv. Mater.* 21, 2881 (2009).
18. E. Beaurepaire, G. M. Turner, S. N. Turner, M. C. Beard, J.-Y. Bigot, C. A. Schmuttenmaer, *Appl. Phys. Lett.* 84, 3465 (2004).
19. R. Waser, “Nanoelectronics and information technology” pg. no. 38-41, John Wiley & Sons (2012).
20. D. D. Cuong and J. Lee, *Integrated Ferroelectrics*, 84, 23 (2006).

21. S E Thomas Wolfram, *Electronic and optical properties of d-band perovskites* (Cambridge University Press, New York, (2006).
22. R. W. Boyd, “*Nonlinear Optics*” (1992).
23. E.Rimini and G.Russo, *Materials Chemistry and Physics*, 9, 257 (1983).
24. P. P. Donohue et.al. *Integrated Ferroelectrics*, 51, 39 (2003).
25. H. Ohno, H. Munekata, T. Penney, et al., *Phys. Rev. Lett.* 68 2664 (1992).
26. H. Ohno, A. Shen, F. Matsukura, et al., *Appl. Phys. Lett.* 69 363 (1996).
27. J. Antony, S. Pendyala, A. Sharma, X. B. Chen, J. Morrison, L. Bergman, and Y. Qiang, *J. Appl. Phys.*, 97, 10D307 (2005).
28. Min Sik Park and B. I. Min, *Phys. Rev. B* **68**, 224436 (2003).
29. G. A. Prinz, *Science*, 282, 1660 (1998).
30. Pavle V. Radovanovic and Daniel R. Gamelin, *Phys. Rev. Lett.* 91, 157202 (2003).
31. W. H. Brumage, C. F. Dorman and C. R. Quade, *Phys. Rev. B*, 63, 104411 (2001).
32. M. Venkatesan, C. B. Fitzgerald, J. G. Lunney, and J. M. D. Coey, *Phys. Rev. Lett.*, 93, 177 (2004).
33. M. Bouloudenine, N. Viart, S. Colis, J. Kortus, and A. Dinia, *Appl. Phys. Lett.* **87**, 052501 (2005).
34. M. Venkatesan, J. G. Fitzgerald, and J. M. D. Coey, *Nature*, 430, 630 (2004).
35. D. Chakraborti, J. Narayan and J. T. Prater, *Appl. Phys. Lett.* **90**, 062504 (2007).
36. P. Zhan et al., *Appl. Phys. Lett.* 102, 071914 (2013).
37. J. Chaboy, et.al, *Phys. Rev. B* **82**, 064411 (2010).
38. B. Choudhury and A. Choudhury, *J. Appl. Phys.* 114, 203906 (2013).

39. S. Zhou, E. Čížmár, K. Potzger, M. Krause, G. Talut, M. Helm, J. Fassbender, S. A. Zvyagin, J. Wosnitza and H. Schmidt, *Phys. Rev. B* **79**, 113201 (2009).
40. J. S. Garitaonandia et. al, *Nano Lett.* **8**, 661 (2008).
41. P. Crespo, et. al, *Phys. Rev. Lett.* **98**, 087204 (2004).
42. G. Lawes and G. Srinivasan, *J. Phys. D: Appl. Phys.* **44**, 243001 (2011).
43. J. P. Rivera, *Ferroelectrics* **161**, 165–180 (1994).
44. I. Kornev, M. Bichurin, J. P. Rivera, S. Gentil, H. Schmid, A. G. M. Jansen, and P. Wyder, *Phys. Rev. B* **62**, 12247 (2000).
45. G. T. Rado, J. M. Ferrari, and W. G. Maisch, *Phys. Rev. B* **29**, 4041 (1984).
46. F. Huang et.al, *Sci. Reports*, **3** 2907 (2013).
47. C. Ederer and N. A. Spaldin, *Phys. Rev. B* **71**, 060401 (2005).
48. Z. X.Cheng, X. L.Wang, S. X. Dou, H. Kimura, and K.Ozawa, *J. Appl.Phys.* **104**, 116109 (2008).
49. J. Silva, A. Reyes, H. Esparza, H. Camacho, and L. Fuentes, *Int. Ferroelectrics*, **126**, 47 (2011).
50. C. Brosseau, V. Castel and M. Potel, *J. Appl. Phys.* **108**, 024306 (2010).
51. N. A. Spaldin, S-W. Cheong, and R. Ramesh, *Phys. Today* **63**, 38 (2010).
52. S-C Yang, A. Kumar, V. Petkov and S. Priya, *J. Appl. Phys.* **113**, 144101 (2013).
53. W. Erenstein, N. D. Mathur, and J. F. Scott, *Nature* **442**, 759 (2006).
54. J.F. Scott, *Nat. Mater.* **6**, 256 (2007).
55. H. Schmid, *Ferroelectrics* **162**, 665 (1994).
56. A.Beck, J. G. Bednorz, C.Gerber, C. Rossel and D. Widmer, *Appl. Phys. Lett.* **77**, 139 (2000).
57. J. F. Scott, *J. Phys. Condens. Mater.* **18**, R361 (2006).

58. R.V.K. Mangalama, N. Ray, U. V. Waghmareb, A. Sundaresan, C.N.R. Rao, *Solid State Commun.* 149, 1 (2009).
59. D. Cao, M. Q. Cai, Yue Zheng and W. Y. Hu, *Phys. Chem. Chem. Phys.*, 11, 10934 (2009).
60. D. I. Woodward, I. M. Reaney, G. Y. Yang, E. C. Dickey and C. A. Randall, *Appl. Phys. Lett.*, 84, 4650 (2004).
61. D. Cao, M-Q Cai, W-Y Hu, P. Yu and H-T Huang, *Phys. Chem. Chem. Phys.*, **13**, 4738 (2011).
62. S. Banerjee, A. Datta, A. Bhaumik and D. Chakravorty, *J. Appl. Phys.* 110, 064316 (2011).
63. K. Potzger, et. al., *J. Magn. Magn. Mater.* 323, 1551 (2011).
64. T. Shimada, Y. Uratani, and T. Kitamura, *Appl. Phys. Lett.* 100, 162901 (2012).
65. T. Woldu, B. Raneesh, M. V. Ramana Reddy and N. Kalarikkal, *RSC Adv.*, 6, 7886 (2016).
66. J. Feinleib, J. deNeufville, S. C. Moss, and S. R. Ovshinsky, *Appl. Phys. Lett.* 18, 254 (1971).
67. M. Lovato, M. Wautelet, and L. D. Laude, *Appl. Phys. Lett.* 34, 160 (1979).
68. V. V. Makarov, T. Tuomi, K. Naukkarinen, M. Luomajärvi, and M. Riihonen, *Appl. Phys. Lett.* 35, 922 (1979).
69. Y. Kanemitsu, I. Nakada, and H. Kuroda, *Appl. Phys. Lett.* 47, 939 (1985).
70. K. A. Rubin, R.W. Barton, M. Chen, V. B. Jipson, and D. Rugar, *Appl. Phys. Lett.* 50, 1488 (1987).
71. H. S. Mavi, K. P. Jain, A. K. Shukla, S. C. Abbi, and R. Beserman, *J. Appl. Phys.* 69, 3696 (1991).

72. G. B. Reddy, A. Dhar, L. K. Malhotra, and E. K. Sharmila, *Thin solid films*, 220, 111 (1992).
73. James S. Im, H. J. Kim, and Michael O. Thompson, *Appl. Phys. Lett.* 63, 1969 (1993).
74. P Arun, A G Vedeshwar and N C Mehra, *J. Phys. D: Appl. Phys.* 32, 183 (1999).
75. X. M. Lu, J. S. Zhu, W. S. Hu, Z. G. Liu, and Y. N. Wang, *Appl. Phys. Lett.* 66, 2481 (1995).
76. S. Halder, U. Boettger, T. Schneller, R. Waser, O. Baldus, P. Jacobs, M. Wehner, *Mater. Sci. and Eng. B* 133, 235 (2006).
77. H. Sugita, T. Honma, Y. Benino, T. Komatsu, *Solid State Communications* 143, 280 (2007).
78. I.A. Palani, Nilesh J. Vasa, M. Singaperumal, *Material Science and Semiconductor Processing*, 11, 107 (2008).
79. S. S. N. Bharadwaja, J. Kulik, R. Akarapu, H. Beratan, and S. Trolier-McKinstry, *IEEE Transactions on Ultrasonics, Ferroelectrics, and Frequency Control*, 57, 2182 (2010).
80. N.M. Ferreira, F.M. Costa, R.N. Nogueira, M.P.F. Grac, *Appl. Surface Sci.* 258, 9457 (2012).
81. L Hong, X C Wang, H Y Zheng, L He, H Wang, H Y Yu and Rusli, *J. Phys. D: Appl. Phys.* 46, 195109 (2013).
82. J. P. B. Silva, A. Khodorov, A. Almeida, J. Agostinho Moreira, M. Pereira, M. J. M. Gomes, *Appl. Phys. A* (2014). (DOI 10.1007/s00339-013-8218-x).
83. A. S. Elshin et.al, *Tech. Phys. Lett.*, 41, 418 (2015).
84. S. S. N. Bharadwaja, A. Rajashekhar, S. W. Ko, W. Qu, M. Motyka, N. Podraza, *J. Appl. Phys.* 119, 024106 (2016).

85. Y. Zhu, J. Zhu, Y. J. Song, and S. B. Desu, *Appl. Phys. Lett.*, 73, 1958 (1998).
86. T. Miyazaki, T. Imai, N. Wakiya, N. Sakamoto, D. Fu, H. Suzuki, *Mater. Sci. and Eng. B* 173, 89 (2010).
87. M. G. Kang, K. H. Cho, S. M. Oh, Y. Ho Do, C. Y. Kang, S. Kim, S. J. Yoon, *Current Applied Physics* 11, S66 (2011).
88. S. S. N. Bharadwaja, F. Griggio, J. Kulik, and S. Trolier-McKinstry, *Appl. Phys. Lett.* 99, 042903 (2011).
89. E. Beaurepaire, J.-C. Merle, A. Daunois, and J.-Y. Bigot, *Phys. Rev. Lett.* 76, 4250 (1996).
90. A. V. Kimel, A. Kirilyuk, P. A. Usachev, R. V. Pisarev, A. M. Balbashov, and T. Rasing, *Nature*, 435, 655 (2005).
91. A. V. Kimel, A. Kirilyuk, A. Tsvetkov, R. V. Pisarev, and T. Rasing, *Nature*, 429, 850 (2004).
92. J.-U. Thiele, M. Buess, and C. H. Back, *Appl. Phys. Lett.*, 85, 2857 (2004).
93. Y. Ren, H. Zhao, Z. Zhang, and Q. Y. Jin, *Appl. Phys. Lett.*, 92, 162513 (2008).
94. A. Kirilyuk, A. V. Kimel, and T. Rasing, *Rev. Mod. Phys.*, 82, 2731 (2010).
95. B. Koopmans, G. Malinowski, F. Dalla Longa, D. Steiauf, M. Fahnle, T. Roth, M. Cinchetti, and M. Aeschlimann, *Nature Mater.* 9, 259 (2010).
96. G. M. Muller, et. al. *Nature Mater.*, 8, 56 (2009).
97. J. Hohlfeld, E. Matthias, R. Knorren and K. H. Bennemann, *Phys. Rev. Lett.* 78 861 (1997).
98. A. Vaterlaus, D. Guarisco, M. Lutz, M. Aeschlimann, M. Stampanoni, and F. Meier, *J. Appl. Phys.* 67, 5661 (1990).
99. A. Vaterlaus, T. Beutler, and F. Meier, *Phys. Rev. Lett.* 67, 3314 (1991).

100. M. B. Agranat, S. I. Ashitkov, A. B. Granovskii, and G. I. Rukman, *Sov. Phys. JETP* 59, 804 (1984).
101. W. Hubner and K. H. Bennemann, *Phys. Rev. B* 53, 3422 (1996).
102. A. Scholl, L. Baumgarten, and W. Eberhardt, *Phys. Rev. Lett.* 79, 5146 (1997).
103. G. P. Zhang, and W. Hubner, *Phys. Rev. Lett.* **85**, 3025 (2000).
104. Koopmans, B., Ruigrok, J. J. M., Longa, F. D. & de Jonge, W. J. M. *Phys. Rev. Lett.* 95, 267207 (2005).
105. C. Stamm, et. al, *Nature Mater.* 6, 740 (2007).
106. C. Boeglin, E. Beaupaire, V. Halté, V. López-Flores, C. Stamm, N. Pontius, H. A. Dürr, and J.-Y. Bigot, *Nature* 465, 458 (2010).
107. C. Stamm, N. Pontius, T. Kachel, M. Wietstruk, and H. A. Dürr, *Phys. Rev. B* 81, 104425 (2010).
108. W. Hubner and G. P. Zhang, *Phys. Rev. B* 58, R5920 (1998).
109. H. Regensburger, R. Vollmer, and J. Kirschner, *Phys. Rev. B* 61 14716 (2000).
110. D. Cheskis, A. Porat, L. Szapiro, O. Potashnik, and S. Bar-Ad, *Phys. Rev. B* **72**, 014437 (2005).
111. J. H. Mentink, et. al, *Phys. Rev. Lett.* 108, 057202 (2012).
112. M. Aeschlimann, M. Bauer, and S. Pawlik, W. Weber, R. Burgermeister, D. Oberli, and H. C. Siegmann, *Phys. Rev. Lett.* 79, 5158 (1997).
113. B. Y. Mueller, A. Baral, S. Vollmar, M. Cinchetti, M. Aeschlimann, H. C. Schneider, and B. Rethfeld, *Phys. Rev. Lett.* 111, 167204 (2013).
114. C. Herring and C. Kittel, *Phys. Rev.* 81, 869 (1951).
115. M. P. Gokhale and D. L. Mills, *Phys. Rev. B* 49, 3880 (1994).
116. E. Carpene, H. Hedayat, F. Boschini, and C. Dallera, *Phys. Rev. B* 91, 174414 (2015).

117. V. Korenman, J. L. Murray, and R. E. Prange, *Phys. Rev. B* 16,4032 (1977).
118. A. J. Pindor, J. Staunton, G. M. Stocks, and H. Winter, *J. Phys. F* 13, 979 (1983);
119. E. Turgut, et. al, *Phys. Rev. B*, 94, 220408(R) (2016).
120. T. Tsatsoulis, C. Illg, M. Haag, B. Y. Mueller, L. Zhang, and M. Fahnle, *Phys. Rev. B* 93, 134411 (2016).
121. K Ando, H Saito, Z Jin, T Fukumura, M Kawasaki, Y Matsumoto, and H Koinuma, *Appl. Phys. Lett.* 78, 7200 (2001).
122. A L Ivanovskii, *Phy. Uspekhi* 50, 1031 (2007).
123. Ashutosh Tiwari, Michael Snure, Dhananjay Kumar, and Jeremiah T. Abiade, *Appl. Phys. Lett.* 92, 062509 (2008).
124. D Chakraborti, J Narayan, and J T Prater, *Appl. Phys. Lett.* 90, 062504 (2007).
125. Hyeon-Jun Lee, Bo-Seong Kim, Chae Ryong Cho, and Se-Young Jeong, *Phys. Stat. Sol. (b)* 241, 1533 (2004).
126. Y S Wang, P J Thomas, and P O Brien, *J.Phys. Chem. B* 110, 21412 (2006).
127. Ranjani Viswanatha, Sameer Sapra, Subhra Sen Gupta, B. Satpati, P. V. Satyam, B. N. Dev, and D. D. Sarma, *J. Phys. Chem. B* 108, 6303 (2004).
128. M Ferhat, A Zaoui, and R Ahuja, *Appl. Phys. Lett.* 94, 142502 (2009).
129. T. -K. Chung, K. Wong, S. Keller, K. L. Wang, G. P. Carman, *J. Appl. Phys.* 106,103914 (2009).
130. Y. Chen, T. Fitchorov, C. Vittoria, V. G. Harris, *Appl. Phys. Lett.* 97, 052502 (2010).
131. D.I. Khomskii, *J. Magn. Magn. Mater.* 306,1 (2006).

132. P. Yu, J.-S. Lee, S. Okamoto, M. Rossell, M. Huijben, C.-H. Yang, Q. He, J. Zhang, S. Yang, M. Lee et al., *Phys. Rev. Lett.* 105, 027201 (2010).
133. J. Seo, W. Prellier, P. Padhan, P. Boullay, J.-Y. Kim, H. Lee, C. Batista, I. Martin, E. E. Chia, T. Wu et al., *Phys. Rev. Lett.* 105, 167206 (2010).
134. X. Zhai, L. Cheng, Y. Liu, C. M. Schlepütz, S. Dong, H. Li, X. Zhang, S. Chu, L. Zheng, J. Zhang et al., *Nat. Commun.* 5, 4283 (2014).
135. A. Bhattacharya and S. J. May, *Annu. Rev. Mater. Res.* 44, 65 (2014).
136. H. Naganuma, M. Oogane, Y. Ando, *J. Appl. Phys.* 109, 07D736 (2011).
137. X.B. Xue, X.Y. Yuan, W.B. Rui, Q.Y. Xu, B. You, W. Zhang, S.M. Zhou, J. Du, *Eur. Phys. J. B* 86, 121 (2013).
138. T. Yu, H. Naganuma, W.X. Wang, Y. Ando, X.F. Han, *J. Appl. Phys.* 111, 07D908 (2012).
139. G. Srinivasan, E. T. Rasmussen, B. J. Levin, and R. Hayes, *Phys. Rev. B*, 65, 134402 (2002).
140. M. Ziese, A. Setzer, I. Vrejoiu, B. I. Birajdar, B. J. Rodriguez, and D. Hesse, *J. Appl. Phys.* 104, 063908 (2008).
141. A. G. Boni, I. Pintlilie, L. Pintlilie, D. Preziosi, H. Deniz, and M. Alexe, *J. Appl. Phys.* 113, 224103 (2013).
142. J. E. Ordoñez, M. E. Gómez, W. Lopera, and P. Prieto, *IEEE Transactions on Magnetics*, 49,1, (2013).
143. M. Izumi et. al, *Phys. Rev. B*, 64, 064429 (2001).
144. M. Izumi, Y. Ogimoto, T. Manako, M. Kawasaki and Y. Tokura, *J. Phys. Soc. Japan*, 71, 2621 (2002)
145. Y. Ogimoto et. al, *J. J. Appl. Phys.*, 42, L369 (2003).
146. A. X. Gray et. al, *Phys. Rev. B*, 82, 205116 (2010).
147. W.E.Picket, D.J. Singh, *J. Mag. Mag. Mater.* 172, 237 (1997).
148. Y. Tokura, Y. Tamioka, *J. Mag. Mag. Mater.* 200, 1 (1999).

149. M. Bowen et al., J. Phys.: Condens. Matter 19, 315208 (2007).
150. Coey M et al., Adv. Phys. 48 167 (1999).
151. Srinivasa Rao Singamaneni, Wu Fan, J. T. Prater, and J. Narayan, J. Appl. Phys. 116, 224104 (2014).
152. Y. Q. Zhang, et. al, Appl. Surface Sci. 367, 418 (2016).
153. J K Furdyna, J. Appl. Phys. 64, R29 (1988).



## **Chapter 2**

# **Characterization techniques**

---

### **Abstract**

This chapter briefly discusses the various techniques which are used in sample characterization in the present work. Here we discussed shortly on the working principle, instrumentation involved and the model the technique used in the study. The techniques are structural characterization techniques like XRD, Raman and TEM, Microstructural characterization techniques like FE-SEM, TEM and AFM, Magnetic characterization techniques such as FMR, PPMS VSM and optical characterization techniques such as UV/VIS/NIR spectrometer, Z-scan nonlinear optical properties characterization and Pump probe techniques.



## **2. Characterization techniques**

### **2.1 X-ray diffraction (XRD)**

X-ray Diffraction (XRD) is the very important technique and is used in many branches of science like, material science, physics, ceramics, geology, mineralogy, etc. It will give great information about the structure of crystalline materials and can be called as finger print information about the materials. Characteristic monochromatic X-rays were useful in X-ray diffraction studies. Most of the x-ray diffractometer use copper  $K\alpha$  with  $1.5406 \text{ \AA}$  wavelength. Here in INEL XRD we have Cobalt  $1.7889 \text{ \AA}$  wavelength X-ray source.

The x-ray diffraction can be carried out for different kind of materials like powder, crystals and thin films etc. In the powder diffraction method the monochromatic X-rays will fall on the powder samples with various random oriented crystallites and diffract in all directions. Fig.2.1 shows the presently used INEL X-ray diffractometer with Co target X-ray tube is used to do X-ray diffraction measurements. The detector is Position Sensitive Detector (PSD) and is filled with P10-gas (10% methane in Argon) will record the diffracted counts.

In the present work the thin film X-Ray diffraction [1] studies were carried out by BRUKER, GI-XRD, with copper  $K\alpha$  radiation of  $1.5406 \text{ \AA}$  wavelength. The GI-XRD technique is helpful in getting the structural information of very thin films of few nanometer thicknesses. The additional or smart feature this diffractometer is that the diffraction will occur only from the film due to the grazing angle incident of X-rays. The  $0.5^\circ$  grazing angle is used in the X-ray diffraction study of all films.

The recorded X-ray diffraction pattern is compared with the available data of Joint Committee on Powder Diffraction Standards (JCPDS) Pcpdf win and National Bureau of Standards.

## 2. Characterization techniques

### 2.1.1 Principle

When the X-rays of wavelength  $\lambda$  interact with the electrons of atoms, the electrons get accelerated and emit the X-rays of same wavelength this procedure can be called as reflectance of electrons from the atomic planes. Partially, the incident X-ray beam will penetrate to the next level of atomic planes and reflects from those set of planes. In Bragg's law, this interaction of X-rays with crystals is equivalent to the reflection of X-rays from a stack of parallel equidistant atomic planes. This is similar to the description of the three-dimensional grating diffraction effects. If the incident angle is  $\theta$  then by conservation of wave vector the reflected angle will be equal to the incident angle and this angle is called here in this case as the Bragg's angle. See fig.2.2 the path difference is equal to the integer multiple of wavelength of incident X-rays. This is the condition to get the constructive interference between two coherent beams.

$$\text{i.e., } 2d \sin\theta = n\lambda$$

Where,  $n$  is the integral number describing the order of reflection,  $\lambda$  is the wavelength of X-rays,  $d$  is inter planar spacing and  $\theta$  is the Bragg angle.



Fig. 2.1 INEL X-ray diffractometer.

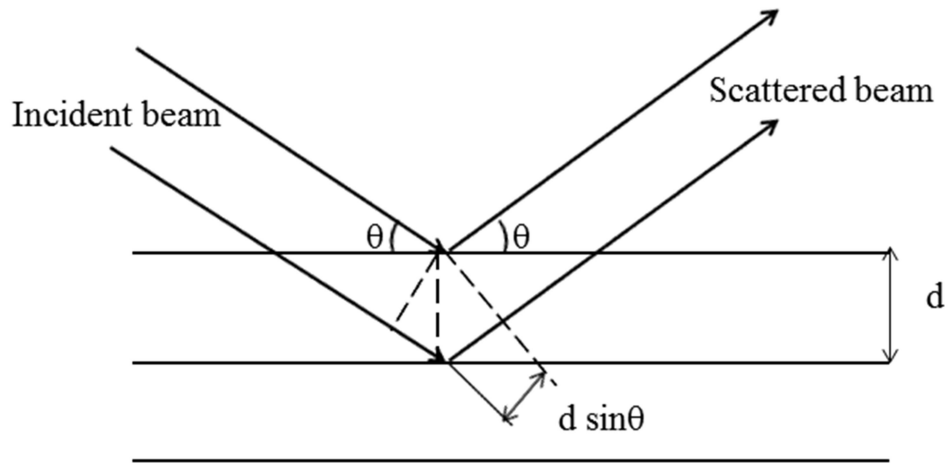


Fig. 2.2 Bragg diffraction of X-rays from a lattice.

In X-ray diffraction, the line broadening is caused by crystallite size distribution; the crystallite size can be estimated from the Scherrer's formula [1].

$$D = \frac{k\lambda}{\beta \cos\theta} \quad 1$$

Where,  $\theta$  is the Bragg angle,  $\lambda$  is the wavelength of the X-rays,  $d$  is the mean dimension of the crystallite size composing the powder sample,  $\beta$  is the full width at half maximum of the pure diffraction profile on the  $2\theta$  scale in radians,  $k$  is a constant. This method is applied to calculate the size of small crystallites.

The strain in the crystal is calculated by the following formula [2]

$$\text{Strain } (\varepsilon) = \frac{d - d_0}{d_0} \quad 2$$

Where  $d$  is the calculated value of distance between two atomic planes and  $d_0$  is the unstrained lattice spacing value taken from standard data of PCPDF or JCPDS.

## 2. 2 Raman spectroscopy

In 1928 Sir C V Raman discovered the Raman scattering. At that time very crude instrumentation was available for scattering experiment. The

## 2. Characterization techniques

development of Raman spectrometer and its various components took place in a span of years of time is summarized in Raman spectroscopy introductory book by John R. Ferraro et. al. [4].

Raman spectroscopy is also one of the major techniques which are highly revolutionary in the scientific society. It is the most sensitive and robust technique. The beauty of this technique is that it doesn't require any sample preparation and it is nondestructive. The main task in the development of this technique that separate outing the Rayleigh Scattered light from the weak inelastic scattered light. Most of the laser light rejection is achieved by holographic grating and multiple dispersion stages. The past Raman spectrometer used photomultipliers as the detectors; these detectors have very long acquisition time. In the modern instrumentation mostly used notch or filters for laser rejection. The schematic diagram of Raman spectrometer [5] is given in fig.2.3. Wide ranges of samples can be used in Raman spectroscopy. Ex. Solids, liquids, thin films, polymers or vapors etc.

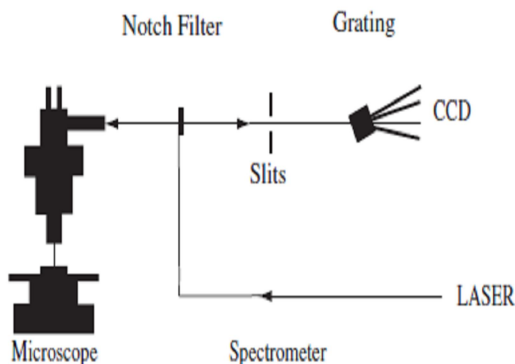


Fig. 2.3 Schematic diagram of confocal Raman spectrometer.

We used HR 800 Horiba Jobin Yvon confocal micro-Raman spectrometer equipped with grating having 1800 groves/mm for our materials and is shown in

## 2. Characterization techniques

Fig.2.4. It has three excitation laser sources. He-Ne laser, Argon ion laser and diode laser, which provides wavelengths of 632 nm, 514 nm and 785 nm respectively. The detecting system is charge coupled device (CCD). The HR 800 uses the notch filter for rejection of the exciting line. The filters are different for different excitation wavelengths. A joy stick is equipped to keep the sample exactly under the illumination spot. The sample holder XY stage is useful in carry out the Raman mapping studies for the sample. In particular the notch filter is used to absorb the entire incident laser light. The small size and high efficiency of notch filter is useful in militarization of the Raman spectroscopy device.

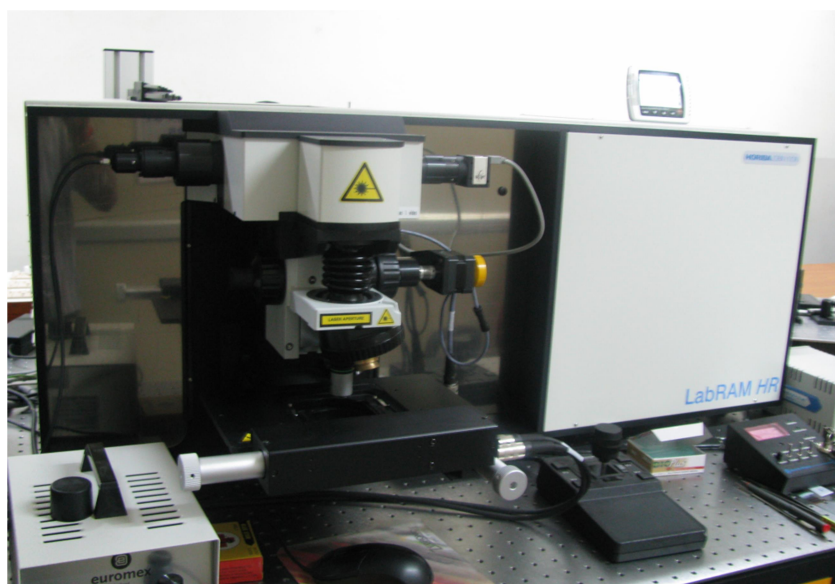


Fig. 2.4 HR 800 Horiba Jobin Yvon confocal micro-Raman spectrometer.

Scattering is the most fundamental phenomena in physics. When the incident particle with certain energy and direction collides or hits the target. The direction and energy of the incident particle may change due to the interaction or collision with the target this phenomenon is called scattering. The incident particle bears different names for scattering like if the incident particles are Neutrons, electrons and photons then corresponding scatterings are called as

## 2. Characterization techniques

Neutron scattering, electron scattering and photon scattering. Depending on the wavelength or energy of photon the photon scattering is further categorized into gamma ray scattering, X-ray scattering and visible light scattering respectively.

The change in energy of incident photon is vital in the scattering process and based on this the scattering of photons can be further divided into Rayleigh scattering, Brillouin scattering and Raman scattering. If the changes are expressed in wavenumber units then if the scattered photon is of same energy to the incident photon then it is termed as Rayleigh scattering thus it is called as elastic scattering also. If the scattered photon energy changes are about  $0.1 \text{ cm}^{-1}$  and above  $1 \text{ cm}^{-1}$  then the scattering processes are termed as Brillouin and Raman scattering respectively [6]. Thus the Raman and Brillouin scatterings are called as inelastic scattering processes.

The Rayleigh part is strong in the scattering process. The Raman scattered signal is very weak ( $10^{-5}$  of the incident beam), it has frequencies of  $\nu_0 \pm \nu_m$  where  $\nu_0$  is the incident radiation frequency and  $\nu_m$  is the vibration frequency of atoms or molecules. The lines corresponding to  $\nu_0 - \nu_m$  and  $\nu_0 + \nu_m$  are called Stokes and Anti - Stokes lines in the Raman scattering [4].

### 2.3 Microscopy

The study of too small objects is very difficult, from some of the well-known techniques microscopy is one which dominates widely. Thus we can say that Microscopy is the study of objects which are very difficult to observe or probe by unaided eye. The sizes of these objects is expressed in terms of submultiples of meter such as micrometer ( $10^{-6}$ ) and nanometer ( $10^{-9}$ ) etc. From the well-known microscopes [7] the most common and first to be invented is photon based optical microscope.

### **2.3.1 Light Microscopy**

The optical microscope uses the visible light for imaging. The normal microscopes are generally used in the experimentation of biological samples. In this the daylight or light from a lamp is directed via lens through the sample into the microscope. This creates a real image of the sample or object on the retina of the eye or in the attached camera. The modern light microscope has the maximum amplification about 1000X [8]. It enables eye to resolve the objects which are separated by 200 nm. The constant efforts by the scientists and engineers to improve the resolution gave hint the light wavelength involvement in the imaging. They found that the resolution is not limited by the lenses used in the microscopy but also depends on the wavelength of light used for illumination. It became difficult to resolve the few nanometer separated samples by visible light. Use of shorter wavelength light (blue or ultraviolet) gave little improvement in the resolution. Another improvement obtained by immersing the specimen and object lens in the higher refractive index liquid. But these two changes could only improve the resolving power to 100 nm.

### **2.3.2. Electron Microscopes**

In the 1920's it was discovered that when the electrons are accelerated in vacuum they resembled the properties of light. It is observed that the wavelength of electrons is about 100,000 times shorter than the visible light and travels in straight line path. In contrast here the electric field and magnetic fields were used to alter the electron beam path like lens in optics.

The first transmission electron microscope (TEM) was built by Ernst Ruska in 1931 at the University of Berlin [9]. This primary electron microscope had two magnetic lenses, three years later he added one more magnetic lens and demonstrated a resolution of 100 nm, this is far better than the optical microscope. The electron microscopes have several advantages like high magnification, large

## *2. Characterization techniques*

depth of focus, high resolution over the optical microscope. The present resolution of electron microscopes is better than 0.05 nm [10]. This is 4000 times better than the normal light microscope and 4,000,000 times better than the unaided eye. The theoretical studies on resolution limit, for visible light based optical imaging was motivating for the development or moving to high resolution based scanning probe techniques. The techniques like STM and atomic force microscopy (AFM), and previously, transmission electron microscopy (TEM) and scanning electron microscopy (SEM) are having great amount of resolution. The specimen is kept at high vacuum in an electron microscope.

### **2.3.2.1 Field Emission-Scanning Electron Microscopy (FE-SEM)**

FE-SEM is an electron microscope in which the electrons which are to be used for scanning are liberated by field emission source [11]. These electrons were used to scan the object in a zig-zag pattern. There are two types of emission processes for electrons, 1. Thermoionic emission. 2. Field emission. These emission processes only makes huge difference between SEM and FE-SEM. In normal electron microscope, the electrons will be generated by thermoionic emission process, in which the tungsten filament is heated to a 2800K temperature [11], whereas in FE-SEM the electrons are ejected by the application of an electric field. The used crystal for this application is LaB<sub>6</sub>. The field emitted electrons will have some advantages like longer life time and high emission yield will give 10X more brightness compared to the thermo ionic emitted beam. But the field emission based microscopes require to be maintaining high vacuum level at the emission source. This increases the cost of microscopes enormously.

The field emission scanning electron microscope provides probing beams with low beam diameter or spot size and high intensity. This improved the spatial resolution and minimized sample damage and charging. The field emission is also two types, cold field emission and Schottky (thermally assisted) field emission.

## 2. Characterization techniques

Thus cold field emission offers very high brightness but varying beam currents. Here no heating but cold source employed. The emission is obtained by placing the filament in gradient electric field. Here a very thin tungsten needle of diameter  $\sim 10^{-7}$ - $10^{-8}$  m is act as a cathode and anode in front of primary and secondary coil respectively. The voltage gradient of 0.5 V to 30 KV is maintained between the cathode and anode. This gives the sufficient gradient at the emitter surface. The emitted high energy electron beam is focused to a spot size of 1 to 5 nm by magnetic lenses. This beam finally passes through the pair of scanning coils, which are helpful in raster the beam across the sample surface (Fig.2.5). As the electron beam produced by field emission is 1000 times smaller than the normal SEM, the image quality is markedly better.

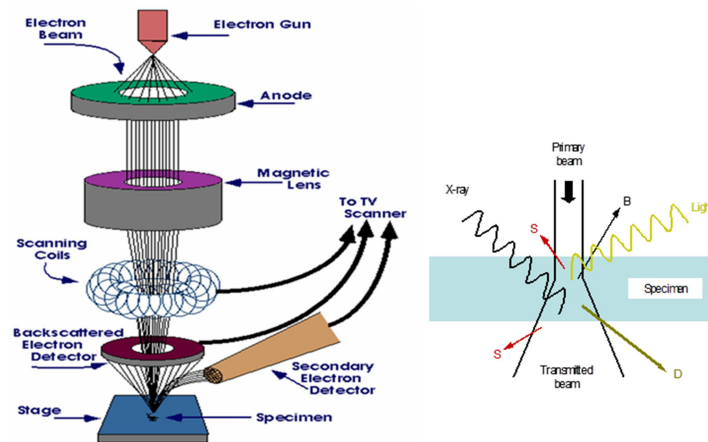


Fig. 2.5 (left) Schematic of Scanning Electron Microscope (SEM). (Right) scattering geometry B= Back scattered electrons, S= Secondary electrons, D= Diffracted electrons

### 2.3.2.1.1 Principle

The accelerated electrons collision with material produces various signals due to the deceleration of high energy electrons and interatomic transitions. Thus the material electron interaction produces secondary electrons, backscattered

## 2. Characterization techniques

electrons, diffracted backscattered electrons photons and heat. Each one of this will be used in determining the sample properties like particle size, elemental analysis etc.

The secondary electrons and backscattered electrons are useful in the construction of SEM image, secondary electrons are vital in the construction of morphology and topography of samples and backscattered electrons are useful in showing the contrast in multiphase sample. The characteristic X-rays which produced in the interaction are used in the elemental analysis of sample. The sample preparation for SEM studies involves it to be made conductive for current and this obtained by coating very thin layer of (1.5-3 nm) thick gold or gold palladium.



Fig.2.6 Field emission scanning electron microscope (model: Carl ZEISS, FEG, Ultra 55).

Energy dispersive X-ray spectrometry (EDS) is the elemental analysis process in SEM in which the X-rays emitted from region of 1 micron is collected and depending upon the characteristic X-rays intensity the presence of

## *2. Characterization techniques*

proportional amount of elements is will be given. Thus it is helpful in quantifying the composition of given sample.

In the present work we have used Carl ZEISS, FEG, Ultra 55 FE-SEM model to analyze surface morphology (fig.2.6).

### 2.3.2.1.2 Technical details of Carl-Zeiss FESEM

This model combined with GEMINI- FESEM column with beam booster contains three direct detection systems. The In-lens SE detector is used for high contrast topography and EsB detector is used for low KV ultrahigh resolution and AsB is for compositional imaging. FE-SEM has the resolution of  $< 2$  nm. The operation maintained in this FE-SEM is less than  $5 \times 10^{-8}$  Pa [12]. This is useful in preventing the electron scattering and discharge.

### **2.3.2.2 Transmission Electron Microscopy (TEM)**

Transmission electron microscope (TEM) also uses very small wavelength electron beam for illumination. It has long cylindrical column of length 2m and an electron emitter is fixed at the top end of this cylinder. Very high vacuum is maintained inside the microscope to avoid the electron collisions. Along the column electromagnetic lenses are placed at regular intervals. This guided electron beam passes through the sample of interest and scatters by the internal structure.

Higher anode voltages are used to accelerate and attain maximum speed of electrons. The de Broglie wavelength is thus given by  $\lambda = h/mv$ . As the resolving power is related to wavelength of electrons, the higher resolution is obtained by increasing the accelerating voltage. The typical ranges of 100 – 300 KV are used for acceleration. The accelerated electrons focused on semitransparent specimen to get the structural and microstructural information. Magnetic lenses are used to magnify the image and are recorded by CCD camera. This CCD detected image is

## 2. Characterization techniques

displayed in real time. TEM can give complete information about the sample, like morphology, crystallographic information, composition and defect studies also.

### 2.3.2.2.1 Modes of operation of TEM

#### 2.3.2.2.1.1 *Bright - Field and Dark - Field Imaging*

The focusing of electrons by magnetic lenses on the sample is the foremost task in the image processing by TEM. These electron waves travelling towards the objective lens forms the diffraction pattern in the back focal plane and this pattern is described by the Fourier transform of the electron wave function at the object plane. In TEM the objective aperture position and size selects the rays or electron paths for image formation. Again by doing the inverse Fourier transform of wave function at the back focal plane will give the wave function of electron at the image plane [13]. Thus the relation between object and its diffraction is simply described by its Fourier transform. This simple fact enables the TEM to create both the images and the diffraction patterns of the object. The important thing to note here is that the diffraction existence is independent of lens. The lens presence is only helpful in determining position of the diffraction pattern along the optic axis.

Depending on the rays selection in the back focal plane we have two types Bright – field and Dark – field modes for imaging [14, 15].

**Bright – field (BF):** In this mode the objective aperture at the back focal plane transmits only the main beam and blocks all other diffracted beams. Thus the undeflected main beam is only used in image formation. The image contrast here occurs due to the subtraction of diffracted beam intensity.

**Dark – field (DF):** Whereas here in this mode contrary to above, the objective aperture at the back focal plane allows the all diffracted beam and blocks the main beam. Thus the image is formed by diffracted beam.

## **2. Characterization techniques**

### *2.3.2.2.1.2 Selected Area Electron Diffraction (SAED)*

In this technique the objective aperture is removed and intermediate aperture is inserted at the image plane of objective lens, it selects the image of interest region which is formed from the normal imaging mode. Now the diffracted mode is switched on and the diffracted pattern is recorded on the screen or by CCD camera. Selected area electron diffraction (SAED) is useful in determining the phase of few selected areas of the sample. The smaller area selection from the image is purely depends on the size of the aperture and its spherical aberration. For nano-diffraction studies the convergent beam electron diffraction (CBED) is employed.

### *2.3.2.2.1.3 Convergent beam Electron Diffraction (CBED)*

The condenser lens system has the great versatility in the illumination of the sample. The angular divergence and cross - section and its time dependent modulation of the incident electron beam can be controlled in the advanced version of TEM. Convergent beam electron microscopy uses few of these features in the nanometer level region diffraction studies.

### *2.3.2.2.1.4 High Resolution Transmission Electron Microscopy (HRTEM)*

HRTEM image cannot be formed by bright or dark – filed techniques. Fourier transforms plays a vital role in HRTEM analysis. The scattering factor distribution  $f(r)$  is related to the atomic arrangement in the crystal. The diffracted electron wave function  $\psi(\Delta k)$  is the Fourier transform of,  $f(r)$ . The selection of range of  $\Delta k$  is carried out by objective in the back focal plane in the imaging technique. Thus a much small aperture is used in the DF and BF imaging whereas large aperture is needed in obtaining the HRTEM images.

In the present work we have used the FEI Tecnai G<sup>2</sup> S-Twin, FEI electron microscope is used and operated at 200 kV using Gatan CCD camera.



Fig. 2.7 Photograph of FEI Tecnai G<sup>2</sup> S-Twin, FEI Transmission electron microscope.

### 2.3.3 Atomic force microscopy

The electron beam based microscopes have difficulty in imaging the objects at the atomic level. Scanning Probe microscope (SPM) is a revolutionary technique which allows scientists to obtain three dimensional image of the surface at the atomic scale. The scanning probe microscopy technique is non-destructive and covers wide ranges of material imaging. Unlike traditional microscopes, scanned-probe systems do not use lenses, so the size of the probe limits their resolution rather than diffraction effects. The scanning probe microscopies can be categorised dozen of classes like Scanning Tunnelling, Atomic Force, Magnetic Force and Piezo Force microscopy etc.

All of these microscopes work by measuring a local property -such as height, optical absorption, or magnetism-with a probe or “tip” placed very close to the sample. The small probe-sample separation (on the order of the instrument's resolution) makes it possible to take measurements over a small area. Among the

## *2. Characterization techniques*

all above mentioned microscopies here we will discuss on Atomic Force Microscopy (AFM).

The first AFM was first developed by Binnig, Quate and Gerber in 1986 [16]. The basic principle of AFM is based on the Van der Waal interactions between the atoms. Thus AFM generates images based on the alteration of inter atomic forces.

The following four major components of AFM are very important in the imaging process. 1. Tip or probe, 2. Position sensitive Photo detector, 3. Piezo electric scanner, 4. Feedback mechanism.

### **2.3.3.1 AFM Tip or Probe**

As it is the van der Waal interaction based scanning of surfaces. The probe or tip which is used for scanning has to be very small it is around 50 nm in size. It is mounted on the 100  $\mu\text{m}$  length flexible cantilever. The very low spring constant cantilever is used, it sensitive to the minute van der Waals forces between surface and tip. The tip senses the force and cantilever responds.

### **2.3.3.2 Position sensitive Photo detector**

In the scanning process as tip approaches the surface the interaction between the cantilever tip and the sample surface leads to small bending of the cantilever. This Deflection detection is carried out by measuring the laser beam which is reflected from the back side of the cantilever. This deflected signal is also used to adjust the interaction force by feedback loop.

### **2.3.3.3 Piezo electric scanner and feedback mechanism**

The samples which are to be imaged are placed on the XYZ piezo scanner [17]. As discussed in the previous section the cantilever position is restored by the feedback loop by adjusting the piezo scanner which lies below the sample. Thus

## 2. Characterization techniques

the piezo movement is also useful in constructing the height image. The schematic of Atomic Force Microscopy is shown in fig. 2.8.

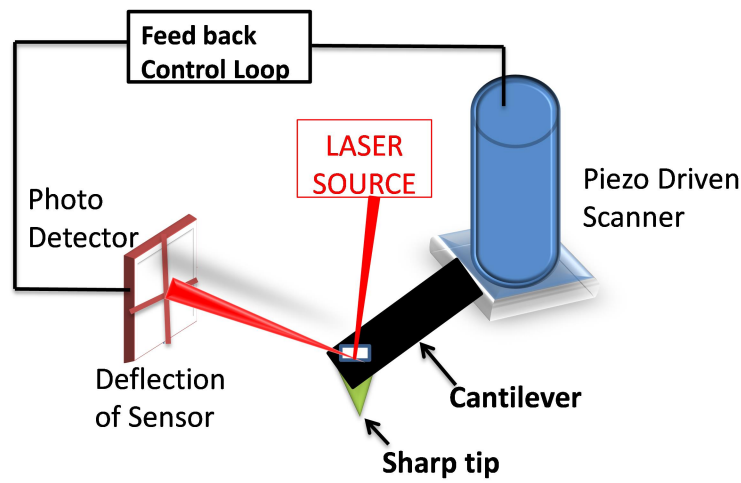


Fig. 2.8 Schematic diagram of atomic force microscopy.

### 2.3.3.4 Operating modes of AFM

The AFM works in two ways by maintaining the constant height or by maintaining constant force between the sample and AFM tip. The constant force is the preferable mode.

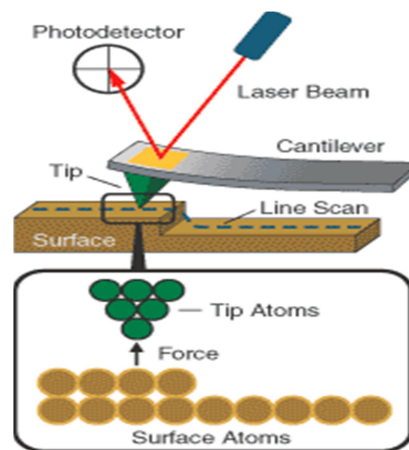


Fig.2.9 Schematic of AFM which depicts how the the van der Waal interactions arises between AFM tip and sample surface atoms.

## 2. Characterization techniques

Depending on the cantilever motion the working of AFM is categorized into two branches, namely static mode and dynamic mode.

- a) Static mode: The cantilever will move across the sample surface and scans by cantilever deflection.
- b) Dynamic mode: In this mode the cantilever oscillates close to its resonance frequency the interaction with the surface modifies the oscillation and hence scans the sample.

Based on the nature of sample and by considering the van der Waal potential curve the AFM scanning modes are classified into three categories. The important point to remember in the contact mode is that the AFM tip is not in contact with the sample, but it will be very near and the force between the sample and tip is repulsive and the working region is shown in fig.2.10 for both contact and non-contact modes. The tapping mode mostly employed in the study of imaging and mechanical properties of biological samples [18-20].

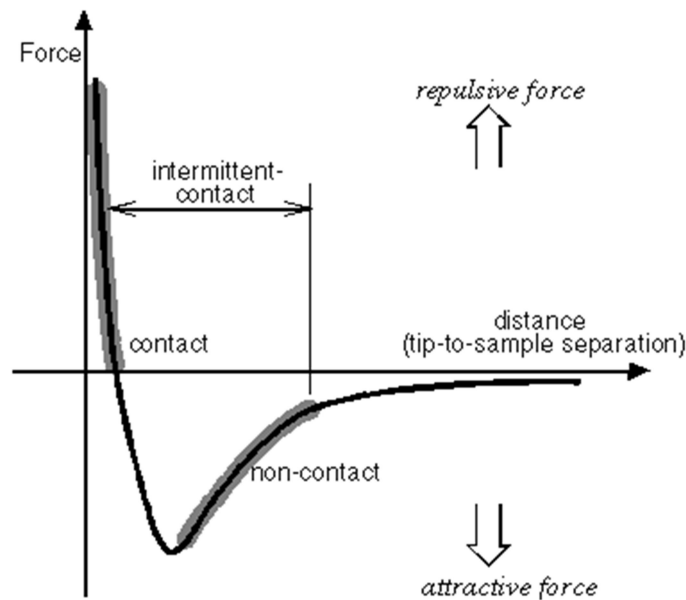


Fig. 2.10 Nature of forces in the Contact and Non-contact mode of AFM operation.

## 2. Characterization techniques

### 2.3.3.4.1 Contact mode

1. The effective force is repulsive.
2. The force between tip and sample is constant.

### 2.3.3.4.2 Non contact mode

1. The cantilever will oscillates slightly above the resonance frequency.
2. Constant oscillations by adjusting the distance.

### 2.3.3.4.3 Tapping mode

1. Cantilever will oscillates near resonance frequency of 2 kHz with a 100-200 nm amplitude.
2. To avoid the damage to surface, when a liquid layer is formed on the surface

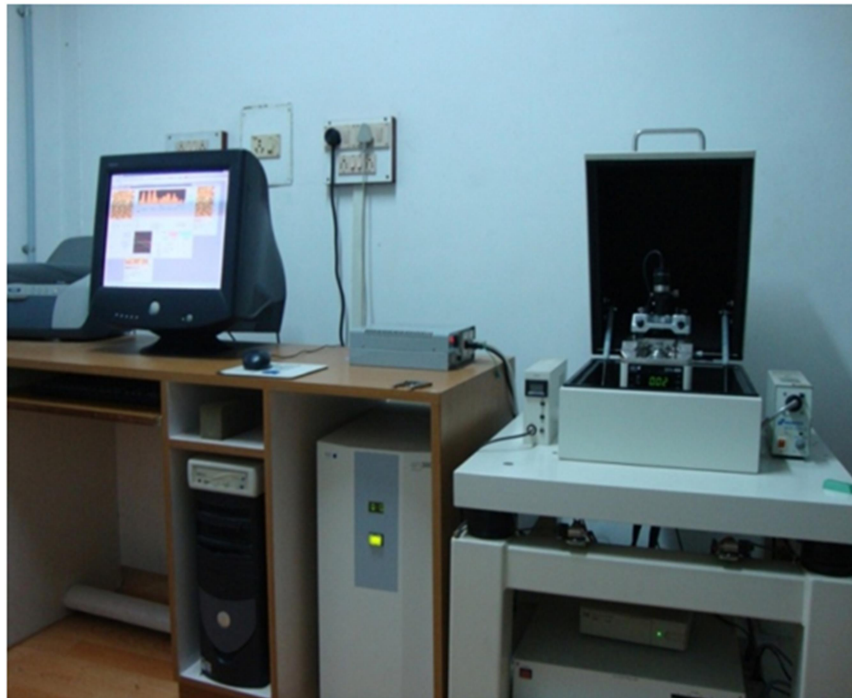


Fig. 2.11 Photograph of the SPA-400 atomic force microscopy used in the present study  
In the present studies we have used the SPA-400 model for imaging of film surfaces.

## **2.4 UV/VIS/NIR Spectroscopy**

Wide range of materials like organic, inorganic, nanoparticles, crystals and thin films can be characterized by spectrophotometer. The coefficient of transmission, Reflectance and Absorption are measured by this instrument. In case of nanoparticles, the measurement of absorption coefficient is effective in extracting the optical properties of the nano particle. Thus, in general absorption spectroscopy is the measure of absorption of radiation by particular material as a function of wavelength. Depending on the wavelength range the spectroscopy can be categorized into infrared or UV/VIS absorption spectroscopy.

### **2.4.1 Instrumentation of UV/VIS/NIR Spectrophotometer**

The schematic diagram of UV/VIS/NIR Spectrophotometer is shown in below fig.2.12. Since it contains three ranges of electromagnetic spectrum, two light sources deuterium lamp for ultraviolet and halogen lamp for VIS and NIR region are used. The vital components of the spectrophotometer are light source, grating, samples holders and detectors.

### **2.4.2 The light source**

Here the light sources are deuterium lamp which produces the ultraviolet range (190-350 nm) range light and Halogen lamp covers remaining VIS/NIR (330-2500 nm) range light [21]. Thus the combination of these two sources will act as light source to characterize the sample in whole range. This light then passes through the grating and splits into single wavelengths.

### **2.4.3 The diffraction grating and the slit**

The diffraction grating and slit is the second most crucial part of spectrophotometer. The grating separates the light source into component wavelengths like a good quality prism by diffraction. Subsequently the slit selects

## 2. Characterization techniques

each of these wavelengths and sends as monochromatic beam into the next section of the spectrophotometer.

### 2.4.4 Sample cell, reference cell

The above selected monochromatic light then passes through beam splitters with the help of mirrors and then splits into two beams, one passes through the reference sample cell and other through the measuring sample cell.

### 2.4.5 Detectors

The light which passed through the sample cell and reference cell is measured by two photo detectors. In most of the spectrophotometers the photomultipliers and lead sulfide (PbS) photocells are used as detectors [21].

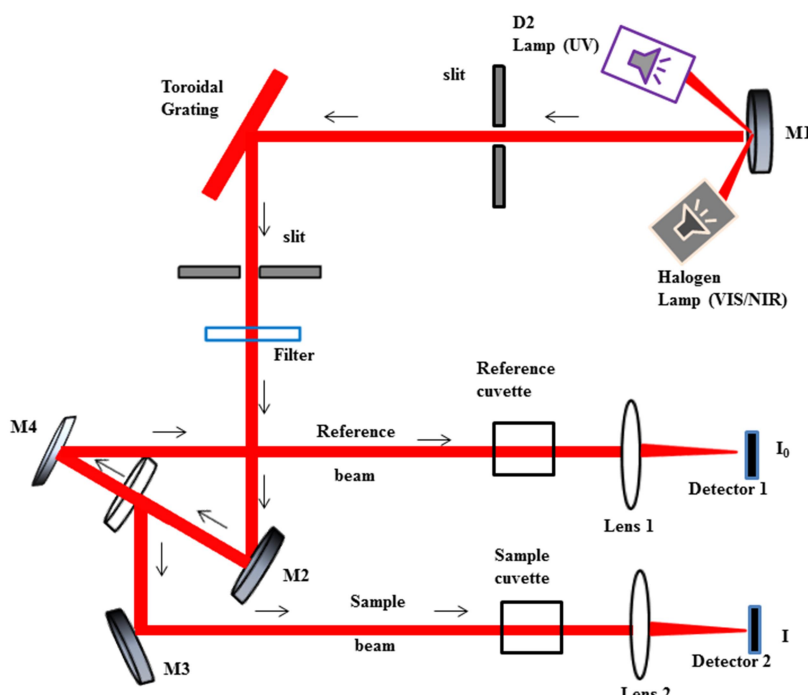


Fig.2.12 Schematic diagram of JASCO-570 UV/VIS/NIR Spectrophotometer.

## 2.5 Magnetic property characterizations

### 2.5.1 Physical Property Measurement System (PPMS)

The Physical Property Measurement System (PPMS) [22] has a flexible, automated workstation which can carry out variety of experiments. But this requires precise thermal control. It can perform measurements like magnetometry (AC susceptibility and DC magnetization), electron transport measurements (Hall Effect, I – V characteristics, ac and dc resistivity and magneto resistance), thermal transport (Thermal conductivity, Seebeck coefficient) and heat capacity etc. Thus it maintains a very good temperature control over a wide range (1.8K to 350K) of temperature. A superconducting magnet is used to produce fields up to  $\pm 9$  Tesla of high uniformity of (0.01 %) within the selected range. The MultiVu software is used for sweeping the magnetic fields in modes like linear and no-overshoot. In linear mode the field attains the set value linearly where as in no-overshoot mode the field rapidly ramped  $\sim 70\%$  of the set value and then increased slowly to avoid the overshooting. The PPMS can also constant magnetic field during these measurements. In the present work the measurements are carried out with PPMS-6000 (Quantum deign) model.

### 2.5.2 DC Magnetometry

In DC measurements the sample is moved rapidly through the both sets of coils in the presence of constant applied magnetic field. According to Faraday law a signal will be induced in the coil. This method is termed as the extraction method. The strength of the induced signal purely depends on the sample magnetic moment and extraction speed. In ACMS the DC servo-motor extracts the samples at speeds of 100 cm/sec. This high speed thus strengths the signal compared to conventional DC extraction systems and the contribution of time-dependent errors like  $1/\text{noise}$  and drift also minimized. The averaging of several scans for each measurement is possible due to the short scan time and thus

## 2. Characterization techniques

the contributions of random errors are also reduced. This leads to the very high sensitivity and great accuracy for this system based measurements. The sample magnetic moment is obtained by analyzing the signal a digital signal processor (DSP).

### 2.5.3 Vibrating Sample Magnetometer (VSM)

Among the many options VSM is one of PPMS option which is a magnetometer with a linear motor transport head, and is fast and sensitive. The location of the sample is done by a compact gradiometer pickup coil. The separate electronic were arranged to drive the linear motor transport and for detecting the response from the pickup coils. The large oscillation amplitude and frequency of 40 Hz of the system will support to detect the magnetization even lower than the  $10^{-6}$  emu with 1 Hz sampling rate.

As the sample is vibrated sinusoidally, the changing magnetic flux induces a time dependent voltage in the pickup coil and given by the following equation,

$$\begin{aligned} V_{coil} &= \frac{d\phi}{dt} = \left(\frac{d\phi}{dz}\right) \left(\frac{dz}{dt}\right) \\ &= 2\pi f C m A \sin(2\pi f t) \end{aligned} \quad 3$$

Where  $\phi$  is the flux passing through the coil,  $z$  is the vertical distance of the sample w.r.t to the coil,  $t$  is time,  $C$  is coupling constant,  $m$  is the DC magnetic moment of the sample and  $A, f$  are the amplitude and frequency of the oscillation.

## 2.6 Magnetic Resonance

The motion of magnetic moment under the influence of external magnetic field is thoroughly carried out by magnetic resonance techniques. The magnetic moment precesses due to the applied strong field  $H$  and a weaker alternating field  $H_1$  is applied in perpendicular to  $H$ . When the  $H_1$  field frequency equals to the

## 2. Characterization techniques

Larmor frequency the magnetic moment will lie along the H direction (radiation will emit) or away from H direction (radiation absorption). Thus depending upon the type of magnetic moment present in the sample resonance absorption techniques are termed as nuclear magnetic resonance (NMR), paramagnetic resonance (EPR) and ferromagnetic resonance (FMR) [23, 24].

### 2.6.1 Electron Spin resonance

Electron paramagnetic resonance (EPR) or Electron spin resonance (ESR) is one of the most sensitive magnetic measurements. It was first discovered by Zavoiskii, Cumberow and Halliday [25, 26]. When the numerical values are substituted in equation given below

$$\omega = - \frac{ge}{2mc} H \quad 4$$

They obtained resonance condition for  $\nu = 1.401gH$ , where  $\nu$  is in Mc/sec and H is in oersted. For a field of few kilo-oersted and  $g = 2$  the resonance frequency falls in the microwave region. Since the variable frequency sources availability is very rare, the experiments were carried out at fixed frequency by varying the magnetic field. The advantage of working in microwave frequency range is due to the larger difference in populations due to the higher magnetic field and hence the absorption will be stronger. The various microwave frequency ranges and applied magnetic fields are summarized in below table.

Table 2.1 different microwave frequencies designation and corresponding used magnetic fields.

Designation	Frequency (GHz)	Wavelength (cm)	Magnetic field (G)
S	3.0	10.0	1070
X	9.5	3.15	3390
K	23.0	1.30	8200
Q	35.0	0.86	12500

### 2.6.2 Ferromagnetic resonance

When the materials have long range magnetic order supported by exchange interactions, the net magnetic moment will be high compared to the magnetic moment due to single spin thus in ferromagnetic materials the macroscopic magnetic moment precesses about the axis of effective magnetic field ( $H_{eff}$ ) [27]. Thus the magnetic resonance in these materials termed as the ferromagnetic resonance and the resonance condition is given by the equation

$$\Omega = \gamma\mu_0 H_{eff} \quad 5$$

Where,  $\gamma$  is the gyromagnetic ratio.

By neglecting the damping terms the equation of motion of Magnetization vector under the influence of effective magnetic field can be described by the following equation [25].

$$\frac{dM}{dt} = \gamma(M \times H_{eff}) \quad 6$$

Here  $H_{eff}$  includes both the applied field and internal anisotropy field.

#### 2.6.2.1 Experimental set up

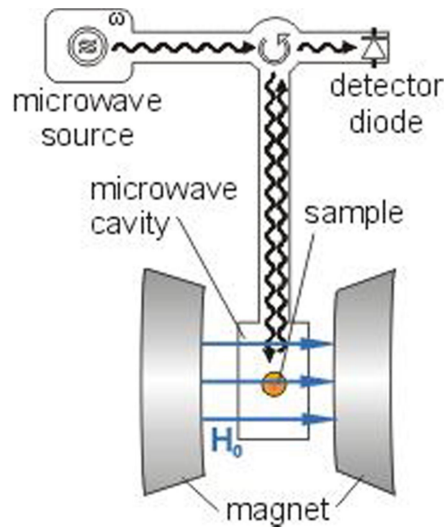


Fig.2.13. Block diagram of ESR/FMR spectrometer

## **2. Characterization techniques**

The Ferromagnetic resonance studies were carried out by (JEOL, JES-FA200) spectrometer in the X-band frequency region.

The block diagram of an ESR/FMR spectrometer is shown in fig.2.13. The major components in the instrumentation this spectrometer are the Klystron which generates the microwave radiation, cavity, variable magnetic field producing electromagnet, and detector. The microwaves which were produced by the klystron were guided to the resonator where the sample exists by rectangular waveguide with an attenuator. The magnetic field is varied across the resonance condition and detector helps in detecting the absorbed signal

### **2.7 Z - Scan Technique/ Nonlinear optical studies**

The Z-scan measurements were carried out by Ti: sapphire laser (Coherent, Legend amplifiers) operating at a repetition rate of 1 kHz with pulse duration  $\sim 2$  ps at 800 nm. The oscillator (Coherent, Micra) sends  $\sim 15$  fs pulses into the amplifiers and then in put beam will come from the amplifiers, which is used in the experiments. This input beam is a pure Gaussian beam and obtained through spatial filters. A 200 mm focal length convex lens is used to focus this 3mm beam to even smaller spot on the sample and then the Z-scan measurements performed [28-32]. A high resolution translation stage is used to move the sample in the beam path and the detector (Si photodiode, SM1PD2A, Thorlabs) output was connected to a lock-in amplifier. The thickness of the films is of the order of  $80 \pm 10$   $\mu\text{m}$ . The linear transmittance is  $\sim 50-55$  % at 800 nm wavelength (for all samples). The measurements were repeated more than once for each sample and the nonlinear parameters were obtained from fitting. The Schematic of the z-scan experiment is shown in fig.2.14

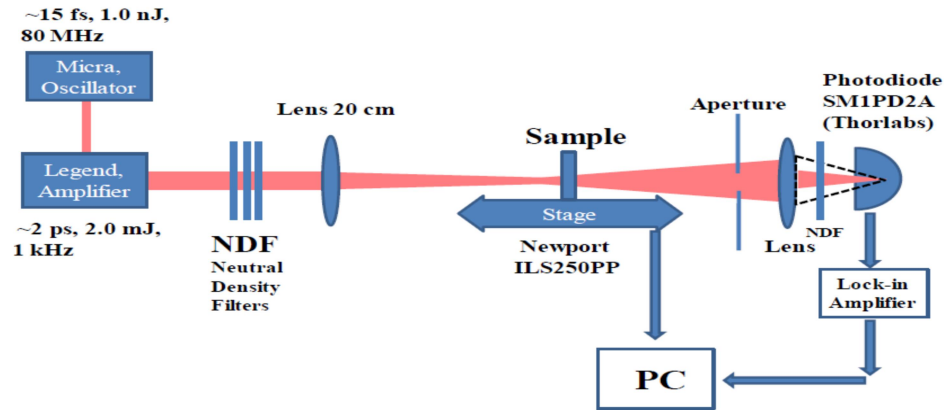


Fig.2.14. Experimental schematic of Z-Scan

### 2.8 Pump – probe Experimental details

The fs pump-probe experiment was carried out using 800 nm wavelengths coming out from LEGEND (amplifier). The MICRA output at ~15 fs FWHM, 800 nm, 80 MHz will act as a seed to the LEGEND amplifying system. This LEGEND (Ti: Sapphire laser system) amplifies the seed pulse and delivers with ~40 fs, 800 nm pulses at 1 kHz repetition rate.

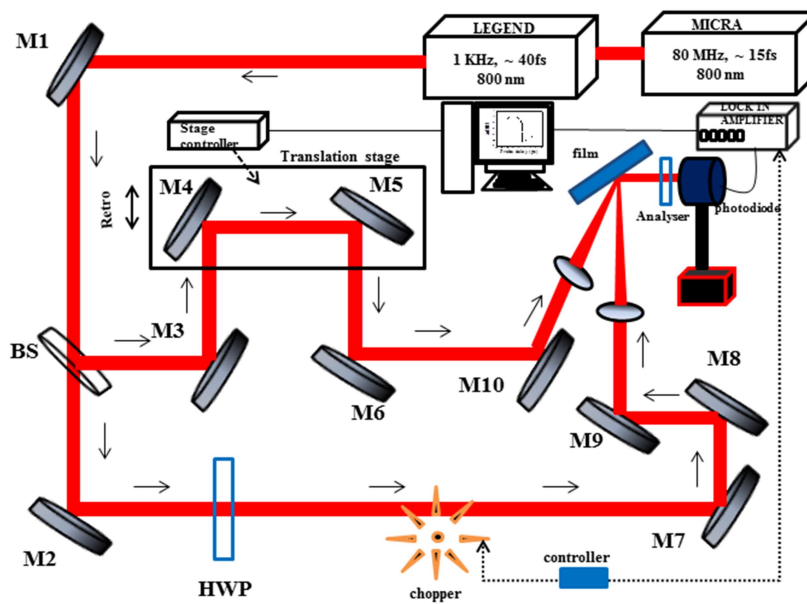


Fig.2.15. Schematic diagram of pump - probe setup for 800 nm wavelength.

## *2. Characterization techniques*

As the experiment contains same wavelengths for pump and probe it is called a degenerate pump-probe experiment [33, 34]. The schematic diagram of the experimental set up is shown in fig. 2.15. The pump energy used in the experiment is  $\sim 80 \mu\text{J}$ . The spot size at the sample is around  $80 \mu\text{m}$ . Hence, the energy density used in the experiment is  $10 \text{ mJ/cm}^2$ . The pulse width is around  $80 \text{ fs}$  by taking into account stretching of pulse due to the optics involved in the experiment. Two lenses of  $150 \text{ mm}$  and  $500 \text{ mm}$  is used to focus the pump and probe on the sample respectively. A chopper is used at  $100 \text{ Hz}$  to modulate the pump beam. Photodiode (SM05R/M, Thorlabs) through lock-in amplifier (7265, Signal Recovery) is used to measure the change in reflectance from the Nickel film. The polarizer is used in the pump beam to get perfectly polarized light and an analyser is used by putting in the probe beam. The diameter of probe beam is smaller than that of pump beam to get the excited material dynamics.

**References**

1. Mario Birkholz, "Thin Film Analysis by X-Ray Scattering", Wiley-VCH (2006).
2. A L Patterson, Phys. Rev., 56, 978 (1939).
3. B D Cullity, Elements of X-ray diffraction, Addison-Wesley Publishing Company, Inc. pg. 434-436 (1956).
4. John R Ferraro, K Nakamoto and Chris W Brown, "Introductory Raman Spectroscopy" Elsevier, (2003).
5. E Smith, G Dent, "Modern Raman Spectroscopy–A Practical Approach" John Wiley & Sons Ltd (2005).
6. Shu-Lin Zhang, "Raman Spectroscopy and its Application in Nanostructures 1<sup>st</sup> edition", John Wiley & Sons, Ltd. (2012).
7. Ray F. Egerton, Physical Principles of Electron Microscopy, Springer, (2005).
8. Y. Leng, Materials Characterization Introduction to Microscopic and Spectroscopic Methods, John Wiley & Sons (Asia) Pte Ltd (2008).
9. M De Graef, "Introduction to conventional Transmission Electron Microscopy" Cambridge University Press, Pg. 137-139 (2003).
10. H Wang, X-Z Yuan, H Li, "PEM Fuel Cell Diagnostic Tools", pg. 336-337, CRC press, (2011).
11. Y Leng, materials characterization Introduction to Microscopic and Spectroscopic Methods, pg. 79-144, JohnWiley & Sons (Asia) Pte Ltd, (2008).
12. L Reimer H Kohl, Transmission Electron Microscopy Physics of Image Formation fifth edition pg. 89, Springer Science (2008).
13. B fultz and J M Howe, "Transmission electron microscopy and diffractometry of materials" 3<sup>rd</sup> edition Sprnger Berlin Heidelberg New York (2008).

## *2. Characterization techniques*

14. A Eades, *Acta Microscopica* 17, 101 (2008).
15. M D Graef, "Introduction to conventional transmission electron microscopy" Cambridge University Press, (2003).
16. G Binning, C F Quate and Ch Gerber, *Phys. Rev. Lett.* 56, 930 (1986).
17. J Malohlava, H Zapletalova, K Tomankova and H Kolarova, Atomic force microscopy: Studying mechanical properties of a cell. In: *Current Microscopy Contributions to Advances in Science and Technology*. Pg. 528–532, Badajoz, Spain: Formatex, (2012).
18. C Heu, A Berquand, C Elie-Caille, L Nicod, *Journal of Structural Biology*, 178 (2012).
19. Y Wang, G Subbiahdoss, J Swartjes, HC van der Mei, HJ Busscher, M Libera, *Advanced Functional Materials*, 21, 3916, (2011).
20. J Adamcik, A Berquand, R Mezzenga, *Applied Physics Letter*, 98, 193701. (2011).
21. JASCO Model V-550/560/570 Spectrometer Manual.
22. Physical Property Measurements System (PPMS), User's Manual, Quantum Design, San Diego, CA, USA, 1084-100A, (2009).
23. J Stohr H C Siegmann, "Magnetism from fundamentals to nanoscale dynamics" Springer-Verlag Berlin Heidelberg, pg. 333 (2006).
24. A H Morrish, 'The Physical Principles of Magnetism' John Wiley & Sons, Inc., Pg. 106-111 (1965).
25. E Zavoisky, *J. Phys. (USSR)* 9, 211 (1945).
26. R L Cummrow and D. Halliday, *Phys. Rev.* 70, 433 (1946).
27. R Meckenstock, Ph.D. thesis, Ruhr-Universität Bochum, (1997).
28. M Sheik-Bahae, A. A. Said and E. W. Vanstryland, *Opt. Lett.* 14, 955 (1989).
29. S Venugopal Rao , T Shuvan Prashant, T Sarma, Pradeepta K Panda, D Swain, Surya P Tewari, *Chem. Phys. Lett.*, 514, 98 (2011).

## *2. Characterization techniques*

30. S Hamad, S P Tewari, L Giribabu, S Venugopal Rao, J. Porphyrins Phthalocyanines, 16, 140, (2012).
31. M Yin, H P Li, S H Tang and W Ji, Appl. Phys. B., 70, 587 (2000).
32. K Venkata Saravanan, K C James Raju, M Ghanashyam Krishna, S P Tewari, S Venugopal Rao, Appl. Phys. Lett., 96, 232905, (2010).
33. D Swain, P T Anusha, T S Prashant, S P Tewari, T Sarma, P K Panda, S Venugopal Rao, Appl. Phys. Lett., 100, 141109 (2012).
34. P T Anusha, D Swain, S Hamad, L Giribabu, T Shuvan Prashant, S P Tewari and S Venugopal Rao, J. Phys. Chem. C, 116, 17828 (2012).

## Chapter 3

# Synthesis and structural, micro structural characterization

---

### Abstract

This chapter briefly discusses the synthesis conditions of nanocrystalline - BaTiO<sub>3</sub> (nc-BTO) and deposition of Nickel film. The ferromagnetic Nickel films of three different thicknesses were deposited by RF-magnetron sputtering. Here we have used two chemical methods for BTO nanoparticle synthesis 1. Sol-gel, 2. Sonochemical method. Four different size BTO particles of sizes ranging between 23-54 nm were prepared by sol-gel method. Using the sonochemical method, the BTO mesocrystals of 200 nm were obtained which are constituted of 5-8 nm size particles.

The structural (phase confirmation) characterization has been carried out by X-ray diffraction (XRD), Transmission Electron Microscopy (TEM) technique. The dislocation and strain existence in the material is also quantified using these two techniques. The 23 nm, 54 nm size particles shown the presence of compressive strain in it, whereas the 31 nm, 34 nm particles shown tensile strain presence in the material. It is found that the dislocations are responsible for the observed strain in the material. The Nickel films show single phase formation and the morphological studies were carried out by Atomic Force Microscopy (AFM).

The above developed materials, various properties were probed by respective characterization technique and completely discussed in the subsequent chapters.



### **3. Synthesis and structural, microstructural characterization**

#### **3.1 Introduction**

Most of the ferroelectric materials have multi atoms. Sol-gel method is one of the best methods to synthesis this kind of materials. The precursors in the sol-gel method are mostly solution based metal compounds, eg. alkoxides [1, 2], acetates, etc. Sol-gel method is widely used in the development of various perovskite materials of  $ABO_3$  formula. The perovskites as we know exhibits various phases depending upon the atoms constitutes of it. Hence, sol-gel method becomes one of the highly used methods to develop materials of high  $T_c$  superconductors, Magneto resistive materials and ferroelectrics and piezoelectric properties. As the sol-gel process contains solution as the starting material before film deposition, hence, it is the highly suitable technique to develop or coat different shape films and microstructures [3]. The different shape, size microstructure can be developed by controlling the thermodynamic parameters P, V, and T. The coating method will be selected by the requirement of area of coating, shape of coating substrates and can vary from spin coating, dip coating to spray coating etc. as per the requirement. The processing temperatures are also low for sol-gel method [4, 5].

There are many synthesis reports for  $BaTiO_3$  by sol-gel method. X. Zhang et.al [6] prepared it by using barium hydroxide octahydrate and tetra butyl titanate as the source precursor chemicals for Ba and Ti elements. The synthesis was carried out in two steps. In the first step, the polyethyleneglycol (PEG) was dissolved in deionized water and then acetic acid added to it. In separate the tetra butyl titanate was dissolved in ethanol and this added to the above solution drop by drop with stirring. This mixture was heated at  $80^\circ\text{C}$  for 1hr then the titanium hydroxide precipitate will form. Then the precipitate was taken out by an appropriate method. In the second step the precipitate and barium hydroxide octahydrate were

### ***3. Synthesis and structural, microstructural characterization***

added to deionised water. In final the mixture was stirred and heated, and the refluxing was carried out at 140°C for four hr. The final powder obtained by centrifuging with successive heating at 50°C for 24 hr. J. Yuk et. al. Carried out the BTO preparation by considering barium acetate and titanium isopropoxide as the precursor chemicals [7]. S. Otsuki et. al. prepared gold nanoparticles embedded BTO films by the sol-gel method they also used barium acetate and titanium isopropoxide as the source Ba and Ti [8]. E. J. H. Lee et. al used barium carbonate and titanium IV isopropoxide as the precursor chemicals for BTO film preparation [9].

In addition to this the one most fundamental method to study the synthesis mechanism or material growth mechanism via chemical synthesis is the sonochemical method.

The mesocrystals will have high internal surface area. It uses the colloidal dispersions, that were treated with ultrasonic radiation and the procedure is termed as sonochemical method. In adult sea urchin spine, each spine composes of a highly oriented array of Mg-calcite nanocrystals embedded with amorphous and macromolecules in it. This diffracts X-rays as a single crystal but fractures like a glassy material. Thus, mesocrystals are the ambitious candidates for providing the simultaneous behavior of single crystal and amorphous materials in the same system. The high porosity or voids in mesocrystals are used for the immobilization of some organic molecules. Thus, mesocrystals have many applications in various fields like Biology, material science, etc. The vital properties of mesocrystals such as high crystallinity, oriented attachment, and the high porosity makes it a potential candidate in the areas of sensing, biomedical materials, optoelectronics, etc. Notably the high porosity of these materials makes them suitable for applications such as energy storage and photocatalysis [10]. Mesocrystals of few materials has been recently found to be efficient in THz generation [11, 12]. It is well known that piezoelectric materials got many

### 3. Synthesis and structural, microstructural characterization

applications from domestic to the industrial sector. It is possible to achieve higher piezoelectric coefficients by crystal axis oriented materials [13]. The [110] oriented BTO materials have got  $d_{33}$  value of 788 pC/N [14] while the normal BTO shows a  $d_{33}$  value of 190 pC/N, which is one-fourth of that of the oriented BTO material [15]. These mesocrystals have many advantages in various field like Biology, material science, etc. In the present case, we are trying to synthesize the ferroelectric BaTiO<sub>3</sub> (BTO) mesocrystals using it THz generation because of oriented attachment and BTO is a high dielectric constant material.

For metal film deposition, there are few physical vapor deposition methods like thermal evaporation, DC Sputtering, and RF-Sputtering. Here, in the present chapter we have used RF-Magnetron sputtering for Nickel film deposition. In addition to this technique is versatile to deposit films from metals to insulators of all kinds.

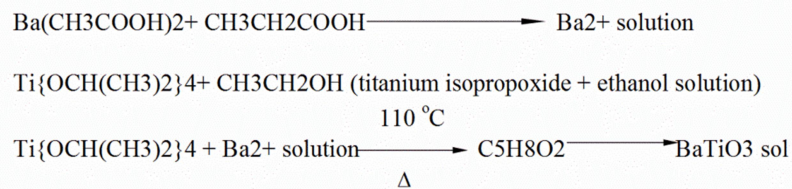
### 3.2 Nanocrystalline-BaTiO<sub>3</sub> (nc-BTO) powder preparation

To carryout various physical property measurements for this system, it is necessary to maintain nano size of the particles. The sol-gel technique is one of the most efficient technique to synthesis the nano materials. The one more efficient technique I have chosen is the sono chemical synthesis of nc-BTO powder.

#### 3.2.1 Sol-gel synthesis

##### 3.2.1.1 Stoichiometric calculations

The chemical reactions that occur in the Sol-gel process are given below.



### 3. Synthesis and structural, microstructural characterization

BTO nanoparticles of various sizes were prepared using sol-gel method [16-18], by taking Barium acetate and Titanium isopropoxide as precursor chemicals. 0.0067 mole of barium acetate is dissolved in 40 ml of propanoic acid and stirred until it gets completely dissolved. Then equal mole of titanium isopropoxide is dissolved into 10 ml of ethyl alcohol in the presence of N<sub>2</sub> atmosphere. Finally, this solution is added drop by drop into dissolved barium acetate in the N<sub>2</sub> atmosphere. Slowly, the Sol is heated to 110°C. Now 0.02 mole of acetyl acetone is added and stirred for 3hrs. The prepared Sol was dried at 200°C for 10 hrs. This dry powder is then calcined at 650°C-800°C temperature range for 1hr

#### 3.2.1.2 Schematic representation of sol-gel method

Fig.3.1 shows the schematic representation BTO sol preparation.

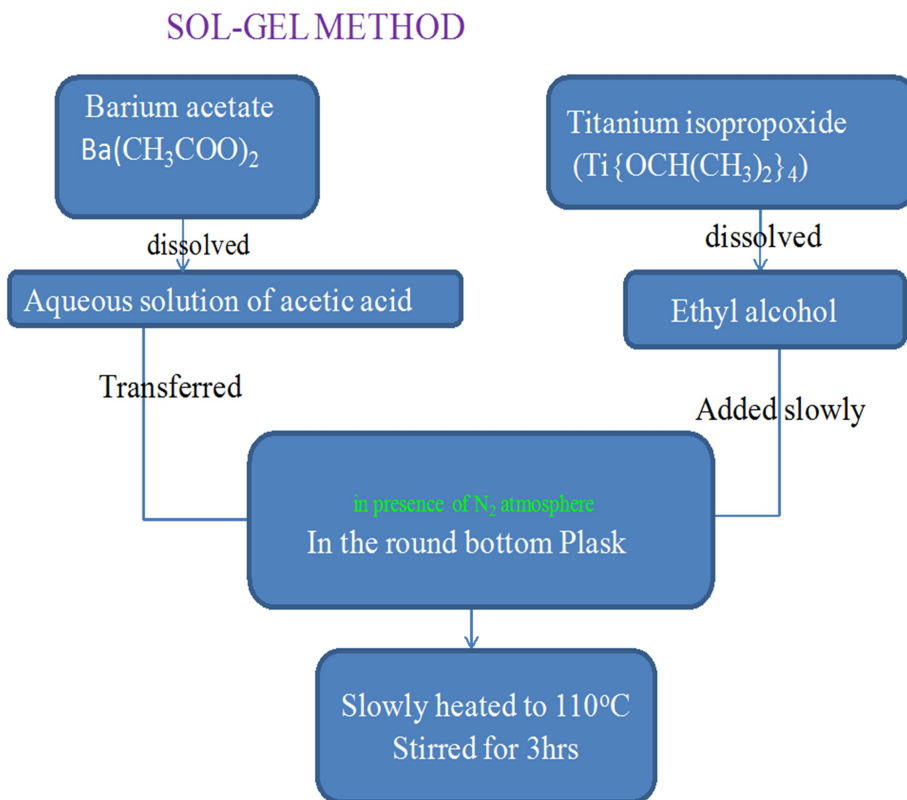


Fig.3.1 Schematic representation of sol-gel method

### 3. Synthesis and structural, microstructural characterization

#### 3.2.1.3 Drying of sol and calcinations at various temperatures

The finally achieved BaTiO<sub>3</sub> sol was dried at 200°C for overnight and calcined at different temperatures like 650°C, 700°C, 750°C and 800°C for 1hr. Calcinations is the heating process in which the stoichiometric phase formation takes place.

#### 3.2.1.4 Nano crystalline BaTiO<sub>3</sub> pellet preparation

The 650°C calcined powder is made into a pellet of 8 nm diameter pellet. This green pellet is sintered at 1000°C temperature for 1 hr. The magnetic measurements were carried out on this pellet.

### 3.2.2 Structural studies by X-ray diffraction (XRD)

#### 3.2.2.1 X-ray diffraction of four different size particles

The structural characterization is carried out by XRD, and it is given in fig.3.2. It shows clear BaTiO<sub>3</sub> phase formation with minor secondary phases of BaCO<sub>3</sub>.

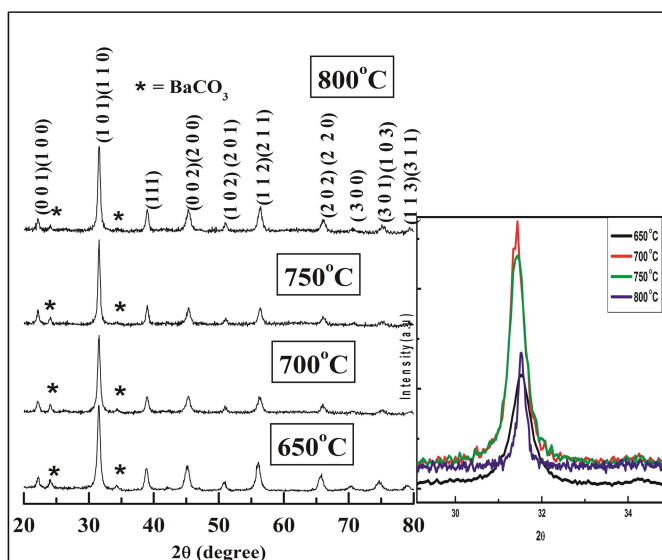


Fig.3.2. XRD pattern of nc-BTO powder obtained by calcinations dried sol at various temperatures

### 3. Synthesis and structural, microstructural characterization

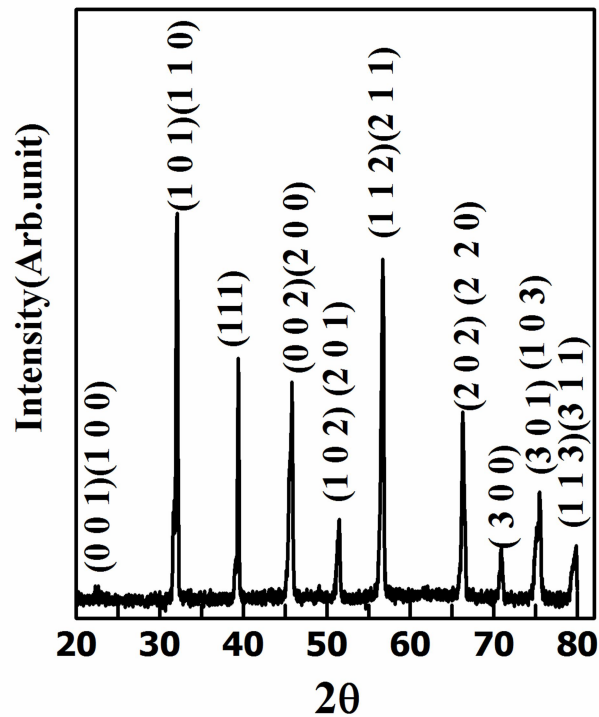
The crystallite size is calculated by Scherrer formula, and the strain is calculated by the following formula

$$\text{Strain } (\varepsilon) = \frac{d - d_0}{d_0}$$

Where  $d$ =experimentally obtained lattice spacing and  $d_0$  is the original lattice spacing taken from PCPDF file of tetragonal  $\text{BaTiO}_3$ . The average crystallite sizes of 23 nm, 31 nm, 34 nm and 54 nm is obtained from XRD patterns of Fig.3.2. It is equal to the grain or particle size obtained from distribution of particle sizes of FESEM images (Fig.3.4).

#### 3.2.2.2 X-ray diffraction nanocrystalline pellet

The below XRD pattern clearly shows the  $\text{BaTiO}_3$  phase with minimum secondary peaks. The crystallite size calculated is around 60 nm.



3.3 XRD pattern of 60 nm nc-BTO pellet

### 3. Synthesis and structural, microstructural characterization

#### 3.2.3 Microstructure studies

##### 3.2.3.1 Morphological studies by FESEM

The particle size distribution is fitted by Gaussian distribution function for the images below for different temperature calcined samples. The sizes were obtained from the fitting is  $23\pm 3$  nm,  $31\pm 3$  nm,  $34\pm 7$  nm and  $54\pm 6$  nm.

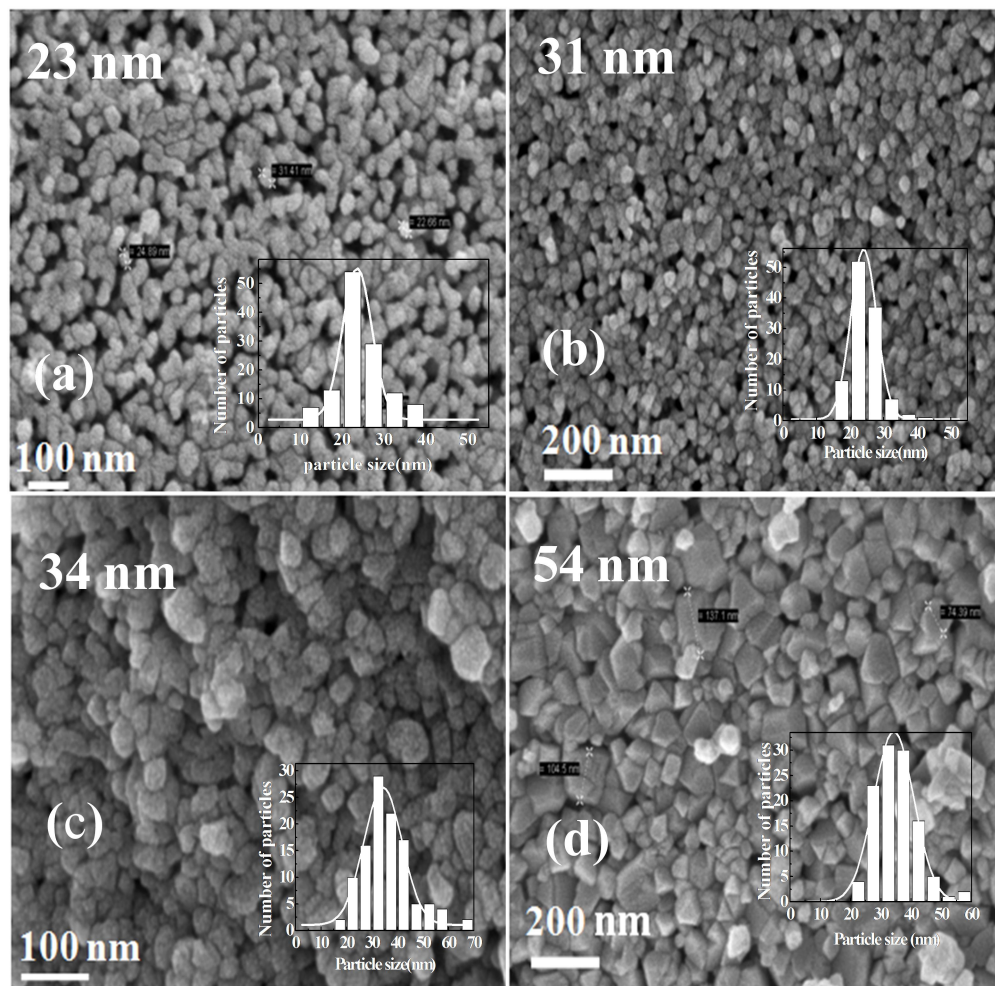


Fig.3.4. FESEM images of nc-BTO nanoparticles of average sizes 23nm, 31 nm, 34 nm and 54 nm. (Calcined at (a) 650°C, (b) 700°C, (c) 750°C and (d) 800°C).

### 3. Synthesis and structural, microstructural characterization

#### 3.2.3.2 Strain studies by TEM

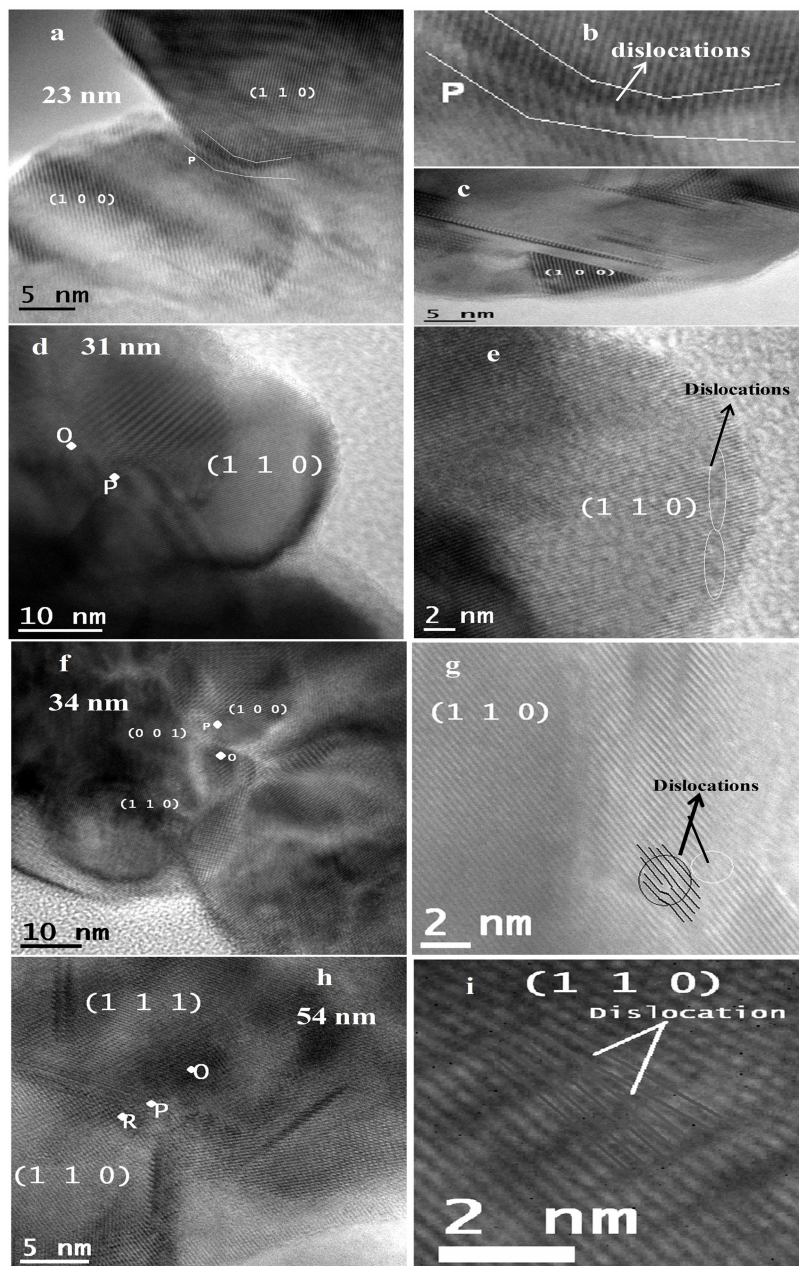


Fig.3.5. (a), (d), (f) and (h) are the HRTEM images of 23 nm-54 nm size BTO particles. (Left) The lattice distortions regions are denoted as P, O and R in respective particles. The right side HRTEM images show the presence of dislocations in them.

### 3. Synthesis and structural, microstructural characterization

Fig. 3.5(a), 3.5(d), 3.5(f) and 3.5(h) are the HRTEM image with lattice distortions of particles of avg. sizes 23 nm, 31 nm, 34 nm and 54 nm respectively. The lattice distortion regions are denoted with P, O and R. Fig. 3.5(b) clearly shows the dislocations formations at the grain boundaries to due to lattice distortions [19, 20]. When the strain induced in the material the lattice, get bending due to this. Hence, the fig.3.5(c) shows the images like amorphous and like crystalline regions. This is because some regions in the lattice get focused while other gets defocused. Hence, one can see regions of lattice planes and some regions like amorphous material. The origin in these materials observed due to the presence of dislocations in it. It is observed that the particles of avg. size 23 nm and 54 nm shows dislocations formation at the grain boundary, where as the particles of sizes 31 nm and 34 nm show the dislocation at the interior part of grains. The lattice distortions at grain boundaries are highly observed for 23 nm and 54 nm size particles. The right side images in Fig.3.5 shows the dislocations formation for corresponding particle size in the left side of image.

Table 1: The avg. particle size, strain of various temperature calcined BaTiO<sub>3</sub> (BTO) sol powder.

S.No	Calcination Temperature (°C)	Avg. particle Size (nm)	Strain
1	650	23	-10.7x10 <sup>-3</sup>
2	700	31	1.4x10 <sup>-3</sup>
3	750	34	0.6x10 <sup>-3</sup>
4	800	54	-2.1x10 <sup>-3</sup>

### 3. Synthesis and structural, microstructural characterization

#### 3.2.3.3 TEM studies of nanocrystalline pellet

The microstructural studies are carried out by TEM and are displayed in Fig. 3.6. Fig. 3.6(a) shows the HRTEM image of BTO nanoparticles, while the inset in Fig. 3.6(a) is the FFT pattern of Fig. 3.6 (a) and shows the existence of [001], [002] and [111] planes in the HRTEM image. Fig. 3.6(b) shows that the particles are 60 nm in size. The HRTEM images in Fig. 3.6(c) and (d) show that the material is poorly crystalline at the surface of a nanoparticle and the colour contrast also reflects it. Thus as the defect formation energy is low for oxygen and the surface shows a contrast in HRTEM image, we expected that the particle is surface defective or disordered. These oxygen defects will create extra electrons and can form  $Ti^{+3}$  ions at the surface. As discussed above the magnetic measurements also support the presence of localized moments (non-correlated) which are created due to the oxygen vacancies at the surface.

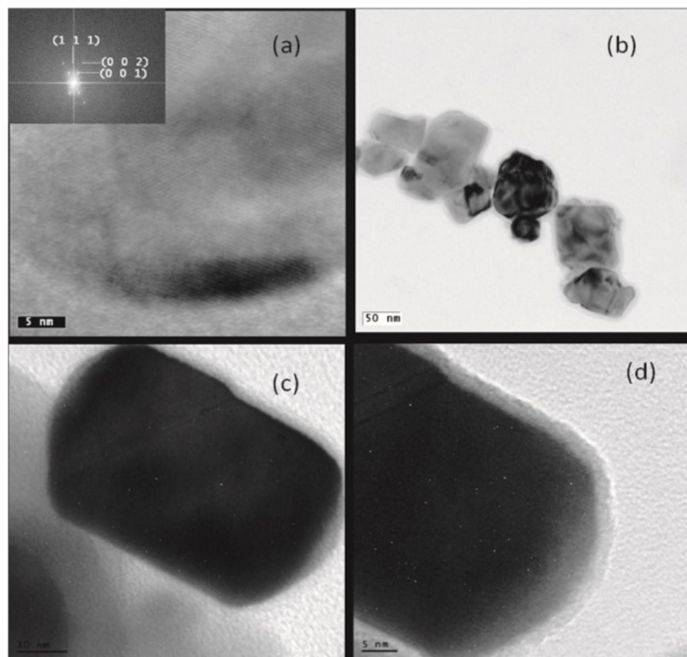


Fig.3.6. Transmission Electron Microscopy image of nc-BTO (a) HRTEM image of nc-BTO (inset FFT). (b) Image of nc-BTO nanoparticles. (c) Image of one nano-particle showing colour contrast. (d) HRTEM image of one nanoparticle.

### 3. Synthesis and structural, microstructural characterization

#### 3.3 Mesocrystals

Mesocrystals are the new class of materials in which small crystals will arrange periodically, the crystallographic axis will be same for all crystals. This way it forms superstructures in 3D or 2D or 1D. This way, it forms superstructures in 3D or 2D or 1D. Mesocrystals are the intermediate structures in the nonclassical crystallization process, and leading to single crystals by single particle fusion [21-23].

##### 3.3.1 Mesocrystal growth mechanism

###### 3.3.1.1 Classical and non-classical crystallization

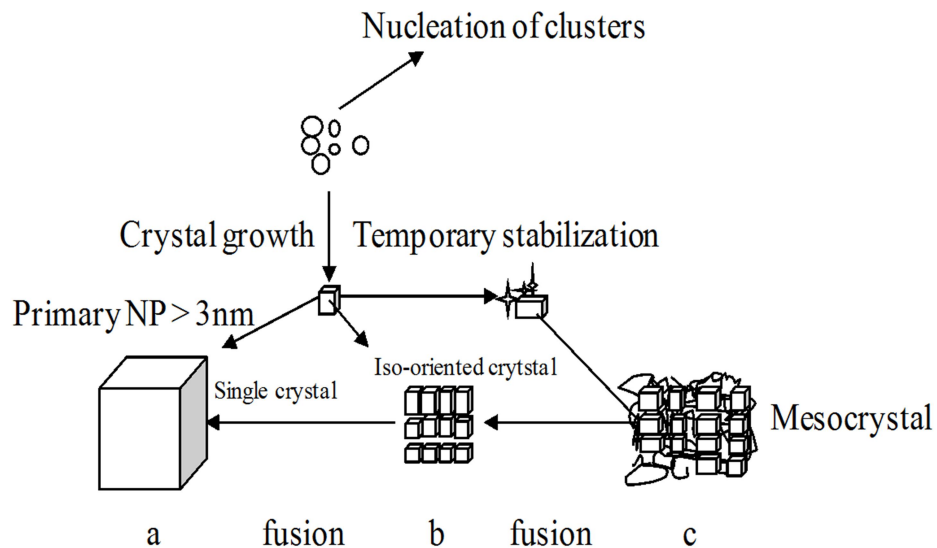


Fig.3.7. Schematic representation of classical vs non-classical crystal growth

The crystallization process of mesocrystal is different from classical crystallization. Mesocrystal formation is contrast to the atom or ion or molecule based classical crystallization process; and it is a particle based non-classical crystallization [24-27]. The schematic representation of these processes is given in fig 3.7. The primary crystallization starts from atoms or ions or molecules and forms clusters. This primary crystallization is by ion by ion attachment and unit

### ***3. Synthesis and structural, microstructural characterization***

cell replication. In the above fig 3.7(c) represents the mesoscale assembly of organic chemical capped mesocrystal. Thus, the mesocrystal formation and oriented crystal attachment are similar processes and the initial mesocrystal formation can lead to a single crystal by many single crystallites fusion as in fig.3.7. Thus, all the crystallites got their crystallographic axes oriented along the same direction [28].

This method supports the oriented mesostructure growth of directional growth. Mesocrystals shows the electron diffraction pattern similar to that of single crystals.

Mesocrystals can be formed by following methods:

- Alignment by Capillary Forces
- Alignment by Additive Coding of Nanoparticles
- Alignment by Minimization of the Interfacial Energy
- Alignment by Hydrophobic Forces and Interface Energies
- Alignment by a Mechanical Stress Field
- Dipole-dipole Interaction Model for Oriented Attachment [27]

F. Dang et.al, reported the ultrasonic assisted mesocrystal synthesis, this gave us inspiration to work towards the synthesis of mesocrystals [21].

#### **3.3.2 Sonochemical synthesis**

BaTiO<sub>3</sub> mesocrystals were synthesized by using the sol-gel method. In a typical procedure, Argon gas was bubbled through 100 ml of distilled water for 30min to remove free oxygen. To the above de-aerated water, 2.227g of BaCl<sub>2</sub>.2H<sub>2</sub>O was added and stirred for 10 min to obtain Ba<sup>2+</sup> solution. 1.0 ml of TiCl<sub>4</sub> was mixed to the above solution resulting in the formation of a suspension. The atomic ratio of Ti and Ba was maintained at 1:1. Finally, 5M of aqueous NaOH solution was added into the prepared mixed suspension at room

### ***3. Synthesis and structural, microstructural characterization***

temperature to maintain the pH at 14. This sol was stirred with a magnetic stirrer for 2h at room temperature to obtain BaTiO<sub>3</sub> gel. This suspension was treated with ultrasonic horn at 60°C and 80°C with varied amplitude and sonication time. The frequency and power were set to 20 kHz and 750 W respectively. This sonicated BaTiO<sub>3</sub> gel was centrifuged to settle down the formed BTO mesocrystal particles at the bottom. This suspended powder dried at 60°C for 48h in a precision hot air oven and washed with water to get the final powder. The synthesis procedure is summarized in Fig.3.8

#### **3.3.2.1 Irradiation with ultrasonic horn**

The above prepared BTO sol is treated for different amplitude and time using 750W ultrasonic processor (VCX 750) operated at 20 kHz. The sol was sonicated for 10, 20, 30 and 40 min. at 40% and 50% amplitude of probe. This process is carried out at two external temperatures 60°C and 80°C. The structural and morphological studies were carried out for these two set of samples. Thus, the structural and morphological studies by XRD and FESEM conclude the optimized conditions for mesocrystal synthesis by the use of 750 W VCX ultrasonic horn.

#### **3.3.2.2 Schematic diagram of sonochemical method**

The above prepared BTO gel was sonicated at 60°C external temperature for different time two amplitudes of VCX 750W ultrasonic processor. The amplitude of VCX 750W processor was fixed at 40% and 50%. The sample which is irradiated at 40% amplitude for 10 min. is denoted as T10A40. Similarly, T20A40, T30A40 and T40A40 represents that the samples were irradiated for 20, 30, 40 min. at same amplitude.

### 3. Synthesis and structural, microstructural characterization

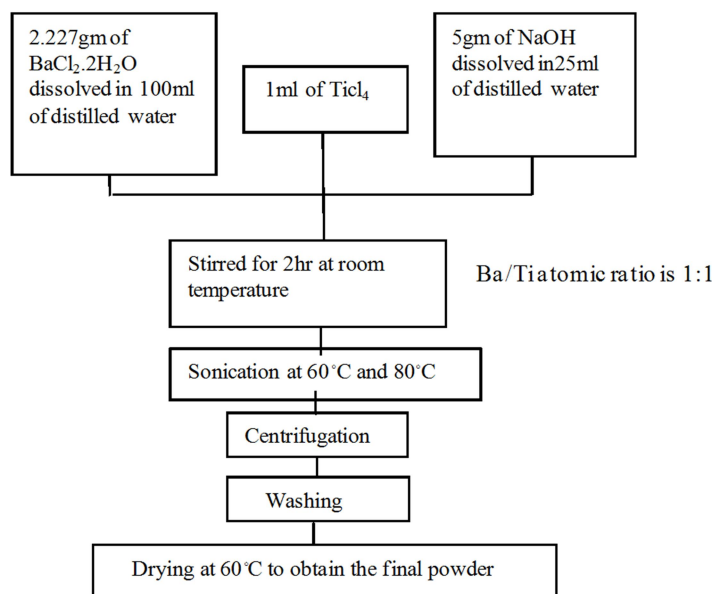


Fig.3.8. Schematic of synthesis procedure for preparation of BaTiO<sub>3</sub> mesocrystal

#### 3.3.3 Structural studies by X-ray diffraction (XRD)

Fig.3.9 shows the XRD pattern of (by INEL Model CPS120) sol-gel derived powders processed at different conditions. Table 2 summarizes the naming of two set of samples irradiated 40% and 50% of the processor.

Table 2: Naming of different time processed samples for two different amplitudes of 40% and 50% of VCX 750 W processor.

Irradiation Time min.	Amplitude		Processing Temperature (°C)
	40%	50%	
	Sample name	Sample name	
10	T10A40	T10A50	60
20	T20A40	T20A50	60
30	T30A40	T30A50	60
40	T40A40	T40A50	60

### 3. Synthesis and structural, microstructural characterization

As shown in fig.3.9 the XRD pattern indicates the formation of two phases  $Ba_4Ti_{12}O_{27}$  and  $Ba_4Ti_{13}O_{30}$  for all different time processed T10A40, T20A40, T30A40 and T40A40 samples.

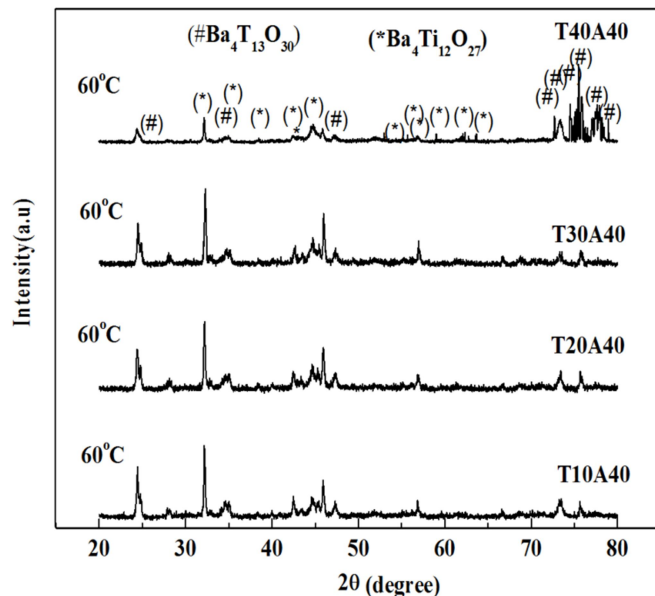


Fig.3.9. X-ray diffraction pattern of BTO powder irradiated at 40% amplitude of VCX 750 W ultrasonic processor for 10, 20, 30 and 40 min. (XRD of T10A40, T20A40, T30A40 and T40A40 samples)

As discussed above the 40% amplitude processed samples don't lead to the formation of  $BaTiO_3$  mesocrystal. Hence, we have increased the processor amplitude to 50% and irradiated for different time duration. Similar to the previous notations these are also named as T10A50, T20A50, T30A50 and T40A50 (see Table 2). The XRD pattern in fig.3.10 shows that as the processing time increased from 10 min.–40 min. The formation of  $Ba_4Ti_{13}O_{30}$  phase is efficient with  $Ba_4Ti_{12}O_{27}$  impurity phase. The increment of amplitude from 40% to 50% also leads to the dominated growth of  $Ba_4Ti_{13}O_{30}$  phase.

### 3. Synthesis and structural, microstructural characterization

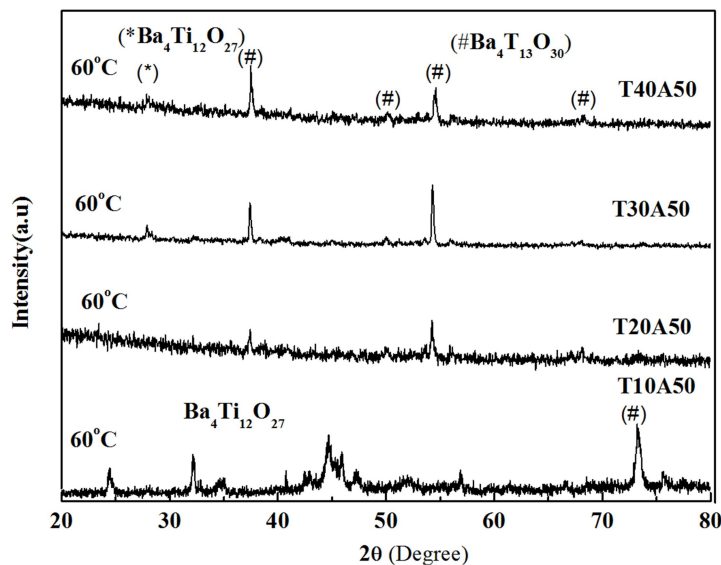


Fig.3.10. X-ray diffraction pattern of BTO powder irradiated at 50% amplitude of VCX 750W ultrasonic processor for 10, 20, 30 and 40 min (XRD of T10A50, T20A50, T30A50 and T40A50 samples)

The formation of  $\text{BaTiO}_3$  mesocrystal generally depends on the irradiation power and processing temperature. As discussed above, the increasing of processor amplitude is not much effective without increasing the temperature beyond  $60^\circ\text{C}$ . Thus, the following two sets summarize the naming samples irradiated for 10, 20, 30 and 40 min. at 40% and 50% amplitude.

Table 3: Naming of different time processed samples for two different (40% and 50%) amplitude at the  $80^\circ\text{C}$  processing temperature.

Irradiation Time	Min.	Amplitude	Processing Temperature ( $^\circ\text{C}$ )	Sample name
10			80	T10A40
20			80	T20A40
30			80	T30A40
40			80	T30A40

### 3. Synthesis and structural, microstructural characterization

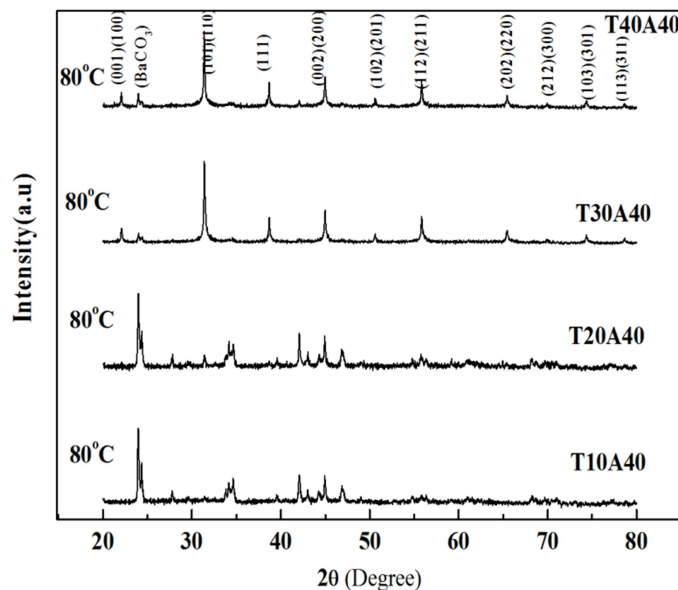


Fig.3.11. XRD patterns of BTO powder processed for 10, 20, 30 and 40 min. at 40% amplitude by VCX 750W processor. (XRD patterns of T10A40, T20A40, T30A40, and T40A40 samples)

Above (Fig.3.11) shows the  $\text{BaTiO}_3$  mesocrystal formation is initiated at 20min. irradiation time of ultrasonic power of 40% VCX 750W processor amplitude. The XRD pattern of T30A40 shows the tetragonal  $\text{BaTiO}_3$  crystal structure.

#### 3.3.4 Morphological studies by FESEM

Thus, the 30min. irradiated sample leads to complete  $\text{BaTiO}_3$  phase formation with 126nm crystallite size. Further increase in irradiation time to 40min. forms the larger crystallite size of 137 nm. The FESEM results in fig.3.12 also support the formation of BTO mesocrystals. The T30A40 and T40A40 images in fig.3.12 clearly show the BTO mesocrystal particles formation of avg. size 126 nm. The high resolution FESEM images of T30A40 sample (in fig.3.13) shows that the 126 nm particles are composed of very small particles of size 8-10nm in size. These very small particles of unidirectional orientation fused to

### 3. Synthesis and structural, microstructural characterization

form mesocrystals of 126 nm (fig.3.13 (A) and 3.13 (B)), which can be clearly seen in fig.3.13 (C). As the time of irradiation increases at 40% amplitude, it leads to the increase in particle size to 137 nm. Here, FESEM images show that the bigger particles composed of very small particles. Hence, we can say that the small size particles of same orientation fused to form bigger particles of avg. size 126 nm in case of T30A40 sample.

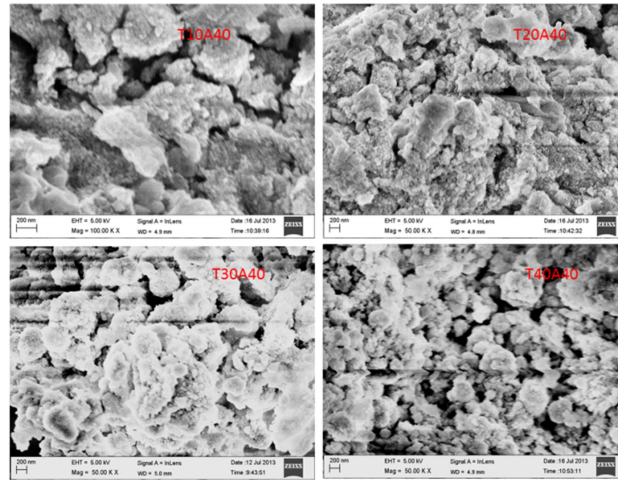


Fig. 3.12 FESEM images of T10A40, T20A40, T30A40 and T40A40 samples.

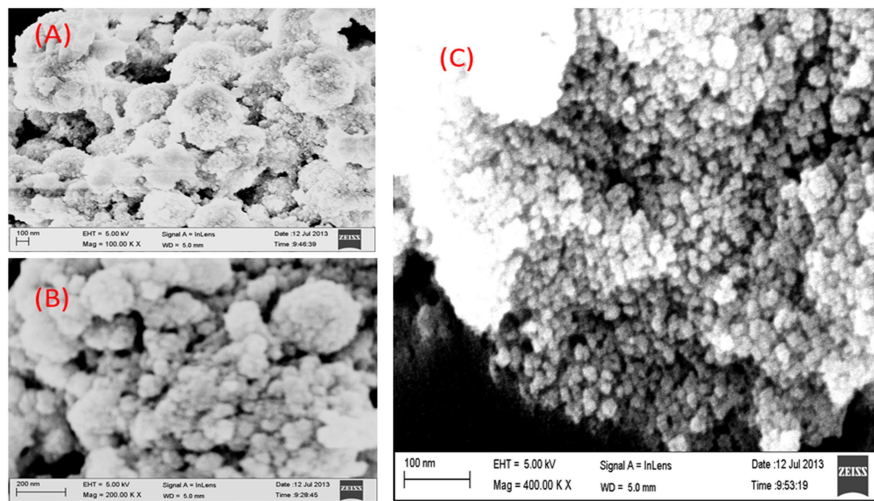


Fig. 3.13 FESEM images of T30A40 sample at higher magnification.

### 3. Synthesis and structural, microstructural characterization

#### 3.3.5 Structural studies by Transmission Electron Microscope

TEM is one of the most widely or needed technique to unfold the mesocrystal nature of material. As discussed above we have selected the T30A40 mesocrystal to carry out the various measurements to study the mesocrystal nature of it.

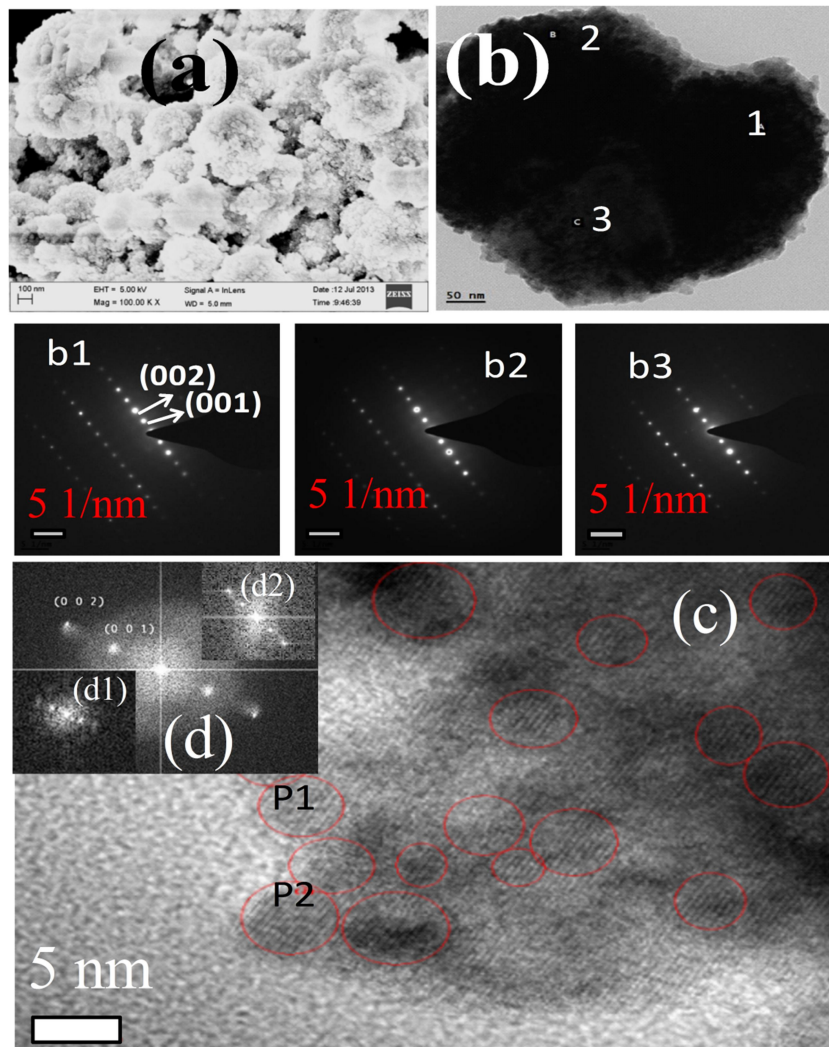


Fig.3.14. (a) FESEM and (b) TEM image of T30A40, b1, b2 and b3 show the selected area diffraction patterns (at 1, 2 and 3) as shown in (b), (c) is the HRTEM image of T30A40 and d is the FFT of image (a), inset d1 and d2 are the FFT's of particles P1 and P2 of mage (c).

### ***3. Synthesis and structural, microstructural characterization***

The Fig.3.14 (a) shows the FESEM image of T30A40 material. Fig. 3.14(b) shows the TEM image of T30A40. The selected area diffraction at different positions on the particle (in Fig.3.14 (b1), b2 and b3) is denoted as 1, 2 and 3. It shows (001) directional growth at all three positions on the particle. The HRTEM image also (fig.3.14(c)) shows the 5nm size particles attached with (001) directional growth. Fig. 3.14(d) shows the FFT image Fig. 3.14 (c). The D1, D2 (inset in fig. 3.14(d)) are the FFTs for particle P1 and P2 of fig.3.14(c) respectively. It is noted that the FFT of one particle is identical to that of the FFT of all particles. Hence, it can be concluded that the 5-8nm size crystallites of the same crystal orientation fused to form larger size particles, establishing that the particle under investigation is indeed a mesocrystal of BTO

### **3.4 RF magnetron sputtering**

In the physical vapor deposition family of thin film fabrication techniques, RF Magnetron sputtering is one of the widely accepted in the research as well as in the industrial level [29-32]. As the AC voltage is applied to the source, it has edge over the DC sputtering technique. Hence, wide range of materials like metals, semiconductors, insulators and superconductors can be deposited by this technique. High rate of deposition, large area deposition, large deposition temperatures, uniformity and reactive sputtering makes it a robust and highly employed technique in the thin film processing.

The RF sputtering which is shown in fig.3.15 consists of 30 liter stainless steel vacuum chamber and three cathodes and target holders. The chamber is maintained at room temperature by circulation chilled water of 15 °C.

### *3. Synthesis and structural, microstructural characterization*



Fig.3.15. Sputtering system used in the present study to deposit Nickel films

The major components of the sputtering are: 1. Stainless steel chamber. 2. Rotary pump. 3. Turbo pump. 4. Gas valves. 5. Gauges (Pirani & Penning). 6. Cathode with sputtering target holder. 7. RF power supply with tuning network. 8. Cold water circulation. 9. Mass flow controller. 10. Processing gas. 11. Substrate heater. 12. Sputtering target. 13. Substrates and magnetron, with substrate rotation provided magnetron sputtering to achieve uniform thickness films.

#### **3.4.1 Working principle**

After creation of high vacuum the processing inert gas is inserted into the chamber to fem mbar and the RF voltage is applied to the inert gas. As the applied voltage is oscillating of RF frequency in the negative half cycle the electron will collide with the inert gas Argon atoms ionizes the gas. In this process the electron will travel in the helical path if the magnetron is provided at the cathode and ionizes more gas. Thus plasma formation will take place now the positive inert gas ions will get attracted by the cathode and collide with the target material and

### ***3. Synthesis and structural, microstructural characterization***

ejects the target atoms from the target. In this process the momentum of Ar ions is transferred to the target atoms and the ejected atoms will travel towards the substrate and the thin film formation will takes place. The main aim of using RF voltage is to avoid the bound charge formation in the deposition of insulating materials.

## **3.5 Deposition of Ni films on Si substrates by RF magnetron sputtering**

### **3.5.1 Deposition conditions**

The ferromagnetic Nickel (Ni) films were deposited by RF magnetron sputtering [33-36] at room temperature (RT). The base pressure of  $3 \times 10^{-6}$  mbar is obtained by turbo pump. The RF power density of  $3 \text{ W/cm}^2$  is constant for all films. The substrate to film distance is 5 cm. The various deposition conditions are summarized in Table 4. The films were deposited at various working pressures of Ar ranging from 10 mtorr to 20 mtorr. Fig.3.16 clearly shows the growth of (200) oriented Ni films at all working pressures (10 mtorr to 20 mtorr). The deposition was carried out for three different time duration namely 15min, 30 min and 2 hr.

Table 4: This table summarizes the deposition conditions and naming of Ni Films deposited at various working pressures of Ar.

S. No	Sample code	Working pressure (mtorr)	Deposition duration (min.)	Thickness (nm)
1	RKNI-05	15	120	1018
2	RKNI-09	20	15	135
3	RKNI-12	10	15	65

### 3. Synthesis and structural, microstructural characterization

#### 3.5.2 Structural studies

The films show the formation of FCC crystal structure in all deposition cases (10 mtorr, 15 mtorr, and 20 mtorr). It is observed from the XRD patterns (Fig.3.16) of these films that the film (RKNI-09) shows the compressive strain presence in the film. Whereas the other two films shows the relaxation of compressive strain in it. Since the films are grown in (100) direction, the anisotropy of the system is depends on the direction field applied. As the deposition duration increased for the films at 10mtorr working pressure, the XRD shows the right shift of (200) peak which clearly supports the relaxation of strain with the increase in thickness of the film. As in the case of bulk Ni, the order of easy direction of magnetization varies as (111), (110) and then (100). As the films are two dimensional, we rule out the (111) stacking direction as the lowest energy direction. Thus, we left with an (110) easy direction of magnetization. As the laser excites the electrons due to spin-orbit coupling, the spin excitation is also inherent process in these kinds of materials. The strain which clearly evident from XRD peak shift will show the high effect on magneto crystalline anisotropy energy (MAE). The calculation of anisotropy and relation between MAE and strain is in progress.

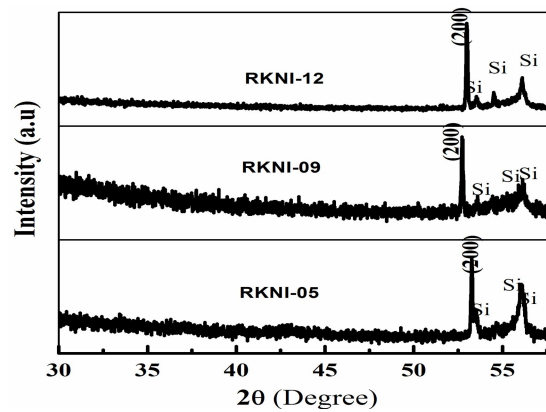


Fig.3.16 (Left) XRD patterns of above deposited nickel films (RKNI-05, RKNI-09 and RKNI-12).

### 3. Synthesis and structural, microstructural characterization

#### 3.5.3 Micro structural studies by Atomic Force Microscope (AFM)

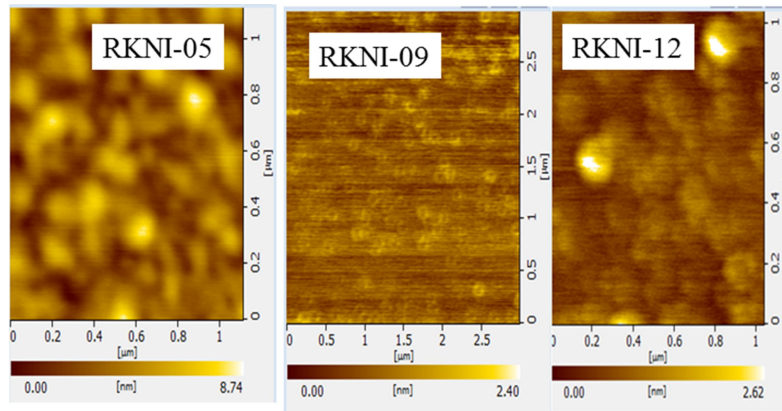


Fig.3.17. AFM images of Nickel films (RKNi-05, RKNi-09 and RKNi-12).

Fig.3.17 shows the AFM images of RKNi-05, RKNi-09 and RKNi-12 films. The images show clear grain growth in the films.

#### 3.6 Pulsed laser deposition

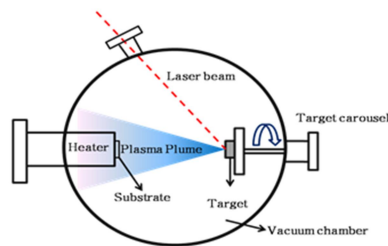


Fig.3.18. Experimental and Schematic diagram of Pulsed laser deposition (PLD) setup.

The PLD experimental setup will have three important sections (Fig.3.18)

1. Laser source
2. Vacuum creation
3. Spherical vacuum chamber with its components

##### Laser source

The laser source can be any wavelength 248 nm, or 193 nm or 266 nm. In the present case we have used excimer laser of 248 nm wavelength beam.

### ***3. Synthesis and structural, microstructural characterization***

#### **Vacuum creation**

This is the most crucial part and one can find common for most of the thin film deposition techniques. In this the rough vacuum is created by rotary pump and then the turbo molecular pump is used to create lower vacuum to develop the high quality films without any contamination.

#### **Spherical vacuum chamber with its components**

The deposition of film will take place in this high vacuum chamber. It contains the carousel target rotating setup, substrate heater setup and attachment of gauges to measure the vacuum.

#### ***Deposition procedure***

The laser beam is directed to target at angle of  $45^\circ$  with the target surface. This interaction of nanosecond laser with target produces the plume of the target material. The plume will get deposited on the substrate kept opposite to the target. The substrate can be kept at various temperatures depending on the requirement. The target carousel arrangement useful in uniform ablation target material and hence plume transport to the substrate will be constant throughout the process.

#### **3.6.1 Deposition of BaTiO<sub>3</sub> films**

The BaTiO<sub>3</sub> thin films are deposited by PLD at various conditions. Since the deposition conditions are very crucial in the laser annealing process. The details of the deposition conditions will be given in chapter 6.

#### **3.7 Summary**

Four different sizes (23-54 nm) particles of BTO were prepared by sol-gel method. The compressive strain is observed in 23nm and 54 nm particles, whereas tensile strain observed in 31nm and 34 nm size particles. Mesocrystals of 200 nm size were prepared by sonochemical synthesis and their agglomeration nature is studied by FESEM and TEM. The Ni film of three different thickness namely 65nm, 135nm and 1018nm is by RF-magnetron sputtering.

### *3. Synthesis and structural, microstructural characterization*

#### **References**

1. K.-I Mimura, K. Hiramatsu, M. Moriya, W. Sakamoto, S. Kawado, Y. Uesu and T. Yogo, *J Nanopart Res.* 12, 1933 (2010).
2. K. W. Kirby, *Mater. Res. Bulletin*, 23, 881 (1988).
3. Sumio Sakka, “Handbook of sol-gel science and technology. 2. Characterization and properties of sol-gel materials and products” (Springer Science & Business Media, 2005).
4. P.P. Phule, S.H. Risbud, *Mater. Sci. Eng. B*, 3, 241 (1989).
5. W. Wang, L. Cao, W. Liu, G. Su, and W. Zhang, *Ceramic Inter.* 39, 7127 (2013).
6. X. Zhang, X. Wang, Z. Tian, T. Sun, and L. Li, *J. Am. Ceram. Soc.*, 93, 3591 (2010).
7. J. Yuk, T. Troczynski, *Sensors and Actuators B* 94, 290 (2003).
8. S. Otsuki, K. Nishio, T. Kineri, Y. Watanabe, and T. Tsuchiya, *J. Am. Ceram. Soc.*, 82, 1676 (1999).
9. E. J. H. Lee, F. M. Pontes, E. R. Leitte, E. Longo, J. A. Varela, E. B. Araujo, J. A. Eiras, *J. Mater. Sci. Lett.* 19, 1457 (2000).
10. X. Yao, X. Liu, T. Liu, K. Wang, L. Lu, *Cryst. Eng. Comm.* 15, 10246 (2013).
11. Z. Liu, X. D. Wen, X. L. Wu, Y. J. Gao, H. T. Chen, J. Zhu, et.al, *J. Am. Chem. Soc.* 131, 9405 (2009).
12. X. L. Wu, S. J. Xiong, Z. Liu, J. Chen, J. C. Shen, T. H. Li, et.al, *Nature Nano tech.* 16, 103 (2011).
13. X. G. Kong, Y. Ishikawa, K. Shinagawa, Q. Feng, *J. Am. Ceram. Soc.* 94, 3716 (2011).
14. S. Wada, K. Takeda, T. Muraishi, H. Kakemoto, T. Tsurumi, T. Kimura, *Jpn. J. Appl. Phys.* 46, 7039 (2007).

### ***3. Synthesis and structural, microstructural characterization***

15. H. Takahashi, Y. Numamoto, J. Tani, S. Tsurekawa, *Jpn. J. Appl. Phys.* **45**, 7405 (2006).
16. E. Orhan, J. A. Varela, A. Zenatti, M. F. C. Gurgel, F. M. Pontes, E. R. Leite, E. Longo, P. S. Pizani, A. Beltran, and J. Andres, *Phy. Rev. B* **71**, 085113 (2005).
17. X. Zhang, X. Wang, W. Z. Tian, T. Sun, and L. Li, *J. Am. Ceram. Soc.* **93**, 3591 (2010).
18. S. Otsuki, K. Nishi, T. Kineri, Y. Watanabe, and T. Tsuchiya, *J. Am. Ceram. Soc.* **82**, 1676 (1999).
19. W Wunderlich, Y Ishida and R Maurer *Script Metallurgica*, **24**, 403 (1990).
20. D H Ping, D X Li and H Q Ye, *J. Mater. Sci. Lett.* **14**, 1536 (1995).
21. F. Dang, K. Kato, H. Imai, S. Wad, H. Hanedad, M. Kuwabara, *Cryst. Eng. Comm.* **12**, 3441 (2010).
22. N. Park, Y. Wang, W. Seo, F. Dang, C. Wan, K. Koumoto, *Cryst. Eng. Comm.* **15**, 679 (2013).
23. J. Fang, B. Ding, X. Song, *Appl. Phys. Lett.* **91**, 083108 (2007).
24. M. Niederberger, H. Colfen, *Phys. Chem. Chem. Phys.* **8**, 3271 (2006).
25. Zhou L, Brien PO, *J Phys Chem Lett.* **3**, 620 (2012).
26. K. Yasui, K. Kato, *J. Phys. Chem. C.* **116**, 319 (2012).
27. D. Hu, X. Kong, K. Mori, Y. Tanaka, K. Shinagawa, Q. Feng, *Inorg. Chem.* **52**, 10542 (2013).
28. R. Song, H. Colfen, *Adv Mater.* **22**, 1301 (2010).
29. K. Sugibuchi, Y. Kurogi, and N. Endo, *J. Appl. Phys.*, **46**, 2877 (1975).
30. J. Im, O. Auciello and S. K. Streiffer, *J. Thin Solid films*, **413**, 243 (2002).
31. A. Roy, A. Dhar, and S. K. Ray, *J. Appl. Phys.*, **104**, 064103 (2008).

### ***3. Synthesis and structural, microstructural characterization***

32. P.Padmini, T.R.Taylor, M.J Leferve, A.S.Nagra, J.Appl.Phy.Lett., **75**, 3186 (1999)
33. M. S. Miller, F. E. Stageberg, Y. M. Chow, K. Rook, and L. A. Heuer, J. Appl. Phys. **75**, 5779 (1994).
34. B. G. Priyadarshini, S. Aich , M. Chakraborty, J Mater Sci. **46**, 2860 (2011).
35. S.K. Wu, S.C. Yen and T.S. Chou, Surface and Coatings Tech. **200**, 2769 (2006).
36. M. Leoni, C. Tosi, P. Scardi, J. Mater. Sci. **40**, 1685 (2005).

## Chapter 4

# Optical studies on BaTiO<sub>3</sub> Nanoparticles and Mesocrystals

---

### Abstract

In the previous chapter, the details of synthesis, structural and microstructural characterizations that were carried out are discussed. In the present chapter, we discuss the linear and nonlinear optical properties of BaTiO<sub>3</sub> (BTO) nanoparticles, and BTO mesocrystals. It is found that the band gap varied between 2.00 eV to 3.2 eV depending upon the size of the particles and preparation method. The sol-gel prepared nanoparticles show band gap variations between 2.53-3.20 eV. This high band gap narrowing is explained by considering the strain, electron-phonon interactions and exchange - correlation interactions in the material. The giant band gap narrowing of 2.00 eV is observed for BTO mesocrystals. It is found that the dielectric confinement effect plays an important role in reducing the band gap to such a low value of 2.00 eV. It is also discussed in this chapter how the band gap narrowing is very important for efficient solar cell development.



## **4. Optical Studies on BaTiO<sub>3</sub> Nanoparticles and Mesocrystals**

### **4.1 Introduction**

When the particle size of a solid is below 100 nm, the translational invariance is significantly broken. Therefore, the plane-wave phonon wave function cannot be used in explaining the lattice dynamics of these Nano particles (NPs). This broken translational symmetry relaxes the phonon wave function selection rules. The quantum confinement effect plays a dominant role in deciding the physical and chemical properties of quantum dots. In semiconductor physics, a significant effort has been made to understand the quantum-confinement effects in such low dimensional systems. This quantum mechanical phenomenon associated with quantum dots made such semiconductors suitable for many electronic and optoelectronic devices. The miniaturization requirement of microelectronic industry demands novel understanding of grain size and free carrier dependent electronic structure of them. The electron-phonon interactions in nanostructures play an important role in the emergence of new properties in it. The interaction of electrons with phonons in the form of polaron plays an important role in explaining many properties like high  $T_c$  superconductivity. It is interesting to note here that the pressure effects on oxygen deficient BaTiO<sub>3</sub> can lead to an insulator to metal transition [1]. It shows that the strain effects in this material play an important role in changing its band structure. Another interesting feature observed in defect originated free carrier containing BaTiO<sub>3</sub>, which is not under strain, is that they too exhibit insulator to metal transition at certain carrier concentrations [2, 3]. Still another feature exhibited by nanocrystalline BaTiO<sub>3</sub> (nc-BTO) nanoparticles (NP) is the existence of magnetism in them that makes it an important system to study. Hence, it is essential to understand the effects of various factors like strain, defect generated charge carrier concentration and grain size on the band structure of nc-BTO.

#### ***4. Optical Studies on BaTiO<sub>3</sub> Nanoparticles and Mesocrystals***

Here we have accounted for a few effects such as strain influence, phonon confinement and phase-space filling of a conduction band in explaining the band gap narrowing in nc-BTO NPs. The concept of band gap narrowing is evolved to understand the filling up of conduction band and valence band [4] in insulators and semiconductors. When a material is doped with n-type carriers, then theoretical models consider it as electron gas in the conduction band. This is agreed as the situation when doping increases charge carrier concentration beyond the Mott critical density.

Recently, the phonon confinement and fast grain growth effects of nanoparticles were found to be useful in thermo sensor based applications. TiO<sub>2</sub> nanoparticles work as thermo sensors using these two effects [5]. These NPs based thermo sensors measures the environment temperature and records the period of all thermal accidents as compared to other thermisters [6-9]. In spite of disappearance of ferroelectric order at nanoscale, the recent claims on the existence of toroidal dipole moment [10, 11] in nano scale has made researchers to focus on these nanomaterials for its potential applications in data storage devices.

##### **4.1.1 Significance of band gap narrowing in photovoltaic's**

Ferroelectrics are recently found interesting for their new kind of photovoltaic effect in them. The photo voltaic effect in ferroelectrics is different from that of p-n junction photo voltaics [12]. The photogenerated carrier current and voltage will have the spontaneous polarization vector. The photo voltaic effect mainly depends on the band gap and current densities. The solar spectrum is identical to the spectrum of Black body radiation at 5900K, which results in the ultraviolet to infrared range wavelength emissions. The open circuit voltage ( $V_{oc}$ ) and short circuit current ( $I_{sc}$ ) in ferroelectrics are strongly dependent on light absorption ability and strength of built in electric field [13]. These two

#### *4. Optical Studies on BaTiO<sub>3</sub> Nanoparticles and Mesocrystals*

parameters, decide the efficiency of photovoltaic devices. But semiconductors show smaller values for these two parameters compared to ferroelectrics. Thus, the band gap versus efficiency curve goes through a maximum in semiconductors [14], and the  $V_{oc}$  is limited by band gap in semiconductors. The existence of remnant polarization in ferroelectrics leads to a high internal electric field in them. Thus, the photo-induced voltage is independent of band gap [12, 15-17], but depends on the inter-electrode distance in the cell. However, the photo absorption requires the band gap to exist in the visible range of the spectrum, which is not the case with ferroelectrics, making them poor light absorbers. Hence, there is a serious need to look for ferroelectrics with band gap coinciding with the visible photon energy range. Another problem associated with using ferroelectrics in light energy harvesting is their high resistivity values. Recently very high photo induced voltages of up to 15V generated in BiFeO<sub>3</sub> films has attracted enormous interest in the study of ferroelectric based photo voltaic effect.

Hence, understanding the band gap reduction in ferroelectric based materials [18] and development of new ferroelectric materials [13] with low band gap are recently much evolved concept in research. Here, we report the reduction in the band gap of NPs of BaTiO<sub>3</sub> to 2.00 eV from the usual value of 3.2 eV by tuning particle size dependent residual stress and electron – phonon interactions in them. This has resulted in these NPs exhibiting a band gap narrowed high optical absorption.

Here we have accounted for a few effects such as strain influence, phonon confinement and phase-space filling of a conduction band and dielectric confinement effects in explaining the band gap narrowing in nc-BTO NPs. The concept of band gap narrowing is evolved to understand the filling up of the conduction band and valence band [3] in insulators and semiconductors.

#### 4. Optical Studies on BaTiO<sub>3</sub> Nanoparticles and Mesocrystals

When a material is doped with n-type carriers, then theoretical models consider it as electron gas in the conduction band. This is agreed as the situation when doping increases charge carrier concentration beyond the Mott critical density.

### 4.2 Theoretical approach to the observed band gap narrowing

#### 4.2.1 When the carrier density is nearer to Mott critical density

In an electron sea, the carrier-carrier Coulomb interaction is screened by the rest of the carriers. Thus, the single-particle properties renormalizes and the many-body interactions leads to an interesting phenomenon called the Band Gap Renormalization (BGR).

When the material is heavily doped (n-type carriers) the carriers form a degenerate electron gas in the conduction band. The band gap shrinkage is considered as an effect of free carriers as well as impurity ions. The edge state energies which define the band gap are calculated by self-energy technique, which involves the exchange and correlation energies of free carriers [19-21].

The band gap shrinkage is given by

$$\Delta E_g = E_g^0 - E_g = (\Delta E_g)_1 + (\Delta E_g)_2 \quad 1$$

In the above expression the  $(\Delta E_g)_1$  shows the band gap shift (shrinkage) due to the local strain present in the material. Whereas the second term  $((\Delta E_g)_2)$  includes the band gap shrinkage due to exchange-correlation, and electron-ionized impurity interactions. The electron density for these samples is of the order of  $10^{19}$ - $10^{20}$  /cm<sup>3</sup>.

The carriers can be considered as non-interacting quasi particles. Hence, quasi particle dispersion for conduction band is given by

#### 4. Optical Studies on BaTiO<sub>3</sub> Nanoparticles and Mesocrystals

$$E_c(\vec{k}, \omega) = E_c^{(0)}(\vec{k}) + \hbar \sum_c(\vec{k}, \omega) \quad 2$$

Where  $E_c^{(0)}(\vec{k})$ , is the unperturbed band energy, and  $\hbar \sum_c(\vec{k}, \omega)$  is the self-energy of electron-electron and electron-impurity scattering.

As discussed above, the nc-BTO behaves as an electron doped system due to an oxygen vacancy. Hence, the electron system exchange and correlation energy can be written as

$$\hbar \sum_c^{ee}(0,0) = -\frac{2e^2 k_F}{\varepsilon \pi} - \frac{e^2 \Lambda}{2\varepsilon} \left[ 1 - \frac{4}{\pi} \tan^{-1} \left[ \frac{k_F}{\Lambda} \right] \right] \quad 3$$

Where  $\Lambda$  is the inverse Thomas - Fermi screening length,  $\varepsilon$  is the static dielectric constant of nc-BTO.

Since the system contains only a few p-type carriers, we can neglect the exchange energy due to holes. The correlation energy for the valence band holes is given by

$$\hbar \sum_V(0,0) = \frac{2e^2 k_F}{\varepsilon \pi} \quad 4$$

The contribution due to the electron-ion interaction is given by

$$\hbar \sum_c^{e-i}(0) = -\frac{4\pi n e^2}{a_H \varepsilon \Lambda^3} \quad 5$$

Therefore,  $(\Delta E_g)_2 = \hbar \sum_c^{ee}(0,0) + \hbar \sum_c^{e-i}(0) \quad 6$

#### 4.2.2 Low carrier density with electron-phonon interactions

When the electron density is lowered, and electron-LO phonon interactions are included in the system, the band gap variation is discussed as follows.

#### 4. Optical Studies on BaTiO<sub>3</sub> Nanoparticles and Mesocrystals

$E_{ex}^0$ ,  $E_c$  are the exchange and correlation energies when the phonon interactions are included.  $E_{e-ph}$  is the electron-phonon interaction self-energy.

Thus, the change of band gap here is given by

$$\Delta E_g = E_{ex}^0 + E_c + E_{e-ph} \quad 7$$

The electron-LO phonon coupling depends on the particle size, free carrier density (n) and on temperature. The polaronic self-energy reduces the band gap. The free carrier concentration (i.e. Electrons in the conduction band and holes in the valence band) reduces the electron-LO phonon coupling. Thus, this screening by free carriers counter renormalizes the band gap. Hence, the gradual weakening of electron-phonon coupling occurs, and the band gap value tends to approach the bulk value [22-24].

The induced strain (it can be compressive or tensile strain) in the system, reduces the symmetry of the system and the degeneracy of the energy bands will be removed. In BaTiO<sub>3</sub> the hybridization of O 2P, and Ti 3d, orbital varies with presence of strain in the material. Materials with tensile strain show higher hybridization of O 2P, and Ti 3d, orbitals whereas compressive strain lowers this hybridization. These p-d hybridization increases the effective mass of electrons in the conduction band and hence, the band gap widens [25, 26].

##### 4.2.3 The dielectric confinement effects

This was mostly considered when the quantum dots or quantum wells or nano wires are being embedded in other material matrix with a different dielectric constant, where the dielectric constant of the matrix is lower than that of quantum dot material. It is also considered for the capping or surface modified cases of the nano materials.

#### ***4. Optical Studies on BaTiO<sub>3</sub> Nanoparticles and Mesocrystals***

This dielectric constant of the matrix with lower value reduces the screening effects and thus, the electron-electron interactions are increased which forms states below the conduction band, or it also forms exciton states within the band gap with enhanced optical absorption and behave like a reduced band gap material.

#### **4.3 UV/VIS/NIR absorption studies of BTO nanoparticles**

The BTO nanoparticles were dispersed in distilled water. The UV/VIS/NIR optical absorption for these particles was carried out by JASCO-570 spectrophotometer. The spectra's are shown in fig.4.1. The band gap of these particles was calculated by using Tauc's relation. It is observed that the band gap values are changing between 2.83 eV to 3.2 eV for sol-gel synthesized samples, and the band gap value is further decreased for the mesocrystalline sample to 2.00 eV. Thus, the particles show narrowed band gap. The schematic of band structure of these particles and band gap narrowing is explored in the sections below.

##### **4.3.1 Band structure analysis of BTO Nanoparticles**

The various types of transitions corresponding to the absorption spectra of fig.4.1 have been shown schematically in fig. 4.2. The mixing of O 2P and Ti 3d, orbital is shown by the curved dotted line in it. The absorption spectra of all these particles have two peaks, where the high energy peak looks as a shoulder for the main peak. The first peak is the upward transition from O2P, (orbital formed by  $2\Gamma_{15}$  states) to the partially filled Ti 3d,  $t_{2g}$  (orbital formed by  $1\Gamma_{25}$  states).

#### 4. Optical Studies on BaTiO<sub>3</sub> Nanoparticles and Mesocrystals

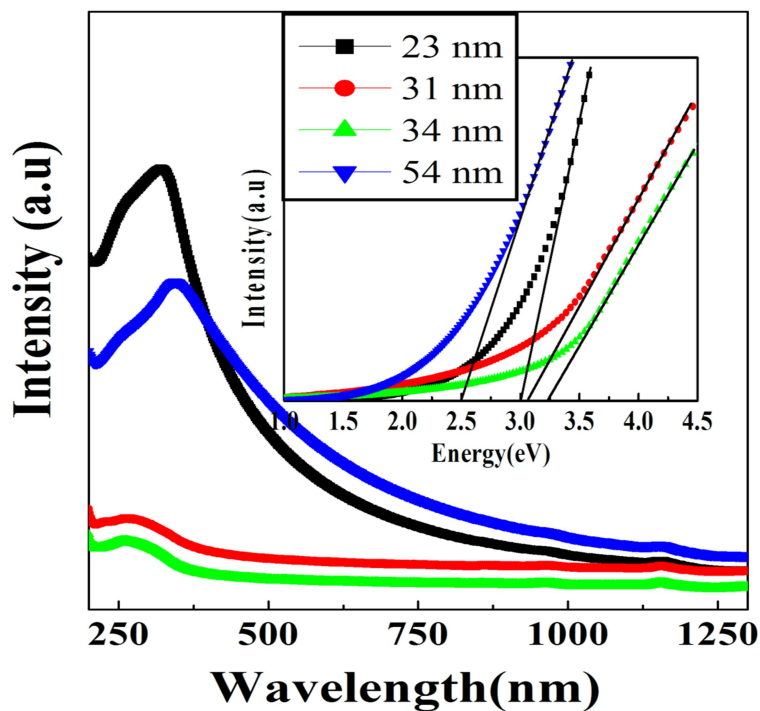


Fig.4.1. UV-VIS-NIR Optical absorption of nc-BTO nanoparticles of four different sizes (23 nm, 31 nm, 34 nm and 54 nm).

And the shoulder at higher energy is the charge transfer absorption from O 2P<sub>o</sub> orbital (formed by  $2\Gamma_{15}$  states) to the Ti 3d, e<sub>g</sub> orbitals (formed by  $1\Gamma_{12}$  states) in the conduction band. The vibrating states [27] induced mixing of O 2P orbital and Ti t<sub>2g</sub> orbital gives opposite parity to the electronic states. Thus, opposite parity leads to the transitions within the Ti 3d, t<sub>2g</sub> orbital (formed by  $1\Gamma_{25}$  state) to Ti 3d, e<sub>g</sub> orbital (formed by  $1\Gamma_{12}$ ) states of a conduction band. The increased absorption for 23 nm and 54 nm (Fig.4.1.) particles could be due to the presence of a higher density of states [28].

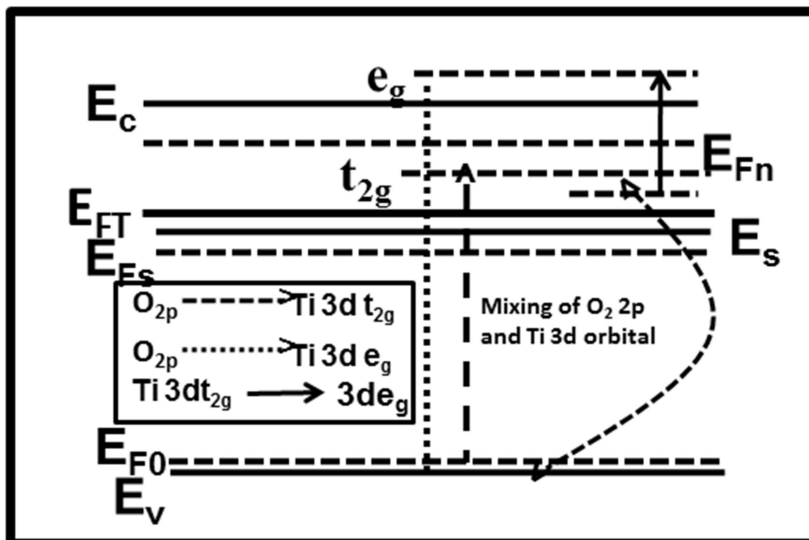


Fig.4.2. Schematic diagram showing various possible transitions in the nc-BTO, resulting in yielding a band gap narrowing.

#### 4.4 Photoluminescence studies in BTO Nanoparticles

The photoluminescence properties were carried out by varying the excitation wavelengths from 230 nm to 600 nm. The above discussed four set of particles do not show any photoluminescence signal, whereas the 1000°C sintered samples showed presence of photoluminescence peak around 530 nm. This is quite important in the charge transfer studies point of view and is discussed in the section below. This will be discussed in next chapter in the charge transfer section.

##### 4.4.1 Charge transfer studies

This is primarily due to the oxygen defects. It may be noted that defect formation energy is lower for oxygen compared to Ti and Ba [29]. The oxygen deficient system is equivalent to an electron doped BTO, because each oxygen vacancy creates extra electrons in the system showing higher conductivity [2, 3].

#### 4. Optical Studies on BaTiO<sub>3</sub> Nanoparticles and Mesocrystals

This oxygen vacancy distorts the octahedra and forms two asymmetric [TiO<sub>6</sub>] and [TiO<sub>5</sub>] clusters [30].

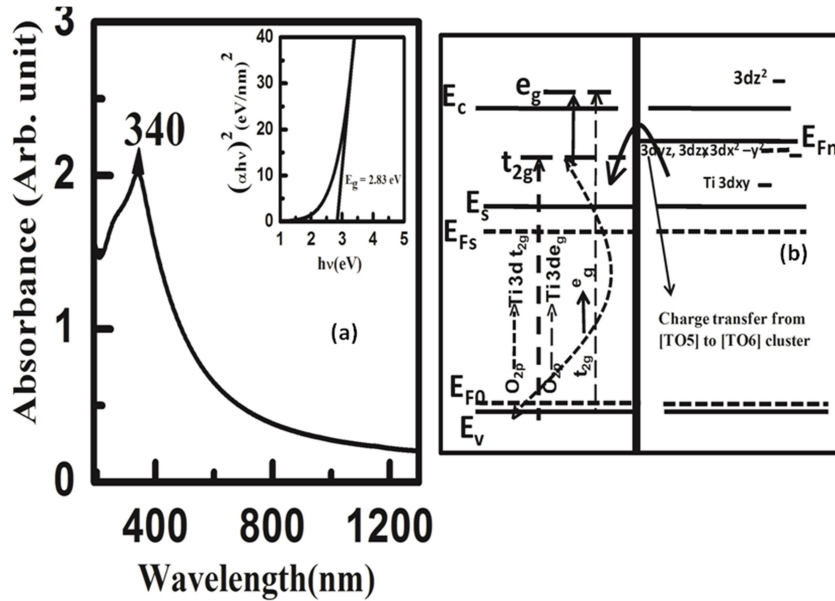


Fig.4.3. (a) UV-VIS-NIR absorption spectrum of nc-BTO, nanoparticles. (b) Schematic diagram of different optical transitions in nc-BTO, nanoparticles.  $E_{F0}$  = Fermi level,  $E_{Fs}$  = surface states at Fermi level,  $E_{Fn}$  = Fermi level free electrons created in the particle,  $E_V$  = Valence band,  $E_C$  = Conduction band.

Therefore, the net charges on these two clusters get the higher negative charge on [TiO<sub>5</sub>] and lower negative charge on [TiO<sub>6</sub>]. This permanent charge gradient is causing the effective charge transfer towards Ti compared to the charge transfer from oxygen [30, 31]. Thus, the oxygen vacancy gives the localization of electron to Ti site, and from a band, just below the conduction band. The dc conductivity measurement by the impedance analyzer indicates that the nc-BTO is in semiconducting state at ambient temperature.

#### 4. Optical Studies on BaTiO<sub>3</sub> Nanoparticles and Mesocrystals

##### 4.5 Raman spectroscopy of BTO nanoparticles

Raman spectroscopy is one of the foremost techniques in studying the electronic structure of nanomaterials. The Raman spectrum of BTO NPs is recorded with LAB-RAM Raman spectrometer. The spectrum has been taken at four to five places, and it is found that the spectrum is identical at all places. Here it is observed that the characteristic peaks exhibited systematic changes from particle to particle, like shift in the phonon mode, variation in intensity of specific mode, etc. From them it is clear that phenomenonas like phonon confinement and electron-phonon interactions are involved in the particles. These two mechanisms are briefly explained in the sections below.

##### 4.5.1 Phonon confinement in BTO Nanoparticles

The oxygen vacancies on the surface of a nanoparticle can change both the short-range and long-range Coulomb forces and cause the shift observed in Raman peak. The E (TO+LO) mode Raman spectral line at 305 cm<sup>-1</sup> is because of opposite moment of oxygen atoms at different sites in the octahedra. A blue shift is observed in E (TO) mode Raman spectrum line at 515 cm<sup>-1</sup> with decrease in the particle size from 54 nm to 23 nm. In bulk crystals, only the q = 0 phonons which are present at the centre of the Brillouin zone are Raman active. As the particle size reduces to nanometer size, the relaxation of q = 0 rule takes place and the phonons with q ≠ 0, from other parts of the Brillouin zone takes part in the Raman scattering. Hence, the onset of asymmetry in the Raman peak is arising from the activation of off-centered phonon modes. Thus, the red shift in E (LO) mode Raman spectral line at 305 cm<sup>-1</sup> with decrease in particle size reveals the presence of phonon confinement [32] effect in nc-BTO nanoparticles [33, 34].

The dispersion relation for 516 cm<sup>-1</sup> (A (TO) E (TO)) is given below by eqn. (8)

#### 4. Optical Studies on BaTiO<sub>3</sub> Nanoparticles and Mesocrystals

$$\omega(q) = \omega_0 + Aq^2 \quad 8$$

$$I(\omega) = \int_0^{\Gamma/2} \frac{4\pi q^2 e^{-q^2 L^2/4}}{\left\{ \omega - \omega(q) \right\}^2 + \left( \frac{\Gamma}{2} \right)^2} dq \quad 9$$

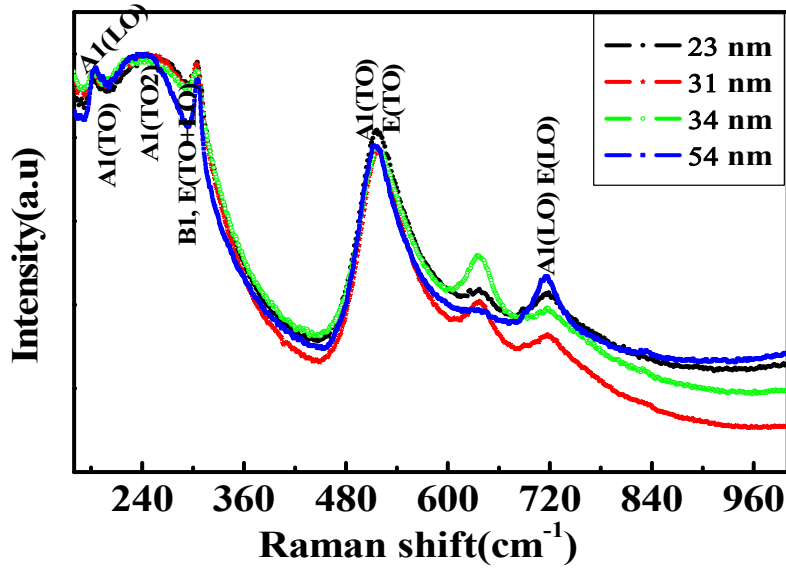


Fig.4.4. Raman spectrum of nc-BTO nanoparticles of sizes 23 nm, 31 nm, 34 nm and 54 nm.

Raman spectrum of most of the materials is best explained by Gaussian phonon confinement model. Hence, the phonon confinement is described by eqn. (9)

#### 4. Optical Studies on BaTiO<sub>3</sub> Nanoparticles and Mesocrystals

The blue shift in E (TO) mode Raman spectral line at 515 cm<sup>-1</sup> with particle size decrement is due to the domination of phonon confinement over the strain effect [32, 35, 36].

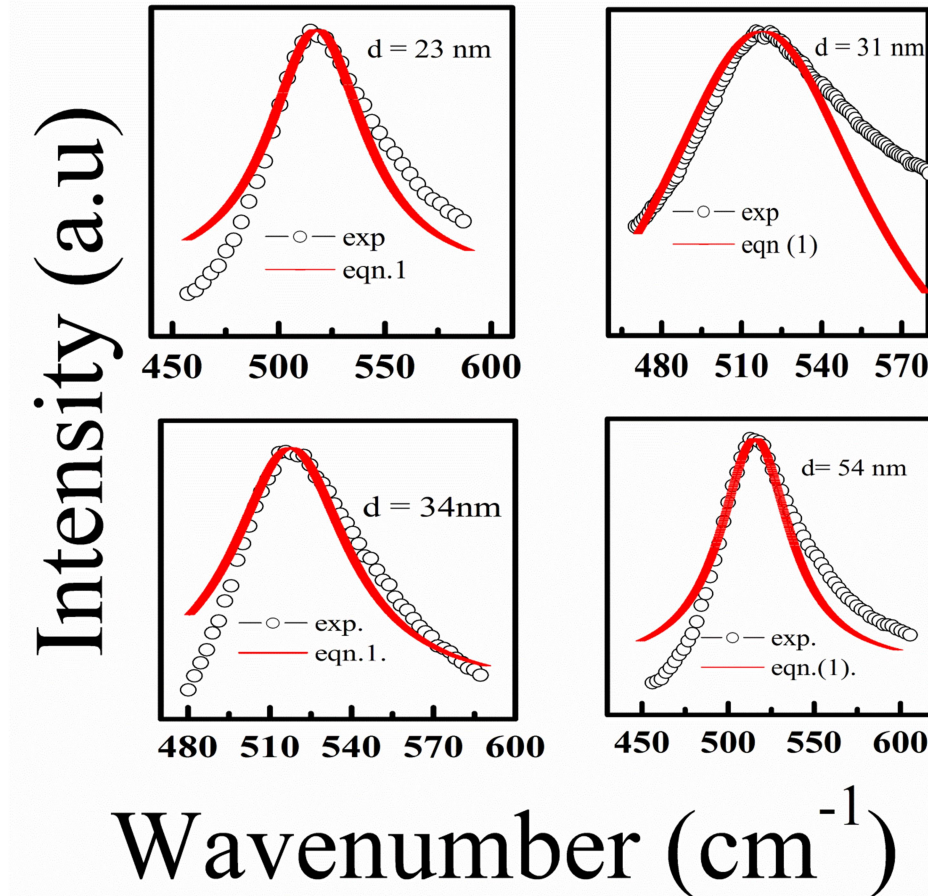


Fig.4.5. Theoretically fitted and experimental Raman spectra of 23 nm, 31 nm, 34 nm and 54 nm size BTO grains.

For each particle the 515 cm<sup>-1</sup> peak is considered for fitting. This Raman peak is fitted using eqn.9. The particle size, central frequency and width of the peak is obtained from the fitting and they are in agreement with the observed experimental values. The experimental observed and theoretically fitted values are given in Table 1.

#### 4. Optical Studies on BaTiO<sub>3</sub> Nanoparticles and Mesocrystals

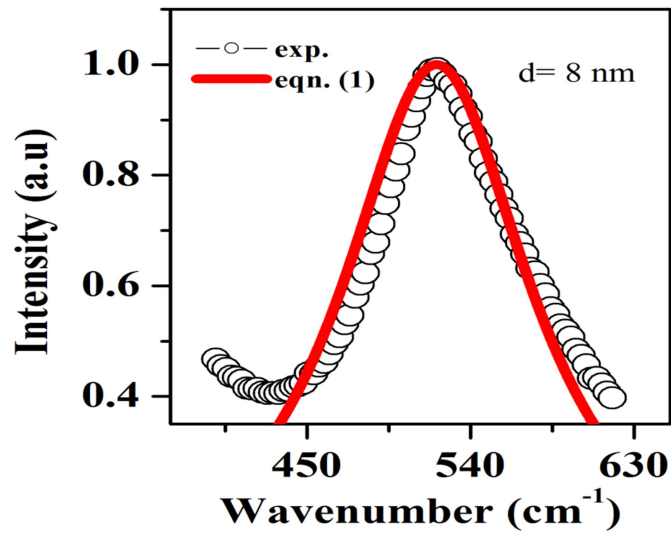


Fig.4.5 (b) Experimental and theoretically fitted Raman spectra for d= 8nm mesocrystals of BTO.

Table 1: The experimental and fitting parameters for different sizes of BTO particles

S. No	Particle size (d) nm	Experimental		Particle size (d) nm	fitted	
		$\Gamma_0$	$\omega_0$		$\Gamma_0$	$\omega_0$
1	8	73	522	8.0	75.0	521.6
2	23	54	518	23.8	55.4	518.0
3	31	55	517	30.0	40.0	518.0
4	34	50	517	34.7	50.8	517.6
5	54	49	515	55.1	49.3	515.4

#### *4. Optical Studies on BaTiO<sub>3</sub> Nanoparticles and Mesocrystals*

##### **4.5.2 Electron-phonon interactions in BTO Nanoparticles**

The band gap variation brought about by crystallographic strain is highlighted in the previous section. It could be noticed that the Raman spectrum that is shown in fig.4.4 also reflects the presence of additional structural changes such as red shift of Raman spectral line at 305 cm<sup>-1</sup>, blue shift of Raman spectral line at 515 cm<sup>-1</sup> and intensity variation of 638 cm<sup>-1</sup> peak. This ensures the involvement of some additional mechanisms in the band gap narrowing of these particles. The oxygen defects are often found in Nanoparticles due to its low defect formation energy compared to Ba and Ti [29]. Thus, the oxygen defects will create extra electrons in the system, and the system behaves as a free carrier doped BaTiO<sub>3</sub>. The electron densities for these, particles are in the range of (10<sup>19</sup>-10<sup>20</sup>/cm<sup>3</sup>) obtained from Z-scan measurements. This is in agreement with previous reports [2, 37, 38]. The maximum carrier density of 1.23x10<sup>20</sup>/cm<sup>3</sup> is obtained for 54 nm size particle. The increase in intensity of E (LO) phonon mode Raman spectrum line, at 715 cm<sup>-1</sup> in the particles of sizes 23nm and 54nm (650°C and 800°C calcined) can be due to the free carriers coupling to E (LO) phonon mode [39]. This, increased intensity of E (LO) mode is an evidence for the presence of electron-LO phonon interaction in the nanoparticles and it plays a major role in renormalization of the band gap of nc-BTO NPs [40]. The peak at 638 cm<sup>-1</sup> is attributed to a surface optical mode which is observed for all the samples [41]. The particles of sizes 31 nm and 34 nm show higher intensity for this mode. Hence, we expect the presence of higher charge carrier concentration in the surface of these particles [42]. The increased intensity of these modes for 31 nm and 34 nm size particles shows the weakening of electron-phonon interactions. Hence, the counter renormalization of band gap is observed for these two particles as discussed in the theoretical approach. These carriers occupy the surface states in the band structure as shown in fig.4.2 and hence, effective in filling up the conduction band. Therefore, it is necessary to involve the above

#### 4. Optical Studies on BaTiO<sub>3</sub> Nanoparticles and Mesocrystals

mentioned electron - phonon interactions in explaining the observed band gap values given in table 2.

### 4.6 Non-linear optical properties of BTO nanoparticles

#### 4.6.1 Open Aperture Z-scan

The open aperture data obtained were fitted initially for pure two photon absorption (2P, A). We combine the linear and two 2P, A ( $\beta$ ) coefficients giving a total absorption coefficient [43] as

$$\alpha(I) = \alpha_0 + \beta I \quad 10$$

Where  $\alpha_0$  is the linear absorption coefficient.

$$I = I(z) = I_{00} / (1 + \frac{z^2}{z_0^2}) \quad 11$$

is the excitation intensity at position  $z$  and  $I_{00}$  is the peak intensity.

2P,A coefficient ( $\beta$ ) can be obtained by fitting the following equation

$$\frac{dI}{dz} = -\alpha(I)I \quad 12$$

Substitute eq (11) in eq (12), then

$$\frac{dI}{dz} = -\alpha_0 I - \beta I^2 \quad 13$$

The transmitted intensity equation through the sample after solving the above differential equation is named as  $I_t(z)$  and the normalized transmittance can be formulated as  $T(z) = I_t(z)/I(z)$

The final equation of the transmitted intensity for 2P,A is

$$T(z) = 1 - \frac{\beta I_{00} L_{eff}}{2^{3/2} (1 + (z/z_0)^2)} \quad 14$$

Where  $L_{eff} = \frac{1 - e^{-\alpha_0 L}}{\alpha_0}$  and  $L$  = sample length

#### 4. Optical Studies on BaTiO<sub>3</sub> Nanoparticles and Mesocrystals

(ii) To interpret the switching of saturable absorption (SA) in reverse saturable absorption (RSA) in the open aperture data, we combine both the coefficients of SA and 2P,A ( $\beta$ ) which yield the total absorption coefficient [43, 44] given by

$$\alpha(I) = \frac{\alpha_0}{1 + I/I_s} + \beta I \quad 15$$

$I_s$  and  $\beta$  can be obtained by fitting the following equation (2)

$$\frac{dI}{dz} = -\frac{\alpha_0}{1 + \frac{I}{I_s}} I - \beta I^2 \quad 16$$

Where  $I_s$  is the saturation intensity.

The transmitted intensity equation through the sample after solving the differential equation (using matlab-ODE45) is named as  $I_f(z)$  and the normalized transmittance can be formulated as  $T(z) = I_f(z)/I(z)$

#### 4.6.2 Closed Aperture Z-scan

Similarly, the normalized closed aperture transmittance can be determined as follows

$$T\left(\frac{z}{z_0}\right) = 1 - \frac{4\left(\frac{z}{z_0}\right)\Delta\phi_0}{\left[\left(\frac{z}{z_0}\right)^2 + 1\right]\left[\left(\frac{z}{z_0}\right)^2 + 9\right]} \quad 17$$

Where  $Z$  is the sample position,  $z_0 = \pi\omega_0^2/\lambda$  is the Rayleigh range,  $\omega_0$  is the beam waist at the focal point ( $Z=0$ ),  $\lambda$  is the wavelength and  $\Delta\phi_0$  is the nonlinear phase shift.

#### 4. Optical Studies on BaTiO<sub>3</sub> Nanoparticles and Mesocrystals

The nonlinear optical properties of these nanoparticles make it useful in optical and electronic devices.

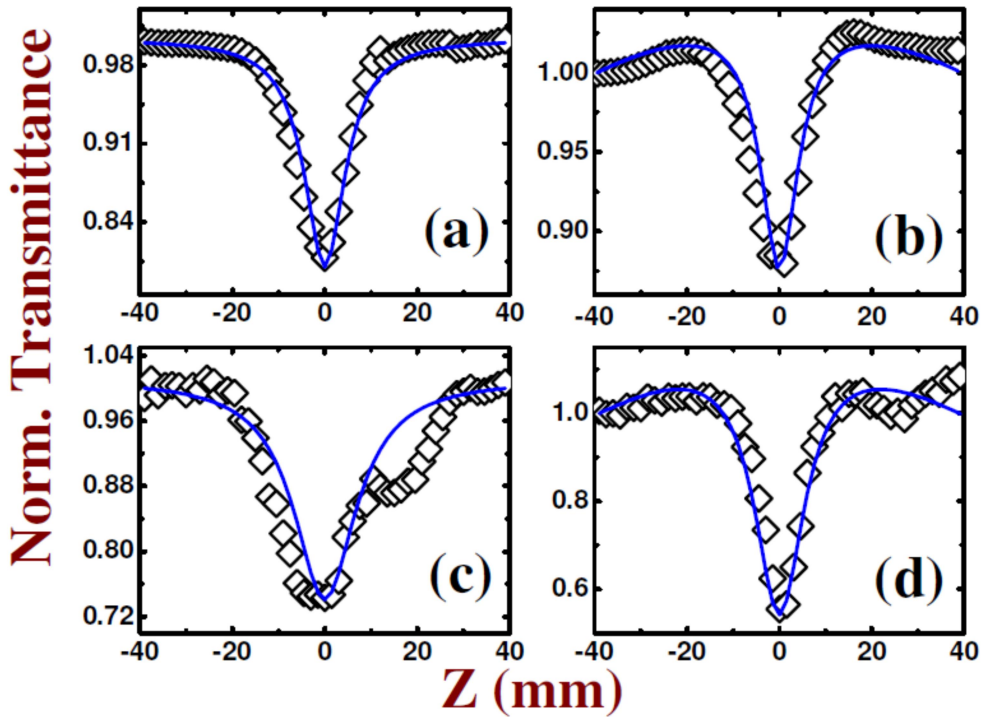


Fig.4.6. Open aperture Z-scan curves obtained for particles of avg. sizes of (a) ~23 nm (b) ~31 nm (c) ~34 nm and (d) ~54 nm at a peak intensity of  $I_{00} = 140 \text{ GW/cm}^2$ . Open squares are experimental points and Blue solid line represent the theoretical fit.

Fig.4.6 (a) to 4.6(d) show the open aperture Z-scan data of particles with average sizes of ~23 nm, ~31 nm, ~34 nm and ~54 nm, respectively, (calcined in the range of 650°C - 800°C) recorded at a peak intensity of 140 GW/cm<sup>2</sup>. The data in fig. 4.6(a) and 4.6(c) indicate simple reverse saturable absorption while the data in fig. 4.6(b) and 4.6(d) demonstrated complex behaviour with switching from saturable absorption (SA) to reverse saturable absorption (RSA). A good fit was obtained for dominant two-photon absorption coefficient ( $\beta$ ) with magnitude of the order of  $10^{-9} \text{ cm/W}$  and saturation intensity  $I_s$  of  $\sim 10^8 \text{ W/cm}^2$  for particles of average size ~31 nm and ~54 nm. No specified nonlinear absorption was observed from the PVA substrate. Solid (blue) lines in the fig.4.6 are theoretical fits. Closed

#### 4. Optical Studies on BaTiO<sub>3</sub> Nanoparticles and Mesocrystals

aperture data along with the corresponding theoretical fits (red, solid lines) for average size of (a) ~23 nm, (b) ~31 nm, (c) ~34 nm and (d) ~54 nm particles is shown in fig. 4.7(a)-4.7(d), respectively. The closed aperture scans for all the samples were recorded with a peak intensity of 80 GW/cm<sup>2</sup>. Open circles represent the experimental data for nanoparticles while the orange solid lines are the theoretical fits [44-49]. In the case of particles of size ~31 nm, the sign of nonlinear refraction  $n_2$  was negative. But in all the other cases, the sign of nonlinearity was positive. We obtained the best fit for  $n_2$  with a magnitude of  $\sim 10^{-13}$  cm<sup>2</sup>/W. All the nonlinear coefficients are summarized in Table 2.

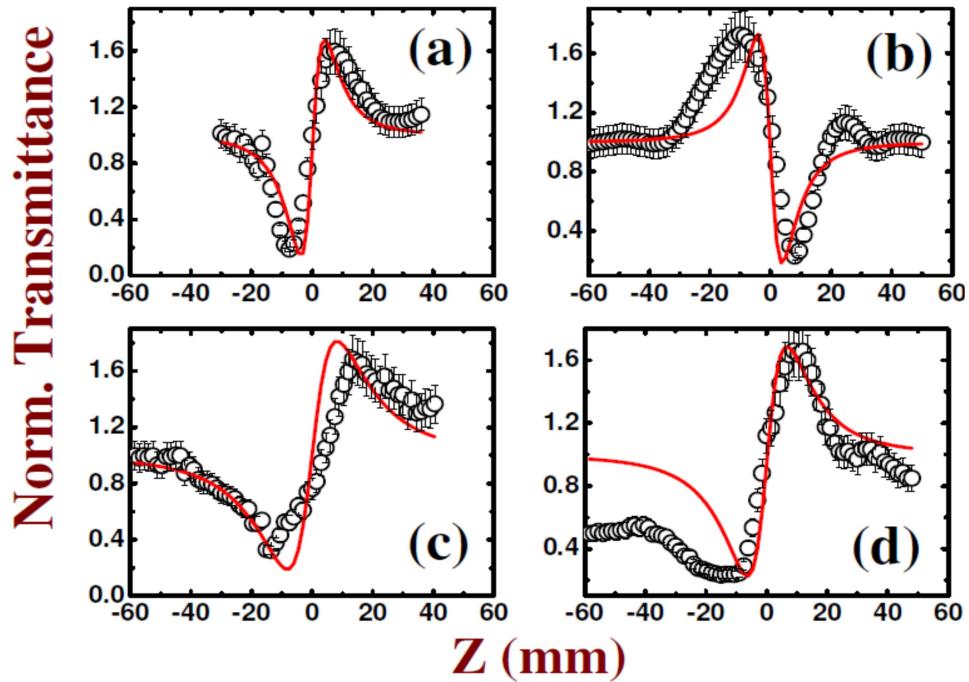


Fig.4.7. Closed aperture Z-scan curves recorded for particles of avg. sizes of (a) ~23 nm (b) ~31 nm (c) ~34 nm and (d) ~54 nm at a peak intensity of  $I_{00} = 140$  GW/cm<sup>2</sup>. Open stars are experimental points and orange solid line represent the theoretical fit.

#### 4. Optical Studies on BaTiO<sub>3</sub> Nanoparticles and Mesocrystals

##### 4.6.3 Charge carrier density calculation in BTO Nano particles

By using the above fitted parameters, we calculated the charge carrier density ( $N_e$ ) for all these particles using the following relation [50, 51].

$$N_e = F \frac{(1-T)}{h\nu} \left[ \alpha + \beta F \frac{(1-T)}{((2\sqrt{\pi})\tau)} \right] \quad 18$$

where F = Fluence, T = Linear transmittance,  $\tau$  = pulse width and  $\alpha$  = linear absorption.

It was observed that higher band gap narrowed samples show higher charge carrier density as expected. Thus, we obtained the concentrations as  $\sim 8.09 \times 10^{19}/\text{cm}^3$ ,  $\sim 8.17 \times 10^{19}/\text{cm}^3$  and  $\sim 9.06 \times 10^{19}/\text{cm}^3$  for particles of average sizes  $\sim 23$  nm,  $\sim 31$  nm, and  $\sim 34$  nm respectively. The higher charge density of  $\sim 1.29 \times 10^{20}/\text{cm}^3$  was obtained for  $\sim 54$  nm particles (Table 2). This is nearer to the Mott critical density for BTO [2, 37, 38].

In the refractive index sign change of these kind of materials, the main factors involved are electronic Kerr effect, optical electrostriction, population redistribution and thermal contribution. Thermal heat induced refractive index change will be negative, but the response time will be high in the nanosecond (ns) range. As we know that the time scale for the energy exchange between the electrons is few fs-100 ps and for electron-phonons typically are in the range of  $\sim$ ns. In the present studies, we have used ps pulses and since the effects relax at ps time scales the observed refractive index change is expected to be electronic in origin. Except in the case of  $\sim 34$  nm size particles (with  $E_g = 3.2$  eV), all other particles displayed small band gap values compared to the band gap of bulk BTO (3.2 eV). But the bleaching of absorption spectrum in particles of this size is evident because of the presence of certain concentration of free carriers induced conduction band filling in them [52].

#### 4. Optical Studies on BaTiO<sub>3</sub> Nanoparticles and Mesocrystals

Table 2: Observed nonlinear coefficients of particles of average sizes of ~23 nm, ~31 nm, ~34 nm and ~54 nm

Calcination Temp. (°C)	Avg. particle size (D) nm	Band gap (eV)	$\beta$ $10^{-9}$ (cm/W) @ ( $I_{00} = 140$ GW/cm <sup>2</sup> )	$n_2$ $10^{-13}$ (cm <sup>2</sup> /W)	Charge carrier density ( $N_e$ )/cm <sup>3</sup>
650	23	2.83	0.85	1	$8.09 \times 10^{19}$
700	31	3.00	0.17	-0.9	$8.17 \times 10^{19}$
750	34	3.2	1.5	0.9	$9.06 \times 10^{19}$
800	54	2.53	1.2	1	$1.29 \times 10^{20}$

As summarized in table 2, the band gap of these particles varied in the range of 2.53-3.2 eV. The samples with higher band gap narrowing demonstrated enhanced optical absorption. The higher band gap narrowing is due to the exchange-correlation interactions between the carriers. The band gap narrowing and involved mechanisms were discussed in our earlier paper [52]. The higher value for  $N_e$  is obtained from Z-scan measurements for all particles. In addition, some of the particles displayed narrowed band, with negative refractive index ( $n_2$ ) and bleached optical absorption. This also supports the presence of higher concentrations of charge carriers in these particles [53-56]. The higher band gap for these particles is expected due to the mixing up of O 2P, states in the valence band and Ti 3d, states in the conduction band. This mixing increases the effective mass of electrons in the conduction band and hence, there is now effective band narrowing like in the other two particle sizes. The magnetic measurements also support these results and will be discussed in the next chapter.

#### *4. Optical Studies on BaTiO<sub>3</sub> Nanoparticles and Mesocrystals*

##### **4.7 Band gap narrowing in BTO nanoparticles**

The optical absorption studies support the band gap narrowing mechanism discussed above. The strain and electron-phonon interactions were obtained by XRD and Raman spectroscopy.

The band gap of two particles (23 nm and 54 nm) is 3.00 eV and 2.53 eV respectively (Table 2). This band gap renormalization is due to the exchange - correlation interactions between the carriers [19-21, 57]. The charge carrier density is very high for 54 nm size particles. Hence, for these particles, band gap can be explained by considering that the electrons form degenerate electron gas in the conduction band as explained in section 4.2.1 in the theoretical approach. Unlike to this case, the particles of sizes 31nm and 34nm (700°C and 750°C calcined) has low carrier density ( $\sim 10^{19}/\text{cm}^3$ ) and show a bleaching in the absorption spectrum (Fig.4.1). This is due to the conduction band filling domination over the band gap renormalization (BGR) [58-61]. Hence, these two particles show a higher band gap of 3.08 eV and 3.2 eV respectively. The lower band gap shrinkage in 31 nm and 34 nm size particles compared to the band gap shrinkage in the particles of sizes 23 nm and 54 nm (650°C and 800°C calcined), is an evidence for the weakening of exchange - correlation interactions in them. Thus, band narrowing in these two sizes of particles can be explained by considering the electron-phonon interaction as discussed in the theoretical approach section 4.2.2. The band gap and shrinkage is given for all these particle sizes in Table 2. Thus, as discussed above, the band gap narrowing in these particles shows the existence of exchange - correlation interactions, in addition to the compressive strain and electron-phonon interactions present in them.

In summary, it is clear that multiple mechanisms are required to explain the observed band gap narrowing of BTO NPs. The XRD analysis shows the presence of strain (chapter 3), and the Raman spectrum indirectly conveys the

#### *4. Optical Studies on BaTiO<sub>3</sub> Nanoparticles and Mesocrystals*

presence of electron-phonon interactions in them. In particular, the enhancement of LO Raman intensity reveals the presence of electron-phonon interactions in the system. The optical absorption spectrum provides the information on the presence of charge carriers in the system. It is showing an enhanced optical absorption in band gap decreased NPs and bleaching of absorption in lesser band gap narrowed nanoparticles. Thus, it shows the bleaching of absorption in particles of sizes 31 nm and 34 nm. The band gap is gradually increases from 3.00 eV to 3.20 eV as the particle size increases from 23 nm to 34 nm. This clearly shows weakening electron-phonon coupling due to screening effects as discussed in sub section 4.2.2. Hence, the counter band gap renormalization occurred and reached a bulk value for 34 nm size particles. The Raman spectrum also reflects these changes very clearly by showing highest intensity for 638 cm<sup>-1</sup> mode in 34 nm particles, and lower intensity for 54 nm size particles. In spite of having large strain in 24 nm size particles compared to 54 nm size particles, the larger band gap narrowing in 54 nm is evidence for the domination of exchange-correlation interactions due to higher carrier charge density of  $1.23 \times 10^{20}/\text{cm}^3$  in them as discussed in sub section 4.2.1. We can say that the band gap of these particles is highly tuned by the exchange-correlation interactions between the charge carriers present in the system. In other words, it opens up an opportunity to tune band gaps of wide band gap materials to match with the required absorption range. It is an important aspect as ferroelectric oxides got large bandwidths absorbing mostly in the UV range. To make them absorb in the visible range and thereby to harness them for energy harvesting applications, this type of understanding of band gap tuning mechanisms are needed. At present, there is a considerable effort going on to exploit the built-in electric field present in ferroelectric domains. This must be done in conjunction with band gap tuning to make them absorb solar radiation and to increase the charge transport so that the photon generated charge carriers can be separated and transported out. Here we

#### *4. Optical Studies on BaTiO<sub>3</sub> Nanoparticles and Mesocrystals*

see that both are happening with the possibility for further exploiting these mechanisms for fine tuning. Then what is remaining for energy harvesting is a means for arranging the electrode patterns to exploit the built in electric field inside the ferroelectric domains.

#### **4.8. Introduction to mesocrystals and their optical studies**

Mesocrystals are a new class of materials in which small crystals are arranged periodically. Thus, all the crystallites got their crystallographic axes oriented along the same direction [62]. This way, it forms superstructures in 3d, or 2D or in 1D. Mesocrystals are the intermediate structures in nonclassical crystallization process, and leading to single crystals by single particle fusion [63-65]. The crystallization process of mesocrystal is different from classical crystallization [66-69]. Mesocrystal formation contrasts with the atom or ion or molecule based classical crystallization process. Instead, it is a particle based non-classical crystallization. The mesocrystals will have high internal surface area. In adult sea urchin spine, each spine composes of a highly oriented array of Mg-calcite nanocrystals embedded with amorphous and macromolecules in it. This diffracts X-rays as a single crystal but fractures like a glassy material. Thus, mesocrystals are the ambitious candidates for providing simultaneous behavior of single crystal and amorphous materials in the same system. The high porosity or voids in mesocrystals are used for the immobilization of some organic molecules. Thus, mesocrystals have many applications in various fields like Biology, material science, etc. In the present case, we synthesized the ferroelectric BaTiO<sub>3</sub> (BTO) mesocrystals and studied their structural as well as photoluminescence properties and explained how mesocrystals are capable of showing tunable photoluminescence unlike to that of crystalline BTO.

The vital properties of mesocrystals such as high crystallinity, oriented attachment, and the high porosity makes it a potential candidate in the areas of

#### 4. Optical Studies on BaTiO<sub>3</sub> Nanoparticles and Mesocrystals

sensing, biomedical materials, optoelectronics, etc. Notably the high porosity of these materials makes them suitable for applications such as energy storage and photocatalysis [70]. Mesocrystals of few materials has been recently found to be efficient in THz generation [71, 72]. It is well known that piezoelectric materials got many applications from domestic to an industrial sector. It is possible to achieve higher piezoelectric coefficients by crystal axis oriented materials [73]. The [110] oriented BTO materials have got  $d_{33}$  value of 788 pC/N [74] while the normal BTO shows a  $d_{33}$  value 190 pC/N, which is one-fourth that of the oriented BTO material [75].

Since the mesocrystals are the intermediate structures to that of crystalline and amorphous materials, the optical properties are of interest to study.

##### 4.8.1 Raman studies/phonon confinement

The Raman spectrum of mesocrystalline BTO is shown in fig.4.8. It depicts various changes that are the consequences of the size of the particle.

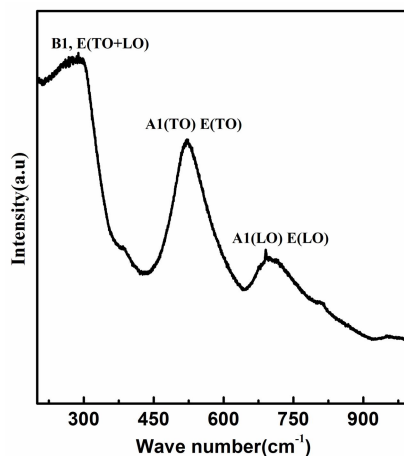


Fig.4.8. Raman spectra of BTO mesocrystal.

The effects are phonon confinement which is inferred from the large shift of A1 (TO) E (TO) peak to 524 cm<sup>-1</sup>. The broadening of 305 cm<sup>-1</sup> (E(TO)+E(LO)) peak shows the weakening of ferroelectric property in mesocrystals. As discussed

#### 4. Optical Studies on BaTiO<sub>3</sub> Nanoparticles and Mesocrystals

above, the mesocrystal is composed of 5-8 nm size crystallites and such small size contributes to the reduction in ferroelectric property of BTO. It shows strong phonon confinement effect by showing strong blue shift of A<sub>1</sub> (TO) E (TO) peak to 524 cm<sup>-1</sup>. The fitting is shown in fig.4.5 (b).

##### 4.8.2 UV/VIS/NIR optical absorption studies

Fig. 4.9 shows the optical absorption spectrum of these mesocrystals taken by UV/VIS/NIR spectrophotometer. The spectrum contains three absorption peaks at 241 nm, 320 nm and a broad peak at 572 nm. The peak at 241 nm is the charge transfer absorption from the valence band to the e<sub>g</sub> orbital (formed by 1Γ<sub>12</sub> state) band in the conduction band, 320 nm peak is the transition from valence band O 2P, to the conduction Ti 3d, t<sub>2g</sub> orbital (formed by 1Γ<sub>25'</sub>) states. In the oxide nanoparticles, the oxygen defects are often widely present. The observed broad 572 nm peak in the absorption spectrum is due to defect states below the conduction band. The linear increase in absorption with the increase in energy is evidence for the presence of continuous distribution of energy states below the conduction band.

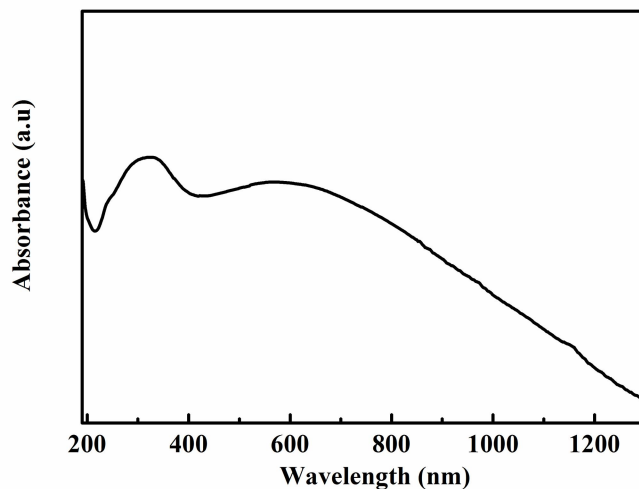


Fig.4.9. Optical absorption of BTO mesocrystals

#### 4. Optical Studies on BaTiO<sub>3</sub> Nanoparticles and Mesocrystals

##### 4.8.3 Photoluminescence

In the oxide nanoparticles the oxygen defects are often widely present. The observed broad 572 nm peak in the absorption spectrum is because of defect states below the conduction band. The linear increase in absorption with the increase in energy is evidence for the presence of continuous distribution of energy states below the conduction band. These continuous defect states (or trapped states) below the conduction band can give photoluminescence tunability with excitation wavelength variation.

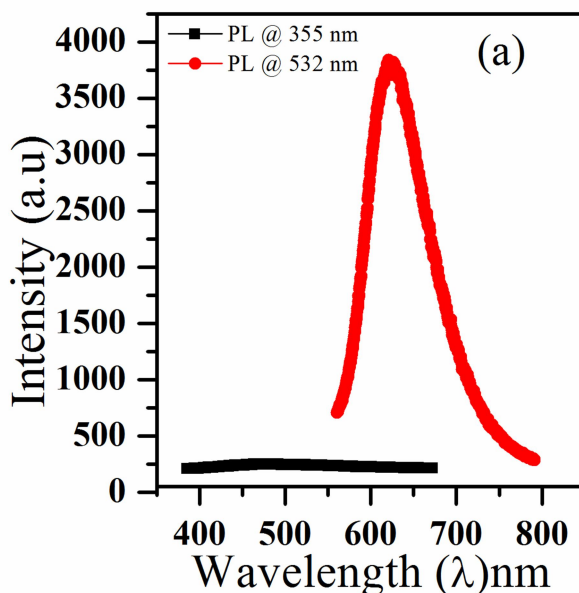


Fig.4.10. Photoluminescence spectrum of BTO mesocrystals for two excitations (355 nm and 532 nm).

The photoluminescence measurements were carried out by WiTec (alpha 300) and are given in fig.4.10. It shows two weak broad peaks at 479 nm and 513 nm when excited with 355 nm wavelength. This emission is due to the radiative recombination of self-trapped excitons in the material [76]. But the quenching of luminescence can form multi phonons in the system. These multi phonons are very useful in absorbing the infrared radiation. Thus, the multiphonons are helpful in absorbing the below band gap radiation and supports the efficient photo voltaic

#### 4. Optical Studies on BaTiO<sub>3</sub> Nanoparticles and Mesocrystals

development. As the excitation wavelength changes to 532 nm, the photoluminescence peak has shifted to 625 nm. But this peak is intense compared to the 355 nm excitation wavelength. This is due to the electron-hole recombination of excitons. Here the exciton binding energy is about 1.2 eV. This large binding energy of exciton is due to the dielectric confinement in the material.

##### 4.8.4 Giant band gap renormalization (BGR)

The band gap of mesocrystal is calculated by Tauc's formula. It is shown in fig.4.11 (b). It shows a band gap of 2.00 eV which is very small compared to the bulk band gap of 3.20 eV. Hence, the band gap reduction is very high and called as giant band gap narrowing.

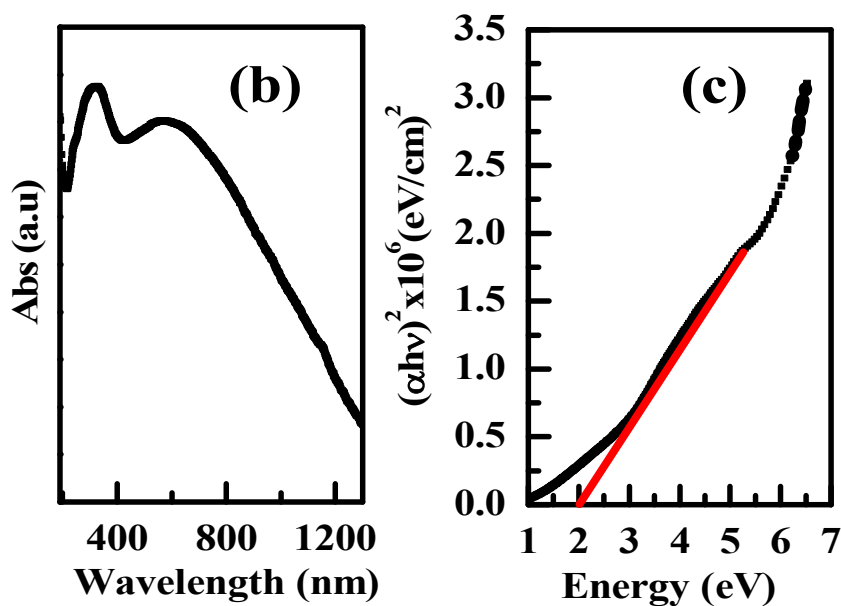


Fig.4.11. (a) optical absorption and (b) Tauc's plot of T30A40 sample.

The exciton - exciton interaction, together with exciton - lattice interaction has some interesting consequences such as a drastic reduction in the electronic energy band gap. The BTO mesocrystals are composed of many small particles or

#### ***4. Optical Studies on BaTiO<sub>3</sub> Nanoparticles and Mesocrystals***

attachment of 5-8 nm sized crystallites of BTO in the present case. Thus, as the particles are attached, and of nano size, the grain boundaries and surface area of these particles will be less dense thanks to oxygen defects and will act as a low dielectric constant material.

Hence, the dielectric confinement occurs in this system. This dielectric confinement causes the reduction in the screening effects and hence, the enhanced electron-electron interactions will cause giant band gap reduction and high excitonic binding energies [77-79]. The dielectric confinement effect is more dominating in quantum dot materials whereas this effect is weak in quantum wells and quantum wires [79].

#### **4.9 Summary**

In summary the involvement of multiple effects in narrowing the band gap of nc-BTO NPs by analyzing XRD (in the previous chapter), Raman and optical spectrum for four different sizes of BTO nanoparticles and BTO mesocrystals were studied. It is found that the strain, electron-phonon interactions, and exchange - correlation interactions were involved in band gap reduction of sol-gel prepared nanoparticles. Whereas, the dielectric confinement effect causes the giant band gap renormalization in BTO mesocrystals.

The increased intensity of LO mode Raman spectral line at  $715\text{ cm}^{-1}$  for particles of sizes 23 nm and 54 nm reveals the presence of electron-phonon interactions in the system. Thus, it is necessary to follow the evolution of the electron-phonon interactions in studying the band gap renormalization of these NPs. The increased intensity of surface optical mode at  $638\text{ cm}^{-1}$  in case of particles of sizes 31 nm and 34 nm signals the presence of more carriers and hence, the conduction band filling is dominated over the band gap renormalization in these particles. The optical studies also reveal the presence of higher carrier density in the 31 nm and 34 nm particle sizes by showing the bleaching of the

#### ***4. Optical Studies on BaTiO<sub>3</sub> Nanoparticles and Mesocrystals***

absorption spectrum. Hence, the higher band gap value is observed for these two sizes of particles compared to the particles of sizes 23 nm and 54 nm. The free carriers in 23 nm and 54 nm particles show the band gap narrowing due to the exchange - correlation interactions within the charge carriers. Thus, the above mentioned results give hints to the involvement of multiple mechanisms namely lattice strain, electron-phonon interactions and exchange-correlation interactions in explaining the observed band gap values in nc-BTO particles. The particles with average sizes of ~31 nm and ~34 nm did not show marginal band gap narrowing. Thus, it can be said that the O 2P, and Ti 3d, states were mixed to yield a counter renormalization of band gap due to increase of the electron effective mass. Therefore, the increased charge carrier concentration increased the magnetic moment values due to the dominant exchange interactions between the carriers. And, band gap narrowing was observed for higher carrier density. These arguments are also supported by the Z-scan measurements where one of the samples showed negative refractive index ( $n_2$ ) in addition to the higher charge carrier density in them. It also confirms the large charge carrier density present in them. The 54 nm size particles with highly narrowed band gap show the charge carrier density nearer to Mott carrier density.

The porous nano structures are ideal systems to show dielectric confinement effect. The band gap of 2.00 eV is obtained. This giant band gap narrowing is explained by considering the dielectric confinement effect. The exciton binding energies were obtained to be around 1.2 eV, this enhanced binding energy values are the consequence of dielectric confinement in the material. The non-radiative decay (weak photo luminescence) at 355 nm excitation hints at the multi phonon states in the system, and these are essential for infrared radiation absorption. Thus, it appears that the BTO mesocrystals are more suitable candidates for solar energy harvesting applications.

**References**

1. Y. Akishige, Y. Yamazaki, T. Nakanishiy and N. Mori, J. Korean. Phys. Soc. **32**, 386 (1998).
2. T. Kolodiazhnyi, Phys. Rev. B **78**, 045107 (2008).
3. T. Kolodiazhnyi, M. Tachibana, H. Kawaji, J. Hwang and M. E. Takayama, Phys. Rev. Lett. **104**, 147602 (2010).
4. D. K. Ferry, Phys. Rev. B **18**, 7033 (1978).
5. J. Wang and L. Huang, Appl. Phys. Lett. **98**, 113102 (2011).
6. N. W. Gong, M. Y. Lu, C. Y. Wang, Y. Chen, and L. J. Chen., Appl. Phys. Lett. **92**, 073101 (2008).
7. M. A. R. C. Alencar, G. S. Maciel, Cid B. de Araujo and A. Patra., Appl. Phys. Lett. **84**, 4753 (2004).
8. A. T. Tilke, L. Pescini, H. Lorenz, and R. H. Blick, Appl. Phys. Lett. **82**, 3773 (2003).
9. D. R. Schmidt, C. S. Yung, and A. N. Cleland, Appl. Phys. Lett. **83**, 1002 (2003).
10. I. Naumov, L. Bellaiche, H. Fu, Nature **432**, 737 (2004).
11. B.J. Rodriguez, X. S. Gao, L.F. Liu, W. Lee, I. I. Naumov, A. M. Bratkovsky, D. Hesse and M. Alexe, Nano Lett. **9**, 1127 (2009).
12. J. Zhang, et.al, Nat. Sci. Rep. **3**, 2109 (2013).
13. G. Zhang, et.al, Nat. Sci. Rep. **3**, 1265 (2013).
14. K. Yao, B. K. Gan, M. Chen, and S. Shannigrahi, Appl. Phys. Lett. **87**, 212906 (2005).
15. J. Seidel, et.al, Phys. Rev. Lett. **107**, 126805 (2011).
16. J. Seidel, et.al, Nat. Mat. **8**, 229 (2009).
17. S. Y. Yang, et.al, Appl. Phys. Lett. **95**, 062909 (2009).

#### 4. *Optical Studies on BaTiO<sub>3</sub> Nanoparticles and Mesocrystals*

18. P. S. V. Mocherla, C. Karthik, R. Uvic, M. S. R. Rao, and C. Sudakar, *Appl. Phys. Lett.* **103**, 022910 (2013).
19. J. C. Inkson, *J. Phys.* **9** 1177 (1976).
20. K. F. Berggren and B. E. Sernelius, *Phys. Rev. B* **24** 1971 (1981).
21. S. Nandy, U. N. Maiti, C. K. Ghosh and K. K. Chattopadhyay, *J. Phys.: Condens. Matter* **21** 115804 (2009).
22. L. V. Keldysh and A. P. Silin, *Sov. Phys. -JETP*, **42**, 535 (1975).
23. G. Beni and T. M. Rice *Phys. Rev. B* **18**, 768 (1978).
24. S. D. Sarma and M. Stopa, *Phys. Rev. B* **36** 9595 (1987).
25. Y. H. Matsuda, et.al, *Phys. Rev. B* **65** 115202 (2002).
26. P. M. Hui, H. Ehrenreich and K. C. Hass *Phys. Rev. B* **40** 346 (1989).
27. S. E. Thomas Wolfram, Newyork Cambridge University Press **9**, (2006).
28. H. Roskos, B. Rieck, A. Seilmeier, W. Kaiser, and G. G. Baumann, *Phys. Rev. B* **40**, 1396 (1989).
29. D. Cao, M. Q. Cai, Y. Zheng and W. Y. Hu, *Phys. Chem. Chem. Phys.* **11**, 10934 (2009).
30. E. Orhan, J. A. Varela, A. Zenatti, M. F. C. Gurgel, F. M. Pontes, E. R. Leite, E. Longo, P. S. Pizani, A. Beltran and J. Andres, *Phys. Rev. B* **71**, 085113 (2005).
31. S. G. Lu, Z. K. Xu, H. Chen, C. L. Mak, K. H. Wong, K. F. Li and K. W. Cheah, *J. Appl. Phys.* **99**, 064103 (2006).
32. M. S. Chen, Z. X. Shen, S. H. Tang, W. S. Shi, D. F. Cui and Z. H. Chen *J. Phys.: Condens. Matter.* **12**, 7013 (2000).
33. W. H. Zhang, L. Chen, Y. T. Tao, J. Chen and J. X. Zhang, *Physica B* **406**, 4630 (2011).
34. P. H. Gosez, X. Goneze and J. -P. Michenaud, *Ferroelectrics.* **206**, 205 (1998).

#### 4. *Optical Studies on BaTiO<sub>3</sub> Nanoparticles and Mesocrystals*

35. K. Rezugui, S. Aloulou, J. Rihani and M. Oueslati, J. Raman. Spectrosc. 43, 1964 (2012).
36. T. Teranishi, N. Horiuchi, T. Hoshina, H. Takeda and T. Tsurumi, J. J. Ceramic. Soc. 118, 679 (2010).
37. S. Lee, G. Yang, R. H. T. Wilke, S. Trolier-McKinstry, and C. A. Randall, Phys. Rev. B 79, 134110 (2009).
38. S. Lee, J. A. Bock, S. Trolier-McKinstry, C. A. Randall, J. Eur. Ceram. Soc. 32 3971 (2012).
39. V. N. Bessolov, E. V. Konenkova, Yu. V. Zhilyaev, B. A. Paez sierra, and D. R. T. Zahn, Appl. Sur. Sci. 235, 274 (2004).
40. C. R. Bennett, K. Guven and B. Tanatar, Phys. Rev. B 57, 3994 (1998).
41. R. Englman and R. Ruppin, J. Phys. C 1, 614 (1968).
42. G. G. Khan, D. Sarkar, A. K. Singh and K. Mandal, RSC Adv. 3, 1722 (2013).
43. S. Venugopal Rao, J. Mod. Opt. 58, 1024 (2011).
44. M. Sheik-Bahae, A. A. Said and E. W. Vanstryland, Opt. Lett. 14, 955 (1989).
45. S. Venugopal Rao , T. Shuvan Prashant, T. Sarma, Pradeepta K. Panda, D. Swain, Surya P. Tewari, Chem. Phys. Lett., 514, 98 (2011).
46. S. Hamad, G K Podagatlapalli, S. P. Tewari, S. Venugopal Rao, J. Phys. D: Appl. Phys., 46, 485501 (2013).
47. M. Yin, H. P. Li, S. H. Tang, W. Ji, Appl. Phys. B. 70, 587 (2000).
48. K. Venkata Saravanan, K.C. James Raju, M. Ghanashyam Krishna, Surya P. Tewari, S. Venugopal Rao, Appl. Phys. Lett. 96, 232905 (2010).
49. G. K. Podagatlapalli, S. Hamad, S. P. Tewari, S. Sreedhar, M. D. Prasad, and S. V. Rao, J. Appl. Phys. 113, 073106, (2013).
50. R Le Harzic, D Dorr, D Sauer, F Stracke, and H Zimmermann, Appl. Phys. Lett. 98, 211905 (2011).

#### *4. Optical Studies on BaTiO<sub>3</sub> Nanoparticles and Mesocrystals*

51. K Sokolowski-Tinten and D Von der Linde, Phys. Rev. B 61, 2643 (2000).
52. S Ramakanth and K C James Raju, J. Appl. Phys. 115, 173507 (2014).
53. B R Bennett, R A Soref, and J A D Alamo, IEEE J. Quantum. Elect. 26, 113 (1990).
54. J G M Alvarez, F D Nunes, and N B Patel, J. Appl. Phys. 51, 4365 (1980).
55. Weitian Wang, Liangsheng Qu, GuangYang, and Zhenghao Chen, Appl. Surf. Sci. 218, 24 (2003).
56. Litty Irimpan, A. Deepthy, Bindu Krishnan, L. M.Kukreja, V. P. N. Nampoore, and P. Radhakrishnan, Opt. Commun. 281(10), 2938-2943 (2008).
57. Y. K. Lakshmi, K. Srinivas B. Sreedhar, M. M. Raja, M. Vithal, and P. V. Reddy, Mater. Chem. Phys. 113, 749 (2009).
58. P. W. Juodawlkis and S. E. Ralph, Appl. Phys. Lett. 76, 1722 (2000).
59. Y. Kostoulas L. J. Waxer, I. A. Walmsley, G. W. Wicks, and P. M. Fauchet, Appl. Phys. Lett. 66, 1821 (1995).
60. M. T. Nenadovit, M. I. Comor, V. Vasiir and O. I. Mitic, J. Phys. Chem. 94, 6391 (1990).
61. K. V. Yumashev, P. V. Prokoshin, A. M. Malyarevich, V. P. Mikhailov, M. V. Artemyev, and V. S. Gurin, Appl. Phys. B 64, 73 (1997).
62. R. Song, H. Colfen, Adv Mater 22,1301 (2010).
63. F. Dang, K. Kato, H. Imai, S. Wad, H. Hanedad, M. Kuwabara, Cryst. Eng. Comm. 12, 3441 (2010).
64. N. Park, Y. Wang, W. Seo, F. Dang, C. Wan, K. Koumoto, Cryst. Eng. Comm. 15, 679 (2013).
65. J. Fang, B. Ding, X. Song, Appl. Phys. Lett. 91, 083108 (2007).
66. M. Niederberger, H. Colfen, Phys. Chem. Chem. Phys. 8, 3271 (2006).

#### 4. *Optical Studies on BaTiO<sub>3</sub> Nanoparticles and Mesocrystals*

67. Zhou L, Brien PO, J Phys Chem Lett., 3, 620 (2012).
68. K. Yasui, K. Kato, J. Phys. Chem. C. 116, 319 (2012).
69. D. Hu, X. Kong, K. Mori, Y. Tanaka, K. Shinagawa, Q. Feng, Inorg. Chem. 52, 10542 (2013).
70. X. Yao, X. Liu, T. Liu, K. Wang, L. Lu, Cryst. Eng. Comm. 15, 10246 (2013).
71. Z. Liu, X. D. Wen, X. L. Wu, Y. J. Gao, H. T. Chen, J. Zhu, et.al, J. Am. Chem. Soc. 131, 9405 (2009).
72. X. L. Wu, S. J. Xiong, Z. Liu, J. Chen, J. C. Shen, T. H. Li, et.al, Nature Nano tech. 16, 103 (2011).
73. X. G. Kong, Y. Ishikawa, K. Shinagawa, Q. Feng, J. Am. Ceram. Soc. 94, 3716 (2011).
74. S. Wada, K. Takeda, T. Muraishi, H. Kakemoto, T. Tsurumi, T. Kimura, Jpn. J. Appl. Phys. 46, 7039 (2007).
75. H. Takahashi, Y. Numamoto, J. Tani, S. Tsurekawa, Jpn. J. Appl. Phys. 45, 7405 (2006).
76. G. G. Siu, X. L. Wu, Y. Gu, X. M. Bao, Appl. Phys. Lett. 74, 1812 (1999).
77. M. M. Ugeda, A. J. Bradley, S. F. Shi, F. H. da Jornada, Y. Zhang, D. Y. Qiu, W. Ruan, S. K. Mo, Z. Hussain, Z.-X. Shen, F. Wang, S. G. Louie and M. F. Crommie Nature Mater. 13, 1091 (2014).
78. J. Even, L. Pedesseau and M. Kepenekian, Phys.Chem.Chem.Phys. 16, 25182 (2014).
79. Y. Masumoto, T. Takagahara, "Semiconductor Quantum Dots: Physics, Spectroscopy and Applications" Springer Science & Business Media, 60-69 (2002).

#### *4. Optical Studies on BaTiO<sub>3</sub> Nanoparticles and Mesocrystals*

## **Chapter 5**

### **Study of origin of magnetism in nc-BTO nano particles**

---

#### **Abstract**

In the current chapter, we discuss the origin of magnetism in nanocrystalline BaTiO<sub>3</sub> (nc-BTO) nano particles. The role of charge transfer effect is discussed in the frame work of Stoner magnetism. The low temperature calcined four different nanoparticles of size in the range of 23 nm-54 nm do not show charge transfer mechanism. Whereas the high temperature calcined nc-BTO and mesocrystal samples show presence of charge transfer effects in it. The field and temperature dependent magnetization measurements indicate that charge transfer absent samples show super paramagnetic behaviour. The charge transfer involved samples show ferromagnetic properties. It is found that the mesocrystals of nc-BTO are showing ferromagnetic ground states with higher T<sub>c</sub> (=131K) compared to sol-gel prepared samples. This gives very strong hint to the increase of electron-electron interactions in these materials through dielectric confinement effect and hence the ferromagnetic ground state.



## 5. Study of origin of magnetism in nc-BTO nanoparticles

### 5.1 Introduction

Recently observed ferromagnetism in ferroelectric [1-5]  $d^0$ -nanomaterials [6-12], makes the ferromagnetism as a trivial property of nanomaterials [13]. The most common property of these materials is that they don't have unpaired electrons in them, but still show magnetism which is counter intuitive. The electron-phonon interactions play an active role when the size of the materials goes to nanometer scale. The electron-phonon and electron-electron interactions are well studied in nanomaterials to explain their optical properties too. But, the particular interaction responsible for occurrence of ferromagnetic phase in these nanomaterials is still under investigation.

Magnetism in ferroelectric materials brings forth an idea of doping ferroelectric materials with magnetic and nonmagnetic ions to study its ferroelectric and ferromagnetic properties [14, 15]. It is expected that such studies will help in coupling the ferromagnetic and ferroelectric property based applications in a single device like electric field tuning of magnetic properties which is required for devices. Magnetism in nanocrystalline  $ATiO_3$  (A- Ba, Sr, Pb, etc.) perovskite oxides is very much influenced by Ti density of states at the Fermi level and on the presence of oxygen vacancy. The oxygen defects will change Ti density of states at the Fermi level, and hence oxygen vacancy is the dominant factor in the emergence of magnetism. These compounds have got large magnetic transition temperature, often above room temperature. Without the existence of magnetic element they exhibit magnetic properties and there by becoming multiferroics increasing their scope.

Ferroelectricity in BTO is due to the off centering of  $Ti^{+4}$  ions in the octahedral site. However, the explanation for magnetism in these materials is still evolving, because of its magnetism as it is a  $d^0$  states. Previous reports use the

### *5. Study of origin of magnetism in nc-BTO nanoparticles*

oxygen vacancy to explain the ferromagnetism of BTO [28]. The defect based mechanism is not in agreement with the experimental results [29]. Very few experimental and theoretical studies have considered the charge transfer phenomenon as a means to explore the magnetism in oxide as well as in metal nanoparticles [30, 31].

The oxygen defects will distort the octahedra in perovskite BTO structures. Photoluminescence is the very sensitive and simple measurement technique for the defects. The photoluminescence of disordered BTO or defective BTO nanoparticles is explained by considering the formation of  $[\text{TiO}_6]$  and  $[\text{TiO}_5]$  clusters [16]. This cluster formation will create a charge gradient in it. Thus, this charge gradient causes the transfer to take place from  $[\text{TiO}_5]$  cluster to  $[\text{TiO}_6]$  cluster. The charge transfer also causes the increase in Ti density of states in addition to the other effects.

Here we considered two set of samples:

1. BTO nano particles of four different sizes in the range of 23-54 nm.
2. High temperature processed BTO samples and mesocrystals.

The first set of samples will not show any charge transfer mechanism, whereas the second set of samples show the presence charge transfer in it. The photoluminescence, optical absorption and Magnetic measurements (M vs T & Zero field cooled–ield cooled (FC-FC)) were carried out for the above two set of samples. Set 2 samples shown photoluminescence peak and hence uniformly distributed distorted  $[\text{TiO}_5]$ - $[\text{TiO}_6]$  cluster formation in it and hence the charge transfer. The magnetic measurements also show clear distinction in their magnetic properties. The charge transfer mechanism is thoroughly considered in explaining the observed ferromagnetic ground state in set 2 by considering modified Stoner criterion.

## **5.2 Introduction to Stoner magnetism**

Finding the conditions to exhibit ferromagnetic ground state or finding the type of materials which show ferromagnetic ground state is highly evolved foremost concept in the field of spintronics. The existence of spontaneous magnetization below Curie temperature is the order parameter in studying the ferromagnetic to paramagnetic phase transitions in magnetic materials. As we know below  $T_c$ , the interactions between the spins align the spin in one direction to minimize energy of the system. This spin alignment is the consequence of Pauli principle and Coulomb interaction. The coulomb repulsion energy is thus different opposite spin and parallel spin electrons. It is known that the parallel electron spin state is of lower energy state in ferromagnetic materials and hence the ferromagnetic occurrence in it.

In addition to this several other concepts like the existence of fractional magnetic moment, origin of Weiss field were not well explained by using the existed magnetic theories. To account for these effects Heisenberg paves attention to the problem by considering the electron exchange interactions. His model is suited in explaining the interactions between localized electrons states. As the localization decreased or increase in delocalization Heisenberg model is failed to explain the observed magnetism in metals. Stoner considered the delocalization concept in his theory and successfully explained the observed magnetism in it.

Consider 'N' electrons system in the absence of applied external magnetic field to obtain the Stoner criterion. Due to the exchange correlation interaction the electronic energy correspond to the spin states will be reduced and this is given by eqn.1 & 2 below two spin states up and down

## 5. Study of origin of magnetism in nc-BTO nanoparticles

$$E_{\uparrow}(\vec{k}) = E(\vec{k}) - \frac{In_{\uparrow}}{N} \quad 1$$

$$E_{\downarrow}(\vec{k}) = E(\vec{k}) - \frac{In_{\downarrow}}{N} \quad 2$$

Where  $N = n_{\uparrow} + n_{\downarrow}$

$$\text{Let define } R = \frac{n_{\uparrow} - n_{\downarrow}}{N} \Rightarrow R \propto M \quad 3$$

From eqn. (3) it clear that R is proportional to magnetization, and by using Fermi-Dirac statistics we can write R as follows

$$R = \frac{1}{N} \sum_k f_{\uparrow}(k) - f_{\downarrow}(k) \quad 4$$

So the Stoner criterion for ferromagnetism is given by

$$I D(E_f) \geq 1 \quad 5$$

### 5.3 Magnetic properties of BTO nanoparticles

#### 5.3.1. M-H measurements for BTO nanoparticles

The Field dependent magnetization (M-H) measurements were carried out for four different size of BTO particles at 300 K (Fig.5.1(a)). The coercivity increases from 55 Oe to 70 Oe as the particle size increases from 23 to 34 nm. Further increase in particle size to 54 nm leads to a drastic reduction in coercivity to 28 Oe (Fig.5.1(b)). From Fig.1 the coercivity and remanence decrease for 54 nm size particle, suggests the presence of strong interactions between BTO particles compared to the other three particle sizes [39].

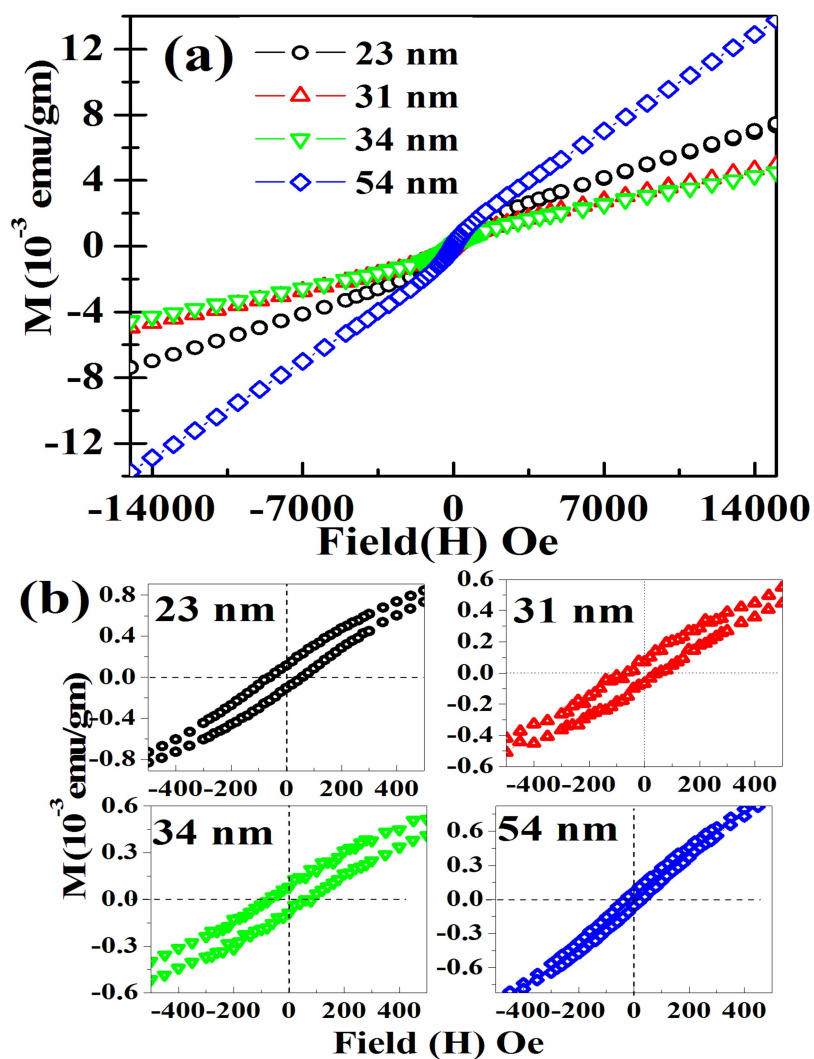


Fig. 5.1(a). M-H curves for particles of different sizes (23 nm- 54 nm) at temperature 300K. and (b) shows the coercivity values.

### 5.3.2. ZFC-FC measurements for BTO nanoparticles

For ZFC (Zero Field Cooled) measurements, the material is cooled to 2K at  $H=0$  Oe, and then the magnetic moment is measured with increasing temperature in the presence of 1 kOe applied field. In FC (Field Cooled) case, the

### 5. Study of origin of magnetism in nc-BTO nanoparticles

sample is cooled to 2K in presence of 1 kOe applied field and then magnetic moment is measured while warming the sample up to 300K in same field.

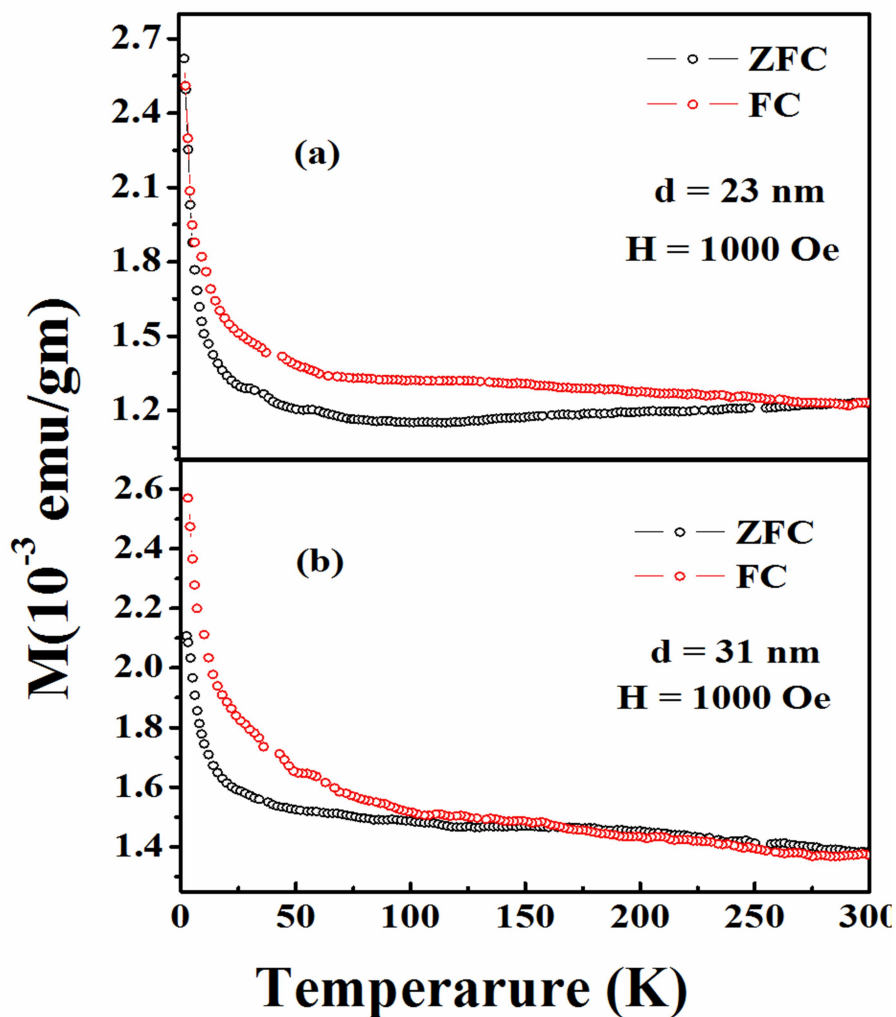


Fig5.2.(a) and (b) ZFC-FC (M vs T) curves for nc-BTO nanoparticles of sizes 23 and 31 nm.

Fig.5. 2 and Fig. 5.3 shows, ZFC- FC curves for nc-BTO nano particles of all four sizes. The particles of sizes  $\sim 23$  nm,  $\sim 34$  nm and  $\sim 54$  nm show higher bifurcation temperature ( $T_b$ ), whereas the  $\sim 31$  nm size particle show lower bifurcation temperature.

### 5. Study of origin of magnetism in nc-BTO nanoparticles

A clear additional peak around 19K is observed for 34 nm size particles, which may be due to the critical temperature for the surface spins alignment along the core spin of the particle [40]

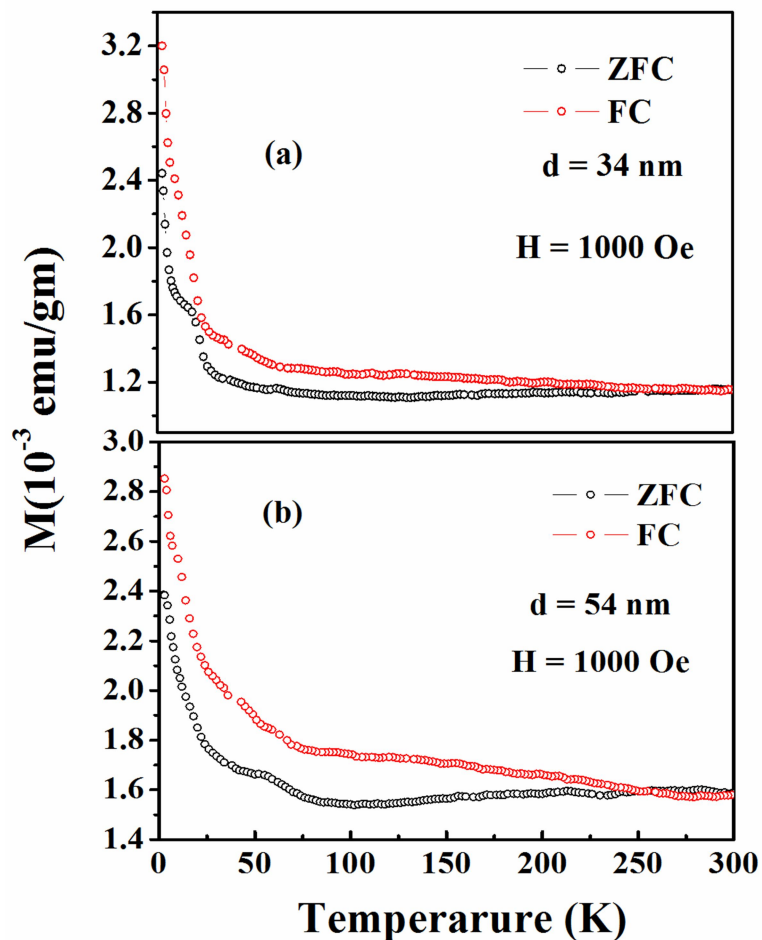


Fig.5.3 (a) and (b) ZFC-FC (M vs T) curves for different sizes (34 nm and 54 nm) of nanoparticles.

The ZFC curve for 23 nm and 54 nm size particles shows a concave like behaviour. After certain temperature, the increase in magnetic moment in these two particles confirms the dominant anti-ferromagnetic interactions compared to other two nano particles (~ 31 and ~34 nm).

### 5.3.3 Variation of magnetic moment with charge carrier density, band gap

The systems considered in this chapter are nano particles, the surface to volume ratio and oxygen defects plays dominant role deciding many properties of it. These changes are evident in band gap of these particles. The band gap variations like band gap narrowing are consequences of many body interactions which involve exchange-correlation interaction in it. These exchange correlation interactions are responsible for their magnetic ground state of the system. Hence in the present section we have focussed to correlate the band gap and charge carriers with observed magnetic properties.

In the refractive index sign change of these kinds of materials, the main factors involved are electronic Kerr effect, optical electrostriction, population redistribution and thermal contribution. Generally thermal heat induced refractive index change will be negative, but the response time will be high in the nanosecond (ns) range. The time scale for the energy to exchange between the electrons is few fs-100 ps and for electron-phonons typically are  $\sim$  ns. In the present studies, we have used ps pulses and since the effects relax at ps time scales, the observed refractive index change is expected to be electronic in origin. Except in the case of  $\sim$ 34 nm size particle (with  $E_g = 3.2$  eV), all other particles displayed small band gap values compared to the band gap of bulk BTO (3.2 eV). But the bleaching of absorption spectrum in 31 and 34 nm particles is due to free carriers induced conduction band filling in them [41].

As summarized in Table 1, the band gap of these particles varied in the range of 2.53 -3.2 eV. The samples with higher band gap narrowing demonstrated enhanced optical absorption. The higher band gap narrowing is due to the exchange-correlation interactions between the carriers. The band gap narrowing and involved mechanisms were discussed in chapter 4. There we have used optical absorption, Raman and Z-scan technique to get the clear understanding of

### 5. Study of origin of magnetism in nc-BTO nanoparticles

mechanisms responsible for the observed band gap values [41]. Since the higher value for N (charge carrier density) is obtained from Z-scan measurements for all particles, in addition the 31 nm particle displaying narrowed band, with negative refractive index ( $n_2$ ) and bleached optical absorption, shows the presence of higher concentrations of charge carriers in these particles [42-45].

Table1. Saturation magnetization, coercivity, charge carrier density and nonlinear coefficients  $\beta$ ,  $n_2$  variation with particle size and band gap.

Calcination Temp. (°C)	Avg. Particle size (D) nm	Band gap ( $E_g$ ) (eV)	$\beta$ $10^{-9}$ (cm/W)	$n_2$ $10^{-13}$ (cm <sup>2</sup> /W)	Charge carrier density (N)/cm <sup>3</sup>	$M_s \times 10^{-3}$ emu/gm) $M_s$ = saturation magnetization	Coercivity ( $H_c$ ) (Oe)
650	23	2.83	0.85 (140 GW/cm <sup>2</sup> )	1	$8.09 \times 10^{19}$	2.2	58
700	31	3.00	0.17 (140 W/cm <sup>2</sup> ) $I_s = 1 \times 10^8$ W/cm <sup>2</sup>	-0.9	$8.17 \times 10^{19}$	1.4	60
750	34	3.20	1.5 (140 GW/cm <sup>2</sup> )	0.9	$9.06 \times 10^{19}$	1.3	68
800	54	2.53	1.2 (140 W/cm <sup>2</sup> ) $I_s = 4 \times 10^8$ W/cm <sup>2</sup>	1	$1.29 \times 10^{20}$	3.2	28

The higher band gap for these particles is expected due to the mixing up of O 2p states in the valence band and Ti 3d states in the conduction band. This hybridization increases the effective mass of electrons in the conduction band and hence there is now effective band narrowing like the other two (23 and 54 nm)

### 5. Study of origin of magnetism in nc-BTO nanoparticles

particle sizes. The magnetic measurements also support these results and will be discussed in the next section (5.4).

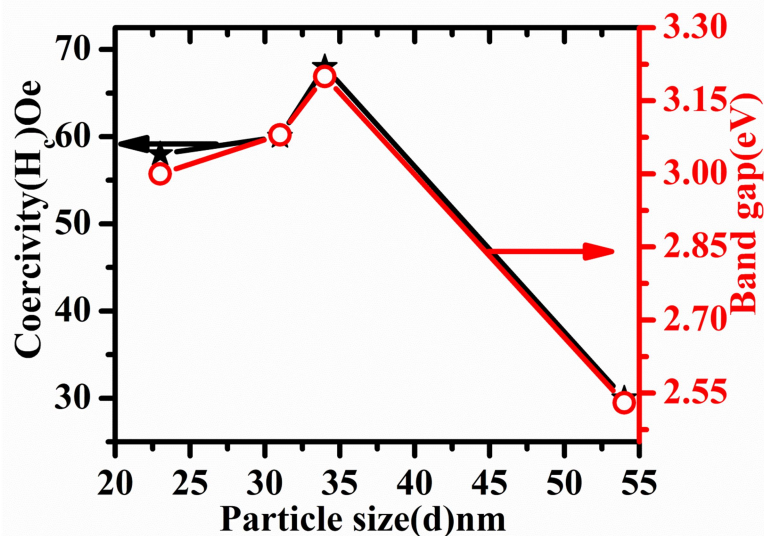


Fig.5.4. Variation of coercivity and band gap with particle size.

The bifurcation temperature ( $T_b$ ) for 31 nm size particle is  $\sim 150$ K. Whereas the particles of sizes  $\sim 23$  nm,  $\sim 34$  nm and  $\sim 54$  nm displayed higher bifurcation temperatures in the range of 250K-270K. Thus, different bifurcation temperatures were observed for four different sizes of particles. It is clear that depending upon the charge carrier density, different interactions occur in these nanomaterials. This indirectly reflected in the varying electron concentration of charge carriers and the presence of different band gaps [46]. As discussed above the  $\sim 54$  nm size particles displayed higher charge carrier density. The mixing up of O 2P and Ti 3d states causes the higher band gap widening in  $\sim 31$  nm and  $\sim 34$  nm size particles [47, 48]. Therefore, we expect that higher concentration of charge carriers provide larger magnetic moment and it is supported by the band gap narrowing due to exchange-correlation interactions between the carriers [49].

## 5.4 Magnetic properties of high temperature annealed BTO

### 5.4.1 M-H measurements

The magnetic measurements show the coercivity (Fig. 5.5) of nc-BTO is 125 Oe and 43 Oe at 5K and 300K respectively. It is expected that grain boundaries are having excess amount of oxygen vacancies (can be ordered oxygen vacancies) and leads to decrease in Ti valence to  $Ti^{+2}$  [50, 51]. At low temperatures, the hopping of electrons between sites reduces and electrons localizes to one Ti site. In addition the exchange correlation induced charge transfer effects can also reduce the Ti valence (lower than  $Ti^{+3}$ ) and behaves as mixed valence system [37, 52]. This  $Ti^{+2}$  ion 3d states will lose the degeneracy in the zero magnetic fields. This energy of splitting in zero fields is denoted as D. Thus  $DS_z^2$  is the single ion anisotropy present in the system ( $S_z$  is the total spin on  $Ti^{+2}$  ion) [53, 54]. This single ion anisotropy of Ti ion could be responsible for the observed coercivity of 125 Oe at low temperature. The non saturating moment at low temperature could be due to the presence of holes in both bands. The observed magnetic moment of  $1.8 \times 10^{-3}$  emu/gm of nc-BTO of size 60 nm is in agreement with the earlier reports [28]. As discussed above, the following results ensure the existence of charge transfer induced states at the Fermi level. It will be also clear that the different state mixing is also playing a dominant role in the ensuing explanation for the magnetism in nc-BTO.

Fig.5.6 shows the ZFC-FC curves for high temperature calcined BTO taken at 8000 Oe applied field. It shows the transition temperature of 56K. Below this temperature, ferromagnetic ground state exists in the system. These measurements are completely different with compared to the low temperature calcined BTO nanoparticle series as discussed earlier. Thus it is highly probable that high temperature calcined samples having more oxygen vacancies and will increase interactions between the carriers to obtain ferromagnetic ground state.

5. Study of origin of magnetism in nc-BTO nanoparticles

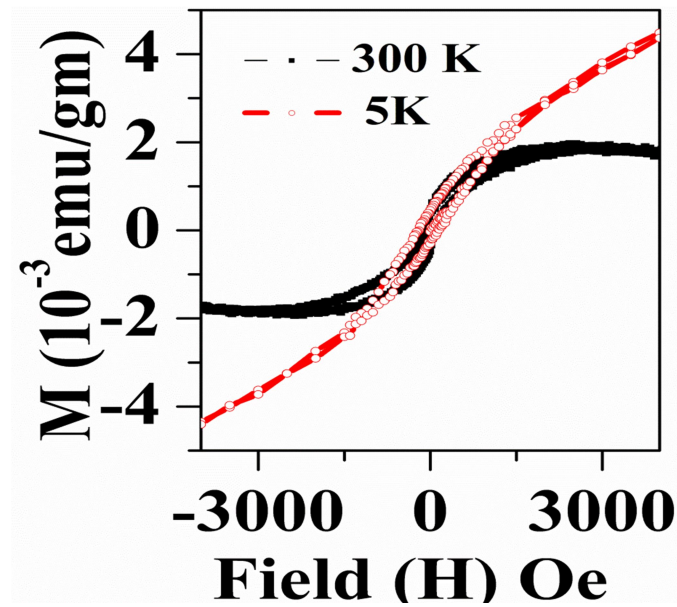


Fig.5.5 M-H curves for high temperature (1000 °C) calcined nc-BTO, at 5K and 300K.

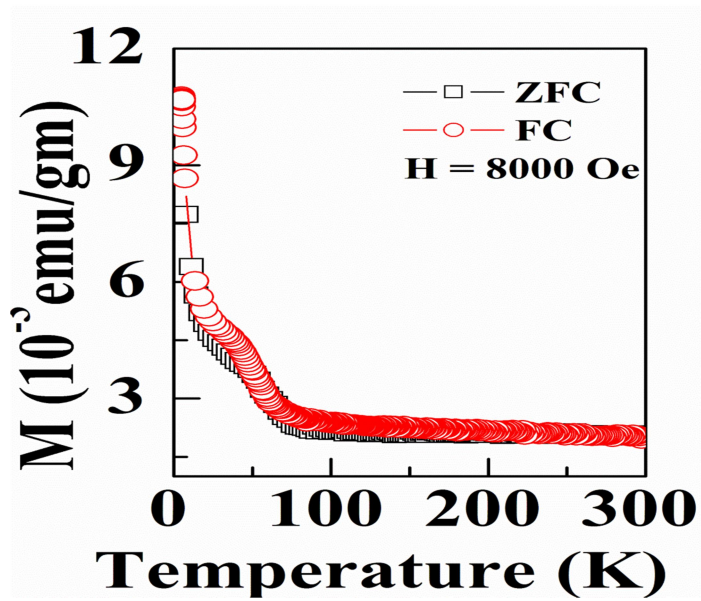


Fig.5.6. ZFC-FC (M vs T) curves for high temperature (1000°C) calcined nc-BTO.

### 5.4.2 Magnetic properties of BTO mesocrystals

To understand the interactions responsible for the occurrence of magnetism in nc-BTO, we have further considered one more system which is intermediate to that of amorphous and crystalline state. The growth mechanism and why it is called at intermediate state is thoroughly discussed in chapter 3. It is found that the transition temperature (Para to Ferro) almost two times to that of conventionally prepared nc-BTO.

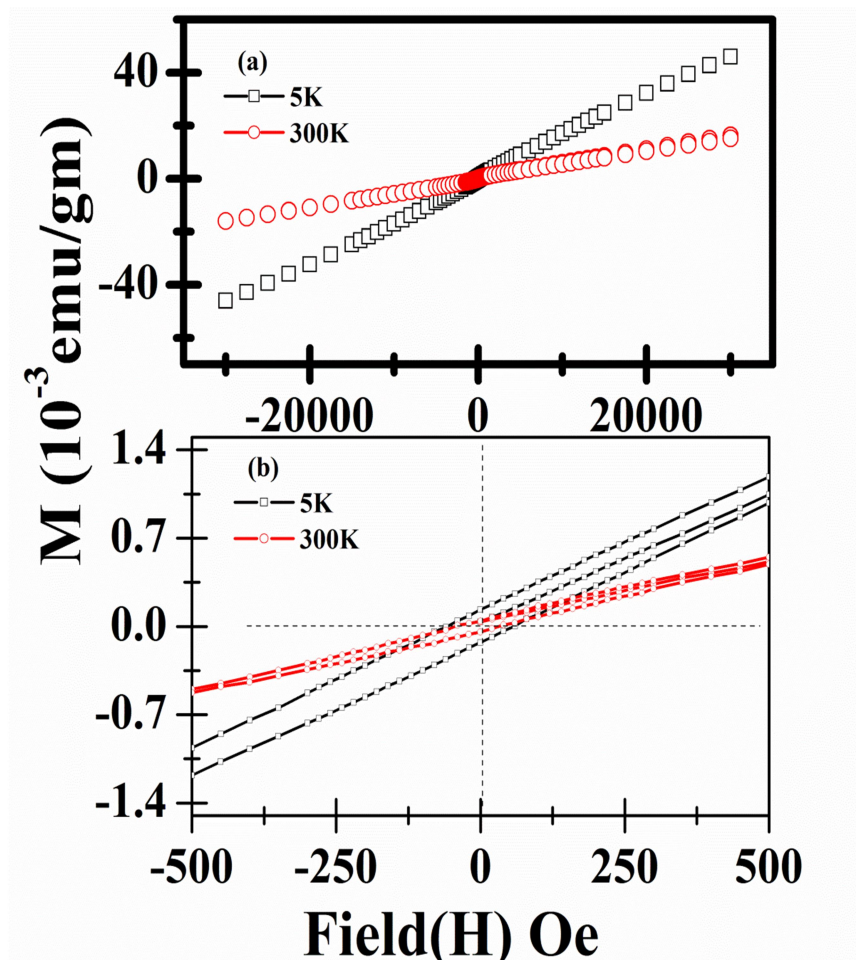


Fig.5.7.(a). M-H loops of BTO mesocrystal at 5K and 300K with  $3T \leq H \leq 3T$  field range. (b) is the enlarged view of (a).

### 5. Study of origin of magnetism in nc-BTO nanoparticles

The magnetic measurements were carried out for BTO mesocrystals (MS-BTO) to find out the magnetic order mechanism responsible for defective BTO. We have considered two types of mesocrystals partially crystalline MS-BTO (PMS-BTO) and crystalline MS-BTO.

The M-H measurements for PMS-BTO were carried out at 5K and 300K temperatures up to max. Field of 3T, it is shown in fig 5.7. The saturation in magnetization is not observed up to 3T applied field and the coercivity is decreased from 57 Oe to 31 Oe as the temperature increased from 5K to 300K. The zero field cooled (ZFC) and field cooled measurements were carried out for the samples at different applied magnetic fields 250 Oe and 1000 Oe. The fig. 5.8 clearly shows the ferromagnetic like ground state existence in above described PMS-BTO. It shows that the below 50K ferromagnetic state existence in the BTO meso crystal samples.

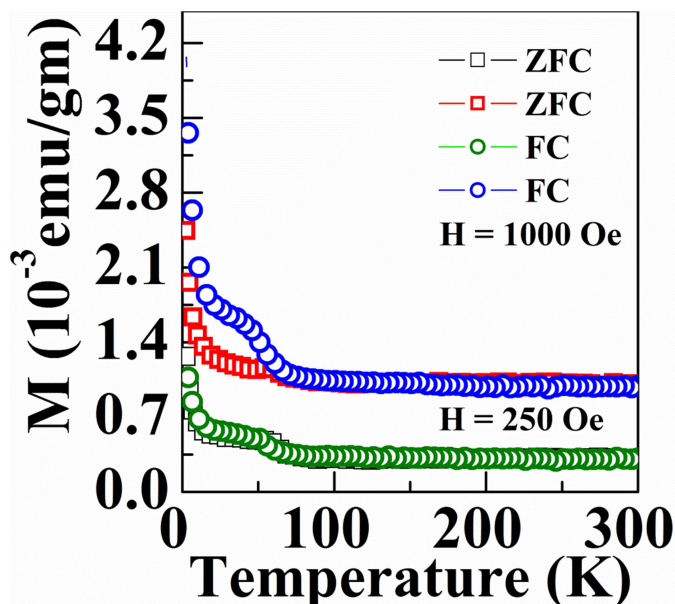


Fig.5.8. ZFC-FC-T curves for PMS-BTO mesocrystal at H=250 Oe and 1000 Oe.

### 5. Study of origin of magnetism in nc-BTO nanoparticles

Fig.5.9 shows the ZFC-FC curves for highly crystalline MS-BTO for two applied magnetic fields namely 500 Oe and 1000 Oe. Here the ferromagnetic transition temperature is increased further to 131K compared to partially crystalline MS-BTO. Thus as described in chapter 3, the mesocrystals are highly oriented single crystalline like material and hence the one can expect the long range ferromagnetic order to exist up to 131K.

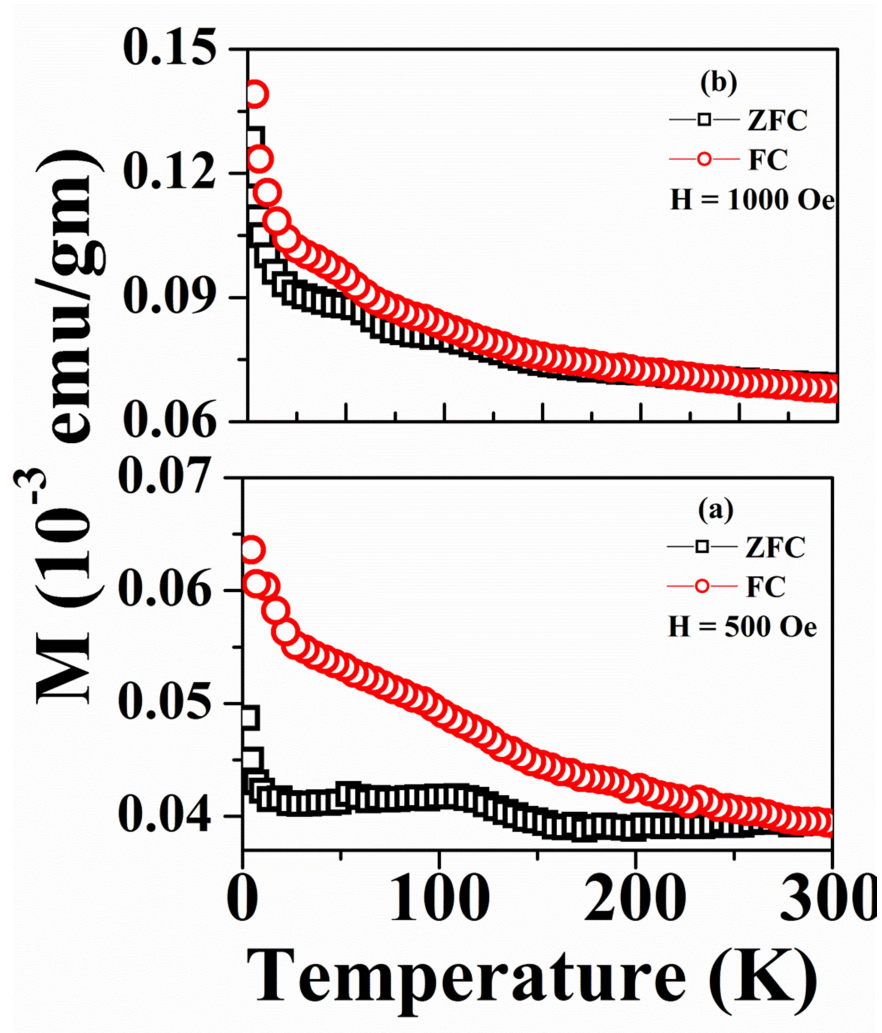


Fig.5.9 ZFC-FC-T curves for MS-BTO mesocrystal at H=500 Oe and 1000 Oe.

### 5.4.3 Charge transfer in BTO

Charge transfer in BTO is primarily due to the oxygen defects. It may be noted that defect formation energy is lower for oxygen compared to Ti and Ba [55]. The oxygen deficient system is equivalent to an electron doped BTO, because each oxygen vacancy creates extra electrons in the system shows higher conductivity [56-58]. This oxygen vacancy distorts the octahedra and forms two asymmetric  $[\text{TiO}_6]$  and  $[\text{TiO}_5]$  clusters [16]. Therefore, the net charges on these two clusters get the higher negative charge on  $[\text{TiO}_5]$  and lower negative charge on  $[\text{TiO}_6]$ . This permanent charge gradient is causing the effective charge transfer towards Ti compared to the charge transfer from oxygen [16, 59].

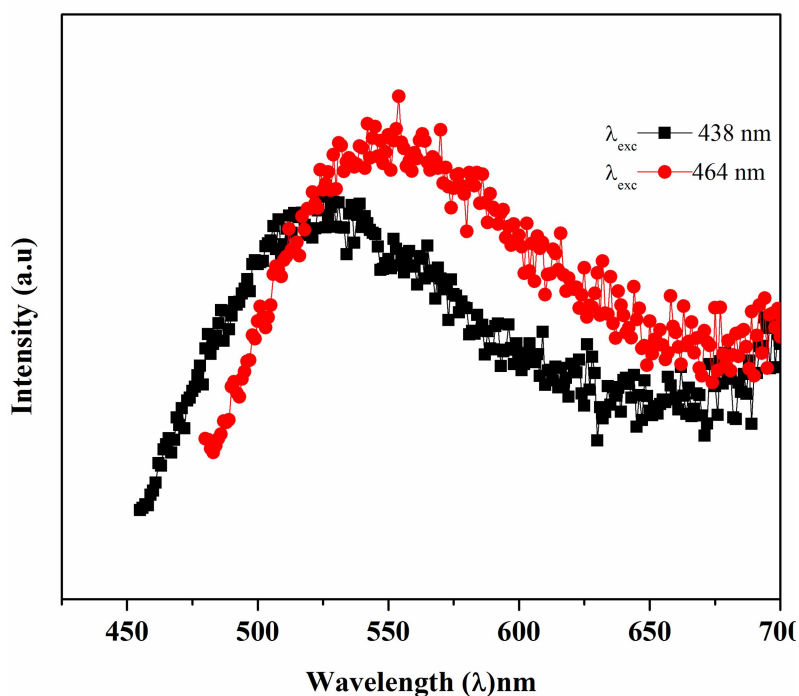


Fig.5.10. Photoluminescence 1000°C sintered BTO pellet at two excitations 438 nm and 464 nm.

The defective BTO shows the photoluminescence (PL) property and it also observed for 1000°C sintered nanocrystalline BTO pellet. The PL is carried

### 5. Study of origin of magnetism in nc-BTO nanoparticles

out at two excitation wavelengths namely 438 nm and 464 nm and it shows the green luminescence [fig.5.10]. It is the indirect evidence for the formation of  $\text{TiO}_5$  and  $\text{TiO}_6$  clusters formation in the material [16].

Thus, the oxygen vacancy gives the localization of electron to Ti site, and from a band, just below the conduction band. The dc conductivity measurement by the impedance analyzer indicates that the nc-BTO is in semiconducting state at ambient temperature. The major conduction in nc-BTO is due to the hopping of non-adiabatic polarons [40]. The  $\sigma T^{3/2}$  vs.  $1/T$  plot gives an activation energy of  $60 \text{ meV} \pm 2 \text{ meV}$  (Fig. 5.11). This polaronic conductivity of nc-BTO hints of a lattice vibration influenced electronic conduction.

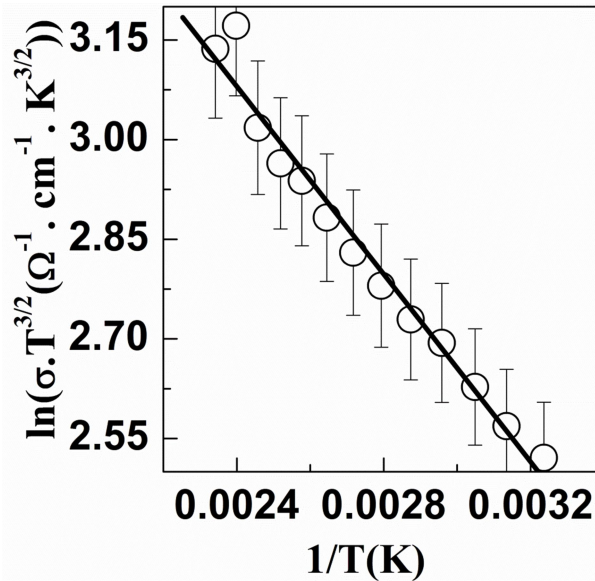


Fig.5.11. Arrhenius plots of small polaron conduction in non-adiabatic region for nc-BTO.

Thus depending on the number of free carriers and size of the nanoparticles, the band narrowing will take place (it is shown in the inset of Fig.5.12 (a)). Fig.5.12 (b), shows undistorted (left) and distorted (right) octahedral band diagrams. This Jahn-Teller like distortion shown in right part of the Fig.5.12 (b) is arising from oxygen vacancy as explained by E. Orhan et al. [16]. The

### 5. Study of origin of magnetism in nc-BTO nanoparticles

surface states of nanoparticles will form a band just below the Ti 3d states and plays a crucial role in the charge transfer towards Ti sites [60]. The occupancy of surface states is determined by their own Fermi level ( $E_{Fs}$ ) which is similar to the quasi Fermi level for trapped electrons in the semiconductor nanoparticles [61, 62]. The state which lies below the conduction level is occupied [63] due to the charge transfer from the asymmetric  $[TiO_5]$  charge gradient involved cluster formation [16]. This causes an increase of density of states for Ti 3d below the conduction band. This type of charge transfer is efficient in nanoparticles due to its size and the presence of oxygen defects and surface states.

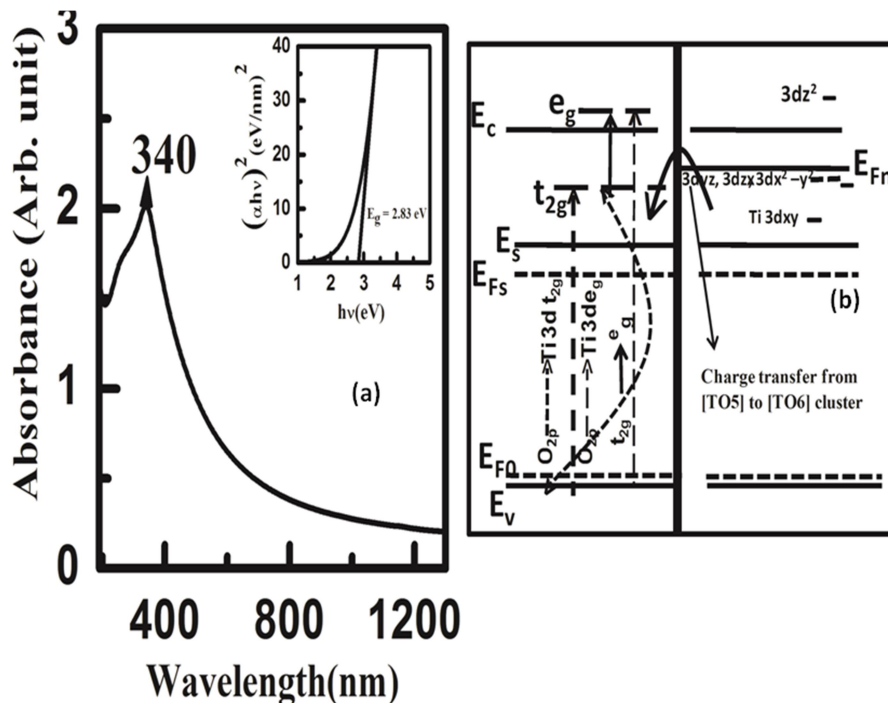


Fig.5.12. (a) UV-VIS-NIR absorption spectrum of nc-BTO nanoparticles.

(b) Schematic diagram of different optical transitions in nc-BTO Nanoparticle,  $E_{Fo}$  = Fermilevel,  $E_{Fs}$  = surface states Fermi level,  $E_{Fn}$  = Fermi level free electrons created in the particle.  $E_v$  = Valence band,  $E_c$  = Conduction band.

### 5. Study of origin of magnetism in nc-BTO nanoparticles

These surface states and deformed octahedra, give additional charge transfer in surface defective oxide nanoparticles in addition to the charge transfer mechanism explained by T. Jarlberg in La doped SrB<sub>6</sub> [37]. Fig.5.12 (a), shows the observed optical absorption spectra of nc-BTO nano particles.

The various types of transitions have been shown schematically in Fig.5.12 (b). Thus, filling of Ti 3d  $t_{2g}$  orbitals is due to the charge transfer effect as discussed above. The mixing of O 2p and Ti 3d orbital is shown by the curved dotted line and charge transfer from distorted to undistorted octahedral is also shown by a curved arrows in fig.5.12 (b). The peak at 340nm (3.64 eV) in Fig.5.12 (a), is the upward transition from O2p (orbital formed  $2\Gamma_{15}$  states) to the partially filled Ti 3d  $t_{2g}$  (Orbital formed  $1\Gamma_{25'}$ ) states. And the shoulder at 264 nm (4.69 eV) is because of charge transfer absorption from O 2P orbital (formed  $2\Gamma_{15}$  state) to the Ti 3d  $e_g$  orbital (formed  $1\Gamma_{12}$  state) in the conduction band. The mixing of O 2p orbital and Ti  $t_{2g}$  orbital due to vibrating states [38] leads to opposite parity for the electronic states. Hence, the nonzero absorption at lower energy around 1154 nm (1.07 eV). This is the transition from Ti 3d  $t_{2g}$  orbital (formed  $1\Gamma_{25'}$  state) to Ti 3d  $e_g$  orbital (formed  $1\Gamma_{12}$ ) states within the Ti 3d states of a conduction band. This is very broad because of high level of vibration state mixing. As we look at the band gap of nc-BTO, it is 2.83 eV (inset in Fig. 5.12 (a).) which is smaller than the band gap of bulk BaTiO<sub>3</sub> crystal. Self-energy and effective mass of polarons are effective in describing the properties of polarons. The polaron self-energy is defined as the difference between the actual polaron energy and energy of the respective uncoupled electrons. In non adiabatic small polaron, the phonon vibration is high compared to electron hopping between the sites. Hence the electron transport occurs for a longer time and modifies the local electron density of states. Thus the polarons will form states just below the conduction band and lowers the conduction band [51, 64-66]. Thus band gap

### 5. Study of origin of magnetism in nc-BTO nanoparticles

shrinkage is also supported by the non-adiabatic small polaron formation in it, and it backs the existence of many-body interactions. The band gap shrinkage also gets influenced by exchange–correlation interactions between the magnetic moments of the conduction band electrons and valence band electrons and also due to many-body effects [67-71]. Hence the relative gain in exchange energy is more than the kinetic energy. As discussed above, the charge transfer effect ensures an increase of Ti density of states. Thus an existence of Fermi level near to defect states, results in additional spin splitting [72]. And it is evidenced by competition between the band filling due to charge transfer (as discussed above) and renormalization effect [73]. The total density of states can be written as  $N = N_{Ti} + N_V$ . Because of non constant partial density of states near  $E_F$ , charge transfer will take place due to exchange splitting ( $\xi$ ) [37, 74] and due to the thermal energy ( $K_B T$ ). Thus, these various kinds of charge transfer effects as discussed above will increase the Ti density of states near the Fermi level in nc-BTO and gives the magnetic behavior as shown in Fig.5.5 & 5.6. This charge transfer effect gives an increase in Coulomb potential energy in addition to exchange energy of free carriers. At the low temperatures (5K), the saturation has not been observed in the field range of 3T. As the temperature increases coercivity decreases from 125 Oe to 43 Oe. Thus, it is showing increment of the ferromagnetic volume fractions by increasing coercivity as lowering the temperature.

The slight decrease in magnetic moment (Fig.5.5) at high temperatures is because of the decrease of effective derivative of bare density of states as the temperature increases (i.e the term  $\int \frac{df}{d\varepsilon} d\varepsilon$  decreases) [37].

### 5.5 Modified Stoner criterion

Here we have discussed the essence of modified Stoner theory in explaining the magnetism in nc-BTO. There have been steady efforts in understanding the  $d^0$  magnetism [32-34]. J M D Coey et al explained the magnetism of oxide nanoparticles by using the charge transfer mechanism [35]. They said that the magnetism in oxide nanoparticles is due to the Fermi level pinning in the local density of states ( $N_s(E)$ ) that leads to a Stoner like split of spin density of states ( $N_s(E)$ ). This mechanism alone will not guarantee a Stoner parameter value greater than 1 to satisfy the Stoner criteria for ferromagnetism.

Hirak Kumar Chandra et al has proven that the magnetism in defective ZnO is a consequence of Stoner's mechanism [36], and the Stoner parameter value lies between 0.2- 0.7, which is not sufficient to satisfy the Stoner criterion. Hence the density of states at the Fermi level has to be corrected for charge transfer also. The charge transfer mechanisms were well explained by T. Jarlborg for La-doped  $SrB_6$  as well as Ce and corrected the Stoner criterion for these cases [37]. He considered La-doped  $SrB_6$  and explained the charge transfer towards La using spin polarized band structure calculations. He found that the correction to stabilization energy is not restricted to exchange energy alone but needs to be extended to potential energy as well. Even this correction is found to be small for Ce [38]. Thus, the modified Stoner criterion is given by T. Jarlborg and can be written for nc-BTO as shown in eqn. (6)

$$\bar{S} = NI_s + \frac{U_0 N'_{Ti} N_V}{N^2} \geq 1 \quad 6$$

Here  $I_s$  is the Stoner exchange integral,  $N'_{Ti}$  is derivative of Ti density of states near the Fermi level,  $N_V$  is rest of the density of states, and N is the total density of states.  $U_0$  Is the potential energy for transferred electron. The additional term in

### *5. Study of origin of magnetism in nc-BTO nanoparticles*

eqn. (6) will ensure that the Stoner criterion could be satisfied in oxide nanomaterials and hence magnetism.

#### **5.6 Summary**

In summary, the magnetic properties of two different set of BTO nanoparticles were carried out. It is observed that the charge carrier density is crucial in understanding the observed magnetism in BTO nanoparticles. The magnetic moment has increased as the band gap of the particles decreased. The particles with average sizes of ~31 nm and ~34 nm did not show marginal band gap narrowing. Thus it can be said that the O 2p and Ti 3d states were mixed to yield a counter renormalization of band gap due to increase of the electron effective mass. Therefore, the increased charge carrier concentration increased the magnetic moment values due to the dominant exchange interactions between the carriers. And, hence, band gap narrowing was observed for higher carrier density. The ZFC-FC measurements show the lower bifurcation temperature ( $T_b$ ) of 150K for 31nm size particles. The ~23 nm, ~34 nm and ~54 nm size particles showed higher bifurcation temperatures in the range of 250K-270K. Thus the higher carrier density samples displayed higher magnetic moment with lower band gap values due to the exchange correlation interactions between the carriers. The variation magnetic moment with particle size gives hint to the presence of super paramagnetic state for low temperature calcined samples.

Whereas, the high temperature calcined samples suppresses this super paramagnetic behaviour and shows a ferromagnetic state with transition temperature of 56K. We also discussed the necessity of involving charge transfer effects in explaining the magnetism in high temperature calcined nc-BTO. Our impedance spectroscopic and optical result helps in understanding the charge transfer in nc-BTO and thus provides hints to the increase of density of states near the Fermi level. The non-adiabatic small polaron conductivity and band gap

### *5. Study of origin of magnetism in nc-BTO nanoparticles*

narrowing shows the presence of many body effects in the system and is helpful in understanding the total energy of the system. In addition the M-H and M-T measurements for partially crystalline and crystalline BTO mesocrystals show the increase of ferromagnetic transition temperature to 131K. This is because due to the dielectric confinement increased electron-electron interactions in the system. Thus the BTO mesocrystals are found to be the most attractive system to study the ferromagnetism in BTO.

## 5. Study of origin of magnetism in nc-BTO nanoparticles

### References

1. R V K Mangalam, N Ray, U V Waghmare, A Sundaresan and C N R Rao, Solid State Commun. **149**, 1 (2009).
2. D Cao, M Q Cai, W Y Hu, P Yu and H T Huang, Phys. Chem. Chem. Phys. **13**, 4738 (2011).
3. T Shimada, Y Uratani and T Kitamura, Appl. Phys. Lett. **100**, 162901 (2012).
4. K Potzger, J Osten, A A Levin, A Shalimov, G Talut, H Reuther, S Arpaci, D Burger, H Schmidt, T Nestler and D C Meyer, J. Magn. Magn. Mater. **323**, 1551 (2011).
5. S. Banerjee, A. Datta, A. Bhaumik and D. Chakravorty, J. Appl. Phys. **110**, 064316 (2011).
6. J M D Coey, P Stamenov, R D Gunning, M Venkatesan, and K Paul, New. J. Phys. **12**, 053025 (2010).
7. P. Zhan, Z. Xie, Z. Li, W. Wang, Z. Zhang, Z. Li, G. Cheng, P. Zhang, B. Wang and X. Cao, Appl. Phys. Lett. **102**, 071914 (2013).
8. P Crespo, R Litran, T C Rojac, M Multigner, J M de la Fuente, J C Sanchez-Lopez, M A Garcia, A Hernando, S Penades, and A Fernandez, Phys. Rev. Lett. **93**, 087204 (2004).
9. S. Zhou, E. Čížmár, K. Potzger, M. Krause, G. Talut, M. Helm, J. Fassbender, S. A. Zvyagin, J. Wosnitza, and H. Schmidt, Phys. Rev. B **79**, 113201 (2009).
10. N H Hong, J Sakai, N Poirot, and V Brizé, Phys. Rev. B **73**, 132404 (2006).
11. S D Yoon, Y Chen, A Yang, T L Goodrich, X Zuo, D A Arena, K Ziemer, C Vittoria and V G Harris, J. Phys.: Condens. Matter **18**, L355 (2006).
12. J M D Coey, Solid State Sci. **7**, 660 (2005).

### *5. Study of origin of magnetism in nc-BTO nanoparticles*

13. A Sundaresan, R Bhargavi, N Rangarajan, U Siddesh and C N R Rao, *Phys. Rev. B* **74**, 161306R (2006).
14. N V Dang, T-L Phan, T D Thanh, V D Lam and L V Hong, *Appl. Phys. Lett.* **111**, 113913 (2012).
15. C Gruber, P O B Velazquez, J Redinger, P Mohn and M Marsman, *E. Phys. Lett.* **97**, 67008 (2012).
16. E Orhan, J A Varela, A Zenatti, M F C Gurgel, F M Pontes, E R Leite, E Longo, P S Pizani, A Beltràn and J Andrès, *Phys. Rev. B* **71**, 085113 (2005).
17. T-K Chung, K. Wong, S. Keller, K. L Wang and G. P Carman, *J. Appl. Phys.* **106**, 103914 (2009).
18. Y. Chen, T. Fitchorov, C. Vittoria and V. G. Harris, *Appl. Phys. Lett.* **97**, 052502 (2010).
19. D. I. Khomskii, *J. Magn. Magn. Mater.* **306**, 1 (2006).
20. T. Tsurumi, T. Hoshina, H. Takeda, Y. Mizuno and H. Chazono, *Ultrasonics, Ferroelectrics and Frequency Control, IEEE Transactions on* **56**, 1513 (2009).
21. Y. Okino, H. Shizuno, S. Kusumi and H. Kishi, *J. J. Appl. Phys.* **33**, 5393 (2004).
22. K. J. Choi et al, *Science* **306**, 1005 (2004).
23. Z. Bi H Aga and S.R. Ramanan, *J. Electroceram.* **28**, 109 (2012).
24. Z. Tang, Z. Zhou and Z. Zhang, *Sens. Actuators B* **93**, 391 (2003).
25. G. Vasta, T. J. Jackson and E. Tarte, *Thin Solid Films* **520**, 3071 (2012).
26. P. Tang, D. Towner, T. Hamano, A. Meier and B. Wessels, *Opt. Express* **12**, 5962 (2004).
27. S. Bahsine, A. Maillard, G. Kugel, and A. Tirbiyine M. *J. Condensed matter* **11**, 18 (2009).

### 5. Study of origin of magnetism in nc-BTO nanoparticles

28. R. V. K. Mangalam, N. Ray, U. V. Waghmare, A. Sundaresan and C. N. R Rao *Solid State Commun.* 149, 1 (2009).
29. D. Cao, M. Q. Cai, W. Y. Hu, P. Yu and H. T. Huang, *Phys. Chem. Chem. Phys.* 13, 4738 (2011).
30. P. Crespo et al, *Phys. Rev. Lett.* 93, 087204 (2004).
31. Z. Vager and R. Naaman, *Phys. Rev. Lett.* 92, 087205 (2004).
32. S. J. Chen, K. Suzuki and J. S. Garitaonandia, *Appl. Phys. Lett.* 95, 172507 (2009).
33. L. S. Dorneles, M. Venkatesan, M. Moliner, J. G. Lunney and J. M. D. Coey, *Appl. Phys. Lett.* 85, 6377 (2004).
34. Y. L. Zheng, C. M. Zhen, X. Q. Wang, L. Ma, X. L. Li and D. L. Hou, *Solid State Sci.* 13, 1516 (2011).
35. J. M. D. Coey, W. Kwanruthai, J. Alaria and M. Venkatesan, *J. Phys. D: Appl. Phys.* 41, 134012 (2008).
36. H. K. Chandra and P. Mahadevan, *Solid State Commun.* 152, 762 (2012).
37. T. Jarlborg, *Phys. Rev. Lett.* 85, 186 (2000).
38. T. Jarlborg, *Phys. Rev. B* 58, 9599 (1998).
39. C Phadnis, D Y. Inamdar, I Dubenko, A Pathak, N Ali and S Mahamuni, *J. Appl. Phys.* **110**, 114316 (2011).
40. T Ghoshal, T Maity, R Senthamaraiakannan, M T. Shaw, P Carolan, Justin D. Holmes, S Roy and M A. Morris, *Sci. Reports* **3**, 2772 (2013).
41. S Ramakanth and K C James Raju, *J. Appl. Phys.* **115**, 173507 (2014).
42. B R Bennett, R A Soref, J A D Alamo, *IEEE J. Quantum. Elect.* **26**, 113 (1990).
43. J G M Alvarez, F D Nunes and N B Patel, *J. Appl. Phys.* **51**, 4365 (1980).
44. W Wang, L Qu, G Yang, Z Chen, *Appl. Surf. Sci.* **218**, 24 (2003).
45. L Irimpan, A. Deepthy, B Krishnan, L.M. Kukreja, V.P.N. Nampoori, P. Radhakrishnan, *Opt. Commun.* **281**, 2938 (2008).

### 5. Study of origin of magnetism in nc-BTO nanoparticles

46. W Qin, X Li, Yi Xie, and Z Zhang, *Phys. Rev. B* **90**, 224416 (2014).
47. Y. H. Matsuda, T. Ikaida, N. Miura, S. Kuroda, F. Takano, and K. Takita, *Phys. Rev. B* **65**, 115202 (2002).
48. P M Hui, H Ehrenreich and K C Hass, *Phys. Rev. B* **40**, 12346 (1989).
49. Y Zhang and S. Das Sarma, *Phys. Rev. B* **72**, 125303 (2005).
50. R.F. Klie, Y. Ito, S. Stemmer, N.D. Browning, *Ultramicroscopy* **86**, 289 (2001).
51. S. E. Thomas Wolfram, *Electronic and optical properties of d-band perovskites*, Newyork Cambridge University Press (2006) pp. 221-222.
52. A. Koehl, D. Kajewski, J. Kubacki, C. Lenser, R. Dittmann, P. Meuffels, K. Szot, R. Waser and J. Szade, *Phys. Chem. Chem. Phys.* **15**, 8311 (2013).
53. B. Loukya, D.S.Negi, K.Dileep, N.Kumar, JayGhatak and R.Datta *J. Magn. Mater.* **345**, 159 (2013).
54. P. Sati, et.al. *Phys. Rev. Lett.* **96**, 017203 (2006).
55. D. Cao, M. Q. Cai, Y. Zheng and W. Y. Hu, *Phys. Chem. Chem. Phys.* **11**, 10934 (2009).
56. T. Kolodiazhnyi, *Phys. Rev. B* **78**, 045107 (2008).
57. T. Kolodiazhnyi, M. Tachibana, H. Kawaji, J. Hwang and M. E. Takayama, *Phys. Rev. Lett.* **104**, 147602 (2010).
58. I. K. Jeong, S. Lee, S-Y Jeong, C. J. Won, N. Hur and A. Liobet, *Phys. Rev. B* **84**, 064125 (2011).
59. S. G. Lu, Z. K. Xu, H. Chen, C. L. Mak, K. H. Wong, K. F. Li and K. W. Cheah, *J. Appl. Phys.* **99**, 064103 (2006).
60. J. Chung and L. Rabenberg, *J. Mater. Res.* **21**, 1215 (2006).
61. I. Mora-Seró and J. Bisquert, *Nano Lett.* **3**, 945 (2003).
62. J. G. Simmons and G. W. Taylor, *Phys. Rev. B* **4**, 502 (1971).

### *5. Study of origin of magnetism in nc-BTO nanoparticles*

63. M-Q Cai, Z. Yin, M. Zhang and X. Sheng, Appl. Phys. Lett. 83, 2805 (2003).
64. K. F. Berggren and B. E. Sernelius, Phys. Rev. B 24, 1971 (1981).
65. S. D. Sarma and M. Stopa, Phys. Rev. B 36, 9595 (1987).
66. A. Korkin, E. Gusev, J. K. Labanowski, and S. Luryi “Nanotechnology for Electronic Materials and Devices” Springer 323-326 (2010).
67. C. Bulutay, C. M. Turgut and N. A. Zakhleniuk, Phys. Rev. B 81, 155206 (2010).
68. M. Yoshikawa, M. Kunzer, J. Wagner, H. Obloh, P. Schlotter, R. Schmidt, N. Herres, and U. Kaufmann, J. Appl. Phys. 86, 4400 (1999).
69. Y. K. Lakshmi, K. Srinivas, B. Sreedhar, M. M. Raja, M. Vithal and P. V. Reddy, Mater. Chem. Phys. 113, 749 (2009).
70. J. G. Lu et al, J. Appl. Phys. 101, 083705 (2007).
71. U. Lindefelt, J. Appl. Phys. 84, 2628 (1998).
72. V. Dwivedi and A. Taraphder, Solid State Comm. 151, 1999 (2011).
73. X. H. Zhou, Q. H. Hu and Y. Fu, J. Appl. Phys. 104, 063703 (2008).
74. Y. Gohda and A. Oshiyama, J. Phys. Soc. Jpn. 79 083705 (2010).

## Chapter 6

# Laser induced crystallization of BaTiO<sub>3</sub> thin films

---

### Abstract

The crystallization of complex oxides at low temperature is a highly challenging task because of its high crystallization temperature and hence the difficulty in making them compatible with silicon based integrated devices. Therefore making functional crystalline materials at room temperature is highly necessary. Here we have found a new way, which is completely different from the usual methods like metal induced crystallization or sonochemical synthesis etc. In the present work we have crystallized the ferroelectric Barium titanate thin films at room temperature through annealing by Excimer laser of 248 nm wavelength. The complete mechanism for the crystallization of these materials is under investigation. As the laser pulse incidents on the material, the temperature may have slowly increased due to the inertial confinement of the laser pulse or due to laser supported shock wave formation. The amorphous state of the material will also have short range atomic order in it. This short range order might have increased further through lattice mending process to form crystalline material.



## **6. Laser induced crystallization of BaTiO<sub>3</sub> thin films**

### **6.1 Introduction**

The conventional experiments to decrease the crystallization temperature are metal induced crystallization, rapid thermal annealing, addition of fluxes, sonochemical synthesis etc. Metal induced crystallization is popular in reducing the crystallization of semiconductors. Fluxes are used in bulk materials. In thin films the residual flux can create problems, especially in a device fabrication process. These methods are not successful in decreasing the crystallization temperatures to a great extent. A higher degree of crystallization at lower temperatures is known to be achievable by use of lasers of appropriate wavelength and pulse width. These laser based crystallization methods are considered as most suitable and flexible to do the crystallization for a required region of a device without damaging the other parts. In order to achieve crystalline ferroelectric films it is necessary to consider the ultraviolet wavelength laser because its energy is of the order of band gap and its non-thermal primary mode of interaction with matter. It is straight forward to assume that annealing the samples by infrared wavelength laser can lead to efficient crystallization in isolated regions without increasing the average temperature of the device substrate. Barium titanate (BTO), Barium strontium titanate (BST) and SrBi<sub>4</sub>Ti<sub>4</sub>O<sub>15</sub> (SBTi) are three materials that are being considered as prototype materials for insertion into devices. First two are already being used in multilayer capacitors, DRAM, tunable microwave devices and for various applications in MEMS and nonlinear optical devices. Hence, in this Chapter our main objective is to study the effect of laser radiation at different energy in crystallizing the thin films of these compositions and to study the temperature rise resulting from this process at various wavelengths so that the right process for device fabrication can be identified.

## 6. Laser induced crystallization of BaTiO<sub>3</sub> thin films

The miniaturization of electronic devices is successful for a long time. Whereas, it became difficult to develop these devices on flexible substrates to make them included in everyday life [1, 2]. To understand the functionality of many proteins and some chemicals it is important to study their atomic structure. Hence, the crystallization of these compounds in biology and chemistry is also highly an evolved field. The laser induced crystallization is found very effective in crystallization of these compounds [3, 4].

Phase transitions in condensed matter are governed by some kind of symmetry breaking [5-8]. Hence the topic of laser induced crystallization requires an examination of such details.

### 6.1.1 Nano second laser matter interaction

For ultrashort pulses ( $\leq 10^{-12}$  s) the heating is isochoric where as it is nonisochoric for longer pulses ( $\geq 10^{-11}$  s) [9]. The ns laser target ablation will produce 1-100 nm range of heat affected zone and it is very small for ultrashort laser pulses. This is due to the short thermal diffusion for ultrashort lasers [10].

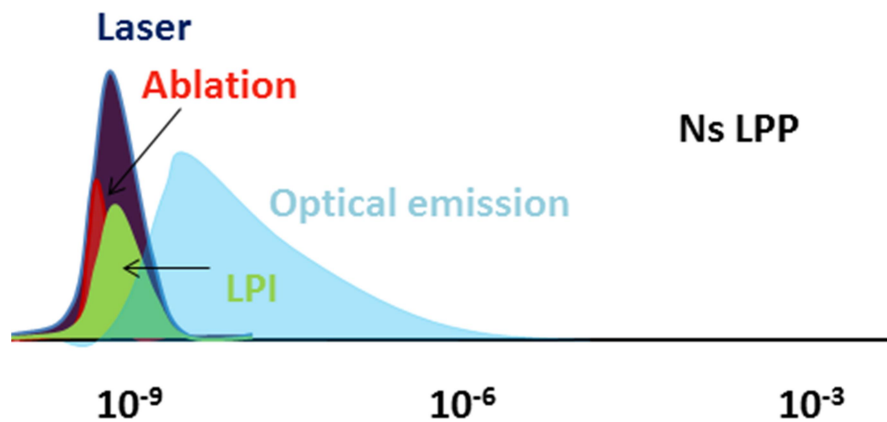


Fig.6.1. An approximate schematic of ns Excimer laser target interaction representing different interaction as the pulse is incident [11, 12]. Laser produced plasma (LPP) and laser plasma interaction (LPI) regions are shown in figure.

In ns laser interaction, part of the pulse produces plasma in the initial process and later part of the pulse interact with this plasma whereas in ultrashort

## 6. Laser induced crystallization of BaTiO<sub>3</sub> thin films

pulse interaction case, this is not the case and all the energy is deposited at once [11, 12]. Most of the dielectrics have the band gap in the range of 5-7eV. In particular the band gap of BaTiO<sub>3</sub> is 3.20 eV. The energy corresponding to 248 nm wavelength is 5 eV above bandgap of BaTiO<sub>3</sub>. Hence most of the energy will get absorbed as the Excimer laser pulse is incident on the film.

### 6.2 Experimental results

#### 6.2.1 BaTiO<sub>3</sub> film deposition by pulsed laser deposition

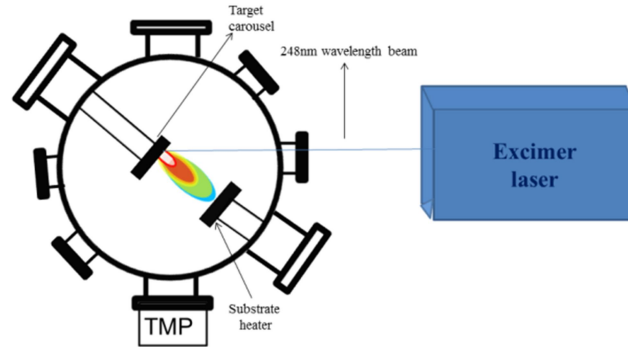


Fig.6.2. Schematic pulsed laser deposition (PLD) setup.

The films were deposited by pulsed laser deposition (PLD) technique. The Excimer laser of wavelength 248 nm is used for target ablation. The distance between target and substrate is maintained at 5cm. The film deposition is carried out at room temperature. The various film deposition conditions are summarized in table 1 below.

Table 1. The deposition conditions of films.

S. No	Sample code	Deposition			Rep. Rate	Working Pressure (mbar)
		Energy density (J/cm <sup>2</sup> )	Deposition counts			
1	RBC1	3.10	9000	5	7X10 <sup>-2</sup>	
2	RBC2	3.10	9000	5	5X10 <sup>-2</sup>	
3	RBC3	3.10	9000	5	2X10 <sup>-2</sup>	

## 6. Laser induced crystallization of BaTiO<sub>3</sub> thin films

### 6.2.2 Laser annealing of PLD deposited films

The above deposited films were annealed by Excimer laser of wavelength 248 nm at different pulse energy. At first the annealing process is carried out at room temperature by varying the pulse energy for a constant number of shots for the three different pressure deposited films. The structure is studied for this by XRD and is given in fig.6.4. In the second set we increased the shots to 300 for 160 laser energy and is named as RBC1-2, RBC2-2 and RBC3-2, whereas the 120 mJ and 250 shots annealed samples are named as RBC1-1, RBC2-1 and RBC3-1.

The table 2 shows the naming and the annealing conditions of this. The laser spot of  $1 \times 2 \text{ cm}^2$  size is used for annealing. The energy and the corresponding energy density or fluence is also given in the table 2.

Table 2: Film naming and annealing conditions.

S. No	Sample code	Incident Energy (mJ)	Abs. Energy Density $F_{\text{abs}}(\text{mJ}/\text{cm}^2)$	Counts	Rep. rate
1	RBC1-1	120	54	250	5
2	RBC1-2	160	72	300	5
3	RBC2-1	120	54	250	5
4	RBC2-2	160	72	300	5
5	RBC3-1	120	54	250	5
6	RBC3-2	160	72	300	5

### 6.3 Laser induced crystallization mechanism

When the light is incident on the materials, depending on the nature of the material (metal or insulator) absorption, transmission and reflection will take place. Their relative magnitude will depend on the property of the material. The absorbed part of energy will cause the heating of material. In materials with a band gap, as the photon is incident on it, the creation of electron-hole with some kinetic energy will take place. After some time these carriers equilibrate their energy between them and this state is plasma. Now this excess energy will be

## *6. Laser induced crystallization of BaTiO<sub>3</sub> thin films*

transferred to lattice through electron-phonon coupling or recombination and phonon generation. Due to this the lattice gets heated up or melts if the energy is high enough.

The materials also have intensity dependent absorption property. The pressure exerted by the electromagnetic wave depends on the intensity of wave. Laser pulses will have enormous intensity compared normal radiation, thus the pressure exerted by lasers will be very high. Depending on the intensity of laser, material's heating is overtaken or dominated by the processes in respective plasma. If the intensity is high, the collision less plasma processes dominates and if it is low the collisional plasma processes will dominate. The energy absorption process creates temperature and pressure gradient in the plasma state of matter, and this pressure gradient drive the mass motion. This plasma motions is similar to that of fluid motion and the conservation of mass, momentum and energy can be applied to characterize the plasma.

As the collisional plasma has the compressibility, the mass movement or motion causes the generation of acoustic waves. Within fraction of time the acoustic waves get piledup as the temperature increases and forms shock waves. This shock wave has the large possibility to alter the state of material through which it passes. Measurements of the velocity or pressure of this shock wave is the major task to get information about the laser matter interaction and its type. The relation between incident laser intensity and shock wave pressure is well known for longer wavelength lasers, but very few reports discusses the short wavelength laser intensity and shock pressure relation. The absorption in the collision less plasma region is higher for short wavelength lasers compared to long wavelength lasers. Hence, the short wavelength lasers are suitable to create higher pressures. The 1D plasma models gives the relation between absorbed laser

## 6. Laser induced crystallization of BaTiO<sub>3</sub> thin films

energy and induced pressure for longer and shorter wavelength lasers as follows [13].

$$P = 1.2I_{\text{abs}}^{2/3} \text{ for } \lambda = 1.06 \text{ } \mu\text{m} \quad 1$$

$$P = 1.5I_{\text{abs}}^{3/4} \text{ for } \lambda = 0.26 \text{ } \mu\text{m} \quad 2$$

Where, the units for P and  $I_{\text{abs}}$  are TPa and  $10^{14}$  W/cm<sup>2</sup> respectively [13].

Above two relations indicate that the pressure is increased with laser intensity and decreases with increase in wavelength. Depending on the intensity, strong ( $\geq 10^{14}$  W/cm<sup>2</sup>), weak ( $\approx 10^{13}$  W/cm<sup>2</sup>) and very weak ( $\leq 10^{10}$  W/cm<sup>2</sup>) are the calculated pressure values by eqn. (2) and are in agreement with the earlier reports [14].

To study the phase transitions whether it is solid - liquid or solid - solid the high pressure or high intensity based studies give the values for thermodynamic quantities by solving the fluid dynamic conservation equations. If the same equations are applied to low intensity laser pulses induced plasma, one will end up with very low shock pressure and temperature values. This low intensity generated shocks are called weak shocks. This weak shock induced amorphous to crystalline phase transition is of current interest.

One of the methods to work at lower intensities while still maintaining thermodynamic quantities equivalent to that of high intensity laser matter interaction is by confining the ablation. In the lower intensity case the pulse duration and spot size will be very large, this leads to the penetration of laser pulse to longer depths in the film or material. In this process the shock wave propagates at subsonic velocity and this is called the laser supported combustion wave. If the laser intensity increases further, absorption will take place and shock travels with supersonic speed.

There exist, different possible arrangement of atoms with particular symmetry within the solid state. This lattice phase changes as a function of

## ***6. Laser induced crystallization of BaTiO<sub>3</sub> thin films***

thermodynamic variables like pressure, temperature and volume. For a laser matter interaction with longer pulse, the study of time dependent dynamics of atoms is highly informative. With time, the material can go from one solid phase to another solid phase. So, the computational method which accounts for the material behavior with time, are highly needed in order to understand the dynamics of atoms in lattice formation point of view.

The dielectric breakdown strength of a material can change with its purity. The important one is the dislocation or defects or void formation in the material that can alter the intensity of threshold break down. In the weak shock generation, these imperfections play a vital role. The weak shock doesn't lead to the melting or vaporization of the material. Since few materials will not be compressible, these kinds of materials require large pressures to melt. Hence the pressures of a few Mbar order also will some time be called as weak shock pressures. Thus it is possible that the weak shocks can change material from one solid phase to other solid phase without melting or vaporization. The thermal shock pressure will be high for such weak shocks.

### **6.4 Results and discussions**

#### **6.4.1 Microstructural studies by FESEM**

The microstructural studies were carried out by FESEM for the above three different pressure deposited films. To understand the laser pulse effects on microstructure the films were annealed for 1, 5, 10 and 300 shots and it is shown in fig.6.3.

## 6. Laser induced crystallization of BaTiO<sub>3</sub> thin films

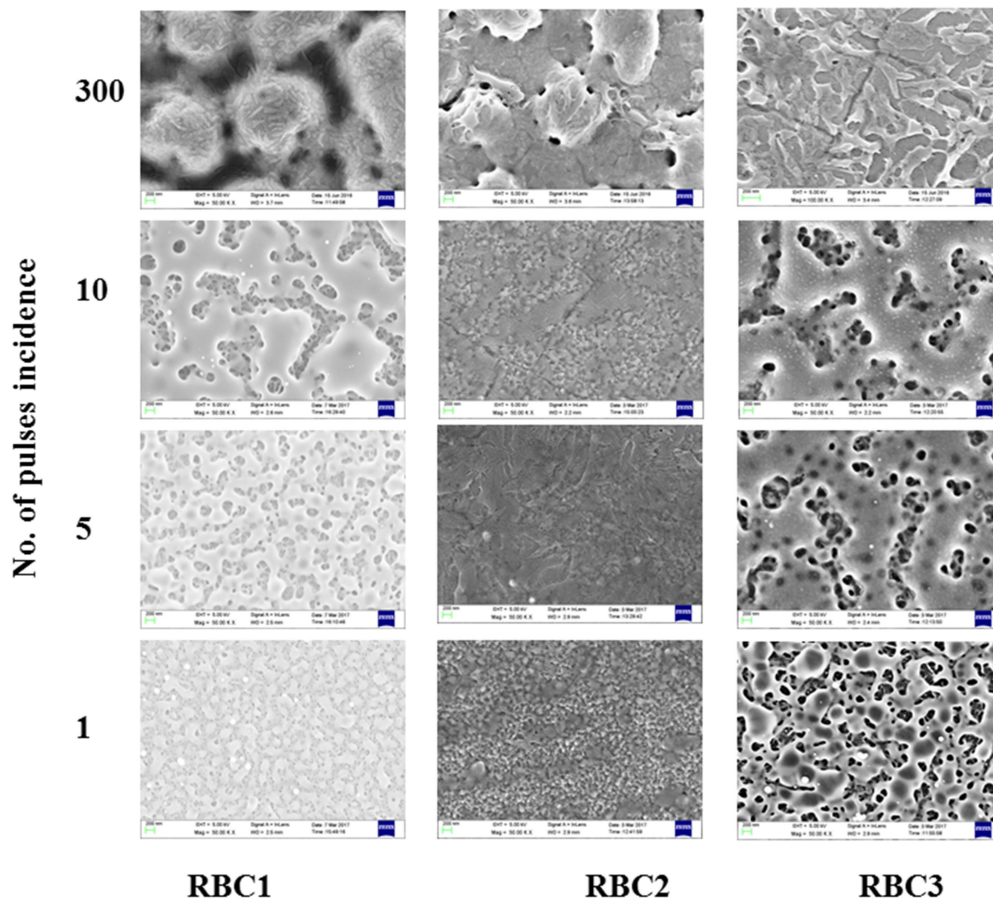


Fig.6.3. FESEM Images of RBC1, RBC2 and RBC3 films annealed at laser energy density  $74 \text{ mJ/cm}^2$ . The number of shots varied between 1-300. It is showed in the increasing order from bottom to top.

The noticeable microstructure changes were observed for films that were deposited at three different pressures but annealed with same number of shots. From the fig.6.3 It is clear that for 10 shots the microstructure for RBC1 and RBC3 film is similar. As the shots increased to 300 the morphology growth is diverse for each film. The films annealed with lower number of shots do not show any XRD pattern.

## 6.4.2 X-ray diffraction studies

After getting confirmed that the microstructure is getting changed even for one shot and it is different for different deposition pressure, the interest grew to see the effect of multiple number of shots. As the films annealed with lower number of shots do not show any phase formation, the number of laser shots were increased to 250. The below fig.6.4 shows the XRD patterns of films annealed at three different energies namely 120, 140 and 160 mJ and number of laser shots are kept constant at 250. The films annealed with few no. of shots do not show any characteristic peaks and hence are not shown here. We further increased the shots to 300 and it is found that the XRD pattern of RBC3 film (fig.6.5) shows more characteristic peaks.

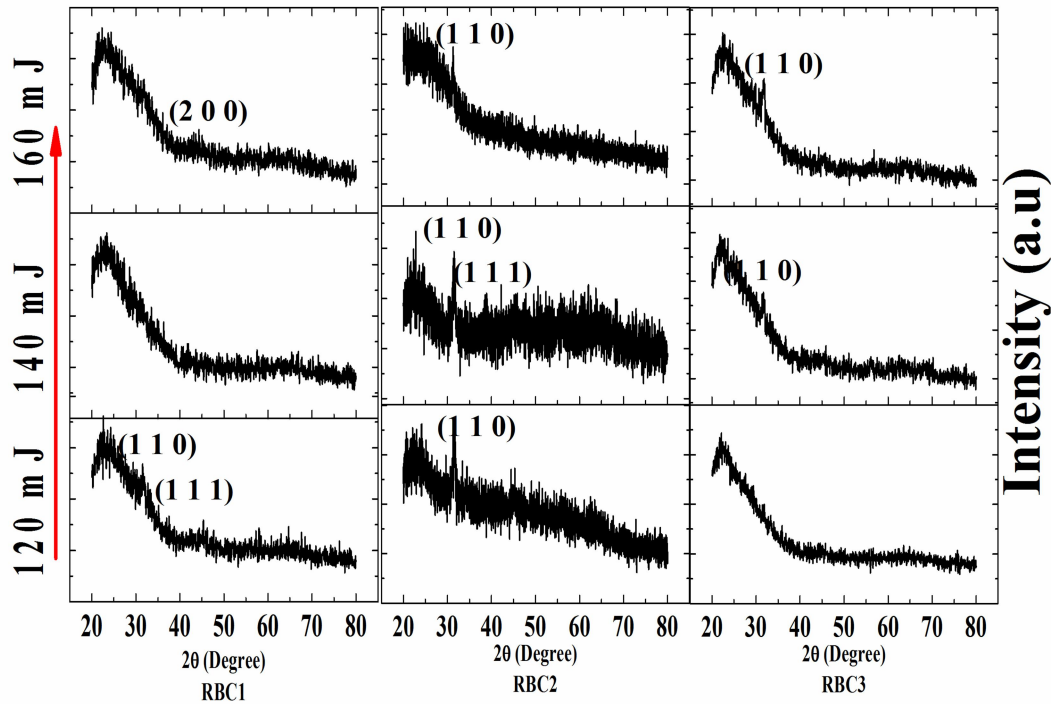


Fig.6.4. XRD diffraction patterns of RBC1, RBC2 and RBC3 films annealed at RT for three different laser energies namely 120, 140 and 160 mJ for 250 shots.

6. Laser induced crystallization of BaTiO<sub>3</sub> thin films

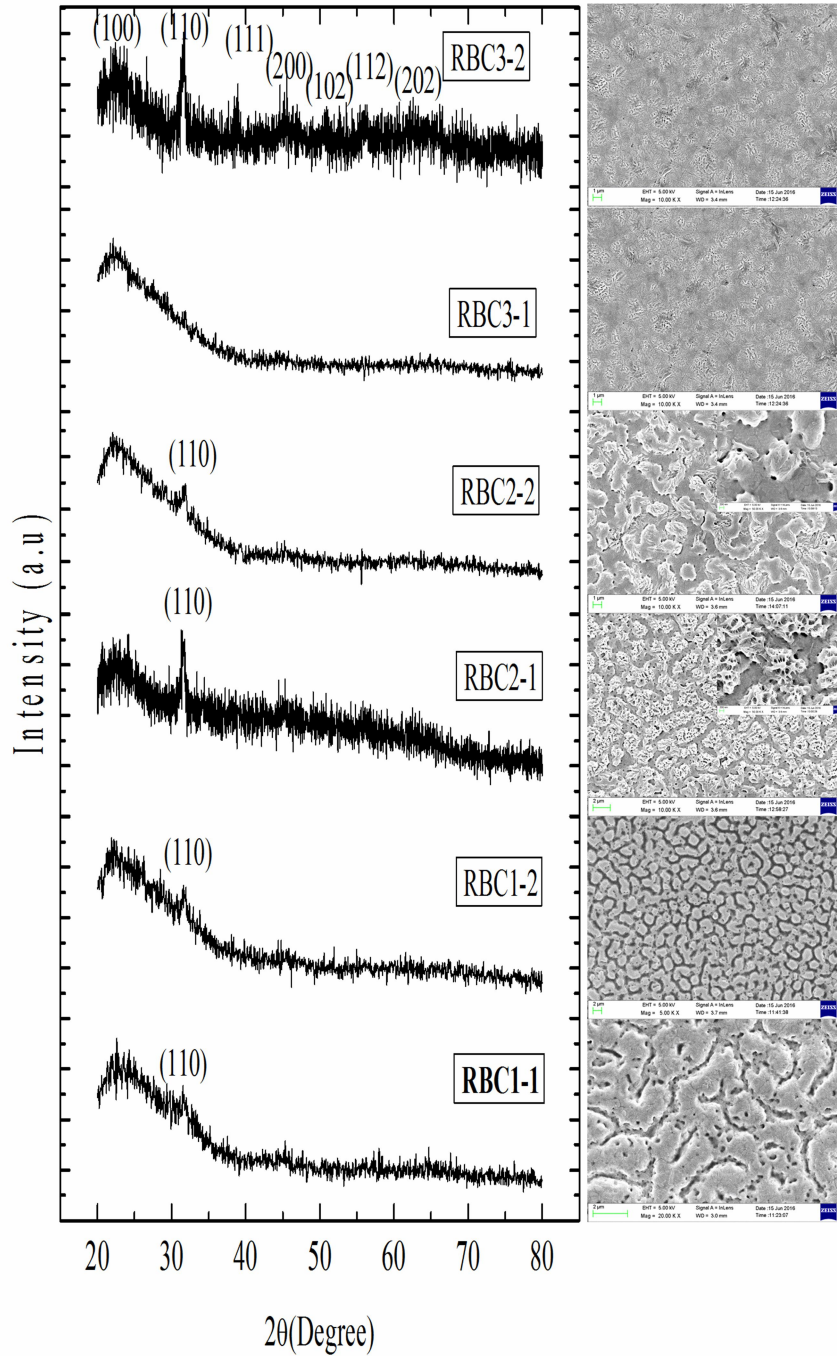


Fig.6.5. (Left) XRD patterns of RBC1, RBC2 and RBC3 films annealed at 250 shots and 300 shots for 120 mJ and 160 mJ energies respectively. (Right) microstructure of respective films

## 6. Laser induced crystallization of BaTiO<sub>3</sub> thin films

Here in this section we have shown the XRD patterns of films deposited at three different pressures and annealed at two different energies and two different no. of shots namely 250 and 300. As the no. of shots increased from 250 to 300, the films deposited at  $2 \times 10^{-2}$  mbar showed good XRD pattern with characteristic peaks of BaTiO<sub>3</sub> phase. The results of 300 shots annealed films are shown in fig.6.5 in comparison with the 250 shot annealed films at two energies namely 120 and 160 mJ. As the no. of shots increased to 300, there is no improvement in the XRD pattern of RBC2 film. That is, for higher counts the film again showing transition towards amorphous state. Hence, we chose the RBC3 film deposition conditions to study the mechanism of phase formation in it.

### 6.4.3 Raman studies

The Raman spectrum of films annealed at 120 and 160 mJ is shown in fig.6.6. Both the films showed the characteristic spectrum of BaTiO<sub>3</sub> phase.

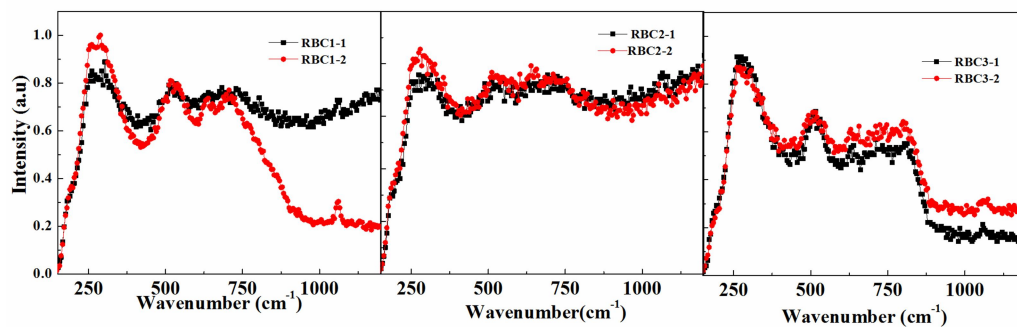


Fig.6.6. Raman spectrum of RBC1, RBC2 and RBC3 films at two energies namely 120 and 160 mJ annealed for 250 shots and 300 shots respectively. (Raman spectrum of RBC1-1, RBC1-2, RBC2-1, RBC2-2, RBC3-1 and RBC3-2 films)

Thus from above results of XRD and Raman spectrum for RT annealed films show the BTO phase formation. Hence we can say now that the phase formation is carried out room temperature. The understanding of laser induced

## 6. Laser induced crystallization of BaTiO<sub>3</sub> thin films

crystalline phase formation is very cryptic. Here in the further discussion we try to explain the crystallization mechanism in the following way.

The femtosecond based lattice recovery studies are well-known, but femtosecond laser doesn't meet the practical requirement of large scale lattice mending. Whereas the nanosecond laser can be more effective in large scale lattice mending processes due to its high thermal diffusion and mobility of solid or particles. Here in the present work, the ultra violet Excimer laser of 20 nanosecond pulse duration and wavelength of 248 nm was used for laser annealing. The spot size while annealing was around 2 cm<sup>2</sup>.

Amorphous solid is a less known state of solids. In crystalline solids the crystal momentum can be considered as quantum number, but this quantum number existing for amorphous solids is less probable. However the long wavelength excitations such as sound waves and spin waves in magnetic materials can be excited and measured. The amorphous state will not be in thermodynamic equilibrium as it is a metastable state. By some non-equilibrium processes we can reach the metastable state. The rate of crystallization and the life-time of metastable states are proportional to  $\exp(-\Delta E/k_B T)$ , the measure of  $\Delta E$  gives the stability of meta stable states [15].

One can observe from the above studies that the deposition parameters are very crucial in the crystallization process. According to Fourier diffusion equation, the temperature rise for few mJ of Excimer laser energy will be of the order of 1000°C. Hence, one can expect the material to become crystalline if the film crystallization temperature is in this range. But, this is not observed in most of the materials. Here, we have observed that the annealing conditions are changing drastically as the deposition conditions are altered even slightly. Hence, it is crucial to understand the effect of deposition parameters on the crystallization process. We have also calculated the shock wave velocity and corresponding

## *6. Laser induced crystallization of BaTiO<sub>3</sub> thin films*

temperature rise using plasma fluid conservation laws. It is found that the shock waves are subsonic in nature with very low velocity  $\sim 150$  m/s. There is no rise in the temperature of material due to these subsonic waves. But as discussed above since the plasma formation is occurring due to the fraction of pulse and the rest of the pulse can be used to pileup the acoustic waves within ps-ns time scale and can form shock wave at a later time, this is identical to the pressure wave formation in the lattice mending mechanism.

The other mechanism one expects is the transition to crystalline phase through a metastable state. It is possible that by periodic incidence of laser pulses can develop a metastable state in the material and hence the transition from amorphous to crystalline can occur.

### **6.5 Summary**

We successfully obtained experimentally the large area room temperature crystallization of complex oxide films using Excimer laser of wavelength 248 nm and pulse duration of 20 ns. The conservation relations based shock wave velocity calculations yield low shock velocity. This low shock speed may support the formation of laser supported combustion waves. This combustion based atomic diffusion and pressure induced lattice mending may be the basic mechanism in the crystallization of these films. The small range order can be expected even in amorphous materials and hence the pores based mending of full lattice could be expected.

## 6. Laser induced crystallization of BaTiO<sub>3</sub> thin films

### References

1. K. Cherenack and Liesbeth van Pieterse, *J. Appl. Phys.* 112, 091301 (2012).
2. M. Kaltenbrunner, T. Sekitani, J. Reeder, T. Yokota, K. Kuribara, T. Tokuhara, Michael Drack, R. Schwodiauer, I. Graz, Simona Bauer-Gogonea, S. Bauer and Takao Someya, *Nature*, 458, 499 (2013).
3. C. Duffus, P. J. Camp, and A. J. Alexander, *J. Am. Chem. Soc.* (2009).
4. B. A. Gartz, et al., *Phys. Rev. Lett.* 77, 3475 (1996).
5. B. A. Gartz, Jelena Matic and Allan S. Myerson, *Phys. Rev. Lett.* 89, 175501 (2002),
6. David W. Oxtoby, *Nature* 420, 277 (2002).
7. L. Leibler, *Macromolecules* 13, 1602 (1980).
8. V. Agrawal, S. M. Barr, J. F. Donoghue, and D. Seckel, *Phys. Rev. Lett.* 80, 1822 (1998).
9. D. Perez, L. J. Lewis, P. Lorazo and Michel Meunier, *Appl. Phys. Lett.* 89, 141907 (2006).
10. Y. Hirayama and M. Obara, *J. Appl. Phys.* 97, 064903 (2005).
11. B. Verhoff, S. S. Harilal, J. R. Freeman, P. K. Diwakar, and A. Hassanein, *J. Appl. Phys.* 112, 093303 (2012).
12. C. R. Phipps, *Laser Ablation and Its Applications* (Springer, New York, 2007).
13. J. P. Romain, *Journal de Physique Colloques*, 45(C8), C8281 (1984).
14. Jeff Colvin, Jon Larsen, *Extreme Physics, Properties and behavior of matter at extreme conditions*, pg. 66, Cambridge University Press, New York, (2014).
15. J A Fernandez-Baca, W-Y Ching, "The Magnetism of Amorphous Metals and Alloys" world scientific, Pg. 176, (1995).

## Chapter 7

# Ultrafast demagnetization of Ni films

---

### Abstract

In the present chapter we studied the ultrafast dynamics of Nickel films by femto sec pump-probe spectroscopy for three different thicknesses of films, namely 65 nm, 135 nm and 1056 nm. It is found that the demagnetization and recovery times are in sub ps and few ps respectively. The transfer of angular momentum from spin system to electron system is of importance in the understanding of ultrafast demagnetization phenomena. We also measured the Gilbert damping parameter from FMR measurements and used these values in calculation of demagnetization times. It is observed that the measured and calculated values are in agreement with measured demagnetization values from pump-probe experiments. This supports the ultrafast unification theory of demagnetization at all - time scales. It is also observed that the Gilbert damping factor is increased with decrease in film thickness. The Gilbert damping factor is inversely proportional to demagnetization time also. In addition to this the films also show THz radiation emission from them and the THz radiation peak-peak amplitude is increased with increase in Gilbert damping factor.



## **7. Ultrafast demagnetization of Ni films**

### **7.1 Introduction**

Since the pioneering experiment by Beaurepaire et al, in 1996 [1], there has been continuous effort by many groups to understand the ultrafast demagnetization phenomena. It is one of the highly evolved mechanisms developed for the high speed read write devices. The energy exchange between different reservoirs takes place at different time scales. Hence, the understanding of energy exchange between the three reservoirs namely spin, electron and lattice is a fundamental problem in ultrafast demagnetization phenomena. Some reports suggest that the well-known spin-orbit interaction is responsible for the transfer of spin angular momentum to electron orbital angular momentum. As compared to the other two exchange mechanisms the finding of spin system energy loss is more important, as the magnetic order is formed of spin system. The one very important hint to the problem is the incident photon energy cannot be directly coupled to spin system in the non-relative frame. The electric dipole selection rule cannot allow these spin based transitions. In addition to the study of ultrafast dynamics in the development of ultrafast read-write memory devices, the ps time scale dynamics gives extra dimension in studying THz radiation from these materials [2-5].

There are large categories of materials having their most useful characteristic information in the low frequency phonons ( $\leq 5\text{THz}$ ) range. The triggering potential is very small for most of the High energy materials and hence interaction with lasers or high intense light or spark will lead to the detonation of these materials in the detection process. The detection of these materials is an important task and hence it requires some other frequency radiation. The frequency of this radiation lies in THz region (0.1-3THz) [6]. There are well-

## 7. Ultrafast demagnetization of Ni films

known materials which supports the THz radiation generation process. But still the materials development for THz generation is an evolving field.

### 7.2 Magnetic studies of Ni films

The M-H measurements for these Nickel films were carried out by Physical Property Measurement System (PPMS) VSM. The M-H measurements were carried out for three different thickness of film namely 65 nm, 135 nm and 1018 nm.

#### 7.2.1 M-H measurements

The figure below shows the M-H loops of Nickel films with three different thicknesses measured by vibrating sample magnetometer (VSM PPMS).

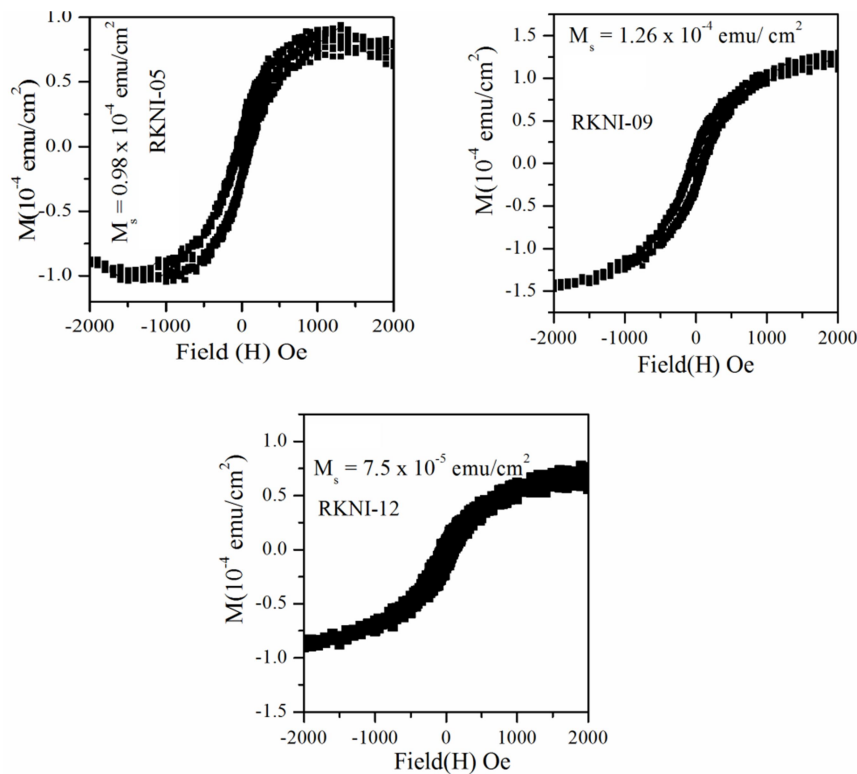


Fig.7.1. M-H loops of RKNI-05, RKNI-09 and RKNI-12 films.

### 7. Ultrafast demagnetization of Ni films

The RF sputtered films RKNI-05, RKNI-09 and RKNI-12 are with thicknesses of 1056 nm, 135 nm and 65 nm respectively. The M-H measurements were carried out in studying the anisotropy effects on FMR signal [7]. The anisotropy calculations need the saturation magnetization values. The saturation magnetization values for the above three films are obtained from M-H loops and their values are  $0.98 \times 10^{-4}$  emu/cm<sup>2</sup>,  $1.26 \times 10^{-4}$  emu/cm<sup>2</sup> and  $7.5 \times 10^{-5}$  emu/cm<sup>2</sup> respectively.

#### 7.2.2 FMR measurements

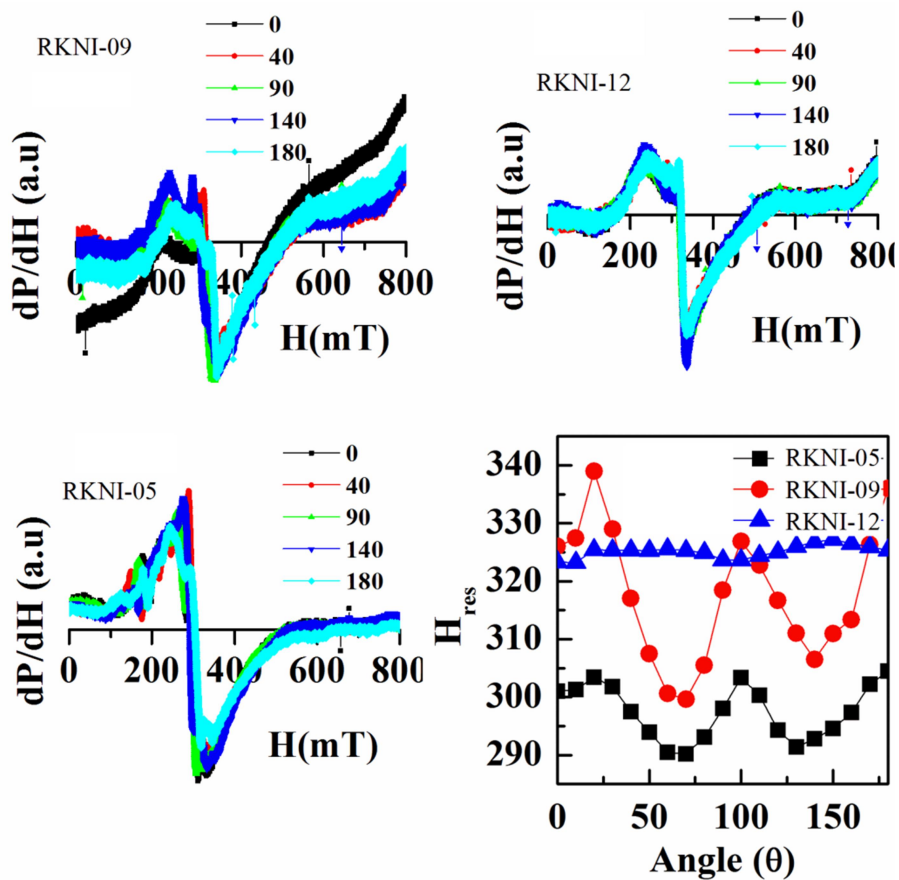


Fig.7.2. Room temperature angle dependent FMR spectra of RKNI-12, RKNI-09 and RKNI-05 films

## 7. Ultrafast demagnetization of Ni films

The Ferromagnetic resonance studies were carried out by (JEOL, JES-FA200) spectrometer in the X-band frequency region. Fig.7.2. shows the FMR spectra of the three films of thickness 65 nm (RKNI-12), 135 nm (RKNI-09) and 1018 nm (RKNI-05). All three films show the asymmetric FMR signal with splitting. This multiple resonances in the film could be due to the spin wave excitations in the film. The Gilbert damping is an important mechanism in explaining the damping in the films. The various parameters like resonance field ( $H_{res}$ ), Peak-peak width  $\Delta H_{pp}$  and Gilbert damping parameter ( $\alpha$ ) etc. are obtained from the FMR measurements and are tabulated in table 1.

### 7.2.3 Gilbert damping parameter calculation from FMR

From the various damping's, Gilbert damping is vital in understanding the ultrafast demagnetization phenomena. R. Urban et. al, [8] investigated the Gilbert damping by ferromagnetic resonance (FMR) in magnetic multilayers. The additional FMR signal broadening demonstrates the electron angular momentum transfer between the magnetic layers that leads to additional relaxation torques.

The Gilbert damping parameter ( $\alpha$ ) is calculated by the following eqn. 1.

$$\alpha = \frac{\gamma^l \Delta H_{PP}}{4\pi f} \quad 1$$

Where  $\Delta H_{PP}$  = FMR peak to peak line width,  $\gamma^l = \frac{\omega}{H}$  and  $f$  is the resonance frequency.

The all above values obtained for these three films are tabulated in table 1. The 65 nm film shows the higher value for  $\alpha$  and it is lowered to 0.0069 for the sample with higher thickness of 1056 nm.

## 7. Ultrafast demagnetization of Ni films

Table 1: Various parameters obtained from VSM and FMR measurements.

Sample code	Thickness (nm)	$H_{R\perp} - H_{R\parallel}$ (Oe)	$\Delta H_{pp}$ (Oe)	Resonance field ( $H_r$ ) (Oe)	Gilbert damping ( $\alpha$ )	$M_s$ ( $10^{-4}$ emu/cm <sup>2</sup> )
RKNI-12	65	0.30	249	3228	0.0106	0.75
RKNI-09	135	6.00	208	3262	0.0088	1.26
RKNI-05	1018	3.00	150	2994	0.0069	0.98

### 7.3 Ultrafast demagnetization studies

#### 7.3.1 Landau-Lifshitz-Gilbert damping

The interaction between magnetic moment and field is fundamental in understanding the magnetization dynamics. If  $M$  is the magnetization per unit volume of a homogeneously magnetized solid, even in a homogeneously magnetized sample can be similar if we consider small regions of the sample in which the magnetization is constant. In such cases the torque on the magnetization by the applied field  $H$  is given by the following expression.

$$T = M \times H$$

Therefore

$$\frac{dL}{dt} = T = M \times H$$

$$\text{But } L = M/\gamma$$

Then the above expression becomes

$$\frac{dM}{dt} = \gamma(M \times H) \quad 2$$

## 7. Ultrafast demagnetization of Ni films

Thus equation (2) describes the precessional motion of magnetization when there is no damping.

The field need not be applied from outside or it is not the only field; it can be a sum of various fields like external field, an isotropy field and demagnetization field etc. Hence, we can write down the field as  $H_{eff}$ . When the dissipation term is added to the equation 2, the equation is termed as Landau-Lifshitz-Gilbert (LLG) damping equation.

$$\frac{\partial M}{\partial t} = \gamma(M \times H_{eff}) + \frac{\alpha}{M} \left( M \times \frac{\partial M}{\partial t} \right) \quad 3$$

Where  $\alpha$  is called the dimensionless phenomenological Gilbert damping constant.

The expression in equation (3) is used to describe the switching dynamics of microscopic magnetic moments [9, 10]. The limitation of LLG equation is that the equation is inadequate in explaining the dynamics if the time scale is shorter than spin-orbit coupling time.

It is found in most of the experiments that the quenching time lies in sub ps time scales [1]. As the laser pulse is incident on the material, a strong - non equilibrium situation will be created between excited electronic degrees of freedom and non-excited spin and lattice degrees of freedom. Thus, in these kinds of systems we have three reservoirs for the energy and momentum transfer. The effective energy and momentum transfer between the reservoirs depends on the strength of coupling. The ultrafast dynamics are well explained by considering the phenomenological three temperature model [1].

For a single quantum particle (e.g., electron), the orbital (L) and spin (S) magnetic moments can change such that the total angular momentum will be conserved. The quenching of S and L or spin flipping is lead to the various other mechanisms like, 1. Stoner-excitations, 2. Electron-Magnon scattering, 3. Phonon-Mediated spin-flip etc [11- 13].

## 7. Ultrafast demagnetization of Ni films

B. Koopmans et. al.[14] tried to unify and explain the ultrafast demagnetization at all-time scales by considering the Landau-Lifshitz-Gilbert equation. It is observed that the demagnetization time is inversely related to the Gilbert damping factor. The Gilbert damping is varied with different arrangement like growing film on different metal substrates like Pt, Cu, etc. It can also be tuned by varying the thickness of the film [15-20].

### 7.3.2 Pump-probe experimental setup

The experimental parameters for pump-probe experiments are given below. The detailed description of the setup is given in chapter 2. The schematic of pump-probe measurement setup is given here also in fig.7.3.

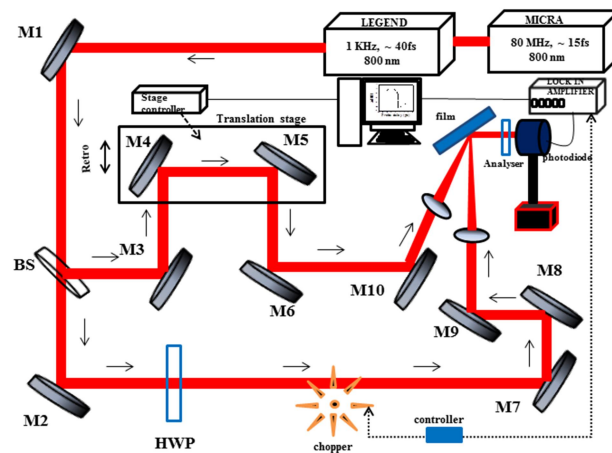


Fig.7.3. Schematic of pump-probe measurement setup.

Wavelength	: 800 nm
Pulse energy	: 80 $\mu$ J
Spot size	: 80 $\mu$ m
Energy density	: 10mJ/cm <sup>2</sup>
Pulse width	: 80 fs
Lenses f1, f2	: 150 mm, 500 mm
Chopper freq	: 100 Hz
Lock-in Ampl	: 7265, Signal Recovery
Photo diode	: SM05R/M, Thorlabs

### 7.3.3 Pump-probe measurements

The presence of pico and femtosecond laser make it easier to study the dynamics in the nano as well as picosecond resolved time scales. In the present case of ferromagnetic material it explores the interaction between the polarized light and magnetization of the material. This interaction changes were correlated by measuring the change in polarization of the incident light. In the small perturbation case the effects are linear and hence one can obtain the magnetization state in the region by measuring the change in reflected light polarization. The pump pulse is of higher intensity compared to probe pulse and the delay between these two pulses is controlled by delay generator. The delay between the pulses is increased and thus the reflectance measured at different delay times. The reflectance signal shows drastic decrease in value and the mechanism of this magnetization decrease is analysed using Landau-Lifshitz-Gilbert equation.

The degenerate pump probe measurements were carried out using 800 nm wavelength laser with a pulse width of 80 fs. As shown in fig.7.3, the sample is kept at 45° to the laser pump, with probe beam in the reflection mode geometry. The fig.7.4 shows the transient reflection spectra of three different Ni films of thicknesses 65 nm, 135 nm and 1018 nm. The transient reflectivity curves are fitted by using eqn. (4). From the fitting the demagnetization time ( $\tau_M$ ) and recovery time ( $\tau_R$ ) were obtained and presented in table 2.

$$\Delta M(t) = -\theta(t) \left[ k_1 \left( 1 - e^{-\frac{t}{\tau_M}} \right) e^{-\frac{t}{\tau_R}} + k_2 \left( 1 - e^{-\frac{t}{\tau_R}} \right) \right] \quad 4$$

## 7. Ultrafast demagnetization of Ni films

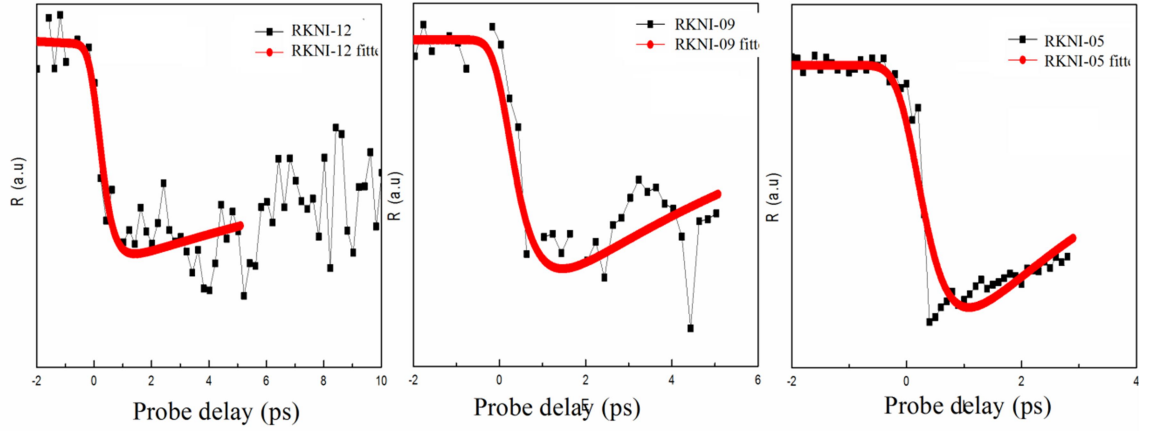


Fig.7.4. Transient reflectance variation with probe delay time in ps of RKNI-05, RKNI-09 and RKNI-12.

### 7.3.4 Demagnetization time/Gilbert damping from pump-probe measurements

The Gilbert damping which is calculated from FMR measurements is used in calculating the demagnetization time. It is found that it is in agreement with the demagnetization value calculated from the pump-probe measurements.

$$\tau_M = \frac{C_0 \hbar}{k_B T_c \alpha} \quad 5$$

Table 2: The pump-probe measured times ( $\tau_M$ ,  $\tau_R$ ) and calculated demagnetization time ( $\tau_M$ ) using the Gilbert damping constant.

S. No.	Sample code	$\tau_M$ (ps)	$\tau_R$ (ps)	Gilbert damping ( $\alpha$ )	Calculated ( $\tau_M$ ) (ps)
1	RKNI-12	0.30	12.00	0.0106	0.285
2	RKNI-09	0.45	8.00	0.0088	0.344
3	RKNI-05	0.40	4.26	0.0069	0.438

## **7.4 THz generation from Ni films**

The evident mechanism for THz generation from ferromagnetic film seems to be the ultrafast demagnetization of ferromagnetic order. But it is observed that Gilbert damping is vital in understanding the generated THz signal intensity. There are only few reports that consider the Gilbert damping effect on THz generation [21, 22]. Here, we have varied the Gilbert damping factor by changing the film thickness, and studied its effect on THz generation.

### **7.4.1 THz generation setup description**

Coherent chameleon ultra-II output beam at 800 nm wavelength and 140 fs with 80MHz repetition rate is used in the THz generation. The fundamental beam is split into two beams using 10:90 beam splitter. The reflected part of the beam is used as a pump beam and focused on to Ni film by using Plano convex lens of focal length 10cm. The incident angle of pump beam is fixed at  $45^\circ$  with the film surface. The 3.8 W pump beam is used for the generation of THz radiation from Ni film. The THz radiation is generated from the Ni films through ultrafast demagnetization process. The combined reflected pump beam and generated THz radiation is allowed to pass through the Teflon sheet of thickness 2mm and diameter of 10mm and black polyethylene filter of 0.2  $\mu\text{m}$  thickness. This filters cutout the visible pump beam part and transmit the generated THz radiation through it. The passed THz radiation pulses collected collimated and then made to focus on THz detector (Baptop SI-GaAs PC antennas) by parabolic mirrors of diameter (D)  $\sim 50$  mm and an effective focal length (fe)  $\sim 150$  mm. The one more transmitted beam from the BS is used as probe beam and is also incident on the detector through a Plano convex lens of focal length 50 cm and detected by PC sampling technique. The PC antenna is connected to a Lock in amplifier (SR 830) through a low noise current amplifier. Thus, the THz induced

## 7. Ultrafast demagnetization of Ni films

voltage is measured. The delay of probe beam is varied to measure the the temporal variation of generated THz radiation.

### 7.4.2 THz radiation temporal profiles for Ni films

The spectral peak amplitudes of generated THz pulses are 4.96 a.u., 4.83 a.u. and 2.81 a.u. for RKNI-12, RKNI-09 and RKNI-05 films respectively and it is extended up to 0.8 THz. The THz temporal signals are shown in fig.7.5. In addition, the peak-peak amplitude is decreasing with increase in film thickness. It can be explained on the basis of Gilbert damping effect on ultrafast demagnetization process, which governs THz generation in Ni films.

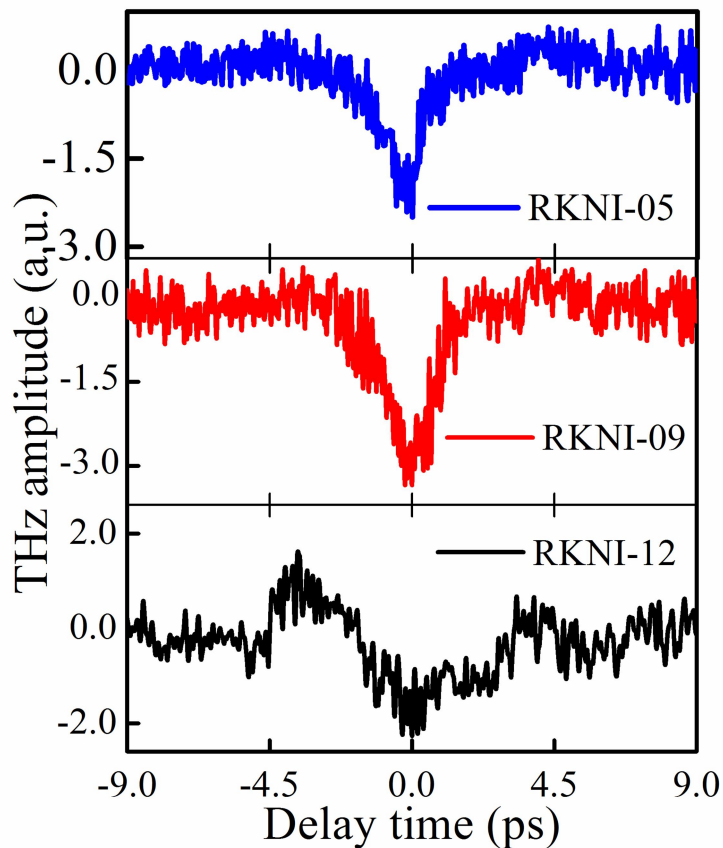


Fig.7.5 THz temporal profile of Ni films

### 7.4.3 Ultrafast demagnetization and Gilbert damping effects on THz radiation

The THz generation is related to ultrafast demagnetization. The pump-probe measurements show that the demagnetization time is in sub ps range. This demagnetization process involves intrinsic spin dynamics that is responsible for the electromagnetic radiation generation with frequency in the THz range. The generated electric field can be written as following eqn. (6)

$$E_y(t) = \frac{\mu_0}{4\pi^2 r} \frac{\partial^2 M_x}{\partial t^2} \left( t - \frac{r}{c} \right) \quad 6$$

The time dependence of magnetization is given by eqn. (4)

Here, in the present case we measured the Gilbert damping coefficient for three different thickness of films by two different methods namely FMR and pump-probe measurements. The THz peak-peak amplitude variation with respect to film thickness are shown in Fig. 7.6 The Gilbert damping values of RKNI-12, RKNI-09 and RKNI-05 films are  $10.6 \times 10^{-3}$ ,  $8.8 \times 10^{-3}$ , and  $6.9 \times 10^{-3}$ , respectively. Therefore, the Gilbert damping values are decreasing with increase in film thickness and hence ultrafast demagnetisation time is increasing. In addition, THz peak-peak amplitude is increasing with Gilbert damping coefficient while it is decreasing with film thickness. Therefore, the high intensity THz pulses can be generated by increasing the Gilbert damping coefficient using ultrathin films.

## 7. Ultrafast demagnetization of Ni films

Table 3: THz P-P amplitude dependence on film thickness, Gilbert damping, demagnetization time.

S. No.	Film	THz (p-p) amplitude (a.u)	Thickness (nm)	Gilbert damping ( $\alpha$ )	$\tau_M$ (ps)
1	RKNI-12	4.96	65	0.0106	0.30
2	RKNI-09	4.83	135	0.0088	0.45
3	RKNI-05	2.81	1018	0.0069	0.40

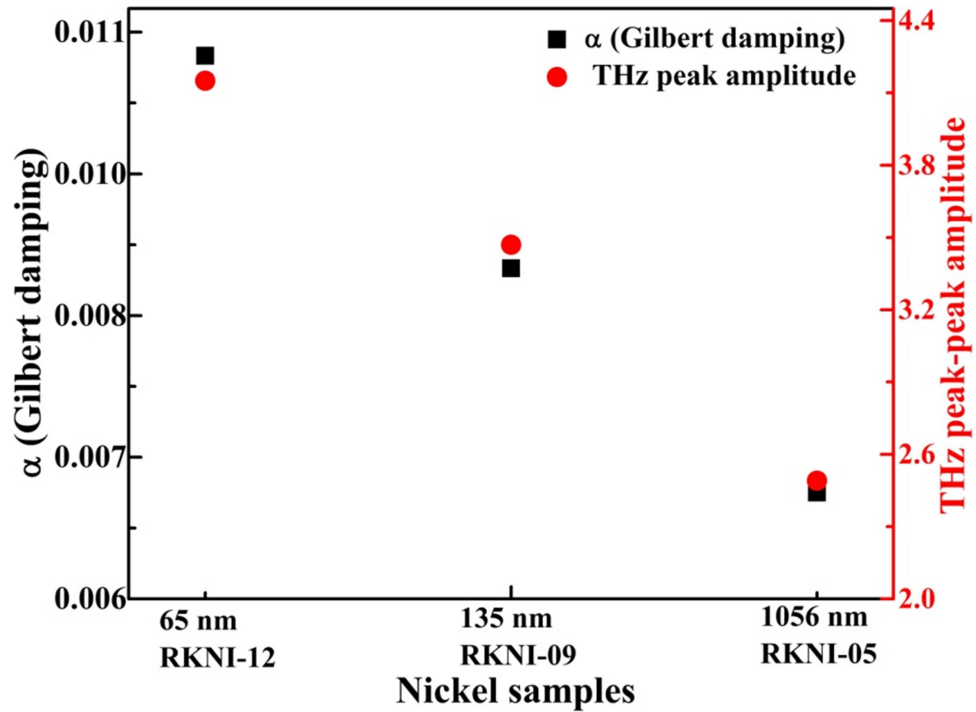


Fig.7.6 Dependence of Gilbert damping coefficient ( $\alpha$ ) on film thickness and variation of THz peak-peak amplitude with  $\alpha$ .

### **7.5 Summary**

The Ferromagnetic resonance measurements on (200) oriented RF-magnetron sputtered three different thickness films show that the Gilbert damping parameter is increased from 0.0069 to 0.0106 with decrease in film thickness from 1056 nm to 65 nm. The ultrafast demagnetization ( $\tau_M$ ) and recovery ( $\tau_R$ ) time values were obtained by the pump-probe measurements. The  $\tau_M$  values are in the ps ranges whereas the  $\tau_R$  values are of few ps. The demagnetization time which was calculated using Gilbert damping parameter is in agreement with the measured values from pump-probe measurements. Thus it helps in unifying the two different time scale phenomena as suggested by B. Koopmans et.al. The THz signal measurements from these films also support the pump-probe measurements. The generated THz peak–peak amplitude is higher for the film having lesser thickness and explained on the basis of Gilbert damping effect.

**References**

1. E. Beaurepaire, J.-C. Merle, A. Daunois, and J.-Y. Bigot, *Phys. Rev. Lett.* 76, 4250 (1996).
2. E. Beaurepaire, G. M. Turner, S. M. Harrel, M. C. Beard, J.-Y. Bigot, and C. A. Schmuttenmaer, *Appl. Phys. Lett.* 84, 3465 (2004).
3. V. V. Kruglyak, M. E. Portnoi, and R. J. Hicken, *J. of Nanophotonics*, 1, 013502 (2007).
4. R. Rungsawang, F. Perez, D. Oustinov, J. Go´mez, V. Kolkovsky, G. Karczewski, T. Wojtowicz, J. Made´o, N. Jukam, S. Dhillon, and J. Tignon, *Phys. Rev. Lett.* 110, 177203 (2013).
5. R. V. Mikhaylovskiy, E. Hendry, V. V. Kruglyak, R. V. Pisarev, Th. Rasing, and A. V. Kimel, *Phys. Rev. B* 90, 184405 (2014).
6. R. Miles, X.-C. Zhang, H. Eisele, A. Krotkus, “Terahertz Frequency Detection and Identification of Materials and Objects” 307-317, (2007).
7. X. Liu, Y. Sasaki, and J. K. Furdyna, *Phys. Rev. B* 67, 205204 (2003)
8. R. Urban, G. Woltersdorf, and B. Heinrich, *Phys. Rev. Lett.*, 87, 217204 (2001).
9. T. L. Gilbert, *Phys. Rev.* 100, 1243 (1955),
10. A. Kirilyuk, A. V. Kimel, and T. Rasing, *Rev. Mod. Phys.*, 82, 2731 (2010).
11. M.G. Munzenberg, *Nature Materials* 9, 184 (2010).
12. B. Koopmans, G. Malinowski, F. Dalla Longa, D. Steiauf, M. Fahnle, T. Roth, M. Cinchetti and M. Aeschlimann, *Nature Materials* 9, 259 (2010).
13. A. M. Kalashnikova, A. V. Kimel, R. V. Pisarev, V. N. Gridnev, P. A. Usachev, A. Kirilyuk, and Th. Rasing, *Phys. Rev. B* 78, 104301 (2008).

### *7. Ultrafast demagnetization of Ni films*

14. B. Koopmans, J. J. M. Ruigrok, F. Dalla Longa, and W. J. M. de Jonge, *Phys. Rev. Lett.* 95, 267207 (2005).
15. S. Jian, Z. Huai-Wu, L. Yuan-Xun, *Chin. Phys. Lett.* 29, 067502 (2012).
16. E. Simanek, B. Heinrich, *Phys. Rev. B* 67, 144418 (2003).
17. S. Mizukami, Y. Ando, and T. Miyazaki, *Phys. Rev. B* 66, 104413 (2002).
18. Y. Tserkovnyak and A. Brataas, Gerrit E.W. Bauer, *Phys. Rev. Lett.* 88, 117601 (2002).
19. J Walowski, M. D. Kaufmann, B Lenk, C Hamann, J Mc Cord and M Munzenberg, *J. Phys. D: Appl. Phys.* 41, 164016 (2008).
20. E. Barati, M. Cinal, D. M. Edwards, and A. Umerski, *Phys. Rev. B* 90, 014420 (2014).
21. J. Shen, X. Fan, Z. Chen, M. F. DeCamp, H. Zhang, and J. Q. Xiao, *Appl. Phys. Lett.* 101, 072401 (2012).
22. S. Jian, Z. Huai-Wu, L. Yuan-Xun, *Chin. Phys. Lett.* 29, 067502 (2012).

## Chapter 8

### Conclusions and scope for future work

---

*The present chapter summarizes the results obtained in the preceding chapters on Magnetism in nanocrystalline BTO, crystallization of pulsed laser deposited BTO films and ultrafast demagnetization of Ni film.*

### 8. Conclusions and scope for future work

#### 8.1 Conclusions

In view of explaining the magnetism in nanocrystalline BTO, the optical properties are studied for nanoparticles, higher temperature calcined nanocrystalline BTO and for mesocrystal BTO in addition to the magnetic measurements. The strain and exchange correlation interactions are very crucial in explaining the observed magnetism.

The study of involvement of multiple effects in narrowing the band gap of nc-BTO NPs by analyzing XRD, Raman and optical spectrum for four different sizes of BTO nanoparticles and BTO mesocrystals were carried out. It is found that the strain, electron-phonon interactions, and exchange - correlation interactions were involved in band gap reduction of sol-gel prepared nanoparticles, whereas, the dielectric confinement effect cause the giant bandgap renormalization in BTO mesocrystal.

The bleaching of optical absorption with higher band gap values is observed for 31 nm and 34 nm particles compared to 23 nm and 54 nm size particles. Thus the band gap renormalization in 23 and 54 nm size particles is due to the presence exchange correlation interactions between the charge carriers. The particles with average sizes of ~31 nm and ~34 nm did not show marginal band gap narrowing. Thus, it can be said that the O 2P, and Ti 3d, states were mixed to

## ***8. Conclusions and scope for future work***

yield a counter renormalization of band gap due to increase of the electron effective mass. Therefore, the increased charge carrier concentration increased the magnetic moment values due to the dominant exchange interactions between the carriers. And, band gap narrowing was observed for higher carrier density. These arguments are also supported by the Z-scan measurements where one of the samples showed negative refractive index ( $n_2$ ) in addition to the higher charge carrier density in them. It also confirms the large charge carrier density present in them. The 54 nm size particles with highly narrowed band gap show the charge carrier density nearer to Mott carrier density.

The band gap of 2.00 eV is obtained for BTO mesocrystals. This giant band gap narrowing is explained by considering the dielectric confinement effect. The exciton binding energies were obtained to be around 1.2eV, this enhanced binding energy values are the consequence of dielectric confinement in the material. Thus the observed bandgap narrowing hints the presence of exchange correlation interactions in the material.

The observation of magnetic moment increase with the decrease in particle size and bandgap confirms the super paramagnetic behavior of low temperature calcined particles. The ZFC-FC measurements show the lower bifurcation temperature ( $T_b$ ) of 150K for 31nm size particles. The ~23 nm, ~34 nm and ~54 nm size particles showed higher bifurcation temperatures in the range of 250K-270K. Thus the higher carrier density samples displayed higher magnetic ordering with lower band gap values due to the exchange correlation interactions between the carriers. The variation in magnetic moment with particle size gives the super paramagnetic characteristic curve for low temperature calcined samples. Whereas, the high temperature calcined samples suppresses this super paramagnetic behavior and shows a ferromagnetic state with transition temperature of 56 K. We also discussed the necessity of involving charge transfer effects in explaining the

## ***8. Conclusions and scope for future work***

magnetism in high temperature calcined nc-BTO. The charge transfer effects were considered and the observed magnetism is explained by considering the modified Stoner criterion.

The M-H and M-T measurements for crystalline BTO mesocrystals show the increase of ferromagnetic transition temperature to 131 K. This is because of the dielectric confinement which increased electron-electron interactions in the system. Thus the BTO mesocrystals are found to be the most attractive system to study the ferromagnetism in BTO.

We obtained experimentally the large area room temperature crystallization of BTO films by Excimer laser (wavelength 248 nm and pulse duration of 20 ns) annealing. The conservation relations based shock wave velocity calculations yield low shock velocity. This low shock speed may support the formation of laser supported combustion waves. This combustion based atomic diffusion and pressure induced lattice mending may be the basic mechanism in the crystallization of these films. The small range order can be expected even in amorphous materials and hence the pores based mending of full lattice could be expected.

The study of ultrafast demagnetization (UFD) ferromagnetic materials is highly developed. From the pump-probe spectroscopy measurements for 65 nm, 135 nm and 1056 nm Ni films, it is found that the demagnetization and recovery times are in sub ps and few ps respectively. The transfer of angular momentum from spin system to electron system is of importance in the understanding of ultrafast demagnetization phenomena. We also measured the Gilbert damping parameter from FMR measurements and used these values in calculation of demagnetization times. It is observed that the measured and calculated values are in agreement with measured demagnetization values from pump-probe experiments. This supports the ultrafast unification theory of demagnetization at

## ***8. Conclusions and scope for future work***

all-time scales. It is also observed that the Gilbert damping factor is increased with decrease in film thickness. The Gilbert damping factor is inversely proportional to demagnetization time also. In addition to this, the films also show THz radiation emission from them and the THz radiation peak-peak amplitude is increased with increase in Gilbert damping factor.

### **8.2 Scope for future work**

The work carried out in the present thesis have created more interest to carry out further research in related fields like magnetism, laser matter interaction and flexible electronics.

1. The bandgap narrowed BTO nanoparticles can be studied for their solar energy harvesting applications.
2. The non-radiative decay (weak photo luminescence) at 355 nm excitation hints at the multi phonon states in the system and these are essential for infrared radiation absorption and hence could be useful in photovoltaics.
3. BTO mesocrystals are found to be very attractive materials in understanding the BTO magnetism and hence magnetic studies can be carried out on this material.
4. The BTO mesocrystals are expected to have high nonlinear optical properties.
5. Study of piezoelectric properties of BTO mesocrystals.
6. Study of magneto electric properties of BTO mesocrystals.
7. Understanding the mechanism of laser induced crystallization (LIC).
8. Crystallization of ferroelectric thin films on flexible substrates by laser annealing.
9. Study of microwave dielectric properties of laser annealed films.
10. Study of magnetism of laser annealed films and defective BTO films.

**List of Publications/Proceedings**

1. **S. Ramakanth** and K. C. James Raju, “Growth of preferred oriented  $\text{Ba}_{0.5}\text{Sr}_{0.5}\text{TiO}_3$  films on amorphous substrates by RF sputtering” **AIP Conf. Proc.** 1447, 1339 (2012).
2. **S. Ramakanth** and K. C. James Raju, “Substrate Effect on Plasmon Resonance of a Gold Nanoparticle Embedded Amorphous  $\text{BaTiO}_3$  Film” **Soft Nano Sci. Lett.** 3, 32 (2013).
3. **S. Ramakanth** and K. C. James Raju, “Charge transfer induced magnetism in sol–gel derived nanocrystalline  $\text{BaTiO}_3$ ” **Solid State Commun.** 187, 59 (2014).
4. **S. Ramakanth** and K. C. James Raju, “Band gap narrowing in  $\text{BaTiO}_3$  nanoparticles facilitated by multiple mechanisms” **J. Appl. Phys.** 115, 173507 (2014).
5. **S. Ramakanth**, S Hamad, S Venugopal Rao, and K. C. James Raju “Magnetic and nonlinear optical properties of  $\text{BaTiO}_3$  nanoparticles” **AIP Advances** 5, 057139 (2015).
6. M. Venkatesh, **S. Ramakanth**, A.K. Chaudhary and K.C. James Raju, “Study of terahertz emission from nickel (Ni) films of different thicknesses using ultrafast laser pulses” **Optical Materials Express** 6, 2342 (2016).
7. J. Pundareekam Goud, A Joseph, **S Ramakanth**, K L Naidu, and K C James Raju, “Microwave dielectric and optical properties of amorphous and crystalline  $\text{Ba}_{0.5}\text{Sr}_{0.5}\text{TiO}_3$  thin films”, **AIP Conf. Proc.** 1728 020293 (2016).
8. J. Pundareekam Goud, **S Ramakanth**, Andrew Joseph, Sandeep Sharma, G Lakshminarayana Rao, and K C James Raju, “Effect of crystallinity on microwave tunability of pulsed laser deposited  $\text{Ba}_{0.5}\text{Sr}_{0.5}\text{TiO}_3$  thin films”, **Thin Solid Films**, 626, 126 (2017).

### *List of Publications/Proceedings*

9. **S. Ramakanth**, G. Swathi and K. C. James Raju “Giant bandgap renormalization in BaTiO<sub>3</sub> mesocrystal: prospects for solar energy harvesting” (**Under Review in Physica E**).
10. **S. Ramakanth** and K. C. James Raju, “Phonon confinement in BaTiO<sub>3</sub> nano particles”. (To be communicated)
11. **S Ramakanth**, P T Anusha, S Venugopal Rao and K C James Raju, “Gilbert damping correlated ultrafast magnetization dynamics in Nickel film”. (To be communicated).
12. **S Ramakanth**, J Pundareekam Goud, K C James Raju, “Laser induced crystallization of BaTiO<sub>3</sub>”. (To be communicated).
13. **S Ramakanth and K C James Raju** “Magnetic properties of BaTiO<sub>3</sub> mesocrystals”. (To be communicated).

### **Conferences/Symposium/ Workshops attended**

1. The 56th DAE-Solid State Physics Symposium (DAE-SSPS) was held at SRM University, Kattankulathur (Chennai) December 19-23, 2011. (Poster presentation).
2. INDO-US International Workshop on Nanosensor Science & Technology, at NIST Berhampur, during 27th February-1st March, 2013. (Poster presentation)
3. Awareness workshop of UGC-DAE consortium for Scientific Research organized by UGC-DAE consortium for scientific Research, Mumbai Centre and School of Engineering Sciences and Technology at University of Hyderabad during 28<sup>th</sup> – 30<sup>th</sup> October, 2013. (Participant).
4. International Conference IUMRS-ICA-2013 at IISc, Bangalore, during 16<sup>th</sup>– 20<sup>th</sup> December, 2013. (Poster presentation).